



[ur] DIMENSIONS

The Journal of Undergraduate Research
In Natural Sciences And Mathematics

Volume **17**
Spring **2015**

(ur) DIMENSIONS

The Journal of Undergraduate Research In
Natural Sciences And Mathematics

Volume **17**
Spring **2015**

Marks of a CSUF Graduate from the College of Natural Sciences and Mathematics

Graduates from the College of Natural Sciences and Mathematics:

Understand the basic concepts and principles of science and mathematics.

Are experienced in working collectively and collaborating to solve problems.

Communicate both orally and in writing with clarity, precision and confidence.

Are adept at using computers to do word processing, prepare spreadsheets and graphs, and use presentation software.

Possess skills in information retrieval using library resources and the Internet.

Have extensive laboratory, workshop, and field experience where they utilize the scientific method to ask questions, formulate hypotheses, design and conduct experiments, and analyze data.

Appreciate diverse cultures as a result of working side by side with many people in collaborative efforts in the classroom, laboratory and on research projects.

Have had the opportunity to work individually with faculty members in conducting research and independent projects, often leading to the generation of original data and contributing to the research knowledge base.

Are capable of working with modern equipment, instrumentation, and techniques.

Dimensions

Dimensions: The Journal of Undergraduate Research in Natural Sciences and Mathematics is an official publication of California State University, Fullerton. Dimensions is published annually by CSUF, 800 N. St. College Blvd., Fullerton, CA 92834. Copyright ©2015 CSUF. Except as otherwise provided, Dimensions: The Journal of Undergraduate Research in Natural Sciences and Mathematics grants permission for material in this publication to be copied for use by non-profit educational institutions for scholarly or instructional purposes only, provided that 1) copies are distributed at or below cost, 2) the author and Dimensions are identified, and 3) proper notice of copyright appears on each copy. If the author retains the copyright, permission to copy must be attained directly from the author.

About the Cover

This year's cover makes use of shape and line to create depth and dimension. The linework and the texture that make up the cover are a reflection upon the intricacies of math and science.

Acknowledgments

Editor-In-Chief

Reina Galvez - Mathematics

Editors

Matthew Scanlon - Biology

Neha Ansari - Chemistry and Biochemistry

Jazmine Titular - Geology

Shiline Nguyen - Mathematics

Phillipe Diego Rodriguez - Physics

Advisor

Amy Mattern - Assistant Dean for Student Affairs

Graphic Design

Niv Ginat - Layout Editor

Alfred Harris - Cover Designer

College of Natural Sciences & Mathematics

Dr. David Bowman - Interim Dean

Dr. Mark Filowitz - Associate Dean

Dr. Kathryn Dickson - Chair, Department of Biological Science

Dr. Christopher Meyer - Chair, Department of Chemistry and Biochemistry

Dr. Phillip Armstrong - Chair, Department of Geological Sciences

Dr. Stephen Goode - Chair, Department of Mathematics

Dr. James M. Feagin - Chair, Department of Physics

College of the Arts

Dr. Jim Tauli - Interim Dean

Dr. Arnold Holland - Associate Dean (Advisor to the Graphic Design Team)

Maricela Alvarado - Interim Assistant Dean for Student Affairs

Special Thanks To

President Mildred García, Interim Dean David Bowman
and **Assistant Dean Amy Mattern** for their support and
dedication to Dimensions.

Biology

Demographics and Movement of a Sky-island Population of the Western Fence Lizard (*Sceloporus occidentalis*)

8 A. D. Barraza, A. C. Castanon, B. D. Rivas,
E. C. Ruelas, P. Shankar, C. R. Tracy, and W. J. Hoese

Making Connections in a Lower Division Undergraduate Biology Class

9 Precious Daileg and Dr. Merri Lynn Casem

Characterizing *Sinorhizobium Meliloti* Strains Overexpressing the *Smb20809* and *Smc02832* Genes

10 David J. Eng, Criselda Dillague, and Esther J. Chen

Examining the Feeding Behavior of *Anthopleura elegantissima* after Low Tide Exposure

11 Joshua N. McKinley and Jennifer L. Burnaford

Graph Interpretation and Construction Tasks in Introductory Biology Textbooks: Preliminary Findings

18 Alicia Mendoza and Eleanor Spangler

California Pipefish Identification Using Morphological Measurements and Genetic Analysis

23 Cristy A. Rice, Douglas J. Eernisse, and Kristy L. Forsgren

Sex Differences in Thermoregulatory Activity of the Common Chuckwalla (*Sauromalus ater*)

30 Emily Sanchez and Christopher Tracy

Chemistry and Biochemistry

Catalytic Phenanthridine Synthesis via Oxidative Cyclization of Substituted 2'-arylbenzaldehyde Oxime Ethers under Photoinduced Electron Transfer Conditions

31 Nicholas Armada, Julie Hofstra, Brittany Grassbaugh, Quan Tran, and Dr. Peter de Lijser

Synthesis and Structure-activity Studies of Drugs that Affect a Cancer Causing Mechanism and Reduce Cell Growth

32 Aneta Jelowicki, Keziah Ellery L. Tan, Elizabeth H.F. Li, Christian A. Martindale, Chiaokai Wen, Christopher M. Ott, Dr. Nilay V. Patel and Dr. Peter de Lijser

Photoinduced Oxidative Cyclizations of o-Arylalkynyloximes Transfer Conditions

33 Michael Ko, Wan Shin Kim, and Dr. Peter de Lijser

Reduction of MM1853 with the Artificial Electron Donor, Dithiothreitol

34 Man Lou and Dr. Madeline Rasche

Green Digital Photographic Method for Protein Assay

35 Theary Monh, Brenna Biggs, Kate Grudpan, Dr. Richard Deming and Dr. Darren Sandquist

Geology

Analysis of a Potential Paleotsunami Deposit at Los Penasquitos Marsh, San Diego County, CA.

36 Jeremy Cordova

Is The Sierra Nevada Frontal Fault System Steep Or Shallow?: Implications For Extention In Owens Valley

50 Brian Gadbois

Geology and Geomorphology of the Three Bare Hills Lake Manly Deposit, Death Valley, California

51 Christopher R. Hugh

Reconstruction of the geographic offset of key fossil localities in Orange County, CA due to faulting on the San Andreas Fault system

58 *Rosa E. Murrieta*

Seismic Hazard Assessment of McCarthy Hall on the California State

59 *Daniel Philo*

Orientation of the Sierra Nevada Frontal Fault Zone near Independence and Lone Pine, California

65 *Greg Shagam*

Reconstructing the Paleoenvironment of Orange County, California Using Eocene Plant Fossils

72 *Daniel Weiherer*

Petrographic and Geochemical Analysis of the Summit Gabbro and Associated Granitoids of the Kern Plateau, Southern Sierra Nevada, California

73 *Elizabeth White*

Did Alpine Glaciers Exist on Sugarloaf Mountain During the Last Glacial (San Bernardino Mountains, California)?

84 *Alex Woodward*

Mathematics

Galois Groups of Special Degree Four Polynomials

85 *Christopher Bang and Joseph Chavoya*

The Impact of Modality Pertaining to Gender and Mathematical Self-Related Beliefs in a High-School Setting

94 *Mirna Dominguez and Erick Venegas*

Importance of Sampling Pattern and Regularization in Under-Sampled Magnetic Resonance Imaging (MRI)

101 *Erick Ortega and Rudolph V. Saenz*

Number Theory in the *Revista Matematică din Timișoara*

113 *Shreya Havaladar*

The Impact of Supplemental Instruction on the SI Leader

116 *Kelly Hartmann and Christina Tran*

Understanding Sophie Germain

121 *Christina Tran*

Physics

Predicting Binary Black Hole Collisions Using Numerical Methods in Collaboration with LIGO

122 *Nousha Afshari*

A time focusing mass spectrometer for electron attachment to nucleotide molecules

123 *Jessica Duron*

Constructing Hybrid Gravitational Waveforms for Merging Black Holes and Neutron stars

124 *Eric Flynn*

Visualizing Binary-Black-Hole Simulations and Exploring Initial Data for Merging Black Holes

125 *Haroon Khan*

Parameter Estimation using Markov chain Monte Carlo

130 *Sean Hatcher*

Studying How Spin Affects Orbits Of Colliding Black Holes

131 *Kevin Kuper*

Orbital Dynamics of Merging Neutron Stars

135 *Phillipe D. Rodriguez*

Demographics and Movement of a Sky-island Population of the Western Fence Lizard (*Sceloporus occidentalis*)

Department of Biological Science, California State University, Fullerton

A. D. Barraza, A. C. Castanon, B. D. Rivas, E. C. Ruelas, P. Shankar, C. R. Tracy, and W. J. Hoese

Abstract

Populations isolated on mountain peaks, sometimes called “sky islands”, often have low genetic diversity and are subject to increasing periods of drought due to climate change, both of which increase the risk of local extinction. Therefore, sky island populations could make good indicators of the effects of climate change. We studied the sky island population of the western fence lizard, *Sceloporus occidentalis*, on Ord Mountain, CA in the Mojave Desert, to examine population demographics and measure individual movement. Based on the demographics of non-isolated populations of *Sceloporus occidentalis*, we hypothesized that we would find three distinct age classes on Ord Mountain and that individuals would be dispersed throughout the habitat. We established four half-hectare plots (50 × 100m), two north and two south of a long-term monitoring site for these lizards on Ord Mountain. We captured *S. occidentalis* over two days in June, marked each individual, and measured mass, snout-vent length (SVL), substrate temperature and GPS coordinates. Individuals fell into three age classes based on SVL: juveniles (51-63mm), sub-adults (66-70mm), and adults (>74mm). Based on recapture data, we estimated the population density to be 35 individuals/hectare, similar to densities in other populations. Movement among individual lizards varied greatly, ranging from 1 to 68 meters (mean: 12.76 m ± 17.19, SD). Movement was generally on the east-west axis and may have followed rock formations. Our findings suggest that some individuals dispersed rather than moving within their home range. Population density and the presence of multiple age classes indicate that the Ord Mountain population is robust, and not at risk of local extinction.

Making Connections in a Lower Division Undergraduate Biology Class

Department of Biological Science, California State University, Fullerton

Precious Daileg and Dr. Merri Lynn Casem

Abstract

Deep understanding is achieved when learners are able to move from lower level thinking (knowledge and factual recall) to higher order thinking (application, analysis, evaluation and synthesis) (Bloom, 1956). The ability of students to recognize relationships between concepts is a first step in this transition to higher order thinking. Gaining these higher order thinking skills is crucial for student success in their college courses (Bissell and Lemons, 2006). The goal of this study was to determine the effectiveness of an instructional intervention geared towards helping students identify and explain connections between concepts. *Concept Cards* represent a variation on the traditional flashcard study aide. The use of *Concept Cards* was tested in a lower division, undergraduate cellular biology supplemental instruction session. We hypothesized that students engaged in the practice of *Concept Cards* during the session would demonstrate improved performance on exam questions that required higher order thinking compared to students that did not. In this preliminary study that included 44 students, we did not find a statistically significant difference between the performance of the control group (2.86 ± 0.14) and the experimental group (2.57 ± 0.29) ($p = 0.27$). In the future, we are planning on expanding the study to include a larger number of students.

Characterizing *Sinorhizobium meliloti* Strains Overexpressing the *Smb20809* and *Smc02832* Genes

Department of Biological Science, California State University, Fullerton

David J. Eng, Criselda Dillague, and Esther J. Chen

Abstract

Endosymbiosis is a mutualistic relationship between the bacterium *Sinorhizobium meliloti* and its legume plant host *Medicago sativa* where the bacteria fixes nitrogen for the plant, which in return supplies the bacteria with carbon sources. The *S. meliloti* ExoS/ChvI two-component system is important for successful endosymbiosis, which is important agriculturally for legumes to grow in soil with low nitrogen content. ExoS/ChvI also regulates many functions in free-living bacteria such as exopolysaccharide production, nutrient utilization and cell envelope integrity. Previous studies in our lab have identified many genes in *S. meliloti* that are transcriptionally regulated by ExoS/ChvI. Here, we characterize two of these genes, *smc02832* and *smb20809*, to better understand the function of these genes. The *smb20809* gene, also called *kpsF1*, encodes arabinose-5-phosphate isomerase and is involved in capsular polysaccharide synthesis. The *smc02832* gene encodes a periplasmic solute-binding protein of an ATP binding cassette (ABC) transporter for amino acids. We have generated overexpression plasmids for both genes and introduced the plasmids into both a *S. meliloti* wild type (WT) strain and the partial loss-of-function *chvI K214T* mutant strain. We observed growth of the strains on different types of media to assess whether overexpression of these genes affected exopolysaccharide production, nutrient utilization, motility, or cell envelope integrity. Our initial results show that overexpression of *smb20809* in WT results in impaired growth on LB, LB containing calcofluor, TY rich media, and minimal media in addition to cell envelope defects and alteration of exopolysaccharide production. Overexpression of *smb20809* in a *chvI K214T* background is toxic to the bacteria and causes a dramatic growth defect. Conversely, overexpression of *smc02832* in WT results in a slight growth defect on LB rich media while overexpression in a *chvI K214T* background affected growth on LB containing calcofluor. Motility was not affected for any of the overexpression strains. Our results show that *smb20809* and *smc02832* are important for *S. meliloti* phenotypes and that changing the expression of these genes affects cell growth and viability.

Acknowledgments

Funding for this project was provided by NSF grant IOS-081981 to E.J.C. and CSU Fullerton Biology Department research funds for students.

Examining the Feeding Behavior of *Anthopleura elegantissima* after Low Tide Exposure

Department of Biology, College of Natural Sciences and Mathematics, California State University, Fullerton

Joshua N. McKinley and Jennifer L. Burnaford

Abstract

In the rocky intertidal zone, animals are submerged in water during high tide and exposed to air during low tide. Exposure to sunlight during low tide can increase body temperatures relative to high tide. High body temperature can damage contractile fibers, leading to impaired movement thus hindering feeding behavior. We asked the question: how does low tide temperature affect the feeding behavior of the anemone *Anthopleura elegantissima*? We hypothesized that the temperature individuals experience during low tide would affect their feeding behavior when the tide came back in. Specifically, we predicted that individuals exposed to high temperatures would recover slower, exhibit weaker responses, and consume fewer food items than individuals exposed to low temperatures during low tide. We exposed anemones to simulated low tides with temperatures of 25°C, 30°C and 35°C and maintained control “high tide” individuals in 16°C seawater. We compared the feeding response of individuals in these four treatments under simulated high tide conditions. We found that individuals exposed to low tides consumed fewer food items on average than control individuals during our trials, but low tide temperature did not affect the total number of food items consumed. However, as we predicted, low tide temperature did have strong effects on anemone behavior (time to opening after submergence and degree of tentacle contraction in response to food items). To understand how ecosystems will respond to climate change, we need to know how temperature affects important species interactions such as predation. Investigations using abundant organisms such as *A. elegantissima* are a good place to start.

1. Introduction

Because the rocky intertidal zone is submerged by water during high tide and exposed to air during low tide, organisms experience different conditions depending on the tide (Bingham et al. 2011, Helmuth 1998). An abiotic condition that plays a major role in the intertidal zone is temperature. An organism’s body temperature is affected by many factors, including solar radiation, evaporation, wind speed and heat exchange with the rocky substratum (Helmuth 1998). Temperature has important effects on ectotherms because body temperature of an ectotherm is regulated by the outside environment (Freeman 2010, Helmuth 1998).

Temperature affects ectothermic animals in many ways on a cellular to organismal level. High temperatures are known to cause an increase in the expression of genes such as the gene that codes for HSP70, a heat shock, or chaperone protein (Han et al. 2013). Heat shock proteins help to prevent cellular damage from denatured proteins (Han et al. 2013). Temperature affects proteins because changes in temperature can alter protein shape by breaking bonds (Somero 2002). High temperatures can affect protein stability because high temperatures have the potential to denature proteins (Han et al. 2013). Muscle performance can also be affected by temperature, because in ectotherms, muscle fibers function best at certain temperatures, which may differ from organism to organism (James 2013).

High tide conditions provide a marine environment in the intertidal zone (Helmuth 1998). Water has a high specific heat, which means that it takes a lot of energy to change the temperature by one degree (Freeman 2010). Therefore due to large amounts of water in the ocean,

water temperature does not fluctuate very much over short periods of time. During high tide, water temperatures in the intertidal zone are relatively constant and cool (approx. 16° C in Southern California; N.O.A.A. 2015). Heat transfer differs in water compared to air. During high tide solar radiation has to diffuse through the water, where convection, heat transfer between a solid and liquid (Freeman 2010) can occur. An ectotherm that is submerged in water during high tide will have a body temperature that is close to the surrounding water temperature due to convection (Helmuth 1998). Due to these conditions ectotherms will not experience many body temperature changes during high tide.

However during low tide, there are more avenues for thermal exchanges while organisms are directly exposed to air (Bingham et al. 2011, Helmuth 1998). Solar radiation from the sun will directly contact the rocky intertidal zone without having to diffuse through water. Substratum and air temperatures in the intertidal zone along the US west coast can have temperatures ranging above 35° C (Helmuth 1998) as opposed to water temperatures of 16° C. At low tide, organisms are exposed directly to wind speed and conduction, which can affect body temperature (Helmuth 1998). Consequently, when the tide goes out, an ectotherm can experience a body temperature change of 15° C or greater over just a few hours (Helmuth 1998).

During low tide, body temperatures can vary over multiple time scales because individuals are exposed to more methods of heat transfer than at high tide and environmental temperatures vary over a variety of time scales. For example, summer days are warmer on average than winter days (Burnaford 2004, Helmuth and Hoffman 2001). On a shorter time scale, low tide intertidal air temperature can increase or decrease 5 degrees during the same month (Burnaford 2004, Helmuth and Hoffman 2001). There can also be day-to-day temperature differences in the intertidal zone (Burnaford 2004, Helmuth and Hoffman 2001). In fact studies have shown that between days in the same month, maximum temperatures can differ by 4.7° C in the rocky intertidal zone (Helmuth and Hoffman 2001). This means that intertidal organisms can experience different temperatures day to day.

In addition to this temporal variation in temperature, in the intertidal zone, there is great spatial variation in temperature. Two organisms which are in different microhabitats can experience very different temperatures

during low tide (Burnaford 2004, Helmuth and Hoffman 2001). For example, in a tide pool temperature will be cooler than a surface that is directly exposed to sunlight (Metaxas and Scheibling 1993). Regions of the intertidal zone that are shaded such as areas under algal canopies or rock will also be cooler than areas exposed to direct sunlight (Burnaford 2004, Gedam et al. 2011). The angle of the substratum has also been shown to affect the amount of heat received at a given area (Helmuth and Hoffman 2001). Therefore individuals can experience different temperatures depending on their location in the rocky intertidal.

In order to investigate the effect of temporal and spatial variation in temperature on organisms in the intertidal zone, we addressed basic questions about the effect of temperature on intertidal ectotherms using the anemone *Anthopleura elegantissima*. *A. elegantissima* is a common sedentary cnidarian in the rocky intertidal zone (Hiebert and Bingham 2012), which is in fact the most abundant intertidal sea anemone along the west coast of the United States (Sebens 1981). *A. elegantissima* belong to the class anthozoa, which use contractile fibers known as actin and myosin to move their tentacles (Jahnel et al. 2014). *A. elegantissima* catch small prey such as intertidal invertebrates and zooplankton with their tentacles and retract them toward a centralized mouth (Sebens 1981).

We examined the effect of low tide temperature on *A. elegantissima* behavior after low tide exposure, with particular attention to the rate of recovery following exposure to different low tide conditions. We addressed three specific questions: 1) How does low tide temperature affect how long it takes individuals to recover after low tide exposure? 2) Does low tide temperature affect the maximum tentacle retraction of individuals after low tide exposure? 3) Does low tide temperature affect the number of food items that individuals consume after low tide exposure? We hypothesized that individuals exposed to high temperature during low tide would: 1) recover more slowly than individuals exposed to cool temperature low tides, 2) have weaker retraction of tentacles than individuals exposed to cool temperature low tides, and 3) eat fewer food items than individuals exposed to cool temperature low tides. We reasoned that individuals exposed to the high temperature treatment may experience cellular stresses such as denaturation of proteins (Han et al. 2013), which may impair contractile fibers. If contractile

fibers were impaired, tentacle movement would be inhibited thus hindering the feeding ability of *A. elegantissima*. Overall we predicted that high temperatures during low tide would negatively affect the feeding behavior of *A. elegantissima* due to the fact high temperatures for anemones correlates to high physiological stress (Sebens 1981).

2. Methods

Collection and Maintenance of *A. elegantissima*.

We collected anemones from the Newport jetty in Corona del Mar, California (117.877 West, 33.592 North). We carefully removed individuals from the rock by using a flat metal paint scraper to loosen their grip. We placed the anemones in a cooler containing seawater and transported them to California State University, Fullerton. Anemones were placed on petri dishes surrounded by artificial turf and maintained in holding tanks in a flow-through seawater system at 16°C. We checked the temperatures daily to ensure water temperature did not go above 16 or below 15°C. Anemones avoid crossing artificial turf (Burnaford, *pers comm*) so this minimized their movement around the tank and allowed us to move anemones between treatments with minimal disturbance. Anemones were held in the lab for three days without food before the start of any experiments.

3. Low Tide Conditions

Each experimental individual experienced a total of 4 different treatment conditions, with 46-50 hours recovery time submerged in the holding tanks between treatments. Four anemones were rotated through the four treatments as a group. Different groups were run during different weeks. For each individual, the order of treatments was determined randomly. Our total sample size was twenty-four individuals (4 anemones/group, 6 groups).

Our four treatments were:

A. No low tide. Individuals were submerged in simulated high tide conditions in the holding tank at 16°C.

We had three low-tide treatments. In each, we placed anemones in an empty 10-gallon aquarium with a heat lamp above it. In preliminary trials we identified heat-lamp settings that resulted in temperatures of 25°C, 30°C, and 35°C for organisms on the

bottom of the aquarium. Subsequently we set the lamps to these predetermined settings before each trial. Each low tide simulation lasted for two hours.

B. Cool temperature low tide: Individuals were maintained at 25°C.

C. Moderate temperature low tide: Individuals were maintained at 30°C.

D. High temperature low tide: Individuals were maintained at 35°C.

We chose these temperatures based on preliminary data which indicated that these were realistic temperatures that organisms can experience in Southern California intertidal zones (Burnaford, *pers comm*). Our high temperature treatment was designed to mimic the conditions during a low tide during summer or early fall.

Observing Rate of Recovery

After two hours in the experimental treatments, all anemones were placed back into the holding tank simultaneously. Individuals in the no low tide treatment were briefly lifted out of the tank to control for the effects of handling the low tide treatment individuals and to create a clear start to the recovery period. Immediately upon submersion (or resubmersion for 'no low tide' individuals), we made observations at 30-second intervals, recording each time whether each anemone was open or closed (Fig. 1). An anemone was considered to be "recovered" if it was open. All anemones used in the experiment opened within 9 minutes of submersion.

Feeding observations

For every group we started feeding all of the anemones simultaneously after the last anemone had fully opened (across groups, this timing ranged from 5 to 9 minutes after submersion). We fed anemones a brine shrimp paste (2 parts brine shrimp to 9 parts seawater) through a pipette. We carefully placed 1 ml of brine shrimp solution onto a tentacle, then started a timer and made observations at 30-second intervals for three minutes. At each interval we assigned each individual a behavioral response category (Fig. 2). For data analysis, we determined the maximum response for each individual in each three-minute period. We repeated the feeding at ten-minute intervals for one hour (each individual received 7 food items in total).

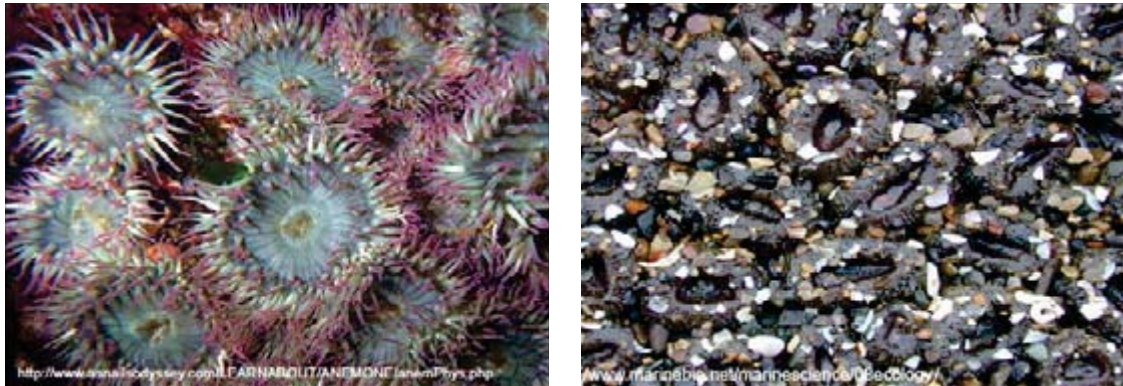


Fig. 1: Closed and open *A. elegantissima*. Closed anemones did not have tentacles exposed, while open anemones did expose tentacles.

Data analysis

Statistical analysis was conducted in JMP 10. For all comparisons, we used Levene's test to determine whether variance was similar among treatments and Sharpio- Wilk's W test to determine whether data were normally distributed within treatments. If necessary, data were transformed to meet test assumptions. In all cases we treated an individual as a block and compared the effects of our treatments after accounting for the effect of individuals.

In order to determine if recovery rate was affected by conditions during low tide exposure we compared time-to-opening (in seconds) among treatments using a blocked ANOVA (treating each individual as a block) on LN-transformed data. We used a Tukey- Kramer multiple comparison test to determine differences among treatments.

To determine if low tide exposure affected behavioral response, we determined the maximum behavioral response for each individual during each observation period. We compared this maximum behavioral response among treatments at time 0 and again at time 60 (= 60 minutes after re-immersion) with separate blocked ANOVAs (each individual = a block) on SQRT-transformed data. We used a Tukey-Kramer multiple comparison test to determine differences among treatments.

To assess if low tide exposure affected consumption we compared the number food items consumed by individuals in each treatment using a blocked ANOVA (treating each individual as a block) on SQRT-transformed data. We used a Tukey-Kramer multiple comparison test to determine differences among treatments.

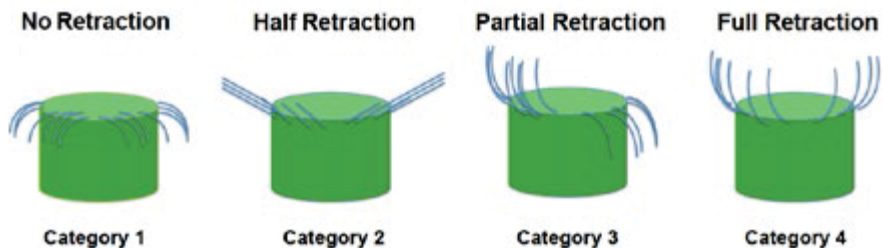


Fig. 2: Behavioral Response Categories. We assigned individuals categories based on position of tentacles. These behaviors were observed in preliminary observational studies. A full retraction was assigned as tentacles 90° above the oral disc, a partial was tentacles on one side 90° above the oral disc, a half retraction was tentacles 45° above oral disc, and no retraction was when tentacles were below oral disc.

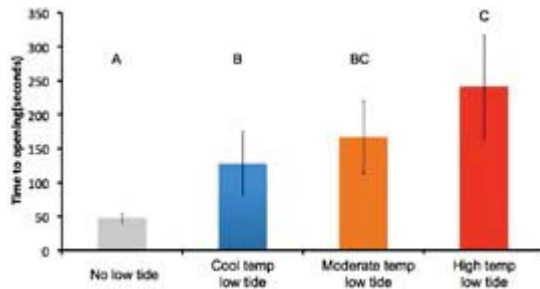


Fig. 3: Effect of low tide exposure on time to opening. Mean (\pm SE) of 24 individuals / treatment. All individuals opened within 9 minutes. Different letters indicate treatments which are different at the $p = 0.05$ level (Tukey-Kramer multiple comparison test).

Low tide exposure and low tide temperature affected time to opening when individuals were returned to high tide conditions (Blocked ANOVA, Individual $F_{23, 69} = 1.34$, $p = 0.18$, Treatment $F_{3,69} = 23.05$, $p < 0.0001$; Fig. 3). When individuals were not exposed to low tide conditions, they recovered in less than a minute on average (Fig. 3). In contrast, individuals exposed to any low tide treatment took on average at least 2 minutes to recover (Fig. 3). Within the low tide treatments, higher low tide temperatures resulted in longer average time to opening from 128 seconds in the cool temperature treatment to 241 seconds in the high temperature treatment (Fig. 3). Therefore, both low tide exposure and high low tide temperatures increased the time it took individuals to recover relative to individuals which were exposed to more benign conditions.

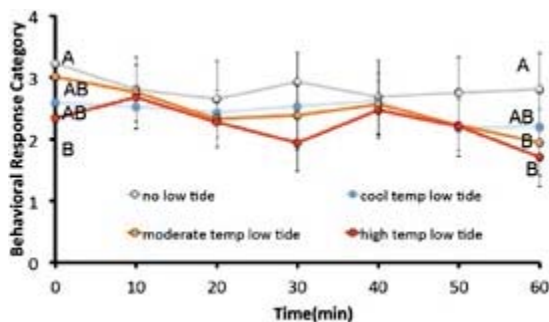


Fig. 4: Effect of low tide exposure on behavioral response. Mean (\pm SE) response on a scale of 1-4 (see Fig. 2 for descriptions of response categories) for 24 individuals / treatment / time. We recorded maximum response for each individual during 3-minute observation periods every 10 minutes for one hour.

Similarly, low tide exposure and low tide temperature both affected behavioral response as measured by the intensity of contraction when an anemone was presented with a food item (Time 0: Blocked ANOVA, Individual $F_{23,69} = 1.44$, $p > 0.13$, Treatment $F_{3,69} = 4.06$, $p = 0.01$; Time 60: Blocked ANOVA, Individual $F_{23,69} = 0.92$, $p = 0.58$, Treatment $F_{3,69} = 4.60$, $p = 0.005$ Fig. 4). Initially differences of average maximum responses between treatments were small, however differences became larger over the course of an hour. At the start of the recovery period, immediately after immersion (= Time 0) more than 50% of 'no low tide' individuals exhibited full retractions. In contrast, across all of the low tide treatments, only 21% of individuals exhibited full retractions. After an hour (= Time 60), 38% of 'no-low tide' individuals exhibited full retractions, while across all of the low tide treatments, only 7% of 'low tide' individuals exhibited full retractions. Within the low tide treatments, higher temperatures resulted in weaker responses; after an hour (= Time 60) 38% of 'cool temperature low tide' individuals did not retract, while 63% of 'high temperature low tide' individuals did not retract. Individuals in all treatments showed weaker contractile responses in response to food over the 1 hour measurement period, but individuals in the warm low-tide treatments showed greater declines than did individuals in the no-low tide treatments (Fig. 4), indicating that warm temperatures during low tide exposure did have some effect.

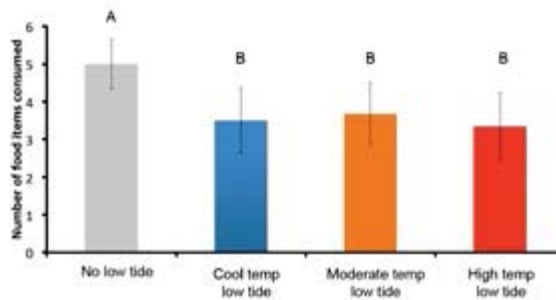


Fig. 5: Effect of low tide exposure on consumption. Data are mean (\pm SE) number of food items consumed by 24 individuals / treatment. Food items (1 ml pellets of brine shrimp) were provided every 10 minutes for one hour. Every individual was provided with 7 pellets. Different letters indicate treatments which are different at the $p = 0.05$ level (Tukey-Kramer multiple comparison test).

In contrast to the results for the first two response variables, low tide exposure affected the number of food items consumed over an hour but low tide temperature did not have an effect (Blocked ANOVA, Individual $F_{23,69} = 4.25$, $p < 0.0001$, Treatment $F_{3,69} = 7.48$, $p = 0.0002$; Fig. 5.). Individuals not exposed to low tide ate 5 food items on average, while across all low tide treatments, individuals ate 3.5 food items on average. Low tide temperature had no detectable effect. Individuals exposed to low tide ate between 3.3 and 3.6 food items on average regardless of the temperature treatment.

4. Discussions

Our results suggest that both low tide exposure and low tide temperature have negative effects on the feeding behavior of *A. elegantissima*. However, low tide exposure itself had a greater overall effect than the temperature during low tide. Individuals that were not exposed to low tide were able to recover faster, consume more food items, and exhibit stronger contractile responses than individuals exposed to low tide. Our data indicate that exposure to low tide can have substantial effects on anemones. Not only are they unable to feed during low tide, but the effect of low tide lingers even after the animals are re-submerged, as food intake is decreased (relative to individuals which have not been exposed to low tide) within the first hour when the tide comes back in. Our data indicate that there is a short lingering effect of low tide temperature after the tide returns. Within the first few minutes of exposure, temperature did affect recovery and response times of anemones in our experiments. Since different microhabitats can have different temperatures due to shading effects and rock orientation (Burnaford 2004, Gedan et al. 2011), anemones that are exposed to low tide but are in different microhabitats could have different recovery times and responses to food when the tide returns. Therefore low tide temperature and exposure can impact feeding behavior of *A. elegantissima* in the rocky intertidal zone.

There are a variety of reasons for why low tide exposure itself could have had such a strong effect on feeding behavior. Anemones could have experienced water loss during low tide since low tide exposure leaves marine organisms at higher risk of desiccation, or dehydration from air exposure that causes physiological damage (Denny and Gaines 2007). Desiccation can be a major stress for ma-

rine invertebrates (Helmuth 1998). Water movement due to water loss and subsequent changes in solute concentration can damage cells (Freeman 2010). Osmotic stress can affect cell function by affecting the structure of macromolecules such as proteins (Lang et al. 1998) as well as causing cells to burst or shrink (Freeman 2010). Anemones can hold water in their gastrovascular cavity during emersion (Burnaford, *pers comm*). We did not measure the degree of desiccation in our study organisms, therefore we cannot assess the actual degree of desiccation in our experimental treatments. However, if animals were desiccated and if cells were damaged then individuals may not have been able to contract their tentacles in response to food items.

For two of our response variables, we did see a short-lived effect of low tide temperature on anemone behavior after low tide. Higher temperatures during low tide resulted in longer recovery time as well as weaker responses over time, but had no effect on consumption. Therefore our hypotheses that higher temperatures would increase recovery time and weaken response were supported. However our hypothesis that higher temperatures would decrease food consumption was rejected. A reason why the temperatures used in our study might not have had as much of an effect as exposure may be due to thermal adaptations of *A. elegantissima*. Previous researchers have found that *A. elegantissima* produce HSP70, a protein chaperone, in response to cellular damage from high temperature (Snyder and Rossi 2004). For example, *A. elegantissima* express more HSP70 on hot summer days than on cooler foggy days (Snyder and Rossi 2004). Increased expression of HSP70 means that more HSP70 proteins can be synthesized, which may protect against protein denaturation (Snyder and Rossi 2004). Since the temperatures used in our experiment did not seem to impair contractile fibers for a long period of time, chaperones such as HSP70 proteins could have prevented sustained impairment of tentacles. This may have allowed anemones to feed and respond regardless of the temperature treatment.

In order to investigate the protective effect of HSP70 and the cost of production, a good avenue for continued study would be the examination of HSP70 expression in *A. elegantissima*. After exposure to each low tide treatment, one could determine levels of HSP70. We expect individuals to express more HSP70 when exposed to high temperature low tides rather than cool temperature low tides. Our study deals with the potential effects of climate

change on the behavior of *A. elegantissima*. *A. elegantissima* is an abundant carnivore in the intertidal zone (Sebens 1981). To understand how ecosystems will respond to climate change, we must know how temperature affects important species interactions such as predation. Although our study temperatures did not affect feeding behavior of *A. elegantissima*, higher temperatures due to climate change may affect their feeding behavior in the future.

References

- Bingham, B. L., Freytes, I., Emery, M., Dimond, J., & Müller-Parker, G. (2011). Aerial exposure and body temperature of the intertidal sea anemone *Anthopleura elegantissima*. *Invertebrate Biology*, 130(4), 291-301.
- Burnaford, J. L. (2004). Habitat modification and refuge from sub-lethal stress drive a marine plant-herbivore association. *Ecology*, 85(10), 2837-2849.
- Denny, M. W., & Gaines, S. D. (2007). Encyclopedia of tidepools and rocky shores. 1st edition. University of California Press, Oakland, CA, US.
- Freeman, S. (2010). Biological sciences. 4th edition. Pearson Education Inc. San Francisco, CA, US.
- Gedan, K.B., Bernhardt, J., Bertness, M. D., & Leslie, H. M. (2011). Substrate size mediates thermal stress in the rocky intertidal. *Ecology*, 92(3), 576-582.
- Jahnel, S.M., Walzl, M., & Technau, U. (2014). Development and epithelial organization of muscle cells in the sea anemone *Nematostella vectensis*. *Frontiers in Zoology*, 11(1), 44-59.
- James, R.S. (2013). A review of the thermal sensitivity of the mechanics of vertebrate skeletal muscle. *Journal of Comparative Physiology B*, 183(6), 723-733.
- Han, G., Zhang, S., Marshall, D. J., Ke, C., & Dong, Y. (2013). Metabolic energy sensors (ampk and sirt1), protein carbonylation and cardiac failure as biomarkers of thermal stress in an intertidal limpet: Linking energetic allocation with environmental temperature during aerial emersion. *Journal of Experimental Biology*, 216(17), 3273-3282.
- Helmuth, B. S. T. (1998). Intertidal mussel microclimates: Predicting the body temperature of a sessile invertebrate. *Ecological Monographs*, 68(1), 51-74.
- Helmuth, B. S. T. & Hofmann, G.E. (2001). Microhabitats, thermal heterogeneity, and patterns of physiological stress in the rocky intertidal zone. *Biological Bulletin*, 201(3), 374-384.
- Hiebert, T.C & Bingham, B. L. (2012). The effects of symbiotic state on heterotrophic feeding in the temperate sea anemone *Anthopleura elegantissima*. *Marine Biology*, 159(5), 939-950.
- Lang, F., Busch, G.L., Ritter, M., Völkl, H., Waldegg, S., Gulbins, E., Haussinger, D. (1998). Functional significance of cell volume regulatory mechanisms. *Physiological Review*, 78(1), 247-306.
- Metaxas A. & Scheibling R. E. (1993). Community structure and organization of tidepools. *Marine Ecology Progress Series*, 98, 187-198.
- National Oceanic and Atmospheric Administration. (2015). Water temperature table of the Southern Pacific coast. www.nodc.noaa.gov/dsdt/cwtg/spac.html
- Sebens K. P. (1981) The allometry of feeding, energetics and body size in three sea anemone species. *Biological Bulletin*, 161(1), 152-171.
- Somero G. N. (2002). Thermal physiology and vertical zonation of intertidal animals: optima, limits, and costs of living. *Integrative and Comparative Biology*, 42(4), 780-789.
- Snyder M.J., & Rossi S. (2004). Stress protein (HSP70 family) expression in intertidal benthic organisms: the example of *Anthopleura elegantissima*. *Scientia Marina*, 68(1), 155-162.

5. Acknowledgments

We thank E. Fan, R. Pound, M. Tran, A. Coral, B. Garces, V. Nguyen, M. Aftab, R. Daniels, N. Kim, P. Ramirez, J. Ballon, E. Montiel and H. Matin, B. Miyamoto, G. Camacho and P. Panchal for lab and field assistance. This project was funded by the CSUF Associated Students, Inc. (ASI) Student Research Grant Program.

Graph Interpretation and Construction Tasks in Introductory Biology Textbooks: Preliminary Findings

Department of Biological Science, California State University, Fullerton

Alicia Mendoza and Eleanor Spangler

Abstract

Graphs are an essential tool for effective communication in science, and increasingly important in engaging the public about complex social issues. However, students commonly struggle with graph interpretation, their ability to extract information or make predictions from the graph. Similarly, students have difficulty with graph construction, their ability to convert data from tabular or graphical form, or concepts, into an appropriate graph. Textbooks represent the largest investment, outside of tuition and housing that many biology students make in college. Given the centrality of the textbook to the introductory biology experience, we were interested in exploring how the most common textbooks present information graphically, as well as what types of questions students are asked about graphing. We first developed a rubric to score each graph, which included categories such as graph type (e.g. bar graph), graph elements (e.g. labels, units) and type of data represented (e.g. categorical or continuous). We also characterized the questions by cognitive level (i.e. identification, analysis, prediction, construction). In our preliminary analysis we found that the most commonly presented graph type is line graph, which appeared 45% of the time. Many graphs lacked key components that might be asked of students; for instance, although axes labels were included in 100% of graphs, units were only present in 68%. Students were most frequently asked analysis or prediction question. Only 18% of questions were graph construction, and over half of those questions presented an example graph with the question. As we continue this project we plan to refine our rubric, evaluate additional textbooks, and better characterize the graphing tasks included in the books.

We hope to use the data from this project to inform new pedagogical approaches to enhancing student graph interpretation and construction skills.

1. Introduction

Graphs are a fundamental tool for communication, not only in science but also in our everyday lives (AAAS, 2010; Glazer, 2011). Being able to interpret and construct graphs, whether students collect their own data or data is given to them, is an important aspect of being not only a successful scientist but also being able to communicate daily. The use of graphs is a method used in a range of fields from medicine to marketing so that we may better present statistical information to our audience (Aoyama, 2007). Understanding the importance and necessity of these skills, it becomes important to understand how instructional approaches and resources support the development in students.

Despite the importance of graphs, students regularly struggle with two sets of skills: *graph interpretation* (interpreting, extrapolating and interpolating from, or translating graphs) and *graph construction* (creating graphical representations of data or concepts) (Friel et al., 2001). Students that struggle with graph interpretation have a difficult time extracting information or making predictions from a graph. According to Glazer, students often time read information from a graph as the literal picture shown instead of looking beyond the bar graph or line graph and trying to understand the information being presented (2011). Furthermore, students struggling

2. Materials And Methods

with graph construction have a difficult time converting data or concepts into a graph, or choosing the appropriate graph type, but very little attention has been spent on how to better support student skills in these areas (Friel et al, 2001).

Textbooks represent the largest resource investment, other than tuition and housing, students make in their college education (Government Accountability Office, 2013), and textbooks are regularly used in introductory science courses. For many biology students, their textbook may be the first time they are exposed to multiple types of graphs depicting biological data and concepts. However, little is known about textbook graph presentation and the tasks in them. If presented with one predominant graph type, students may be more likely to use that graph type in their coursework. If graph construction tasks are consistently at a low cognitive level, students may be slower to develop the skill necessary to graph complex data or concepts. An understanding of the graph comprehension and construction tasks in textbooks may help guide future research and instruction on student skills in those areas. To better understand how textbooks incorporate graphs, we began a study to survey the qualities and cognitive requirements of graphs and graphing tasks in common college level introductory biology textbooks.

Selecting A Textbook

In order to review the types of graphs presented in textbooks, we decided to focus our research on introductory biology textbooks. We began by choosing a commonly used introductory textbook used at California State University, Fullerton, *Biological Science* by Scott Freeman 5th ed. We decided to use an introductory textbook in order to see what issues, if any, may be present within the textbook that may cause students to have struggle with graph interpretation and construction.

Creating A Rubric

We began by developing a rubric to score graph type, graph elements, data type, and question type. We created a spreadsheet including the key characteristics that we thought are essential for constructing a proper graph as well as being necessary for graph interpretation. In the rubric, we decided to include: chapter number, figure number, page, whether the question was found in a chapter or end of chapter, cognitive level, type of graph, titles, labels, units, and data type. The cognitive level of each graphical question was measured using the following key (listed in decreasing cognitive level):

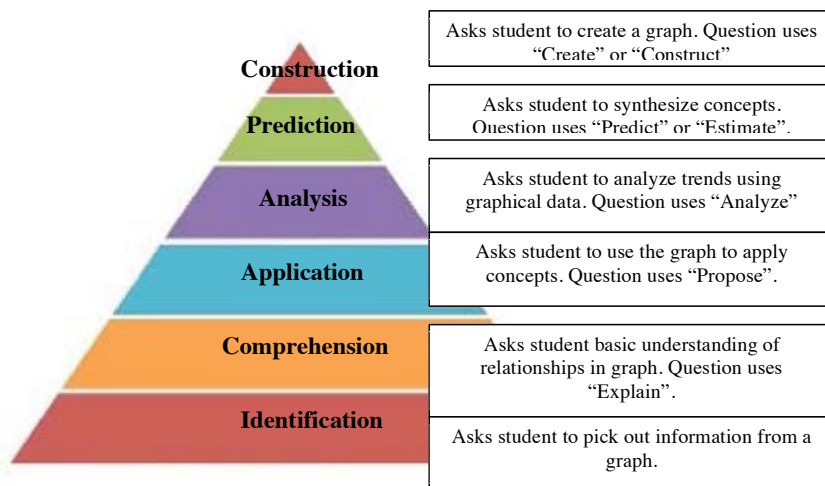


Figure 1: Cognitive level developed to classify graph questions with construction being the high level of cognition and identification being the lowest level of cognition.

Although the final draft of the rubric used contained the previously mentioned characteristics, we did a few revisions before we continued to score every graph found. For example, we originally included pictographs, which we did not see once in the first few chapters we did a trial run. We also quickly learned that a comments section was very much needed in order to help each other communicate with questions or clarifications.

Data Collection

Mendoza reviewed every page throughout the book to categorize each graph based on its graph type (e.g. bar graph), graph elements (e.g. labels and units), and data type (continuous or categorical). Continuous data is quantitative data meaning that the information being collected or presented is a numerical value (e.g. temperature, age, and distance). Categorical data is qualitative data in which the data collected or presented in a graph falls within a category (e.g. color, letter grade). Spangler carefully reviewed every page of the book to categorize the graphing questions according to cognitive level (Figure 1). As we encountered a graph or question, we scored it in the rubric by placing a '1' under each category it fulfilled. We also included where in the textbook the graph or question was found. Once every graph in the textbook had been scored we summarized the results.

3. Results

Graph Presentation

The most common type of graph seen throughout the chapters (figures in text) were line graphs, which made up 46% of the graphs (Figure 2). The scatter plot, bar graph, and histogram were the other most commonly seen graphs throughout the textbook (20%, 18%, and 12%), while the pie chart was less seen (4%) (Figure 2). In addition, many of the graphs did contain the components we were interested in, with 98% of graphs having labels and 99% of graphs having units (Figure 3). Slightly more than half of the graphs (55%) were comprised of continuous vs. continuous data (Figure 4). Approximately 42% of the other graphs were comprised of continuous vs. categorical data, while only a few contained categorical vs. categorical data (Figure 4).

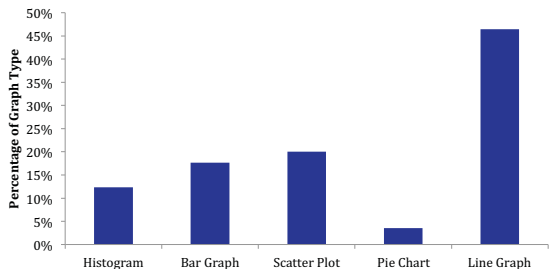


Figure 2. Percentage of each graph categorized by type summarized from Freeman, *Biological Science 5th ed.* Line graph was the most observed type of graph (46%). The least observed type of graph was the pie chart (4%) (n=170).

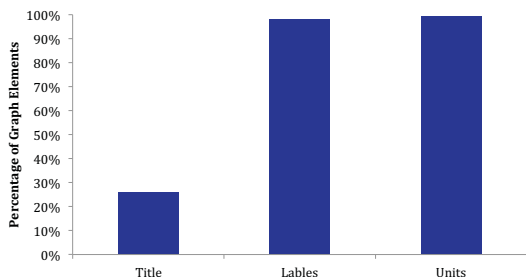


Figure 3. Percentage of graph elements included per graph summarized from Freeman, *Biological Science 5th ed* (n=170). Although the majority of graphs presented in the text contained labels and units, only 26% of graphs had a graph title.

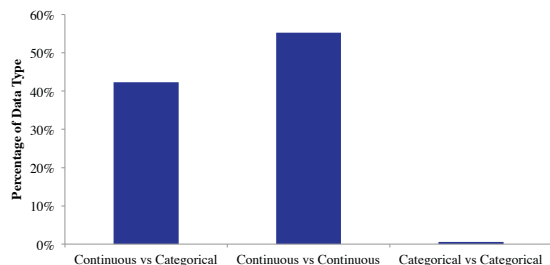


Figure 4: Data types graphed in Freeman, *Biological Science 5th ed* (n=170). The majority of graphs were continuous vs. categorical (42%) or continuous vs continuous (55%). Very few graphs showed categorical vs. categorical data (3%).

Graphing Questions

The majority of question types about graphs presented in the chapters and end of chapter question were prediction questions (31%) and construction questions (18%). However only 7% of the questions were identification. There were a similar amount of comprehension (15%), application (16%), and analysis (13%) question types seen throughout the textbook (Figure 5).

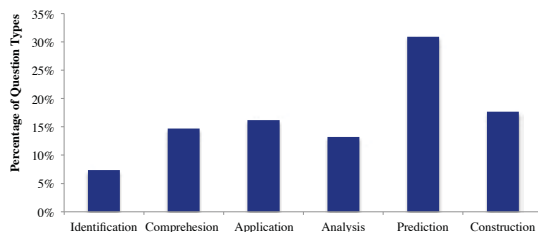


Figure 5: Percentage of each graph question type observed in Freeman, *Biological Science* 5th ed (n=68). The most common question type was prediction (33%), while the least common was identification (7%). The majority (62%) of graphing questions presented in Freeman were higher order questions (analysis, prediction, or construction).

4. Discussion

Although we were able to categorize every graph we encountered, there were a few that were more difficult to classify. There were a few figures that at a quick glance looked like any other graph but upon further analyzing, it was reasoned to be a type of diagram even though it may contain axes and some labels. The majority of graphs categorized were found to be line graphs (Figure 2); this may relate to the frequency of measurements that biologist take related to change over time. The majority of the graphs, accordingly, showed continuous vs. continuous data (Figure 4). Roth et al. (1999) found that the most common type of graph in six high school biology textbooks was the line graph, which suggests that this finding may hold across other college level biology textbooks as well. These findings could reflect the nature of biological research, which often focuses on change in some variable over time, or could reflect a bias towards that graph type by textbook authors.

We were surprised to find that the majority of questions asked throughout the text were of higher cog-

nitive level (construction and prediction); based on our preliminary scanning of textbooks and previous work on introductory biology exam questions (Crowe et al. 2008), we expected to find that most questions would be of lower-order. This finding, if it holds across other common introductory textbooks, would be encouraging.

Friel et al. (2011) points out that students need to be able to ask questions about graphs in order to better understand them. This involves having educators making better use of in-text graph questions. Students often time read information from a graph as the literal picture shown instead of looking beyond the bar graph or line graph and trying to understand the information being presented (Glazer, 2011). By understanding how graphs are being presented to students and knowing what type of graph questions are being asked, we can better understand how to help students use textbooks to aid in their learning of graphing.

As we continue our research, we plan to further refine our rubric to better characterize the graphing tasks as well as calculate inter-rater reliability to code graphs. We also would like to evaluate additional textbooks to see if we find similar results. We hope to use the data from the project to better inform pedagogical approaches to enhance student graph interpretation and construction skills. By understanding what issues students struggle with involving graphing, we can better understand how to help students use appropriate resources to their advantage. As we saw in the *Biological Science* textbook there are sufficient graphs to study and questions to answer about graphs that are of higher cognitive level, therefore we need to figure out a way to better use this resource in order to help students become more comfortable with creating and interpreting graphs in order to help them succeed in science.

5. Acknowledgments

We would like to thank our advisor, Joel K. Abraham, and the Abraham Lab members for their continued support and guidance. This research was funded by a CSUF Faculty Intramural Grant and the Department of Biological Science.

References

- AAAS. Vision and Change: A Call to Action. Washington, DC: AAAS; 2010. [accessed 30 January 2015]. <http://visionand-change.org/files/2013/11/aaas-VISchange-web1113.pdf>
- Aoyama, K. (2007). *Investigating a Hierarchy of Students' Interpretations of Graphs*. International Electronic Journal of Mathematics Education. 2(3)
- Bowen, G. M., Roth, W. M., & McGinn, M. K. (1999). Interpretations of graphs by university biology students and practicing scientists: Toward a social practice view of scientific representation practices. *Journal of Research in Science Teaching*, 36(9), 1020- 1043.
- Freeman, Scott. (2014). *Biological Science*. 5th ed. Pearson
- Friel, S., Curcio, F., & Bright, G. (2001). Making sense of graphs: Critical factors influencing comprehension and instructional implications. *Journal for Research in Mathematics Education*, 32(2), 124-158
- Glazer, Nirit. (2011). *Challenges with Graph Interpretation: A Review of the Literature*. *Studies in Science Education* 47.2: 183-210.
- Government Accountability Office. (2013). College Textbooks: Students have greater access to textbook information. (GAO Publication No. 13-368). Washington, D.C: U.S. Government Printing Office. [accessed 30 January 2015]. <http://www.gao.gov/assets/66-0/655066.pdf>.
- McKenzie, D. L., & Padilla, M. J. (1986). The construction and validation of the test of graphing in science (TOGS). *Journal of Research in Science Teaching*, 23(7), 571-579.
- Roth, W-M., Bowen, G. M. and McGinn, M.K. (1999). Differences in graph-related practices between high school biology textbooks and scientific ecology journals. *J. Res. Sci Teach.* 36: 977-1019.

California Pipefish Identification Using Morphological Measurements and Genetic Analysis

Department of Biological Science, California State University, Fullerton

Cristy A. Rice, Douglas J. Eernisse, and Kristy L. Forsgren

Abstract

In southern California, there are six commonly reported pipefish species [kelp pipefish (*Syngnathus californiensis*), bay pipefish (*S. leptorhynchus*), barcheek pipefish (*S. exilis*), chocolate pipefish (*S. euchrous*), barred pipefish (*S. auliscus*), and snubnose pipefish (*Cosmocampus arctus*)]. Pipefishes are cryptic in nature and many species have similar color patterns and overlap in habitat type making species identification time consuming. In an effort to aid in accurate pipefish identification in the field, we reexamined the morphological traits emphasized in currently utilized dichotomous keys. Typical morphological measurements overlapped in kelp pipefish, bay pipefish, barcheek pipefish, and chocolate pipefish. Color patterns and snout length were determined to be reliable characters in the separation of barred pipefish and snubnose pipefish. Analysis of mitochondrial 16S and COI partial gene sequences indicated that rather than six distinctive pipefish species, it is likely that only three species are present in southern California: the kelp pipefish (*Syngnathus californiensis*), which includes the kelp pipefish, bay pipefish, barcheek pipefish, and the chocolate pipefish, the barred pipefish (*S. auliscus*), and the snubnose pipefish (*Cosmocampus arctus*). Based on these data, a more comprehensive dichotomous key can be developed for pipefish identification.

1. Introduction

Pipefishes (Syngnathidae) are primarily found in seagrass and kelps beds along the California coastline (Phillips and Meñez 1998, Heck et. al. 2003, Shikro et. al. 2009). In southern California, four commonly observed pipefishes;

kelp pipefish (*Syngnathus californiensis*; Storer 1845), bay pipefish (*Syngnathus leptorhynchus*; Girard 1854), barred pipefish (*Syngnathus auliscus*; Swain 1882), and the snubnose pipefish (*Cosmocampus arctus*; Jenkins and Evermann 1889), are commonly reported. However, two additional pipefish species, the barcheek pipefish (*Syngnathus exilis*; Osburn and Nichols 1916) and the chocolate pipefish (*Syngnathus euchrous*; Fritzsche 1980) are commonly observed and frequently caught in survey trawls (Fritzsche 1980, J. Allen unpubl.).

The cryptic nature and similar color patterns of different species makes conclusively identifying pipefishes time consuming (e.g., counting body rings) or requires the use of a microscope, making identification difficult in the field. Additionally, the exact number of species has been debated from three to eight numbers of species. The currently used dichotomous keys for pipefish identification include The Guide to the Coastal Fishes of California (Miller and Lea 1972) and A revisionary study of the eastern Pacific Syngnathidae (Pisces: Syngnathiformes), including both recent and fossil forms (Fritzsche 1980). While some work on pipefishes has been conducted (e.g., Wilson et al. 2001, Louise 2003; Wilson 2006, Mobley et al. 2011, Wilson and Orr 2011), a clear and accurate picture of local pipefish populations is needed.

The aim of the current research was to 1) identify the pipefish species commonly observed along the southern California coastline, 2) establish reliable morphological characters to quickly and accurately identify different pipefish species, and 3) confirm species identification using genetic tools. We established several morphological characters and measurements of for each of the pipefish species and verified species identification using mitochondrial DNA.

2. Materials and Methods

Adult pipefishes [kelp pipefish (*Syngnathus californiensis*), bay pipefish (*S. leptorhynchus*), barcheek pipefish (*S. exilis*), chocolate pipefish (*S. euchrous*), barred pipefish (*S. auliscus*), and snubnose pipefish (*Cosmocampus arctus*)] were collected from seagrass beds and kelp beds by minnow seine, otter trawl and/or beam trawl from San Diego County, Orange County, Los Angeles County, and Ventura County from June 2012 to August 2014. Pipefish were euthanized using buffered tricaine methanesulfonate (MS-222; 50 mg/L). Standard length from the end of the maxilla to the base of caudal fin (mm), body weight (g), and the sex of each individual were recorded for each species. Pipefish were identified with the aid of dichotomous keys (Miller and Lea 1972, Fritzsche 1980, J. Allen unpubl.), which focus on counting of various body rings, which are counted as a band of bony scutes along the length of the fish. Body rings are separated into trunk rings (referred to as body rings in Miller and Lea 1972), which are located from the operculum to the anal fin and tail rings, which are located on the tail beginning at the anal fin. Additionally, subdorsal rings counted as those rings under the dorsal fin (overlapping regions of trunk and tail rings) were documented.

Given the large number of characters and morphological traits that overlapped between species, additional morphological measurements were also recorded. Using digital calipers (mm \pm SEM), the following measurements were taken: head length (mm) from the end of the maxilla with mouth closed to the posterior edge of operculum; head height (mm) on the left lateral side of the head measuring dorsal to ventral perpendicular to the center of the eye, snout length (mm) from the end of maxilla with mouth closed to the left nostril at the center when viewing fish dorsal-anteriorly; and snout width (mm) from the left lateral to the right lateral side of the snout measured horizontally and dorsally at the nostrils (Fig. 1). Distinguishable characters were also used to identify pipefish species (e.g., color patterns including bars, speckles, mottling).

A small piece of tissue from the tail of identified pipefish species (kelp pipefish (n = 6), bay pipefish (n = 4), barcheek pipefish (n = 10), chocolate pipefish (n = 3), barred pipefish (n = 4), and snubnose pipefish (n = 4) was collected and stored in ethanol at -80°C until they were prepared for DNA analysis (Thermo Fisher Scientific GeneJET Blood and Tissue Genomic DNA kit, Thermo Fisher

Scientific Inc., Waltham, Massachusetts) following the manufacturer's protocol. The mitochondrial 16S and COI partial gene sequences were generated for selected vouchers of our studied putative pipefish species by an independent laboratory (National Exposure Research Laboratory, Environmental Protection Agency). We downloaded all available 16S and COI sequences available for Syngnathidae from GenBank, and performed a multiple sequence alignment for each gene region using MAFFT (<http://mafft.cbrc.jp/alignment/software/>). We performed phylogenetic analysis using the maximum likelihood algorithm implemented for RAxML (<http://embnet.vital-it.ch/raxml-bb/>). Fish were handled under an approved protocol that followed the policies and guidelines of California State University, Fullerton's Institutional Animal Care and Use Committee.

A two-way analysis of variance (ANOVA) followed by a Bonferroni's multiple comparisons test was used to compare male to female morphometric data, since male and female data were largely not significantly different, male and female data were combined and analyzed using a one-way analysis of variance (ANOVA) followed by a Tukey multiple means comparison test (Prism 6 for Macintosh, GraphPad Software, Inc. 2003). The level of significance was determined at $p < 0.05$.

3. Results

The standard lengths of male kelp pipefish, bay pipefish, chocolate pipefish, and barred pipefish were significantly ($p < 0.05$) greater than female pipefish (Table 1). Male barcheek pipefish were not significantly different ($p = 0.82$; Table 1). Only three male and two female snubnose pipefish were conclusively identified, thus standard length measurements were combined since statistical analysis was not feasible for separate sexes (Table 2). For comparison purposes between pipefish species, the standard lengths of males and females were combined (Table 2). Kelp pipefish, bay pipefish, barcheek pipefish, and chocolate pipefish standard lengths were not significantly different ($p > 0.05$; Fig 2A). Barred pipefish standard length was significantly different ($p = 0.0007$) from snubnose pipefish (Fig. 2A).

Kelp pipefish, bay pipefish, barcheek pipefish, and chocolate pipefish weight was not significantly different ($p > 0.05$; Fig. 2B). The weight of barred pipefish was not

significantly different ($p = 0.098$) from snubnose pipefish (Fig. 2B). The head lengths of kelp pipefish, bay pipefish, barcheek pipefish, and chocolate pipefish were not significantly different ($p > 0.05$; Fig. 2C). Barred pipefish head length was significantly different ($p < 0.0001$) from snubnose pipefish (Fig. 2C). Kelp pipefish, bay pipefish, barcheek pipefish, and chocolate pipefish head heights were not significantly different ($p > 0.05$; Fig. 2D). The head height of barred pipefish was not significantly different ($p = 0.15$) from snubnose pipefish (Fig. 2D).

Kelp pipefish, bay pipefish, barcheek pipefish, and chocolate pipefish snout lengths were not significantly different ($p > 0.05$; Fig. 2E). Barred pipefish snout length was significantly different ($p = 0.002$) from snubnose pipefish (Fig. 2E). The snout widths of kelp pipefish, bay pipefish, barcheek pipefish, chocolate pipefish, and barred pipefish were not significantly different ($p > 0.05$; Fig. 2F). Snubnose pipefish snout width was significantly narrower ($p < 0.05$) than the snout widths of kelp pipefish, bay pipefish, barcheek pipefish, chocolate pipefish, and barred pipefish (Fig. 2F).

The numbers of trunk ring, tail rings, and subdorsal rings were counted for all pipefish species (Fig. 3). The number of trunk rings along the bodies of kelp pipefish, bay pipefish, barcheek pipefish and chocolate pipefish were not significantly different ($p > 0.05$). There were fewer trunk rings on the barred pipefish and snubnose pipefish but they were not significantly different from each other ($p = 0.96$). The numbers of tail rings counted along the bodies of kelp pipefish, bay pipefish, barcheek pipefish, chocolate pipefish, and barred pipefish were not significantly different ($p = 0.71$). The number of subdorsal rings counted along the bodies of kelp pipefish, bay pipefish, barcheek pipefish, and chocolate pipefish were not significantly different ($p = 0.14$). Barred pipefish and snubnose pipefish had fewer subdorsal rings than the other pipefish species and were significantly different from each other ($p = 0.90$).

A variety of coloration, spotting and barring patterns were used to describe the external appearance of pipefishes. The coloration patterns of kelp pipefish and bay pipefish varied and a reliable pattern that could be used for identification was not determined for either species. A dark diagonal bar from behind the eye to the base of the operculum was consistently observed in barcheek pipefish although the length of the bar varied between individuals. The chocolate pipefish were a uniform brown color with

random speckling. A vertical bar after each 4-5 body rings was consistently present on barred pipefish. The snubnose pipefish had a truncated snout in comparison to other pipefish species and two parallel rows of dark spots running vertically along each side of the body.

Mitochondrial DNA results indicated that the kelp pipefish, bay pipefish, barcheek pipefish, and chocolate pipefish are not distinctively separate species. Barred pipefish, however, are a distinct species that is a sister taxa to the kelp pipefish, bay pipefish, barcheek pipefish, and chocolate pipefish group. Snubnose pipefish are also a distinct species placed into an outgrouping from the kelp pipefish, bay pipefish, barcheek pipefish, chocolate pipefish, and barred pipefish.

4. Discussion

Overall, kelp pipefish, bay pipefish, barcheek pipefish, and chocolate pipefish overlapped in all morphometric measurements and body ring counts. Kelp pipefish and bay pipefish could not be discerned by the aid of visual characters. Although it has been suggested (Frische 1980, M. Horn pers. comm.) that the snout of the kelp pipefish has a more of a compressed shape compared to the rounded snout shape of the bay pipefish, we did not consistently observe that feature. Due to their similarity, identification of kelp pipefish and bay pipefish has traditionally been determined based on the habitat in which the pipefish was found (Miller and Lea 1972, Fritzsche 1980, M. Horn pers. comm., J. Pascerelli pers. comm.). Despite a recent study demonstrating that stable isotope analysis was not significantly different between the kelp or bay pipefishes (Flisik 2009), kelp pipefish have been so identified if observed associated with kelp beds, whereas bay pipefish are localized to shallow bays and estuarine areas (Miller and Lea 1972, Fritzsche 1980).

Interestingly, we could identify the barcheek pipefish and chocolate pipefish with the use of specific visual characters (i.e., diagonal bar running from eye to base of operculum, all over brown color). Mitochondrial DNA analyses revealed that specimens identified as the kelp pipefish, bay pipefish, barcheek pipefish, and chocolate pipefish, were indistinguishable for their combined 16S + COI sequences, so this data set provided no evidence for separating them into individual species.

Thus, we propose that the kelp pipefish, bay pipefish, barcheek pipefish, and chocolate pipefish be identified as the “kelp pipefish group”.

There were multiple similarities between the barred pipefish and the snubnose pipefish including: weight, head height, body rings (i.e., trunk, tail, subdorsal). However, the barred pipefish was a larger fish with respect to standard length, head length, and snout length. Additionally, the barred pipefish had distinct vertical barring every 4-5 body rings. Results from the partial gene sequences of the 16S and COI indicated that the barred pipefish is a sister taxa to the kelp pipefish group.

Because of the extremely truncated snout and smaller size, the snubnose pipefish were relatively easy to identify. Visually, snubnose pipefish were distinguishable from the barred pipefish and the kelp pipefish group. Analysis of our mitochondrial gene data sets together with other Syngnathidae 16S or COI sequences available in GenBank have supported the distinction of the snubnose pipefish and placed them in a distinct lineage from the kelp pipefish group, barred pipefish and other members of Syngnathus. Only two other of the approximately 15 recognized species of *Cosmocampus*, the genus to which the snubnose pipefish is assigned, are currently represented in GenBank, and these are only represented as COI sequences. Our preliminary observation is that these two other species do not group together with our snubnose pipefish COI sequences as a monophyletic group, so our

data are relevant to resolving the phylogenetic relationship of *Cosmocampus* species within Syngnathidae.

Overall, the current study has determined that only three pipefish species inhabit the coastal waters of southern California. The kelp pipefish group (kelp pipefish, bay pipefish, barcheek pipefish, and chocolate pipefish) cannot be separately identified visually and are not significantly different with respect to the 16S and COI mitochondrial partial gene sequences. We propose that the kelp pipefish group adopt the oldest scientific name of the group, *Syngnathus californiensis* (Storer 1845). The barred pipefish (*Syngnathus auliscus*; Swain 1882) and snubnose pipefish (*Cosmocampus arctus*; Jenkins and Evermann 1889) are the other two locally identified pipefish species.

5. Acknowledgments

Funding provided by the Southern California Ecosystems Research Project under the National Science Foundation (UMEB-DBI 1041203) and the Southern California Academy of Sciences. Thanks to Dr. Erik Pilgrim (US Environmental Protection Agency, Ecological Exposure Research Division, National Exposure Research Laboratory) for help with DNA sequencing. Special thanks to Julianne Passarelli (Cabrillo Marine Aquarium), Heather Gliniak (DFW), Eric Miller (MBC Applied Environmental Science), Chris Lowe (CSULB), and the Southern California Association of Ichthyological Taxonomists and Ecologists (SCAITE).

6. Figures

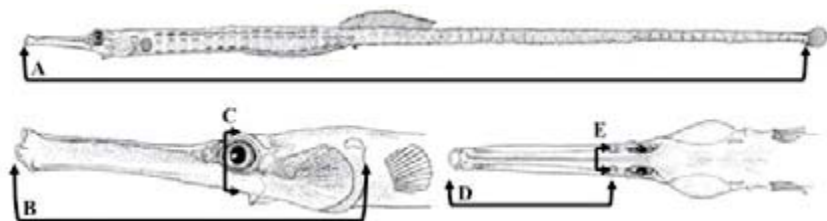


Figure 1: Morphometric measurements used in the identification of pipefishes collected in southern California. (A) Standard length (mm) - from the end of the maxilla to the base of caudal fin; (B) Head length (mm) - from the end of the maxilla with mouth closed to the posterior edge of operculum; (C) Head height (mm) - on the left lateral side of the head measuring dorsal to ventral perpendicular to the center of the eye; (D) Snout length (mm) - from the end of maxilla with mouth closed to the left nostril at the center when viewing the fish dorsal-anteriorly; and (E) Snout width (mm) - from left lateral to the right lateral side of the snout measured horizontally and dorsally at the nostrils. Illustrations by Atsuhiko Kubo.

Common Name	Scientific Name	Sex	Standard length (mm)	Weight (g)	Head length (mm)	Head height (mm)	Snout length (mm)	Snout width (mm)
Kelp pipefish	<i>Syngnathus californiensis</i>	Male	235.08 ± 19.46	1.72 ± 0.12	29.91 ± 2.20	3.16 ± 0.11	13.08 ± 0.06	1.87 ± 0.10
		Female	205.28 ± 8.90	1.67 ± 0.06	26.37 ± 1.08	3.18 ± 0.07	12.70 ± 0.27	1.97 ± 0.07
Bay pipefish	<i>Syngnathus leptorhynchus</i>	Male	178.00 ± 9.56	2.58 ± 0.85	21.50 ± 1.33	3.87 ± 0.36	14.28 ± 1.27	1.84 ± 0.13
		Female	170.40 ± 5.61	1.59 ± 0.23	20.98 ± 0.65	3.51 ± 0.13	12.08 ± 0.88	1.53 ± 0.13
Barcheek pipefish	<i>Syngnathus exilis</i>	Male	198.06 ± 4.94	1.86 ± 0.12	24.51 ± 0.52	3.48 ± 0.10	13.53 ± 0.42	1.77 ± 0.07
		Female	199.61 ± 4.48	2.00 ± 0.15	24.70 ± 0.55	3.73 ± 0.08	14.57 ± 0.39	1.61 ± 0.05
Chocolate pipefish	<i>Syngnathus eucnourus</i>	Male	196.81 ± 10.58	2.00 ± 0.42	21.18 ± 0.82	4.00 ± 0.24	11.84 ± 0.64	1.60 ± 0.16
		Female	160.76 ± 5.36	1.60 ± 0.40	17.50 ± 0.75	3.66 ± 0.30	11.19 ± 1.05	1.75 ± 0.19
Barred pipefish	<i>Syngnathus auliscus</i>	Male	118.39 ± 7.54	0.40 ± 0.12	12.80 ± 0.79	2.46 ± 0.24	4.35 ± 0.45	1.29 ± 0.04
		Female	108.57 ± 4.91	0.31 ± 0.09	12.26 ± 0.56	2.46 ± 0.31	4.61 ± 0.65	1.20 ± 0.28
Snubnose pipefish	<i>Cosmocampus arctus</i>	Male	80.33 ± 12.05	0.22 ± 0.11	6.81 ± 0.79	2.14 ± 0.36	2.42 ± 0.54	0.88 ± 0.09
		Female	60.50 ± 1.50	0.10 ± 0.00	5.50 ± 0.50	1.90 ± 0.10	2.15 ± 0.05	0.90 ± 0.10

Table 1: Male and female pipefish standard length (mm), weight (g), head length (mm), head height (mm), snout length (mm), and snout width (mm; mean ± SEM) of pipefishes collected in southern California.

Common Name	Scientific Name	Standard length (mm)	Weight (g)	Head length (mm)	Head height (mm)	Snout length (mm)	Snout width (mm)
Kelp pipefish	<i>Syngnathus californiensis</i>	175.22 ± 6.99	1.80 ± 0.09	23.11 ± 0.52	3.18 ± 0.08	12.76 ± 0.33	1.77 ± 0.05
Bay pipefish	<i>Syngnathus leptorhynchus</i>	161.15 ± 6.33	1.30 ± 0.15	20.29 ± 0.85	3.21 ± 0.12	11.41 ± 0.57	1.54 ± 0.06
Barcheek pipefish	<i>Syngnathus exilis</i>	180.96 ± 4.31	1.63 ± 0.12	22.24 ± 0.54	3.25 ± 0.38	12.59 ± 0.35	1.56 ± 0.04
Chocolate pipefish	<i>Syngnathus eucnourus</i>	154.04 ± 9.90	1.46 ± 0.37	20.40 ± 1.37	3.15 ± 0.21	11.83 ± 0.84	0.56 ± 0.10
Barred pipefish	<i>Syngnathus auliscus</i>	98.73 ± 6.65	0.35 ± 0.07	11.39 ± 0.88	2.46 ± 0.19	4.77 ± 0.39	1.24 ± 0.12
Snubnose pipefish	<i>Cosmocampus arctus</i>	72.40 ± 7.27	0.17 ± 0.06	6.28 ± 0.50	2.04 ± 0.17	2.31 ± 0.25	0.89 ± 0.05

Table 2: Combined standard length, weight, head length, head height, snout length, and snout width (mean ± SEM) of pipefishes collected in southern California.

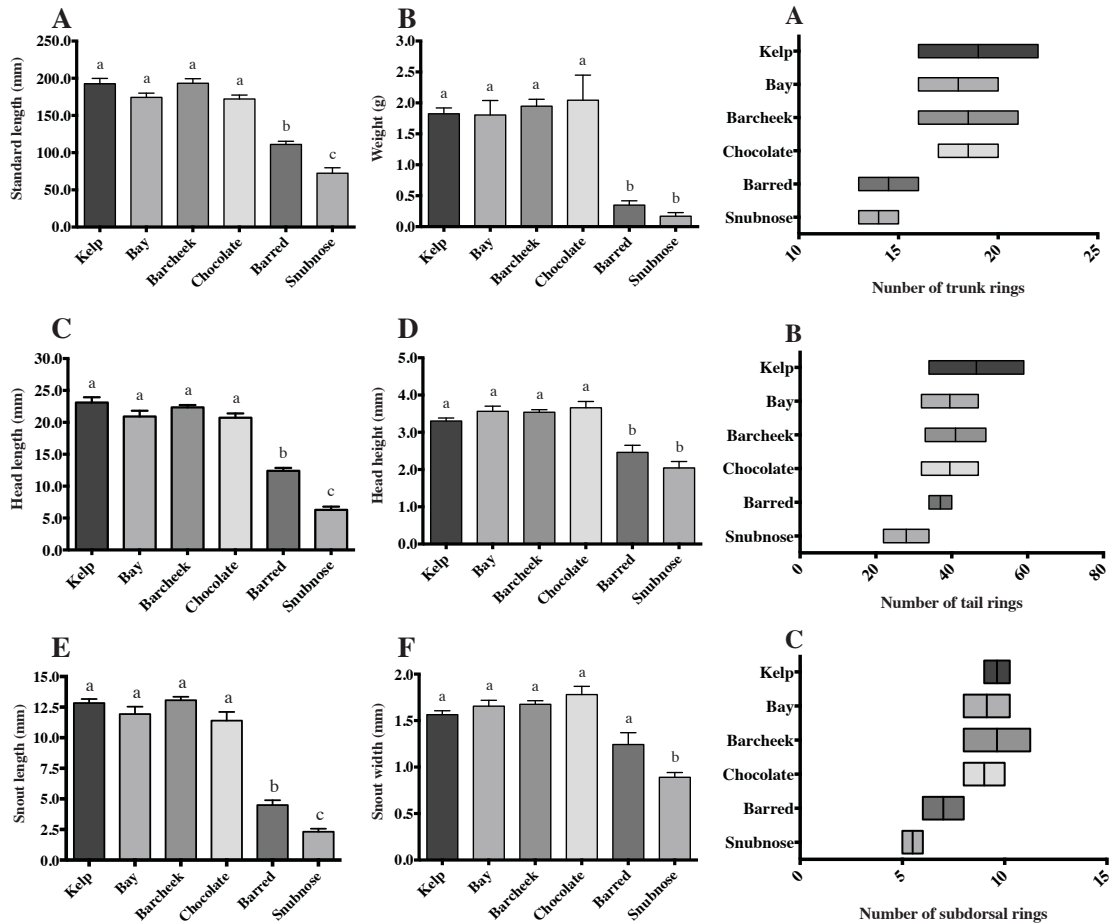


Figure 2: Comparisons of morphological characters for pipefishes collected in southern California [kelp pipefish (*Syngnathus californiensis*; $n = 87$), bay pipefish (*S. leptorhynchus*; $n = 54$), barcheck pipefish (*S. exilis*; $n = 131$), chocolate pipefish (*S. euchrous*; $n = 44$), barred pipefish (*S. auliscus*; $n = 27$), and snubnose pipefish (*Cosmocampus arctus*; $n = 5$)]. (A) Standard length (mm); (B) Weight (g); (C) Head length (mm); (D) Head height (mm); (E) Snout length (mm); and (F) Snout width (mm). Letters indicate significant differences ($p < 0.05$).

Figure 3: Trunk, tail, and subdorsal ring ranges of kelp pipefish (*Syngnathus californiensis*; $n = 87$), bay pipefish (*S. leptorhynchus*; $n = 54$), barcheck pipefish (*S. exilis*; $n = 131$), chocolate pipefish (*S. euchrous*; $n = 44$), barred pipefish (*S. auliscus*; $n = 27$), and snubnose pipefish (*Cosmocampus arctus*; $n = 5$). (A) Trunk rings ($p = 0.41$); (B) Tail rings ($p = 0.71$); (C) Subdorsal rings ($p = 0.14$). Line within the box represents the mean.

References

- Flisik, T.J. and Horn, M.H. 2012. Effects of a partial diet of pipefish, a low-quality prey, on the growth of captive elegant tern chicks. Masters Thesis, California State University Fullerton, CA, USA, pp. 1-67.
- Fowler, H. W. 1923. Records for west coast fishes. Proceedings of the Academy of Natural Sciences 75: 279-301. (Swain identification).
- Fritzsche, R.A. 1980. A revisionary study of the eastern Pacific Syngnathidae (Pisces: Syngnathiformes), including both recent and fossil forms. Proceedings of the California Academy of Sciences 42: 181-227.
- Girard, C. F. 1854. Observations upon a collection of fishes made on the Pacific coast of the United States. Proceedings of the Academy of Natural Sciences 7(4): 142-156.
- Heck Jr., K.L., Hays, G., and Orth, R.J. 2003. Critical evaluation of the nursery role hypothesis for seagrass meadows. Marine Ecology Progress Series 253:123-136.
- Starks, E. C., and E. L. Morris. 1906. The marine fishes of southern California. University of California Publications in Zoology 3(11): 159-251. (Jenkins and Evermann).
- Louie, K. D. 2003. Genetic structure and phylogeography of four eastern Pacific estuarine species, with an emphasis on eelgrass dependent taxa. PhD Thesis, University of California at Los Angeles, Los Angeles, CA, USA; pp. 1-54.
- Love, M. S. 2011. Certainly more than you want to know about the fishes of the Pacific Coast: A postmodern experience. Santa Barbara, CA: Really Big Press. pp. 213-214.
- Miller, J. D., and Lea, R. N. 1972. Guide to the Coastal Marine Fishes of California. [Sacramento]: State of California, Department of Fish and Game, 89.
- Mobley, K. B., Small, C. M., and Jones, A. G. 2011. The genetics and genomics of Syngnathidae: pipefishes, seahorses and seadragons. Journal of Fish Biology 78: 1624-1646.
- Orth, R. J., Carruthers, T. J. B., Dennison, W. C., Duarte, C. M., Fourqurean, J. W., Heck, K. L., Hughes, A. R., Kendrick, G. A., Kenworthy, W. J., Olyarnik, S., Short, F. T., Waycott, M., and Williams, S. L. 2006. A global crisis for seagrass ecosystems. Bioscience 56: 987-996.
- Osburn, R. C., and J. T. Nichols. 1916. Shore fishes collected by the 'Albatross' expedition to lower California with descriptions of new species. Bulletin of the American Museum of Natural History 35: 139-181.
- Phillips, R. C. and Meñez, E. G. 1998. Seagrasses. Smithsonian Contributions to the Marine Sciences, No. 34. Smithsonian Institution Press, Washington D.C. pp. 104.
- Shokri, M. R., Gladstone, W. and Jelbart, J. 2009. The effectiveness of seahorses and pipefish (Pisces: Syngnathidae) as a flagship group to evaluate the conservation value of estuarine seagrass beds. Aquatic Conservation: Marine Freshwater Ecosystems, 19: 588-595.
- Storer, D. H. 1846. Memoirs of the American Academy of Arts and Sciences, New Series 2: 253-550.
- Wilson, A.B. and Orr, J.W. 2011. The evolutionary origins of Syngnathidae: pipefishes and seahorses. Journal of Fish Biology 78: 1603-1623.
- Wilson, A. B., Vincent, A., Ahnesjö, I., and Meyer, A. 2001. Male pregnancy in seahorses and pipefishes (family Syngnathidae): rapid diversification of paternal brood pouch morphology inferred from a molecular phylogeny. Journal of Heredity 92: 159-166.

Sex Differences in Thermoregulatory Activity of the Common Chuckwalla (*Sauromalus ater*)

Department of Biological Science, California State University, Fullerton

Emily Sanchez and Christopher R. Tracy

Abstract

Climate change may decrease the amount of time environmental temperatures are suitable for ectotherm activity, thus reducing time available for energy acquisition, territorial displays and reproduction. To assess potential impacts of climate change on populations, it is important to study how lizards use their time for activity. Male common chuckwallas (*Sauromalus ater*) do not use all of the time where temperatures are suitable for activity (outside of rock crevices), suggesting that climate change will have minor effects on their ability to perform such activities. We studied female thermoregulatory behavior for comparison because sex differences in the use of suitable activity time, especially during their reproductive season in spring, could result in reduced reproductive output of the population in the face of climate change. Males may have higher above ground activity in order to defend territories, search for mates, and forage, whereas females may only use above ground activity for foraging and some thermoregulation, but otherwise remain below ground to avoid predation. We measured body temperatures (T_b) of 5 females and 1 male chuckwalla in a semi-natural enclosure every 15 minutes during summer. To determine how chuckwallas used the thermal environment, we compared (T_b) to environmental temperatures (T_e), measured with copper models that mimic heat exchange of chuckwallas. The proportion of time females were active relative to the time with suitable T_e (0.54 ± 0.061) did not differ from that of the male (0.64) in the enclosure ($t = -3.67$, $p = 0.021$). Further, the amount of time the male and females spent thermoregulating inside rocks vs. outside did not differ. The proportion of time the male was active (0.78) relative to the time with suitable T_e was greater than wild males (0.45 ± 0.210) from the previous study ($t = -3.850$, $p = 0.012$). Because the use of suitable activity time does not appear to differ between female and male chuckwallas during summer months, chuckwalla populations may not be greatly affected by minor reductions in suitable activity time as a result of climate change. However, the use of suitable activity time may vary across seasons which may reveal season specific sex differences, so female thermoregulatory behavior will be investigated during spring.

Catalytic Phenanthridine Synthesis via Oxidative Cyclization of Substituted 2'-arylbenzaldehyde Oxime Ethers under Photoinduced Electron Transfer Conditions

Department of Chemistry and Biochemistry, California State University, Fullerton

Nicholas Armada, Julie Hofstra, Brittany Grassbaugh, Quan Tran, and Dr. Peter de Lijser

Abstract

Organic heterocycles are abundant in natural and pharmaceutical products and discovering new routes to synthesize these compounds can help provide more effective methods to produce them commercially. Understanding the mechanisms behind the synthesis reactions of heterocycles can also show insight on how the enzymes that create these types of products operate. Oxime carbonates on biaryl substrates have been shown to form nitrogen containing heterocycles through an iminyl radical intermediate. In this project we present a new reaction that causes substituted biaryl oxime ethers to undergo an intramolecular cyclization reaction to form corresponding substituted phenanthridines in the presence of 9,10 – dicyanoanthracene (DCA) as a catalytic photosensitizer. Mechanistic studies suggest that this oxidation reaction is initiated by an electron transfer followed by a nucleophilic attack by the aryl ring on the nitrogen of the oxime ether. Our Hammett plot shows a concave downward trend for strong electron-donating substituents, which suggests a change in the rate-limiting step. Our reaction minimizes the formation of unwanted nitrile side products, has shown to be regiospecific when the 2' – aryl ring is substituted in the meta position, and is an environmentally friendly route to synthesizing substituted phenanthridine compounds.

Synthesis and Structure-activity Studies of Drugs that Affect a Cancer Causing Mechanism and Reduce Cell Growth

Department of Chemistry and Biochemistry, California State University, Fullerton

Department of Biological Science, California State University, Fullerton

Aneta Jelowicki, Keziah Ellery L. Tan, Elizabeth H.F. Li, Christian A. Martindale, Chiaokai Wen, Christopher M. Ott, Dr. Nilay V. Patel and Dr. Peter de Lijser

Abstract

A survey of data obtained from a variety of biological assays on a drug library consisting of more than 200 synthesized small organic molecules has revealed significant potential anticancer activity for molecules containing a specific structural motif. Previously, several of the compounds in a library of drugs, which were designed to activate the Wnt pathway (to promote stem cell pluripotency), were found to decrease the β -catenin levels in the cell. The dysregulation of β -catenin has also been linked to various types of cancer and we therefore decided to investigate the potential influence of these drugs on cell proliferation. The drugs tested in the assays consisted of compounds containing chalcones, amines, amides, small peptides, esters, aldehydes, ketones as well as oximes and oxime ether functionalities. Cell proliferation was determined by the CyQuant assay, which uses DNA content of the cells to quantify the number of plated cells. HeLa cells were treated with the drug (10 μ M) for 24 hours and the DNA content was quantified. Preliminary results show that several drugs inhibit cell proliferation significantly, in some cases even better than known anticancer drugs such as mitomycin C and cisplatin. Further studies are currently underway to determine the mechanism of action underlying the anti-proliferative effect of these drugs. A structure-activity analysis of the most active drugs suggests that many of them have an amide linker as a common functionality. Further work is underway to expand the drug library in order to find more potent drugs.

Photoinduced Oxidative Cyclizations of o-Arylalkynylloximes Transfer Conditions

Department of Chemistry and Biochemistry, California State University, Fullerton

Michael Ko, Wan Shin Kim, and Dr. Peter de Lijser

Abstract

The synthesis of heterocycles is a popular field of study often associated with drug and natural product synthesis. In such applications, many studies have explored the possibility of using oximes and oxime ethers as a building block for heterocycle synthesis, but very few studies have explored the radical or radical cation cyclization pathways. Previous work completed on o-arylbenzaldehyde oximes and oxime ethers has shown that the oxime ether radical cations react with the aromatic group forming a cyclized product, while the iminoxyl radicals did not. This work is focusing on a series of o-arylalkynylloximes to determine the behavior of the alkyne moiety with respect to intramolecular cyclization reactions. Experiments were carried out with a variety of o-arylalkynyl oximes and oxime ethers derived from benzaldehyde and acetophenone under different conditions to find the desired cyclization pathway of the oximes and to better understand the reactivity of the reactive intermediates. Product analysis (GC-MS and ^1H NMR) was used to determine the formation of heterocyclic compounds. Using chloranil as the sensitizer at 350 nm in benzene or acetonitrile, no cyclic products were formed; the majority of the starting material was found to undergo syn-anti isomerization. Using 9,10-dicyanoanthracene (DCA) at 420 nm in acetonitrile did not produce cyclized products for the oxime ethers, however, ^1H NMR analysis of the product mixtures indicated that the o-alkynylacetophenone oximes did form cyclic products via a proposed 6-exo-dig cyclization pathway. On the basis of these results we conclude that the oxime ether radical cation is not an appropriate intermediate for the oxidative cyclization pathway of o-arylalkynyl oximes. Instead, the reaction seems to involve a radical addition pathway. Current studies are focusing on isolation, characterization and quantification of the cyclization products.

Reduction of MM1853 with the Artificial Electron Donor, Dithiothreitol

Department of Chemistry and Biochemistry, California State University, Fullerton

Man Lou and Dr. Madeline Rasche

Abstract

For decades, methane was known to be a potent greenhouse gas, which may play a role in climate change. Methane-producing microbes are known as methanogens, are archaea found in rumenal systems, undersea volcanos, and other anaerobic (O₂-free) environments. The cofactor tetrahydromethanopterin (H₄MPT) is a critical requirement for microbial methane production. There are eighteen proposed enzymes in the pathway of H₄MPT synthesis, many of which have not been characterized. The focus of this work is to gain information on the function of the *Methanosarcina mazei* protein MM1853, a homolog of the H₄MPT synthesis enzyme Orf19. The specific function of Orf19/MM1853 in synthesizing H₄MPT has not been discovered; however, the *MM1853* gene clusters with *MM1854*, which codes for the final enzyme of H₄MPT synthesis, dihydromethanopterin reductase (DmrX). From gene cluster evidence and the structural prediction that MM1853 contains a flavin cofactor, it was hypothesized that MM1853 could serve as an electron donor for DmrX in vitro. As a first step in testing this hypothesis, a six-histidine tagged version of MM1853 was produced in *Escherichia coli* and purified using nickel-nitrilotriacetic acid agarose chromatography. The purified protein was yellow, consistent with the presence of the predicted tightly bound flavin cofactor. The protein was treated with increasing concentrations of the reducing agent dithiothreitol (DTT) and UV-visible spectrum scans were taken. The successful reduction of MM1853 was observed through decreases in the absorbance of the flavin peaks at 380 nm and 460 nm. These results provide the foundation for future studies to understand the specific reaction catalyzed by this enzyme in the pathway of H₄MPT biosynthesis.

Green Digital Photographic Method for Protein Assay

*Department of Chemistry and Biochemistry, California State University, Fullerton
Chiang Mai University, Thailand*

Theary Monh, Brenna Biggs, Kate Grudpan, Richard Deming and Dr. Darren Sandquist

Abstract

One of the most common analytical techniques used for trace analysis is spectrophotometry. However, spectrophotometers are expensive, wasteful, and do not allow for simultaneous sample measurements. We devised a digital photographic method for protein assay that takes simultaneous measurements, is less expensive, and less wasteful than the traditional method. Standard BSA protein samples with concentrations ranging from 0 $\mu\text{g/ml}$ to 300 $\mu\text{g/ml}$ were created using the Modified Lowry Protein Assay method, which turned the protein samples blue. The intensity of the color was directly proportional to the concentration. Samples of fish sauce, soy sauce, beauty drinks, and chicken essence were also prepared using the Modified Lowry method to determine protein concentration. The standards and samples were placed on a well plate and photographed using an iPhone camera. The RGB values of the photo were analyzed using the Apple DigitalColor Meter application, and the sample concentrations were determined using a standard calibration graph. The photographic method sample concentrations were compared to the results of the spectrophotometer, which indicated the coefficient of determination was 0.94. This suggested that the digital photographic method could serve as a viable replacement for the spectrophotometric method for protein assay.

Analysis of a Potential Paleotsunami Deposit at Los Penasquitos Marsh, San Diego County, CA.

Department of Geological Sciences, California State University, Fullerton

Jeremy Cordova

1. Introduction

In recent years much geologic research has focused on characterizing recently deposited tsunami sediments in regions such as Thailand, the Andaman Islands, Mexico, and Indonesia, in order to improve our knowledge of future tsunami risk and past occurrences (Herrera et al 2013, Ilayaraja et al 2012, Peters and Jaffe 2010, Rhodes et al 2011). The knowledge acquired from studying these deposits can be extrapolated to possible tsunami deposits from the recent geologic past in order to more properly understand the long-term risks coastal communities face (Uslu et al 2010). The location selected for study in this research is the Los Penasquitos marsh, which lies along

the Pacific shoreline northeast of Torrey Pines State Park, in San Diego County, CA (Figure 1). Los Penasquitos is an excellent study location because the wetland is located along the Pacific shoreline in a tectonically active area, and the infilling of the lagoon by mud and peat serves to preserve its geologic record.

Three days were spent at Los Penasquitos collecting 21 reconnaissance cores from three general areas within the marsh, at its most inland extent, and along its southern and northern edges (Figure 2). The goal of reconnaissance was to determine the lagoon's stratigraphy and locate potential tsunami deposits for later analysis.

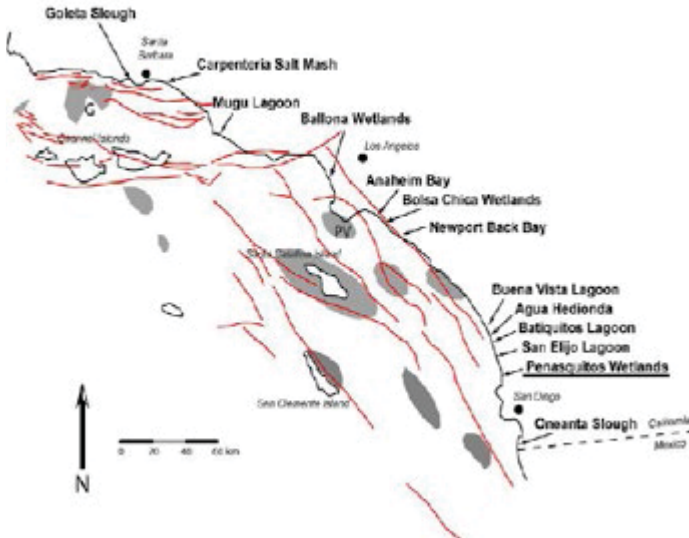


Figure 1: shows possible tsunami sources in the Southern California region, with the location of Los Penasquitos underlined. Other suitable locations for study are as well on the map. Faults are shown as red lines, offshore landslides as grey shapes indicating the mapped extent of debris.



Figure 2: Google Earth image of Los Penasquitos wetland, with a reference map on the top right. Numbered locations show reconnaissance core locations, with shell-hash recovery locations in red. Scale is located on the bottom left, the photo is oriented N/S.

Reconnaissance coring was followed by the collection of a 2.5cm diameter piston core from the PEN-012 sample location (Figure 2). The piston core penetrated a shell-hash layer, also present in four other reconnaissance cores, of approximately 10cm thickness, and all occurring at 180-280cm depth. Analyses of this core were conducted in order to test the hypothesis that the shell-hash layer is debris from a prehistoric tsunami.

It should be established that the term “prehistoric”, within the San Diego area will be considered anything before 1769, when the local native American tribe, the Kumeyaay, note within their oral history the arrival of father Juniperra Serra, a Spanish missionary who established settlements in the area (Connelly and Carter, 2013). It is stated by the Kumeyaay tribe on their official website that previous encounters occurred with missionaries and explorers but no settlements were established in the area until 1769. The age of the shell-hash is significantly older than 1769, and therefore is easily classified as prehistoric.

2. Los Penasquitos Wetland

The Los Penasquitos lagoon/wetland is located at N 32° 55'38 W 117° 15'01, west of Interstate 5, within Torrey Pines State Park, in the city of Del Mar, CA (Figure 2). The wetland occupies roughly 3.5 km². The modern wetland consists largely of a patchwork of pickleweed, 4-winged saltbush, and other common wetland plants, among elevated dry patches of soil, and low-lying spaces containing saline pools. The surrounding geology consists of Pleistocene sedimentary rocks (Grine, 2010), which define the boundaries of the wetland and outcrop along the surrounding steep slopes that are covered by sagebrush, and the endemic Torrey pines. The wetland is separated from the Pacific Ocean by a baymouth bar, on which the Pacific Coast Highway was constructed, except for a single open tidal channel spanned by a highway overpass. Within the wetland there is no construction other than a railroad which travels NE/SW through the marsh.

3. Field Methods

Field work within Los Penasquitos initially consisted of reconnaissance coring using a manually inserted (push) 2.0 cm-diameter open-sided soil probe. At each sample location the GPS coordinates were recorded, and a push core was examined (Figure 3). Once inserted to maximum depth the core cylinder is turned in one full circle, to account for the open side not making a cut in the sediment. Once turned the soil probe is pulled from the ground, laid flat, and the open surface of the core is scraped clean. Then the stratigraphy of the core was logged in the field. Significant fossils were collected and bagged for future use.



Figure 3: Example of cut 2.0cm diameter recon core, ready to be described in the field

Figure 4 shows the core logs from the 21 reconnaissance cores taken at Los Penasquitos, arranged from seaward to inland (approximately west to east). The shell-hash layer was found within the cores at a depth zone defined by the dark green intervals on Figure 4. The shell-hash layer was penetrated by 5 cores. The distribution of the layer suggests that the shell hash layer was deposited over a significant, but irregular and/or patchy region, and therefore is not likely to have formed within a tidal channel as a lag deposit.

Reconnaissance coring was followed up by taking a 2.5cm diameter piston core from the PEN-12 coring site (Figure 2). To collect a core, the piston corer, consisting of an open-bottom steel cylinder with a T-bar handle at the top, was inserted into the ground roughly 10 cm from the previous core hole left by the soil-probe during reconnaissance. The process of using the piston core involves inserting the steel cylinder into the ground while maintaining the tension of a steel cable that controls a piston, which seals the bottom of the steel cylinder once it is filled by sediment. Once the cylinder has reached its maximum depth in the ground it is pulled back upward with the steel cable released, allowing the bottom to seal and the sediment to be retrieved. At the surface the cylinder containing the sediment from the drive is laid

horizontally, the bottom lid is opened, and the sediment is extruded from the cylinder into a PVC tube, and wrapped in plastic wrap and tin foil for transport and cold-storage at CSUF. The 285 cm long piston core PEN-12 was retrieved in four drives that reached 75cm in depth. The fact some cores were shorter than the core cylinder is interpreted as having two causes: Material lost from the core cylinder while removing the core from the ground, and compaction of the near- surface water-logged sediments. The loss of material and some compaction of sediment can explain the gaps in recovery at intervals 60-75cm and 140-150cm. The lack of gaps in recovery (and thus apparent lack of compaction) in the lower two drives, drives three and four, can possibly be attributed to a higher proportion of sand lower in the core leading to greater cohesion of sediment within the core cylinder, and the operators inability (given the equipment used) to compact sand.

4. Laboratory Methods

In testing the hypothesis that the shell-hash layer was deposited by a tsunami, multiple analyses were performed on the sediment in the piston core. These analyses included Magnetic Susceptibility (MS), grain size, and Loss On Ignition (LOI) at 550°C and 950°C. Previous studies indicate that tsunami deposits display a relatively high MS reading (Herrera, 2013, Wassmer et al, 2010). The reason tsunami deposits have a high MS reading is because their nearshore and offshore source, which is dominantly sands, contain significant accumulated primary metallic minerals, such as hematite and magnetite (Edwards et al, 1998). Conducting LOI at 550°C and 950°C allows for calculation of the differential amounts of organic matter and carbonates, respectively. Grain size analysis provides quantitative information on the degree of sorting and grading the shell-hash layer displays, and was done using a Malvern laser diffraction grain-size analyzer.

LOI at 550°C was used to measure the variation of the sediment's organic component with depth. Changes in organic content reflect changes in the lagoon's biological activity over time (Dean, 1974). To measure the total organic carbon content in the sediment, samples were taken at a 1 cm interval throughout the core, and heated to 100°C for one hour. This heating dries the samples, removing the water so as not to skew the organic carbon mass calculations.

After initial heating samples were weighed, and placed in an oven, then heated to 550°C for three hours. After heating the samples were again weighed to calculate a differential mass, the mass of organic carbon within the sediments.

LOI at 950°C measures the changes in carbonate content of the sediments. Changes in carbonate content indicate changes in the lagoon's circulation, salinity, and aridity (Dean, 1974). To measure the carbonate content in the sediments samples from each 1 cm interval were weighed and then heated to 950°C for 3.5 hours. After heating the samples are weighed again to produce a second differential mass, the mass of carbonates in the sediment.

Grain size analysis was conducted on the shell-hash layer, including the 5.0 cm of sediment above and below the shell-hash, to determine the range and distribution of grain sizes within the sediment. In order to prepare sediment from the PEN-012 core samples approximately 2 grams of sediment were taken from each centimeter of depth and placed in a beaker, and visible shell fragments were removed. When submerged in the solution Sodium Hexametaphosphate, a disaggregate diluted with deionized water, the sediment separates into individual grains. Heating to 250°C and the addition of 30ml of 30% peroxide solution then breaks down the organic matter within the sample. This is necessary so that organic particles are excluded from the grain size analysis. After pipetting the remaining water off the samples, the samples are soaked in 10ml of 1M HCl for 24 hours in order to break down the biogenic silica grains within the sample. The addition of 10ml of 1M NaOH to each sample, and running the samples in a centrifuge twice for 15 minutes, neutralizes and removes the HCl from the sediment. The NaOH is then diluted with deionized water and removed after centrifuging. Once chemically prepared the sediment from core PEN-012 was weighed and passed through a 2mm sieve to remove any grains too large for the analyzer. Once these steps were complete the samples were diluted to 1-3% light obscuration and placed in a Malvern laser diffraction grain size analyzer in order to obtain the range and distribution of grain sizes in each sample.

Magnetic susceptibility analysis is done to give a profile of the distribution of magnetic minerals in the sediments, which can be used to constrain the sediment's source. In order to measure MS samples from each 1 cm interval were placed in a plastic sample container and

then inside a Bartington MS2B magnetic susceptibility system, which exposes the sample to a magnetic field and measures the alteration in that field relative to a non-magnetic sample. The result is given as a dimensionless number which, within the studied sediments, ranges from 0 to 7.0.

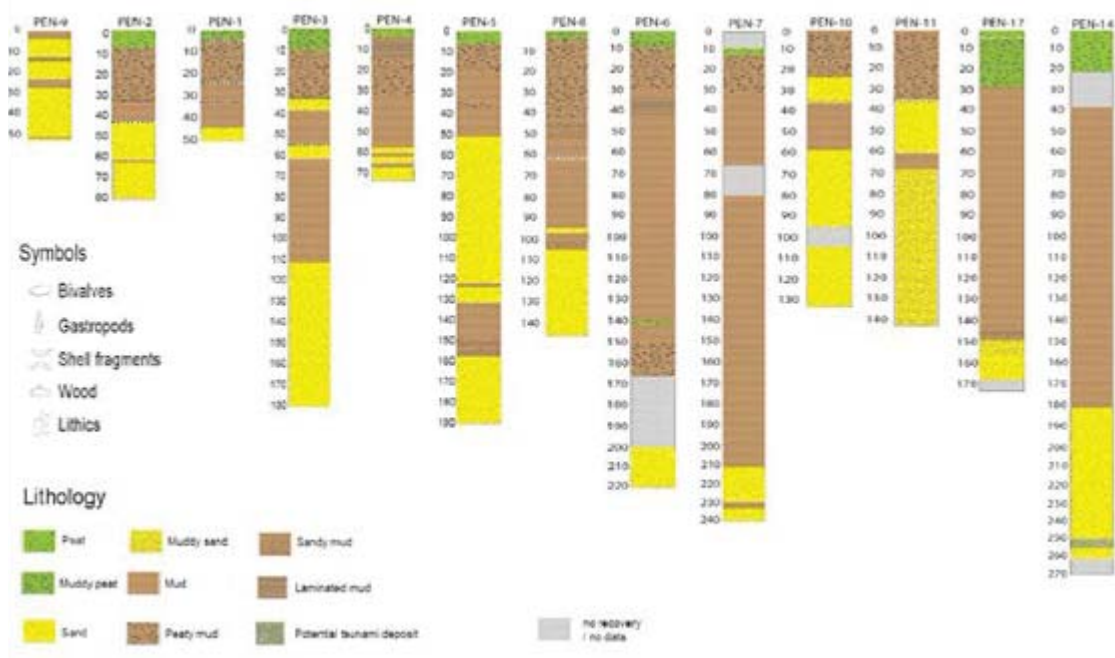
5. Results

In order to test the hypothesis, that Los Penasquitos contains a prehistoric tsunami deposit, a large volume of data from numerous sources was collected on the shell-hash layer (Figure 5). These data document a high energy deposit of poorly sorted sand, mud, and shell fragments, of marine origin, deposited within the lagoon sediments. Organic-rich sediment at the surface seems to represent deposition in the modern wetland. Mud present below the peat often appears mottled brown and black, and as the mud is mixed with silt these sediments likely represent deposition in a lagoon. Thickness of the peat is anywhere from 5-35 cm. Mud below the surface peaty sediment occupies a depth of anywhere from 15-100cm, grading between mixes of muddy silt and silty mud. Based on the presence of fine sands, muds, and silts, as mixed sediments, the infilling of the lagoon most likely occurred in a tide-dominated setting (Boggs, 2012). Nearly all of the cores bottom out in sand or muddy sand because of the difficulty in pushing the soil probes through sandy sediment.

The following is a visual description of the piston core PEN-12, from which figure 5 was created. The upper 11 cm consists of dark brown/black peaty mud, which contains abundant plant fibers. Below the peaty mud from 11-56 cm depth there is brown mud, grading from light downward to dark, and becoming silty, then mottled brown and black, then silty again. At 57 cm depth fine sandy silt is present, but recovered sediments have a gap between 60 and 75cm depth. At 75 cm depth the sediment is again mottled dark colored muds, grading into silty then sandy mud until approximately 120 cm depth, when sand becomes more prevalent than silt or mud. The sand which has an upper contact at 120 cm depth contains largely subangular quartz, with about 20% muscovite, biotite, and feldspars. Below the mica, feldspar, and quartz sand is a recovery gap of 8cm, underlain by mottled brown/black mud, which gradates alternately into silty and sandy muds until 209 cm depth. At 209 cm depth is a bed of heavily oxidized

< Seaward

Los Penasquitos Reconnaissance Core Stratigraphy



6. Description of the Shell Hash Layer

med to coarse quartz sand of 3.5 cm thickness. Below the med to coarse sand unit is mottled mud, then dark mud occupying 20 cm of depth, above the shell-hash layer.

The shell-hash layer is overlain by mud, with which the shell-hash has a poorly defined upper contact. Within the shell-hash is poorly sorted sand, silt, and clay, filled with fossil shell fragments. The basal contact of the shell-hash is sharp, and is underlain by silty fine sand that appears largely uniform within the 40 cm of depth it has been documented, with respect to the sands structure, color, appearance, sorting, and resulting signature from the completed analyses. At 284 cm depth the sediment became impenetrable to the piston core that was in use. Given the core description provided, mixed poorly oxidized fine-grained sediments, it appears that Los Penasquitos exhibits typical lagoonal facies within the measured upper 3 m of sediment.

Description of the shell-hash layer, from 235-245 cm depth below the surface, was done in the lab from a visual inspection of the 5 cm diameter core PEN-012. Sediment below the shell-hash layer consists of well-sorted oxidized muddy medium quartz-sand. Above the muddy sand the shell-hash begins with an irregular but sharp base, suggestive of an erosive contact (Figure 5). The upper contact of the deposit is gradational into the overlying mud. Internally, the shell-hash structure is chaotic, but the matrix shows a fining upward trend visible in the grain size data, discussed below. The deposit is extremely poorly sorted, relative to the surrounding units.

The fossil shells within the unit are primarily angular fragments 1-3 cm in their longest dimension. The identified fossils are of the following genera: Spirotropis, Mitrella, Nassarius, Pecten, Venus, Macoma, and an unknown genus of oyster. All of these genera live in calm salt water,

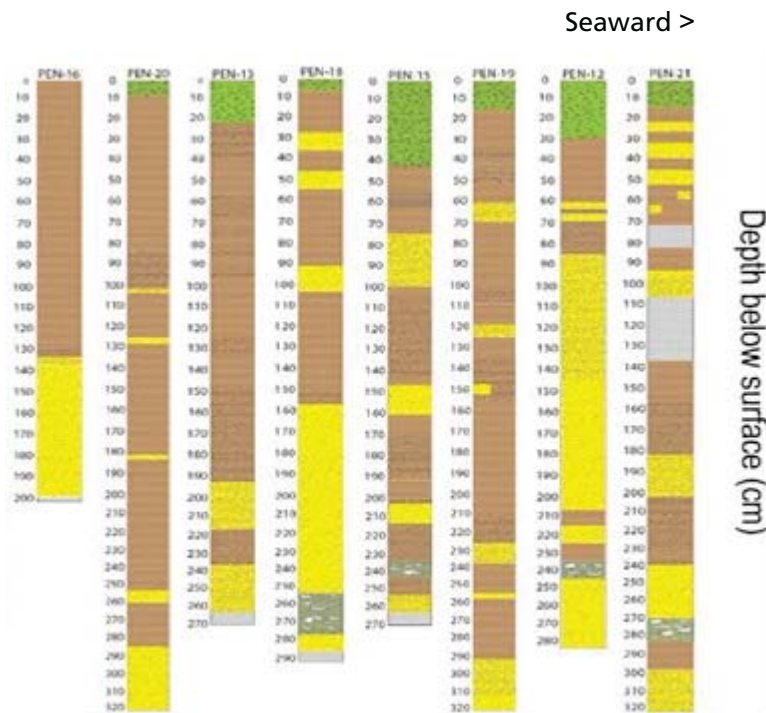


Figure 4: 21 Recon core descriptions from Los Peñasquitos, arranged from seaward inland, with the surface at the top. These cores were taken with a 2.5cm diameter open-sided soil probe. Legend indicates the lithology and symbols on the lower left. Core stratigraphy is generally consistent, and shows 5-25cm of peat, followed by mud, and then alternating mud and sand, or sandy mud/muddy sand. The shell-hash occurrences are highlighted by a green rectangle on the lower right.

below the fair weather wave-base offshore, or in lesser diversity and density within lagoons (Choe et al, 2012, Duer, 2008). The presence of these fauna within a potential tsunami deposit could be a result of the tsunami wave picking up offshore material and depositing it in what was then a restricted lagoon. The broken and jumbled appearance of the shells supports this interpretation, as the shells would have travelled at least one kilometer through roiling debris-filled water to reach their current location.

In order to constrain the age of the shell-hash one sample each of an unidentified bivalve, a gastropod, and an oyster, were collected from the PEN-12 core and sent to an AMS radio carbon dating laboratory at the University of California Irvine. Using a mass spectrometer the C^{14} can be separated from the C^{12} and their ratio of abundances determined. Determination of the carbon isotope ratio, and the knowledge that the half-life of C^{14}

is 5,730 years, allows for the calculation of an age based on the amount of decay of C^{14} into C^{12} which has taken place. After calibration of the C^{14} ages for the marine reservoir the three samples cluster at a final age of 1,400 years before present, +/- 20 years, as shown in figure 6. Calibration was performed by Robert Leeper, of the USGS, using the program Oxcal.

Magnetic Susceptibility (MS) results for core PEN-12 are summarized in Figure 7. The average MS value for the core was 2.3. Sand layers alone gave an average of 2.0, while the mud average was higher at 2.7. The shell-hash had an average reading of 4.6, with values as high as 7.0. Values for MS within the shell-hash were higher than any other unit within the core. The higher MS values in the shell hash layer suggests that the shell hash layer was derived from a different source than enclosing lagoonal sediments.

Photo of Deposit

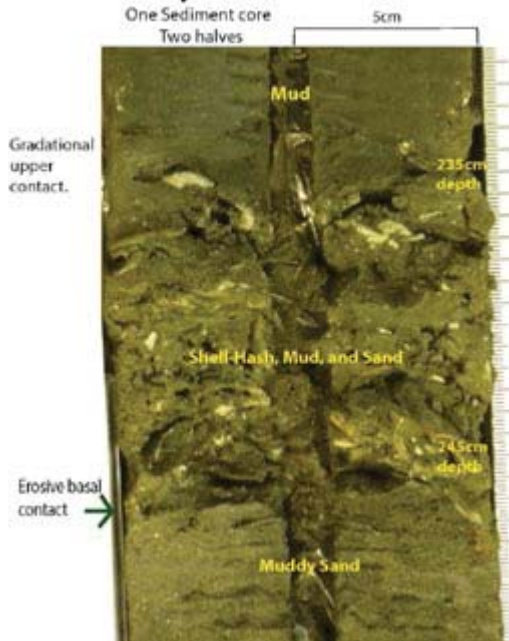
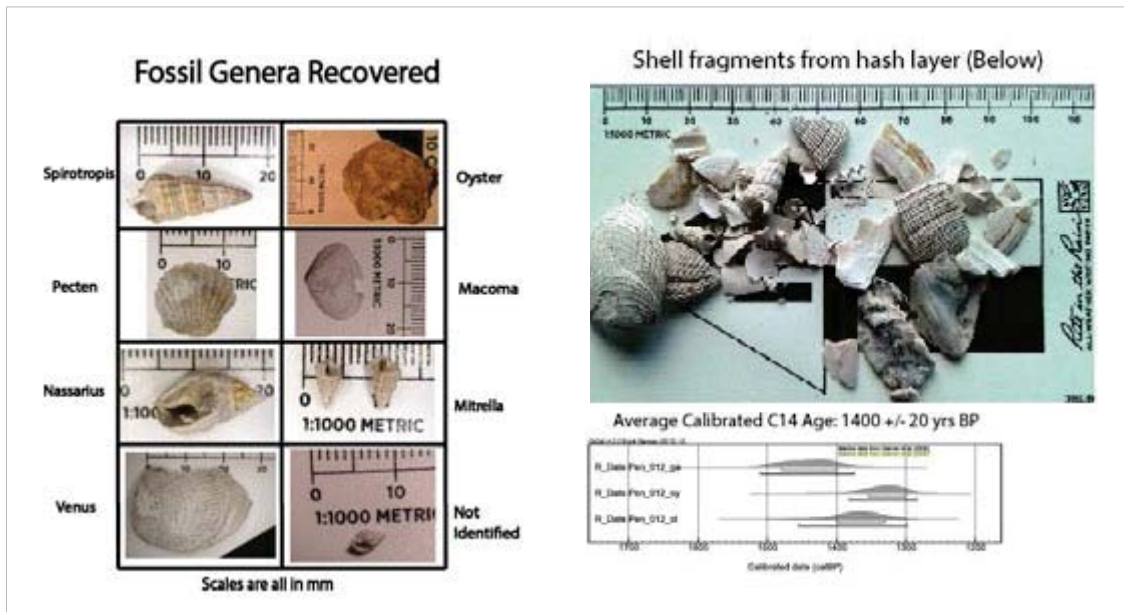


Figure 5: (left) Photograph of the shell-hash deposit from 5cm diameter core PEN-012, with depth indicated along the right side. Lithology and significant features are noted in text.

Figure 6: (bottom) Fossil genera recovered relatively intact from the shell-hash are shown on the left, with identification. On the right is a representative photo of the shell fragments, showing their angularity, and demonstrating that whole shells were not common. Below on the right is an age plot from three carbon dated shells, produced by Robert Leeper on OxCal. Calibrated dates cluster at 1400yrs BP, and are from a bivalve, oyster, and gastropod sample.



PEN-12 Sediment Core Data Recovery Location: WGS84 11s: 0477124 3643271

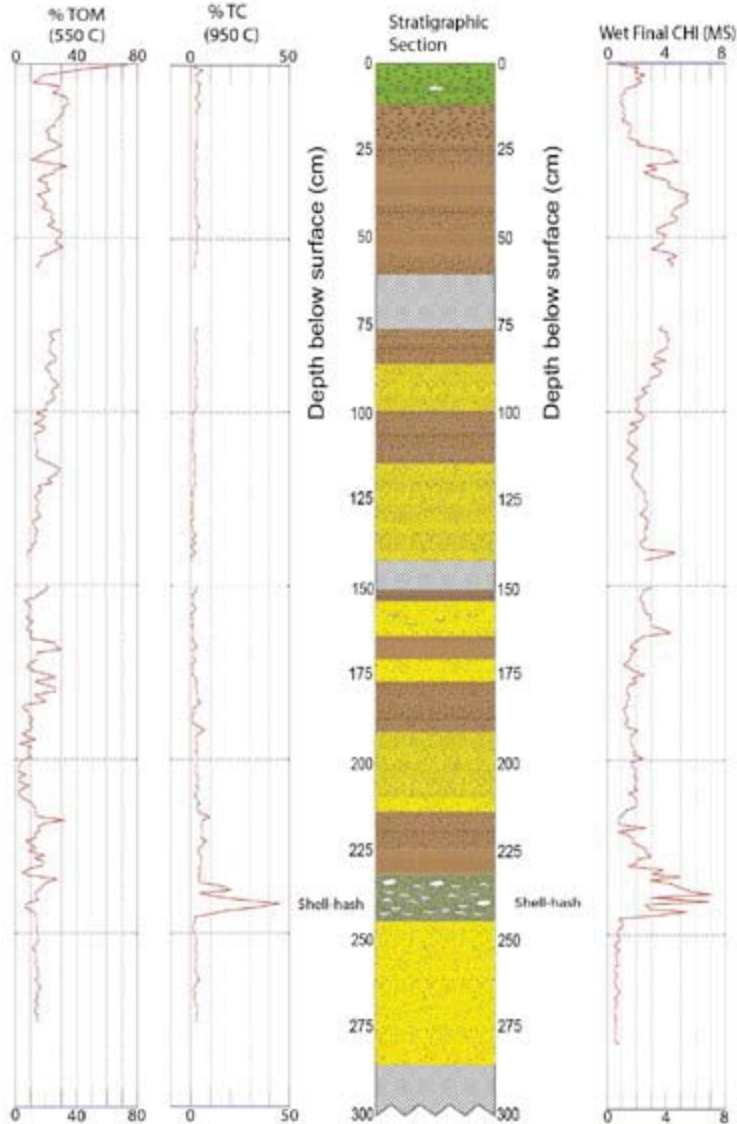


Figure 7: Results of analyses on 2.5 cm diameter piston core PEN-012. On the Left is total organic matter (LOI 550), in which the modern peaty sediment is clearly visible by an increase in organic matter in the upper 55cm. Left of center is total carbonates (LOI950), which clearly shows the shell-hash as a massive spike in carbonates between 235-245cm depth. Right of center is an illustration of core PEN-012, with the same legend as figure 4. On the right is the magnetic susceptibility plot, which shows the shell-hash by a significant increase in primary metallic minerals.

Mass percent of carbonates are displayed graphically in Figure 7. Carbonate does not exceed 25% by mass in the core, except for in the shell-hash layer, where the total percent mass of carbonates reached 45% due to the large proportion of shell fragments in the shell- hash. The overall low total carbonate readings indicate a wet cool environment, in which carbonates remain in solution moving further offshore through tidal action, rather than precipitating inside the lagoon, as happens in dry arid climates where lime muds and evaporites are common (Boggs 2012). Readings below 4% for TC can be attributed to dewatering of clays in fine grained sediments such as those within the Los Penasquitos wetlands (Dean, 1974).

Grain size analysis (Figure 8) was completed at a 1 cm interval between 230-250cm depth. This interval included the shell hash and the sediment immediately below and above. The data from each sample was split into fifty size categories to create a distribution of grain size. None of the samples contained grains > 2 mm. Throughout the analyzed interval, percentages of silt and sand are inversely related, with the proportion of

sand generally increasing with depth. The proportion of clay within the analyzed interval is consistently low, but significantly lower within the shell-hash layer. Percent clay is 10% at 230 cm depth, but within the shell-hash layer drops to 5% or less (Figure 8). Above the shell-hash layer, sand and silt exist in roughly equal 45% proportions, but with increasing depth the sand percentage climbs as high as 83% and the silt percentage drops as low as 13%. The grain-size data suggests a distinct normal grading within the shell-hash layer.

Determining the lateral extent of the shell-hash is an important component of testing the paleotsunami hypothesis. Examination of the five coring locations that contained the shell-hash layer gives a minimum estimate of the lateral extent of the shell-hash. The shell-hash was preserved over an area of approximately 400 meters east/west by 100 meters north/south (Fig. 2). Therefore the known lateral extent of the shell-hash is approximately four hundred square meters, with the possibility of a larger extent being determined by more reconnaissance coring in the future.

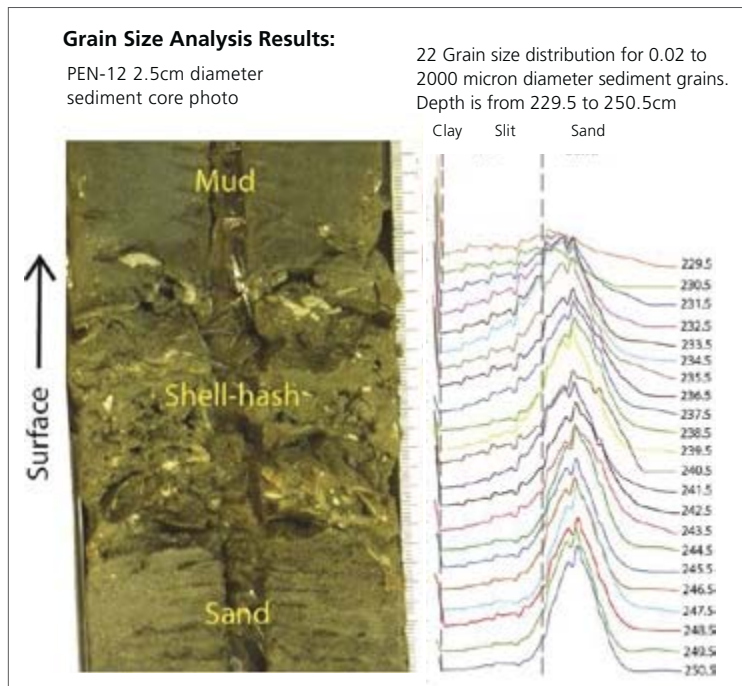


Figure 8: shows the results of grain size analysis conducted with a Malvern grain size analyzer, and divided into 50 separate size classes, producing distributions shown on the right side of the figure. Clearly visible is the wider range of values within the shell-hash, as well as more small clasts at the top, and larger clasts at the base, displaying a fining upward sequence.

7. Distinguishing Tsunami Deposits from Tempestites and Channel Lag Deposits

Comparing the shell-hash to the known characteristics of storm deposits, or tempestites, proves crucial in determining the origin of the shell-hash layer. Tsunami deposits and tempestites have similar textures and morphologies (Figure 9) which must be closely examined to determine the origin of an individual deposit. Storm surges are known to normally deposit a more layered package of sediments than tsunami deposits, and in a generally thicker unit (Morton et al, 2007). Tempestites generally contain lesser amounts of heavy minerals than tsunami deposits, possibly as a result of the lower energy associated with a storm surge relative to tsunamis (Phantuwongraj and Choowong, 2012). Tempestites do not generally contain the dense shell fragments seen in the shell-hash, but paleotsunami deposits such as those described in Norway, Oman, and Tasmania commonly contain up to 50% by mass carbonate shell material (Bondevik et al, 1997, Clark et al, 2011, Donato et al, 2008). The presence of such dense shell material is possibly a result of the higher energy associated with tsunamis, relative to storms, which could be capable of dislodging organisms from burrows and scouring the offshore shelf surface. Tidal channel lag deposits are sometimes similar to the Los Penasquitos shell-hash layer, but generally contain less abundant shell fragments, much lower shell diversity, a higher degree of sorting, and have a more constrained lateral extent (Scasso et al, 2012). As well sedimentary structures such as cross-bedding and herringbone cross-stratification are very

common in tidal-channels (Fenes and Faugeres, 1997), but were not present in the Los Penasquitos shell-hash layer. Lastly it would be very unusual for a channel-lag deposit to contain graded muddy sediment, channels are normally filled by well sorted cross-bedded sandy sediments (Penderson et al, 1998).

8. Discussion

The hypothesis that the shell-hash layer is a paleotsunami deposit has been tested using a wide range of techniques. The interpretation of all the data suggests that the shell-hash layer found in Los Penasquitos wetland was deposited by a high energy event, collecting offshore or beach sediment and transporting it into what was then a restricted lagoon. No other explanation can sufficiently explain the unique structure, data signature, and composition of the shell-hash, and evidence found so far does not fully support any other mode of deposition.

Review of the deposits characteristics leads to the conclusion that a high energy event brought the debris which comprises the shell-hash layer into the lagoon, as far as the lagoon's inner edges. The higher proportion of sand and larger grain-size range within the shell-hash indicate a high energy depositional setting. The lagoonal sediments are typically muddy and fine-grained, but offshore sediments are more sandy and well sorted (Boggs, 2012).

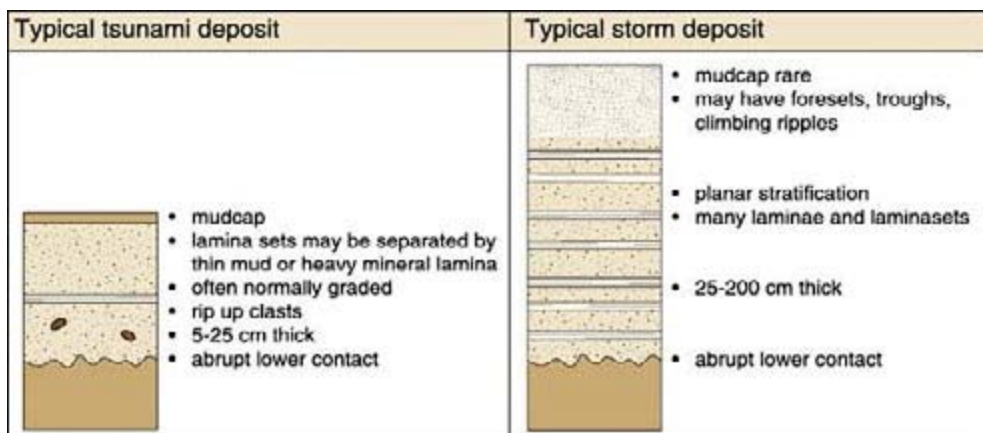


Figure 9: Depiction of the common differences between tempestites (storm surge deposits) and tsunami deposits, taken from Morton et al, 2007. Of interest is the fact that the shell-hash displays every one of the described characteristics for tsunami deposits.

Structural and compositional differences such as grading, the mixture of mud and sand with fossils, and the lack of bedding, also denote the differing sediment source and depositional process of the shell-hash layer.

The event that resulted in the shell-hash layer was of a far higher energy level than the events which brought the more recent shell-free sands into the lagoon. The difference in energy level at time of deposition is shown by the more uniform composition of the younger sands, which contain few or no fossils, and lack erosional contacts or grading.

While identifying tsunamigenic sediments is still a developing branch of geologic study previous studies of recent known tsunami sediments provides information that facilitated this research. All fossil species found are Holocene and can be readily identified. Sediments at Los Penasquitos consist dominantly of fine grained muds, silts, and sands, which sharply contrast tsunami deposits in terms of their small clast size, good sorting, dark or mottled color, and the often gradational contacts lagoonal sediments display. The shell-hash layer is unique within the 1,400 years of studied sediments. Samples taken from the shell-hash produce significantly higher MS values than the surrounding sediments. The difference in MS values is a result of the difference in composition between lagoonal sediments and the shell-hash layer. Interestingly the pre shell-hash MS readings for the sediments average 0.7, but never return to that low or consistent of readings after the shell-hash event, suggesting a sudden but long lasting environmental or sediment source change. A tsunami impacting the lagoon could be responsible for such a change, as it may have raised the land surface, filled tidal channels, or altered topography, in a way that prevented a return to the previous environmental conditions.

Grain size analysis (figure 6) quantified an interesting trend in the deposit, shown by analyzing the shell-hash and surrounding sediment, in terms of grain size range and distribution versus depth. The finest measured particle sizes, clay (>2 microns), are at levels of less than 5% of the total sample at and below the base of the shell-hash layer, but increase three-fold beginning in the top 2 cm of the shell-hash layer, and continuing upward into the overlying sediment. At the top of the shell-hash, clay comprises 10% of the sample, its highest value achieved, possibly a result of a mud-cap deposited as the energy of this event diminished and the water became unable to transport sandy sediment (Reinhardt et al, 2012). Silt

(2-60 microns) shows a trend similar to clays, increasing from as low as 15% at the base to as high as 55% near the top of the deposit. Sand size clasts (60-2000 microns) decrease approaching the surface dramatically, which is a trend opposite the silt and clay, with 83% sand at the base and 41% sand at the top of the shell-hash. This analysis suggests that the shell-hash deposit is poorly sorted, but crudely graded, with a sandy base, and muddy top.

9. Conclusions

A consideration of the evidence presented above leads to the tentative conclusion that the shell-hash was deposited by a tsunami event 1400 +/- 20 years BP. All the data is consistent with that interpretation. The source of the shell-hash layer is likely from the beach or offshore, since the lagoonal sediments do not contain the heavy minerals or coarse sandy sediment that is present in the shell-hash layer. The percent sand and angularity of shell fragments indicate relatively high energy deposition (when compared to the wetland sediments). Poor sorting of the deposit, as well as its fossil density and diversity, do not at this time support a storm surge or tidal-lag depositional setting.

Examination of the USGS inundation map for Los Penasquitos (Figure 10) shows modeled tsunamis producing inundations which stop up to a kilometer short of the shell-hash recovery locations. This research indicates the USGS model may be too conservative, and gives a dated deposit as physical evidence. In light of these facts it would be pertinent to expand the search for paleotsunami deposits in order to more properly model and predict the risks and timelines coastal communities are facing. Many articles concerning the activity of the Cascadia subduction zone (Clarke and Carver, 1992, Nesse and Witter, 2006, Priest et al, 2014) highlight the threat of tsunamis along the Northwest coast. This research illustrates the possibility of that same threat along the California coast, where the highly developed beaches of Los Angeles, San Diego, and Orange County, lie amidst some of the country's most economically critical shipping ports and manufacturing yards, between hundreds of resorts, neighborhoods, and recreational areas. All facing a poorly understood threat of underestimated ferocity, occurring along a timeline not currently known. These facts necessitate the furthering of paleotsunami research and modelling to create safer coastal communities.

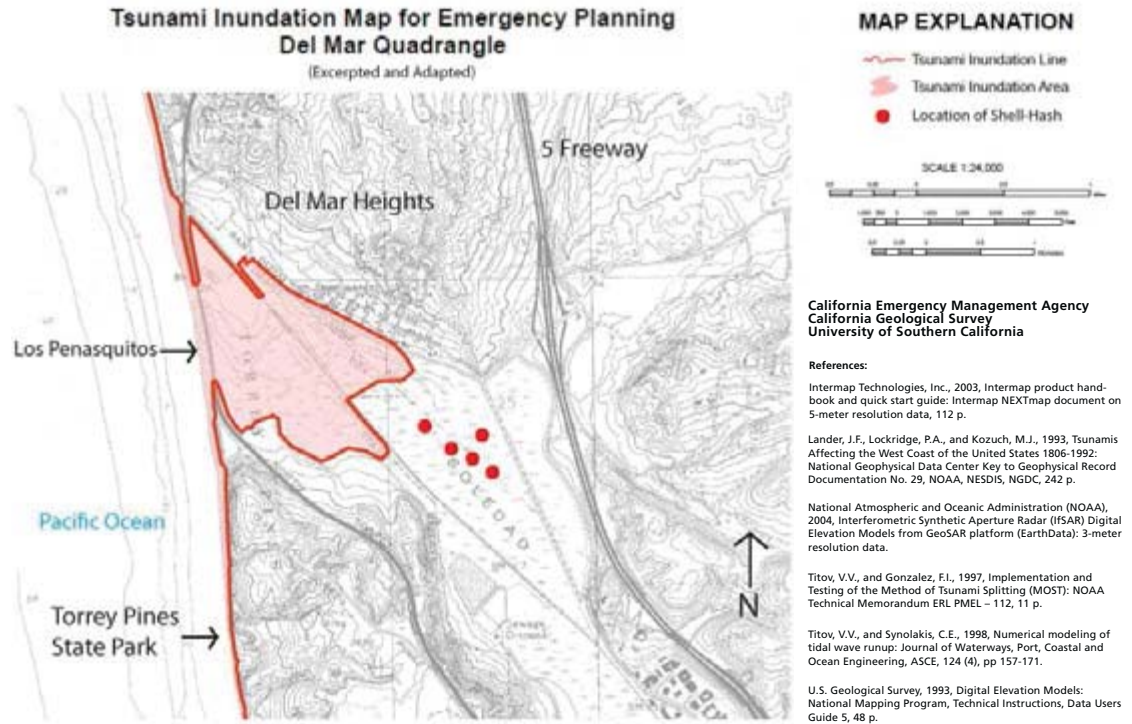


Figure 10: shows a predicted tsunami inundation zone map for southern California, produced by the USGS. Deposit recovery locations are shown with red circles. Of importance is the fact that the tsunami inundation zone ends up to a kilometer seaward of the shell-hash recovery locations. Although this area is of low topographic relief, that amount of distance still calls for notice.

10. Acknowledgments

The completion of this research would not have been possible without the assistance I received from those involved in the Southern California Paleotsunami Project. My advisors Professors Brady Rhodes and Matthew Kirby have been with me every step of the way. Fellow student and USGS employee Robert Leeper contributed advice, help with figure construction and layout, and the calibration of C14 dates. Dr Nicole Bonuso was essential in the identification of fossils recovered from the sediment cores. And lastly the funding we received from the NSF and SCEC, which made this work possible. All these people were essential parts of what has been a collaborative effort to understand southern California's past and future tsunami history.

References

- Bradley, Raymond. Paleoclimatology: Reconstructing Climate of the Quaternary. Elsevier Academic Press, Boston Massachusetts. 1999.
- Brian Atwater, Uri ten Brink, Mark Buckley, Robert Halley, Bruce Jaffe, Alberto M. Lopez-Venegas, Eduard Reinhardt, Maritia Tuttle, Steve Watt, Yong Wei. Geomorphic and stratigraphic evidence for an unusual tsunami or storm a few centuries ago at Anegada, British Virgin Islands. *Nat Hazards* (2012) 63:51–84.
- Bondevik Stein, Svendsen John, Mangerud Jan. Tsunami Sedimentary Facies Deposited by the Storegga Tsunami in Shallow Marine Basins and Coastal Lakes, Western Norway. *Sedimentology*, 1997. 44, pages 1115-1131.
- Borrero Jose , Dolan James, and Emmanuel Synolakis Costas. Tsunamis Within the Eastern Santa Barbara Channel. *Geophysical Research Letters*, VOL. 0, NO. 0, PAGES 0-0, M 0, 2000.
- Choe, B. , Kim, D. , Hwang, J. , Oh, Y. , & Moon, W. (2012). Detection of oyster habitat in tidal flats using multi-frequency polarimetric sar data. *Estuarine Coastal and Shelf Science*, 97, 28-37.
- Clarke, S. , & Carver, G. (1992). Late holocene tectonics and paleoseismicity, southern cascadia subduction zone. *Science*, 255(5041), 188-192.
- Carrazana-Edwards, A., Bocanegra Garcia G. , Rosales-Hoz, L. , & de Pablo Galán, L. (1998). Beach sands from baja califonia peninsula, mexico. *Sedimentary Geology*, 119(3), 263-274.
- Clank, Kate, Cochran, Ursula, and Mazengarb, Colin. Geologic evidence for prehistoric tsunamis and coseismic uplift during the AD 1854 Ansei-Tokai earthquake in Holocene sediments on the Shimizu Plain, central Japan *The Holocene* July 1, 2014 24: 814-827
- D. Grine, The Geology of Torrey Pines State Natural Reserve, published by the Torrey Pines State Park, 2010.
<http://www.torreypine.org/geology/geology.html>
- Dean, Walter Jr. Determination of Carbonate and Organic Matter in Calcareous Sediments and Sedimentary Rocks by Loss on Ignition: Comparison With Other Methods. *Journal of Sedimentary Petrology*, 44, No. 1, v. 242- 248 FIGS, 1-9, MARCH 1974.
- Donato, S.V, E.G Reinhardt, J.I Boyce, J.E Pilarczyk, and B.P Jupp. "Particle-size Distribution of Inferred Tsunami Deposits in Sur Lagoon, Sultanate of Oman." *Marine Geology*, 257.1 (2009): 54-64.
- R. Duerr. 2008. Two new species of *Mitrella* (Gastropoda: Neogastropoda: Columbellidae) from the lower Miocene Chipola Formation of northwestern Florida. *The Nautilus* 122(3):151-154
- Fenies, Hugues, and Jean-Claude Faugères. "Facies and Geometry of Tidal Channel-fill Deposits (Arcachon Lagoon, SW France)." *Marine Geology*, 150.1 (1998): 131-148.
- M. Connelly, N. Carter. Official Timeline of the Kumeyaay Tribe, 2014. <http://www.kumeyaay.com/kumeyaay-history.html?id=1:timeline&catid=1>
- K. Ilayaraja, R. R. Krishnamurthy, M. Jayaprakash, P. M. Velmurugan, S. Muthuraj. Characterization of the 26 December 2004 tsunami deposits in Andaman Islands (Bay of Bengal, India). *Environ Earth Sci* (2012) 66:2459–2476.
- R. Thompson, J. Bloemendal, J. A. Dearing, F. Oldfield, T. A. Rumery, J. C. Stober and G. M. Turner. Environmental Applications of Magnetic Measurements. *American Association for the Advancement of Science*. Vol. 207, No. 4430 (Feb. 1, 1980), pp. 481-486.
- Kirby Matthew, Poulsen Christopher, Lund Steve, Patterson William, Reidy Liam, and Hammond Douglas. Late Holocene lake level dynamics inferred from magnetic susceptibility and stable oxygen isotope data: Lake Elsinore, southern California (USA). *Journal of Paleolimnology* 31: 275–293, 2004.
- Kirby Matthew, Lund Steve, Anderson Michael, Bird Broxton. Insolation forcing of Holocene climate change in Southern California: a sediment study from Lake Elsinore. *Journal of Paleolimnology* (2007) 38:395–417.
- Morton Robert A, Gelfenbaum Guy, Jaffe Bruce. Physical criteria for distinguishing sandy tsunami and storm deposits using modern examples. *Sedimentary Geology* 200 (2007) 184–207.

- Martitia Tuttle, Alan Ruffman, Thane Anderson, Hewitt Jeter. Distinguishing Tsunami from Storm Deposits in Eastern North America: The 1929 Grand Banks Tsunami versus the 1991 Halloween Storm. *Seismological Research Letters* January/February 2004 Volume 75, Number 1 129.
- M. R. Legg and M. J. Kamerling. Large-scale Basement-involved Landslides, California Continental Borderland. *Pure and Applied Geophysics*. Volume 160. Published 2003. Pages 2033-2051.
- Nelson, A. , Kelsey, H. , & Witter, R. (2006). Great earthquakes of variable magnitude at the cascadia subduction zone. *Quaternary Research*, 65(3), 354-365.
- Nesse, William. *Introduction to Mineralogy: Second Edition*. Oxford University Press, 2012. Pages 394-395.
- Ramírez-Herrera María-Teresa, Lagos Marcelo, Hutchinson Ian, Kostoglodov Vladimir, Machain Maria, Caballero Margarita, Goguitchaichvili Avto, Aguilar Bertha, Chagué-Goff Catherine, Goff James, Ruiz-Fernández Ana-Carolina, Ortiz Modesto, Nava Hector, Bautista Francisco, I. Lopez Gloria, Quintana Patricia. Extreme wave deposits on the Pacific coast of Mexico: Tsunamis or storms? — A multi-proxy approach. *Geomorphology* 139–140 (2012) 360–371.
- Reinhardt, E. , Pilarczyk, J. , & Brown, A. (2012). Probable tsunami origin for a shell and sand sheet from marine ponds on anegada, british virgin islands. *Natural Hazards*, 63(1), 101-117.
- Rhodes Brady, Kirby Matthew, Jankaew Krkawun, Choowong Montri. Evidence for a mid-Holocene tsunami deposit along the Andaman coast of Thailand preserved in a mangrove environment. *Marine Geology* 282 (2011) 255–267.
- S. Srinivasalu, Jonathan M., Thangadurai N. V., Ram-Mohan. A study on pre- and post-tsunami shallow deposits off SE coast of India from the 2004 Indian Ocean tsunami: a geochemical approach. *Nat Hazards* (2010) 52:391–401.
- Scasso, R. , Dozo, M. , Cuitiño, J. , & Bouza, P. (2012). Meandering tidal-fluvial channels and lag concentration of terrestrial vertebrates in the fluvial-tidal transition of an ancient estuary in patagonia. *Latin American Journal*
- Pendón, J.Gabriel, Juan A Morales, José Borrego, Inmaculada Jimenez, and Mercedes Lopez. "Evolution of Estuarine Facies in a Tidal Channel Environment, SW Spain: Evidence for a Change from Tide- to Wave-
- Peters, Robert, and Jaffe, Bruce E. , 2010, Identification of tsunami deposits in the geologic record; developing criteria using recent tsunami deposits: U.S. Geological Survey Open-File Report 2010-1239, 39 p. [<http://pubs.usgs.gov/of/2010/1239/>].
- Phantuwongraj, Sumet. Choowong, Montri. Tsunamis versus storm deposits from Thailand. *Nat Hazards* (2012) 63:31–50. DOI 10.1007/s11069-011-9717-8
- Priest, G. , Zhang, Y. , Witter, R. , Wang, K. , Goldfinger, C. , et al. (2014). Tsunami impact to washington and northern oregon from segment ruptures on the southern cascadia subduction zone. *Natural Hazards*, 72(2), 849-870.
- USGS Tsunami inundation prediction map for California: http://www.conservation.ca.gov/cgs/geologic_hazards/Tsunami/Inundation_Maps/SanDiego/Documents/Tsunami_Inundation_DelMar_Quad_SanDiego.pdf
- Uslu Burak, Eble Marie, Titov Vasily, and Bernard Eddie. Tsunami Hazard Assessment Special Series: Vol. 2 Distant tsunami threats to the ports of Los Angeles and Long Beach, California. NOAA OAR Special Report, May 2010.
- Williams Harry, Hutchinson Ian, and Nelson Alan. Multiple sources for late-Holocene tsunamis at Discovery Bay, Washington State, USA. *The Holocene* 2005 15: 60.
- Wassmer, P. , Schneider, J. , Fonfrère, A. , Lavigne, F. , Paris, R. , et al. (2010). Use of anisotropy of magnetic susceptibility (ams) in the study of tsunami deposits: Application to the 2004 deposits on the eastern coast of banda aceh, north sumatra, indonesia. *Marine Geology*, 275(1), 255-272.

Is The Sierra Nevada Frontal Fault System Steep Or Shallow?: Implications For Extension In Owens Valley

Department of Geological Sciences, California State University, Fullerton

Brian Gadbois

Abstract

The eastern boundary of the Sierra Nevada is defined by a system of east-dipping normal faults known as the Sierra Nevada Frontal Fault Zone (SNFFZ). It generally is assumed that these faults dip at about 60° E. Recent work on the northern section of the SNFFZ near Bishop shows normal faults that dip 35°-46° - much less than the assumed typical dips. Holocene to Pleistocene extension rates are 0.2 - 0.3 mm/yr., but these estimates are based on a 60° dip. If fault dip is shallower than 60°, computed long-term horizontal extension rates will be significantly greater than initially assumed because the horizontal component of slip will be as much as four times greater than expected. My new work shows that normal faults west of Lone Pine dip 35° E. This study uses detailed fault mapping of surface exposures west of Lone Pine at Tuttle Creek across ~300 m of elevation change to further constrain fault dip. Normal fault and footwall fractures at Tuttle Creek dip ~34° E. Estimated long-term extension rates based on a measured dip of 34° are an average of 1.2 mm/yr., which is four times greater than those based on assumed 60° dips.

Geology and Geomorphology of the Three Bare Hills Lake Manly Deposit, Death Valley, California

Department of Geological Sciences, California State University, Fullerton

Christopher R. Hugh

Advisor: Jeffrey R. Knott, Ph. D

Abstract

The Three Bare Hills (TBH) is a prominent Lake Manly outcrop; however, its existence is ambiguous. The suspected outcrop area is composed of platey, rounded to sub-rounded, imbricated boulder to gravel. These deposits were found overlaying Tertiary sedimentary rock at elevations ranging from 3 to 72-m above sea level (asl). In addition, at 53-m asl, a west-facing riser with a 5° slope and 3.2-m height was found. Finally, the greatest concentration of platey, sub-rounded clasts was found in a 3-m-high deposit that extends from a Tertiary bedrock hill and trends S20W for about 0.8 km at S20W, with the southern end of the feature curving to a N40E trend. These clasts are more rounded and oblate compared to adjacent alluvial-fan deposits, which is consistent with clasts rounded in Lake Manly; the 53-m asl horizontal riser is consistent with a lake-eroded shoreline angle; and, the 0.8-km-long deposit of platey, sub-rounded clasts is a spit formed by north-to-south currents. The TBH 53-m-asl shoreline angle is at a higher elevation than the Beatty Junction Bar Complex (46 m). The 72-m-asl maximum elevation of the TBH Lake Manly deposits is similar to the elevation of Lake Manly deposits on the southern Hanaupah fan. The putative spit supports previous work that inferred W-E paleowind and N-S paleocurrents in pluvial Lake Manly.

1. Introduction

According to Knott et al. (2012), Lake Manly, the pluvial lake that occupied Death Valley during cooler, wetter climate conditions, is a key component in climate models of the western USA and subsequently the northern latitudes

(Fig 1; e.g., Matsubara and Howard, 2009; Peterson et al., 2010). The Three Bare Hills (TBH; Fig. 2) is a prominent Lake Manly outcrop (Hunt and Mabey, 1966; Machette et al., 2001); however, its existence is in doubt. Hunt and Mabey (1966) mapped Lake Manly deposits east of the TBH (Fig. 3) and Wright and Troxel (1993) mapped the same location as alluvial-fan deposits (Fig. 4). In addition, Hunt and Mabey (1966, pg. 69) found that the Lake Manly deposits at the TBH have foreset beds that dip 10° NW. This foreset direction is contrary to the inferred paleowind direction in Death Valley (Knott et al., 2012; Fig. 5). Knott et al. (2012) suggested mapping of the TBH Lake Manly deposits may clarify the paleowind direction.

In this study I found:

The deposits at the TBH are composed of platey, rounded to sub-rounded, imbricated boulder to gravel that overlie Tertiary sedimentary rock at elevations ranging from 3 to 72-m above sea level (asl), which is consistent with clasts rounded by Lake Manly.

A west-facing riser with a 5° slope and 3.2-m height found at 53-m asl, is consistent with a Lake Manly shoreline angle.

The greatest concentration of platey, sub-rounded clasts was found in a 3-m-high deposit that extends from a Tertiary bedrock hill and trends south for about 0.8-km at S20W, with the southern end of the feature curving to a N40E trend. I interpret this feature as a spit formed by north-to-south trending currents, which supports previous work that inferred W-E paleowind and N-S paleocurrents in pluvial Lake Manly.

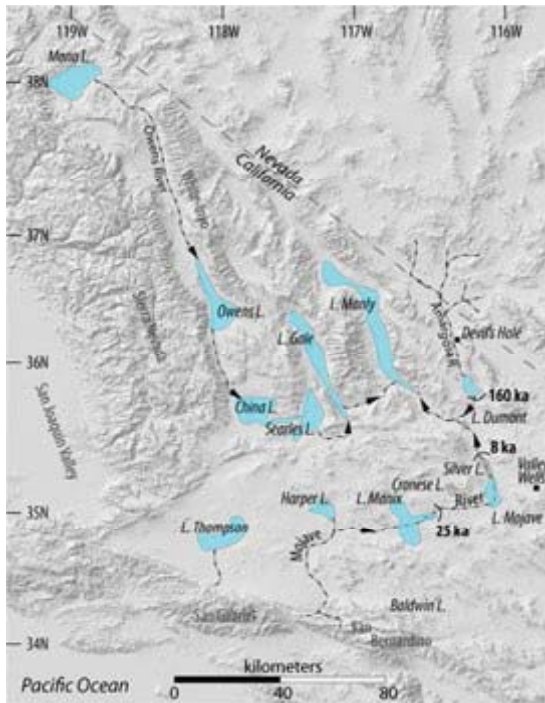


Figure 1: Shaded relief map of Southern California and Southern Nevada showing major ranges and relative sizes of the hypothesized pluvial lakes of the Owens, Amargosa and Mojave Rivers. Lake Manly occupies Death Valley (from Knott et al. 2012).



Figure 2: Photograph looking NE of the putative Lake Manly deposits east of the Three Bare Hills. Lake Manly deposits are the light-colored beds in the center of the photograph.

Location

The TBH are located 15 km (~9 miles) north of Furnace Creek, 6.5 km (~4 miles) north of Park Village and east of Highway 190 in Death Valley, California. The TBH lie approximately 7 km (~4.35 miles) southwest of the Funeral Mountains, which are a part of the Amargosa Mountain Range. In relation to known Lake Manly deposits, the TBH are 7.8 km (~4.9 miles) southeast of the Beatty Junction Bar Complex (BJBC).

Background

Lake Manly is the name of the ancient pluvial lake that filled the Death Valley basin during the Pleistocene epoch. Machette et al. (2001) documented 30 locations with relict Lake Manly features such as terraces, platforms, shorelines, strandlines, spits, bars, foreset beds, and tufa deposits. The majority of Lake Manly's relict features are found on the east side of Death Valley (Fig. 5) and are restricted to elevations between 2 and 137-m (relative to mean sea level). The elevation difference is attributed to both variations in lake volume over time and tectonics. Finally, the 180-120 ka age of Lake Manly deposits (Ku et al., 1998; Machette et al., 2008; Owen et al., 2011) has resulted in substantial erosion of the deposits.

Initially, existence of a lake in Death Valley was suggested by Russell (1885) and Gilbert (1890), and given the name of Death Valley Lake by Gale (1914). Levi Noble (1926) identified strandlines incised into ancient gravels at Mormon Point as relict lake features in Death Valley. Given that the strandlines are located between 122 and 153-m above the lowest point in Death Valley, it was his hypothesis that Lake Manly was at least 122-m deep with a minimum length of 121-km. In addition, Noble assumed that Lake Manly was likely contemporaneous with lake deposits of the adjacent Amargosa Valley.

Blackwelder (1933) hypothesized that the upper-most layer of salt located on the valley floor was most likely the remnants from Lake Manly's period of dessication, whereas the underlying clay would represent an expansionary period. In addition, Blackwelder asserted that Lake Manly was one of possibly several hundred temporary lakes located in the current desert, which had developed within undrained basins during previous cooler, moister environments. Furthermore, he described the ecosystem of which Lake Manly played a primary role, as well as the mechanics by which Lake Manly most likely functioned.

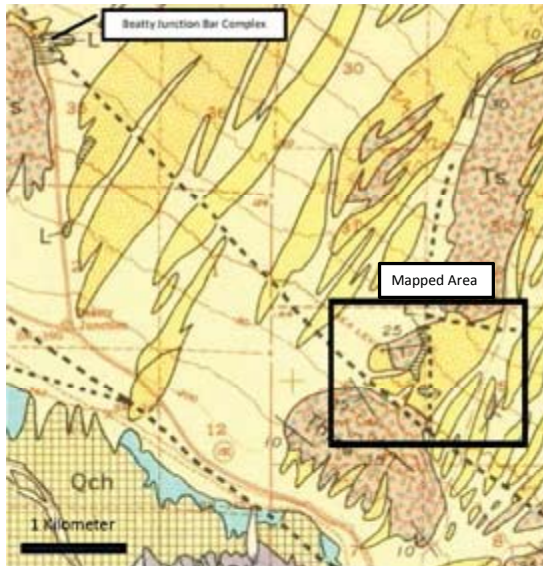


Figure 3: Three Bare Hills deposit of Lake Manly (Hunt and Mabey, 1966). Ts is Tertiary Sediment. L is Lake Manly deposits. Qch unit is salt playa. Remaining units are alluvial-fan units.

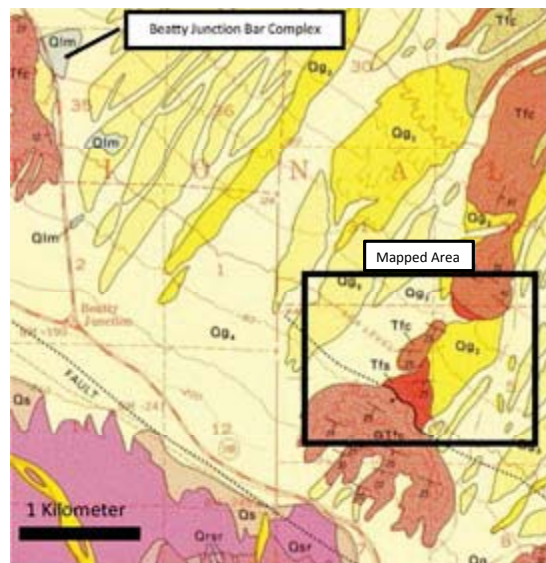


Figure 4: Three Bare Hills outcrop location, as mapped by Wright and Troxel (1993). Tfc is Furnace Creek Formation. Qtfc is Funeral Formation. Qlm is Lake Manly deposits. Qg4, Qg3, and Qg2 are alluvial-fan deposits. Tfc is Furnace Creek Formation. Qsr and Qsr are salt plays.

His conjecture was that the lake was regulated by influxes of water and evaporation. Lastly, based on extensive erosion, he hypothesized that Lake Manly was older than other similar pluvial lakes surrounding Death Valley (i.e., Lake Bonneville), which are thought to date to the Tioga period (Last Glacial Maximum), and speculated the age as Tahoe glacial equivalent (middle Pleistocene). Hunt and Mabey (1966) included Lake Manly deposits in their map of Death Valley (Fig. 3). Hunt and Mabey (1966; pg. 69) stated that the deposits are composed of, “small embankments of shingled gravel, evidently beach or near-shore bar deposits of late Pleistocene lakes are numerous but widely scattered along the north and east sides of Death Valley at altitudes as high as 380 feet above sea level.”

With respect to the TBH, Hunt and Mabey (1966, pg. 69) stated:

“Three miles southeast of this bar [BJBC] is another well-developed one forming an arcuate deposit half a mile long and 500 feet wide, resting on a bench of No. 2 gravel. The bar curves through the arc of 90°. The gravels are shingled, cross-bedded, and usually about an inch in diameter,

like those in the bar above Betty Junction. The foreset beds in the gravel dip 10° NW. The top of this bar is nearly level and is less than 100 feet above sea level.

No other shoreline features were found between this bar and the one near Betty Junction. The temptation is strong to assume that the 2 bars, which are similar and highly exceptional features in this area, were formed at the same time and that the difference in level is attributable to 50 feet of post-lake faulting of tilting between the two localities”

Wright and Troxel (1993) mapped the TBH area as well (Fig. 4); however, they mapped the Lake Manly deposits of Hunt and Mabey (1966) as older alluvial-fan deposits. Knott et al. (2012) determined that the current wind regime of the Death Valley area was consistent with wind conditions when Lake Manly was present. They determined that the paleowind was dominantly W-E or NW-SE with significant topographic funneling. The 10° NW foreset dip at the TBH described by Hunt and Mabey (1966) is inconsistent with W-E and NW-SE winds.

Knott et al. (2012) stated:

“A marked anomaly in our hypothesis is the Lake Manly deposits at the Three Bare Hills about 5 km south-east of the BJBC. There Hunt and Mabey (1966, p.69) described foreset beds dipping 10o northwest and a bar crest that arcs over 90°. This wide sweep of the bar crest and the position of the deposits behind prominent hills may explain the unusual configuration and foreset dip; however, we did not explore this location and this is an obvious object of future work.”

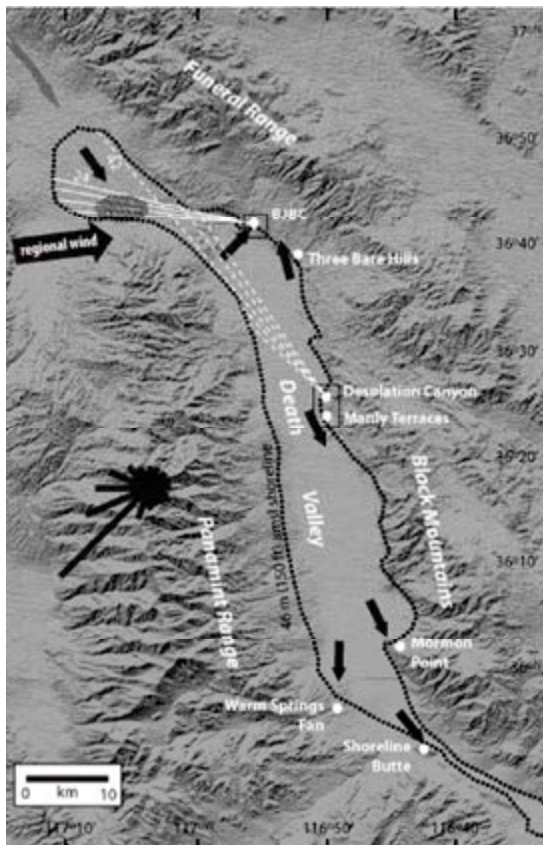


Figure 5: Shaded relief map with wind rose from Panamint Range and significant Lake Manly localities. Small black arrows show wind direction inferred from sedimentary structures. Dotted line is 46 m elevation of Lake Manly. Dashed white lines are fetch lengths across lake. Large black arrow shows regional wind direction. (Knott et al. 2012). Note the NW direction at the Three Bare Hills, found by Hunt and Mabey (1966).

2. Methods

Geologic and geomorphic mapping was completed using Google Earth imagery after the methods used by Knott et al. (2012). Mapping extended to the surrounding alluvial-fan and Tertiary deposits, in order to establish relative-age relations among the various deposits. In addition, on-site visual analysis of clasts, was performed to determine the likely depositional history of the associated geologic units.

3. Results

Geologic Units

At the TBH, five separate geologic units were identified within the mapping area (Fig. 6). The oldest rocks are reddish conglomerate and mudstone of the Pliocene Furnace Creek Formation (Tfc). The angular, poorly-sorted conglomerate to mudstone of the Plio-Pleistocene Funeral Formation (Qtfc) form the hills on the map (Fig. 6).

The putative Lake Manly deposits (Qlm) are composed of platey, rounded to sub-rounded, imbricated boulder to gravel, at elevations ranging from 3 to 72 m-asl. The surface expression is characterized by darkly-varnished desert pavement (Fig. 7) and are elevated above the active channel. The subsurface expression is characterized by “bleached” clasts that are whiter than the sediment located in the active channel (Fig. 8), with an imbrication angle varying 18-to-54 degrees to the east/northeast. The thickness varies between 1 to 5-m. At the maximum lake elevation, where Qlm terminates into the QTfc, the lake deposits are overlain by alluvial-fan deposits.

The alluvial-fan units are composed of unsorted, angular clasts and ranging in age from intermediate-age fan deposits to younger active channel deposits (Qg4). Intermediate alluvial-fan deposits (Qg3a, Qg3b) are characterized by moderate varnish and feature subdued bar-and-swale topography; while, active channel deposits (Qg4) are characterized by creosote bushes and bar-and-swale topography, with the swales featuring a fine infill and boulder size rocks in the bars.

Geomorphic Features

Two prominent geomorphic features are present at the TBH. The first is a horizontal tread and riser system located at 53-m-asl (Fig. 9). The west-facing riser has a 5° slope and 3.2 m height. This riser is visible on the ground, whereas similar horizontal features are visible on aerial

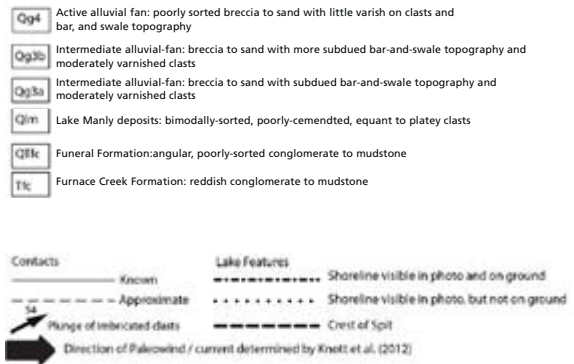
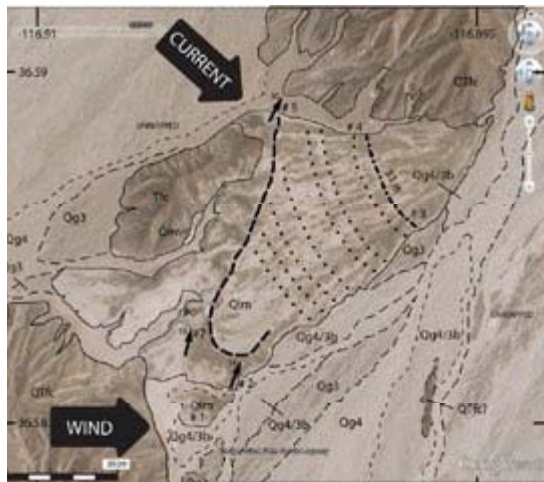


Figure 6: Geologic and Geomorphic map of the Three Bare Hills (TBH). Base is a Google Earth image. Geologic units after Hunt and Mabey (1966) and Wright and Troxel (1993). Numbered locations indicate sites where geomorphic data was collected, corresponding to field-notes.

images only (Fig. 6). No faults or rock type changes are associated with these features.

The second geomorphic feature is a bar of platy, sub-rounded clasts found in a 3-m-high deposit that extends from a hill of Tertiary Furnace Creek Formation (Fig. 10). The mound trends south for about 0.8 km at S20W. The southern end of the mound curves to a N40E trend. This is the bar feature described by Hunt and Mabey (1966; pg. 69).

4. Discussion

Geomorphic Features

The geomorphic field criteria of Gilbert (1890) were used to infer the geologic processes responsible for the 53-m-asl riser at the TBH. Specifically, the criteria are as follows: Wave-cut benches, or strandlines, are (1) independent of underlying structure, (2) associated with clastic lacustrine deposits at either end (e.g., bars and spits), and (3) the base of the riser is horizontal. In contrast, fault-generated benches and risers (scarps) (1) correspond to underlying structure, (2) are not associated with clastic lacustrine deposits, and (3) the base of the riser may or may not be horizontal.

Using the criteria of Gilbert (1890), the horizontal riser at 53-m-asl is consistent with a lake-eroded shoreline

angle (Fig. 9). This interpretation is based foremost on the fact that the riser is horizontal for the entire 0.35 km length (Fig. 6). Lower, parallel-lineations, are visible in the aerial images only. The TBH 53-m-asl shoreline is at a higher elevation than the BJBC (46 m), which suggests that the depth of pluvial Lake Manly may have been deeper than previously thought. The lower shorelines, which are not visible on the ground, are inferred to be shorelines formed by a shorter pause in lake recession compared to the 53-m shoreline. Lastly, faulting is not present within the mapping area, and thus, neither tectonic deformation nor uplift are likely factors in explaining the provenance of these geomorphic features.

The 0.8 km long deposit of platy, sub-rounded clasts is interpreted as a spit formed by north-south trending currents, which supports previous work by Knott et al. (2012) that inferred W-E paleowind and N-S paleocurrents in pluvial Lake Manly. This spit is connected to only one terrestrial outcrop at the north and decreases in elevation from 25 to 15-m asl to the south. A bar is connected to two terrestrial outcrops and maintains a constant elevation. The “hook” shape is consistent with a spit pushed east by W-E winds. I found only NE imbrication directions (Fig. 6), which is different from the 10o NW imbrication direction found by Hunt and Mabey (1966). The northeast imbrication direction and arcuate shape of the spit is explained by a north-to-south current behind the hill and a westerly wind.



Figure 7: Photograph showing the surface expression of Qlm deposits. Notice the darkly varnished desert pavement, which is contrasted by bar and swale topography of the alluvial-fan related deposits.



Figure 8: Photograph showing Qlm deposits at Three Bare Hills (Location #2). Longer length of the notebook is parallel to the imbricated clasts.



Figure 9: Photograph of shoreline showing tread and riser system with a 3.2-m-height and tilted at 5 degree to the west (Location #3). Taken facing in a northeasterly direction. Person is standing on top of the riser.

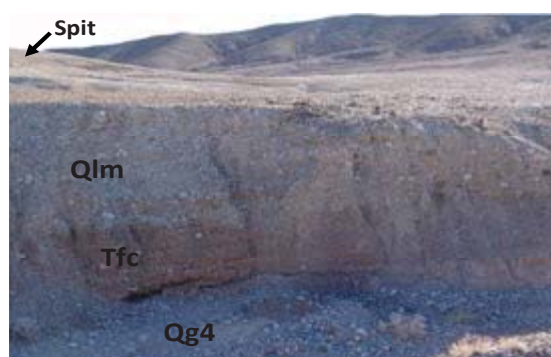


Figure 10: Photograph of Lake Manly deposits (Qlm) overlying Furnace Creek Formation (Tfc) with active channel deposits (Qg4) in the foreground. The Qlm is 4 to 5-m thick. Photograph is from Location #6 on Fig. 6.

Geologic Units

The putative Lake Manly (Qlm) clasts are more rounded and oblate compared to adjacent alluvial-fan deposits (Fig. 10), which is consistent with clasts rounded in lake waves. At TBH, the Qlm is interpreted as an alluvial fan whose surface has been reworked by Lake Manly waves. Evidence of this interpretation is present at Location #6 (Fig. 6 and 10), where an angular unconformity forms the contact between Qlm and QTfc. In addition, the 72-m asl maximum elevation of the TBH Lake Manly deposits is similar to the elevation of Lake Manly deposits on the southern Hanaupah fan (Hooke, 1972).

5. Conclusion

The deposits at the TBH were formed by pluvial Lake Manly. This is based on the horizontal riser, spit, and more rounded and oblate clasts compared to the adjacent alluvial fan deposits. This interpretation is consistent with the mapping of Hunt and Mabey (1966) rather than Wright and Troxel (1993). The bar of Hunt and Mabey is a spit based on the extension from a bedrock promontory. The shape of the spit is consistent with E-W winds and north-to-south currents inferred by Knott et al (2012). In this respect, the geologic and geomorphic mapping of the TBH area supports previous research and provides additional information to the established knowledge of pluvial Lake Manly.

References

- Blackwelder, E., 1933, Lake Manly-An Extinct Lake of Death Valley: *Geographical Review*, v. 23, p. 82-92.
- Gale, H.S., 1914, Prospecting for Potash in Death Valley, California: *U.S. Geological Survey Bulletin* 549, p. 407-412.
- Gilbert, G.K., 1890, Lake Bonneville: *U.S. Geological Survey Monograph* 1, 438 p.
- Hooke, R.L., 1972, Geomorphic evidence for late-Wisconsin and Holocene tectonic deformation, Death Valley, California: *Geological Society of America Bulletin*, v. 83, p. 2073-2098.
- Hunt, C.B. and Mabey, D.R., 1966, Stratigraphy and Structure Death Valley, California. *United States Geological Survey Professional Paper* 494-A, p. 162.
- Knott, J.R., Tinsley III, J.C. and Wells, S.G., 2002. Are the benches at Mormon Point, Death Valley, California, USA, scarps or strandlines? *Quaternary Research* 58, p. 352-360.
- Knott, J.R., Fantozzi, J.M., Ferguson, K.M., Keller, S.E., Kajidi, N., Rath, C. A., Tarnowski, J.M. and Vitale, M.L., 2012, Paleowind Velocity and Paleocurrents of Pluvial Lake Manly, Death Valley, U.S.A.: *Quaternary Research*, v. 78, p. 363-372.
- Ku, T.L., Luo, S., Lowenstein, T. K., Li, J., and Spencer, R. J., 1998, U-series chronology of lacustrine deposits in Death Valley, California: *Quaternary Research*, v. 50, p. 261-275.
- Machette, M.N., Slate, J. L., and Phillips, F.M., 2008, Terrestrial cosmogenic-nuclide dating of alluvial fans in Death Valley National Park, California: *U.S. Geological Survey, Professional Paper* 1755, <http://pubs.er.usgs.gov/usgspubs/pp1755>.
- Matsubara, Y. and Howard, A.D., 2009, A spatially explicit model of runoff, evaporation, and lake extent: application to modern and late Pleistocene lakes in the Great Basin region, western United States., *Water Resources Research*, v. 45, <http://dx.doi.org/10.1092007WR00593>.
- Noble, L.F., 1926, Note on colemanite deposit near Shoshone Calif., with a sketch of the geology of a part of the Amargosa Valley: *U.S. Geological Survey Bulletin*, 785. Pp. 63-73.
- Owen, L. A., Frankel, K.L., Knott, J.R., Reynhout, S., Finkel, R.C., Dolan, J.F. and Lee, J., 2011, Beryllium-10 terrestrial cosmogenic nuclide surface exposure dating of Quaternary landforms in Death Valley *Geomorphology*, v. doi:10.1016/j.geomorph.2010.10.024.
- Peterson, C.D., Stock, E., Hart, R., Percy, D., Hosteler, S.W., Knott, J.R., 2010. Holocene coastal dune fields used as indicators of net littoral transport: West Coast, USA. *Geomorphology*, v. 116, p. 115-134.
- Russell, I.C., 1885, Geological history of Lak Lahontan, a Quaternary lake of northwestern Nevada: *U.S. Geological Survey Monograph* 11, p. 288.
- Wright, L.A., Troxel, B.W., 1993, Geologic map of the central and northern Funeral Mountains and adjacent areas, Death Valley region, Southern California. *U.S. Geological Survey Map* I-2305 1:48,000.

Reconstruction of the geographic offset of key fossil localities in Orange County, CA due to faulting on the San Andreas Fault system

Department of Geological Sciences, California State University, Fullerton

Rosa E. Murrieta

Abstract

Movement on right-lateral strike slip faults of the San Andreas Fault system in Orange County, California region moved fossil localities in a northwestern/southeastern trend. The reconstruction modeling of the four time intervals – 40 mya, 23.5 mya, 12 mya, and 5 mya, suggests that the offset of the San Andreas Fault of 1.34 cm/ year, yields an estimated maximum offset average recurrence of 2°29' of latitude for every 10 million years. Analysis of the reconstructed geographic offset of the 16 key fossil localities within Orange County with the slip rate of the nearest fault, the Whittier Fault, at a maximum of 3.0 mm/year reveals an average of the localities moved 22.65 miles during the past 23.5 million years to 3.6 million years. Recognition of this geographic offset extends the known area of the origin of the formations to the southeast, and fault-related movement in a northwestern direction on the San Andreas Fault system.

Seismic Hazard Assessment of McCarthy Hall on the California State

Department of Geological Sciences, California State University, Fullerton

Daniel Philo

Advisors: Dr. Harmony Colella and Dr. David Bowman

Abstract

California State University, Fullerton (CSUF) is located in southern California, amidst, arguably, the most complex fault system in the world. This study explores and compares the two most current Uniform California Earthquake Rupture Forecast (UCERF) models, UCERF2 and UCERF3, to determine which fault or faults pose the greatest hazard to the CSUF main campus. Hazardous faults are identified by disaggregation of hazard curves and by generation of shake maps to determine ground motion from possible ruptures. The UCERF2 model identifies the Whittier and Coyote Hills faults as the most hazardous to the CSUF main campus, while UCERF3 identifies the Peralta Hills and the Compton fault as the most hazardous. Because UCERF3 identifies many more possible ruptures than UCERF2, and UCERF3 allows for complex multi-fault ruptures, UCERF3 identifies hazardous faults that may not have been considered hazardous with the previous model.

1. Introduction & Background

California State University, Fullerton (CSUF) is located in the city of Fullerton, California, which is situated in the Los Angeles basin in southern California (Figure 1). The Los Angeles basin is a sedimentary basin that consists of Miocene to Quaternary deposits (Yerkes et al., 1965). The basin is cut by both strike-slip faults that strike to the northwest and thrust faults that strike east-west (Yerkes et al., 1965).

The main buildings on the CSUF campus, which includes 6-story McCarthy Hall, 7-story Langsdorf Hall, and the 8-story Humanities Building, each resonate at a period of approximately 1 second (s). The 6-8 story buildings on

the CSUF campus are most susceptible to failure from ground motion with a spectral acceleration (SA) of 1 s. These buildings contain hazardous chemicals, natural gas pipes, and, combined, have more than 600 classrooms, labs, and offices. The results presented here are for the geology building: McCarthy Hall.

This study employs the Uniform California Earthquake Rupture Forecast 2 (UCERF2) (Field et al., 2008) and the Uniform California Earthquake Rupture Forecast 3 (UCERF3) (Field et al., 2013), which were developed by the Working Group on California Earthquake Probabilities (WGCEP), a group of experts from several earthquake science fields, and the Southern California Earthquake Center (SCEC), to explore different earthquake scenarios. UCERF2 was developed in 2008, and has been the standard earthquake rupture forecast for the past six years. UCERF3 was developed from 2012 to 2013 and includes several improvements over the older UCERF2 model. Some improvements include increased specificity in fault deformation models, updated slip-rate models, and the possibility for complex multi-fault ruptures.

2. Methods

2.1 Fundamental Period

This study focuses on the seismic hazard for McCarthy Hall. McCarthy Hall is not only the geology building, but was constructed in 1963, which makes it the oldest building on the CSUF campus. The building is located on the southern end of campus, just north of Nutwood Avenue and 400 meters west of California State Route 57. The exact location of McCarthy Hall based on Global Positioning System (GPS) is N 33.880, W -117.886.

The Uniform Building Code (UBC) defines the resonance period of a building as the fundamental period (International Conference of Building Officials, 1997). The fundamental period of McCarthy Hall is calculated by:

$$T=CtH^{3/4}$$

where T is the fundamental period, Ct is a numerical coefficient, and H is the height, in feet, of the building (Goel and Chopra, 1997). This study employs a numerical coefficient of 0.035 and a height 86 feet for McCarthy Hall. Based on the values above the fundamental period for McCarthy Hall is calculated to be 0.99 seconds. A period of 1 second of spectral acceleration is adopted as an acceptable approximation to determine which earthquake scenario(s) will result in the most damage to McCarthy Hall.

2.2 Software

OpenSHA (Field et al., 2003) software, an open-source, Java-based platform, is employed to generate hazard curves via the Hazard Curve Calculator Application, to assess the seismic hazard for McCarthy Hall. Hazard curves for SA of 1 s are generated from both the UCERF2 and the UCERF3 earthquake rupture forecasts (ERFs). The curves are disaggregated at 10% probability of exceedance in 50 years to find the faults and the specific ruptures that contribute to the hazard for McCarthy Hall (for a detailed explanation of hazard curve disaggregation, see Bazzurro and Cornell [1999]).

Hazard Curve Calculator requires a velocity model and attenuation relationship be defined for disaggregation. The specific velocity value for CSUF is inferred from the CGS/Wills (2006) (Wills and Clahan, 2006) velocity model. The velocity model averages the shear wave velocity through the upper 30 m of material in the subsurface, and is one parameter used to characterize surface ground motion. The attenuation relationship employed for this study describes the attenuation of seismic waves within the sediments of the Los Angeles basin (Abrahamson and Silva, 2008).

The Southern California Earthquake Center - Virtual Display of Objects (SCEC-VDO), a Java 3D based object visualizer (Jordan, 2013) that integrates deformation models with fault models, is employed to determine the slip rates and the strike and dip and to display the faults in a 3-dimensional environment. SCEC-VDO is used to investigate both UCERF2 and UCERF3 and provides a side-by-side comparison of the differences in these fault models.

SCEC-VDO has the ability to incorporate HAZUS data, KML files, and shapefiles to provide a comprehensive geographic information systems (GIS) analysis of earthquake hazard, however those capabilities were not explored in this study.

Another OpenSHA application, Scenario ShakeMap, generates shake maps for the fault sections and subsections that are identified as hazardous through the disaggregation process. Scenario ShakeMap also requires a velocity model and attenuation relationship to calculate the ground motion intensity that most accurately resembles the ruptures identified through disaggregation. The CGS/Wills (2006) velocity model and the Abrahamson and Silva (2008) attenuation relationship are also employed in Scenario ShakeMap.

3. Results

3.1 Results from UCERF2

Disaggregation of hazard curves from the UCERF2 model identified the Whittier fault (Figure 2) and Coyote Hills fault (Figure 3) as the greatest contributors to the hazard to McCarthy Hall. The Whittier fault contributes 12.84% to the overall hazard, while the Coyote Hills fault contributes 7.49%. The magnitudes most likely to produce earthquakes with SA of 1 s are Mw6.95 (Figure 4) and Mw6.65 (Figure 5) on the Whittier and Coyote Hills fault, respectively. The remainder of the hazard is assigned to various faults within the Elsinore, San Andreas, and San Jacinto fault systems.

The Whittier fault is a right lateral strike-slip fault that strikes northwest through the Puente and Whittier Hills, north of the community of Brea and south of Hacienda Heights, respectively. The Whittier fault is the northern segment of the Elsinore fault. The Whittier fault is 40 km in length and dips 60°-80° to the northeast for most of its length. The Whittier fault has a slip rate of 2.5-3 mm/yr and has the potential to generate an earthquake \leq Mw7.2 (SCEDC, 2013).

The Coyote Hills fault is a blind thrust fault that strikes east-west from northern Orange County to Los Angeles and dips to the northeast 25°-30°. The fault is part of the Puente Hills fault system and has a length of approximately 11 km. The fault has a slip rate of 4.5-5 mm/yr and has the potential to generate an earthquake \leq Mw7.5 (SCEDC, 2013). The Puente Hills fault system was responsible for the 1987 Whittier Narrows earthquake (Marquis, 2004), however the Coyote Hills fault did not rupture during that earthquake.

3.2 Results from UCERF3

Disaggregation of hazard curves from the UCERF3 model identified the Peralta Hills fault (Figure 6) and the Compton fault (Figure 7) as the greatest contributors to the hazard to McCarthy Hall. The Peralta Hills fault contributes 2.46% to the overall hazard, and the Compton fault contributes 1.49%. The magnitudes most likely to generate an earthquake with a SA of 1 s are Mw6.42 (Figure 8) on the Peralta Hills fault and Mw7.39 (Figure 9) on the Compton fault. The remainder of the hazard is assigned to various faults on the Elsinore, Puente Hills, and San Andreas fault systems.

The Peralta Hills fault is a thrust fault that strikes east through the Anaheim Hills and dips 60° to the north. The fault is located south of the Whittier fault and has a length of approximately 10km (Fife and Shlemon, 2010). The fault has a slip rate of 0.4 mm/yr and has the potential to generate an earthquake \leq Mw6.5. There is surface rupture associated with the fault that is Holocene in age, and the Peralta Hills fault may be responsible for the Mw5.4 2008 Chino Hills earthquake (SCEDC, 2013).

The Compton fault, the largest thrust fault system in the Los Angeles Basin (Leon et al., 2009), dips strikes northwest and dips ~20° to the east. The fault lies beneath Seal Beach, Long Beach, and Los Angeles and is ~40km in length. The fault has a slip rate of 1.2-2.0 mm/yr and has the potential to generate an earthquake \leq Mw7.5 (Leon et al., 2009). The Compton fault has generated at least six earthquakes $>$ Mw7 in the last 14,000 years (Leon et al., 2009); Evidence suggests the largest earthquake produced by the fault was a Mw7.4 in the Holocene (Leon et al., 2009).

4. Discussion and Conclusion

UCERF2 and UCERF3 are employed to determine the faults in the Los Angeles basin that pose the greatest hazard to McCarthy Hall on the CSUF campus. UCERF2 identifies the Whittier fault and Coyote Hills fault as the largest contributors to the hazard to McCarthy Hall, in which each fault contributes 12.84% and 7.49% to the total hazard, respectively. UCERF3 identifies the Peralta Hills fault and the Compton fault as the largest contributors to the hazard to McCarthy Hall, in which each fault contributes 2.46% and 1.49% to the total hazard, respectively. Clearly, UCERF2 and UCERF3 generate different conclusions about the faults that pose the greatest hazard to McCarthy Hall, and the degree to which each fault contributes to the overall hazard.

The primary difference in the conclusions from UCERF2 and UCERF3 stems from the number of rupture scenarios recognized and how the interaction between faults is calculated. UCERF2 typically identifies a small number of large ruptures for any given fault. Additionally, UCERF2 does not recognize the possibility of multi-fault ruptures. These limitations may not accurately describe the true nature of fault ruptures in southern California. Conversely, UCERF3 segments all faults in the model into 7 km subsections and assigns slip rates and rupture probabilities to each subsection. Additionally, UCERF3 allows for the possibility of multi-fault ruptures. Probabilities are calculated for the interaction of each and every fault subsection, which allows for hundreds of thousands of possible rupture combinations. These additions to UCERF3, presumably, result in a more accurate representation of how faults rupture and interact in Southern California.

Another significant difference between UCERF2 and UCERF3 is that UCERF2 requires the user to *a priori* decide whether a fault is active or inactive, while UCERF3 does not identify any faults as inactive but instead assigns a minimum slip rate to all faults in the model. Most notably, disaggregation of the hazard curve from UCERF3 identifies the Compton fault as the most hazardous fault to McCarthy Hall, while UCERF2 assumes the Compton fault is inactive. This assumption is contrary to a recent study by Leon et al., (2009) that determines the Compton fault to likely be active.

Disaggregation of the hazard curves from each model also generates a significant difference in the number of ruptures that contribute to the overall hazard for McCarthy Hall. Disaggregation of the hazard curves from UCERF2 identifies the 10 most hazardous ruptures constitute 46.11% of the total hazard to McCarthy Hall, while the 10 most hazardous faults in UCERF3 constitute 18.81%. Furthermore UCERF3 indicates more possible ruptures as hazardous, which significantly lowers the contribution to the hazard for each rupture. This makes it difficult to confidently identify which faults truly pose the most hazard to any given site.

SCEC-VDO and OpenSHA are currently the only software that can explore UCERF3. Both these programs are under development, and they have limitations of their own. The most recent iteration of SCEC-VDO requires several gigabytes of hard drive space, and a minimum of 16 gigabytes of RAM to run properly. SCEC-VDO also requires access to the University of Southern California

(USC) server to obtain the most recent and on-going updates. OpenSHA is a more accessible and smaller program than SCEC-VDO that does not require excessive hard drive space or access to the USC servers; however, UCERF3 includes >250,000 possible ruptures, which can make the hazard curve calculations impossible on machines with less than 16 gigabytes of RAM.

This study focuses on the generation of hazard curves for UCERF2 and UCERF3 and identification of the faults that pose the greatest hazard to McCarthy Hall on the CSUF main campus, however this study is by no means exhaustive. A larger number of faults that may contribute to the overall hazard could be examined. This study only examines the two primary contributors for each rupture forecast, however disaggregation through OpenSHA

identifies up to 100 faults that can contribute to the hazard. In addition, a more comprehensive study of the affected area could be explored with the GIS tools within SCEC-VDO. SCEC-VDO also has the capability to determine affected populations, potential monetary costs, and casualty estimates, which could provide useful information as to how to prepare for a large earthquake at CSUF.

5. Acknowledgments

I would like to thank Dr. Harmony Colella and Dr. David Bowman for their guidance with this project. I would also like to thank the entire 2013 SCEC Use/IT intern class for its tireless work perfecting SCEC-VDO.



Figure 1: Location of CSUF within the Los Angeles basin. Grid lines are 1° and longitudinal trend north-south with north at top of map.



Figure 2: SCEC-VDO visualization of the Whittier fault. The fault surface is in yellow, and the fault dips to the northeast.



Figure 3: SCEC-VDO visualization of the Coyote Hills fault. The fault surface is in yellow, and the fault dips to the north.

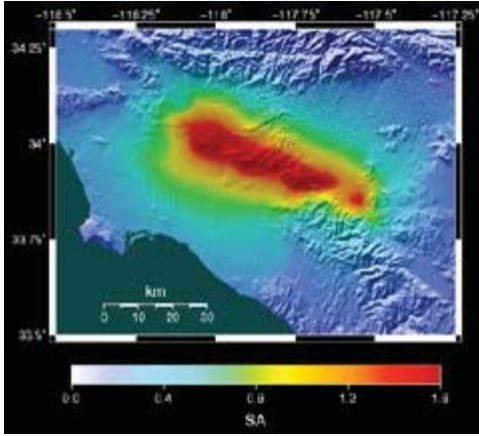


Figure 4: OpenSHA shakemap of a simulated Mw6.95 on the Whittier fault. SA is measured as a fraction of g at the 10% exceedance level.

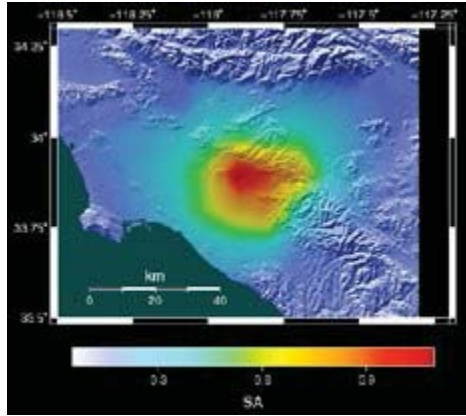


Figure 8: OpenSHA shakemap of a simulated Mw6.42 on the Peralta Hills fault. SA is measured as a fraction of g at the 10% exceedance level.

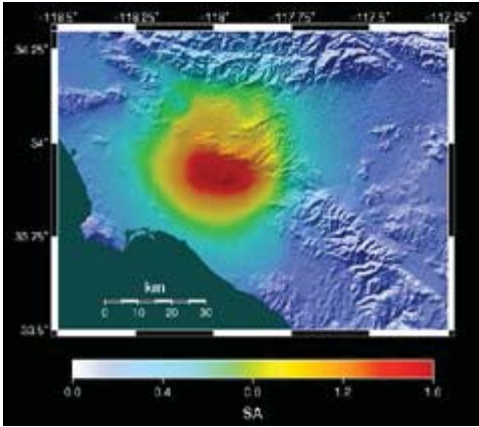


Figure 5: OpenSHA shakemap of a simulated Mw6.65 on the Coyote Hills fault. SA is measured as a fraction of g at the 10% exceedance level.

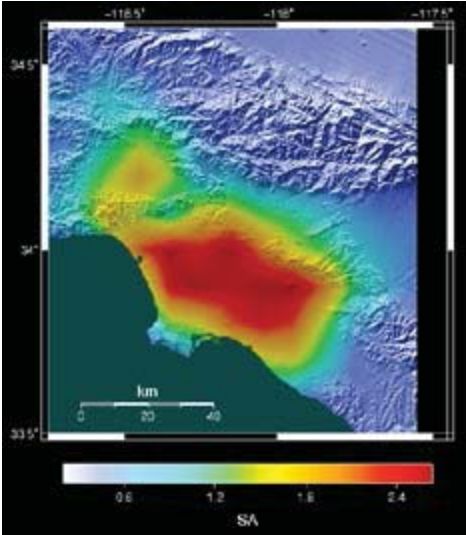


Figure 9: (top) OpenSHA shakemap of a simulated Mw7.39 on the Compton fault. SA is measured as a fraction of g at the 10% exceedance level.



Figure 6: (left) SCEC-VDO visualization of the Peralta Hills fault. The fault surface is in yellow and the fault dips to the north.

Figure 7: (right) SCEC-VDO visualization of the Compton fault. The fault surface is yellow and the fault dips to the northeast.

References

- Abrahamson, N. A., and Silva, W.J., 2008, Summary of the Abrahamson & Silva NGA ground-motion relations: Earthquake Spectra, v. 24(1), p. 67-97.
- Bazurro, P., and Cornell, C.A., 1999, Disaggregation of seismic hazard: Bulletin of The Seismological Society of America, v. 89, 2, p. 501-520.
- Field, E.H., T.H. Jordan, and C.A. Cornell (2003), OpenSHA: A Developing Community- Modeling Environment for Seismic Hazard Analysis, Seismological Research Letters, v. 74, no. 4, p. 406-419.
- Field, E.H., Dawson, T.E., Felzer, K.R., Frankel, A.D., Gupta, V., Jordan, T.H., Parsons, T., Petersen, M.D., Stein, R.S., Weldon, R.J., II, and Wills, C.J., 2008, The Uniform California Earthquake Rupture Forecast, Version 2 (UCERF 2): U.S. Geological Survey Open-File Report 2007-1437 and California Geological Survey Special Report 203, <http://pubs.usgs.gov/of/2007/1437/>
- Field, E.H., Biasi, G.P., Bird, P., Dawson, T.E., Felzer, K.R., Jackson, D.D., Johnson, K.M., Jordan, T.H., Madden, C., Michael, A.J., Milner, K.R., Page, M.T., Parsons, T., Powers, P.M., Shaw, B.E., Thatcher, W.R., Weldon, R.J., II, and Zeng, Y., 2013, Uniform California earthquake rupture forecast, version 3 (UCERF3)—The time-independent model: U.S. Geological Survey Open-File Report 2013-1165, 97 p., California Geological Survey Special Report 228, and Southern California Earthquake Center Publication 1792, <http://pubs.usgs.gov/of/2013/1165/>
- Fife, D.L., and Shlemon, R., 2010, Peralta Hills fault a previously unrecognized active transverse range “blind thrust” Orange County, CA, in Proceedings, Cordilleran Section - 106th Annual Meeting, and Pacific Section, American Association of Petroleum Geologists: Geological Society of America Abstracts with Programs, v. 42, no. 4, p. 103.
- Goel, R.K., and Chopra, A.K., 1997, Period formulas for moment-resisting frame buildings: Journal of Structural Engineering - ASCE, v. 123, p. 1454-1461.
- International Conference of Building Officials, 1997, Uniform Building Code, USA, v. I, 432 p.
- Jordan, T.H., 2013, SCEC Virtual Display of Objects (SCEC-VDO), v.2013, http://www.scec.org/scec-vdo/SCEC_VDO.jnlp
- Leon, L.A., Dolan, J.F., Shaw, J.H., and Pratt, T.L., 2009, Evidence for large Holocene earthquakes on the Compton thrust fault, Los Angeles, California: Journal of Geophysical Research, v. 114, B12.
- Marquis, J., 2004, SCEC: <http://www.scec.org/research/030404dolan.html> (accessed June 2014).
- SCECDC, 2013, Southern California Earthquake Center. Caltech. Dataset. doi:10.7909/C3WD3xH1
- Wills, C.J., and Clahan, K.B., 2006, Developing a map of geologically defined site-condition categories for California: Bulletin of The Seismological Society of America, v. 96, 4A, p. 1483-1501.
- Yerkes, R.F., McCulloh, T.H., Schoellhamer, J.E., and Vedder, J.G., 1965, Geology of the Los Angeles basin California - an introduction: U.S. Geological Survey Professional Paper 420-A, <http://pubs.usgs.gov/pp/0420a/report.pdf>

Orientation of the Sierra Nevada Frontal Fault Zone near Independence and Lone Pine, California

Department of Geological Sciences, California State University, Fullerton

Greg Shagam

Advisor: Phil Armstrong Ph. D

Abstract

The western side of the Owens Valley is bound by the east-dipping normal fault system called the Sierra Nevada Frontal Fault Zone (SNFFZ). Published calculations of long-term horizontal extension across Owens Valley and the rest of the western Basin and Range generally assume a relatively steep fault dip of 60°. Recent studies conducted by Phillips and Majkowski (2011) along the SNFFZ north of Bishop show that this boundary is better represented by lower angle dips of 26° to 52°. To test the hypothesis that faults south of Bishop in the Owens Valley might also dip more shallowly than the assumed 60°, I used differential GPS to map one strand of the SNFFZ at Independence Creek and two strands at Shepherd Creek, both west of the towns of Independence and Lone Pine, California. GPS locations and elevations were taken approximately every 5-10 meters along the surface exposure of the faults for up to 2 km distance in order to capture maximum elevation variation along the fault traces. The fault orientations were determined using a program that evaluates the best-fit fault dip of all x,y,z data points assuming a planar fault. The Independence Creek segment has a strike of N12W and dips 29°E. The eastern Shepherd Creek strand strikes N44W and dips 34°E, whereas the western strand strikes N40W and dips 34°E. Because of this low-angle dip geometry, long-term horizontal extension rates calculated from 60° dips need to be re-evaluated. Extension rates determined from 60° dipping faults could be one-third the rates determined from 30° dipping faults.

1. Introduction

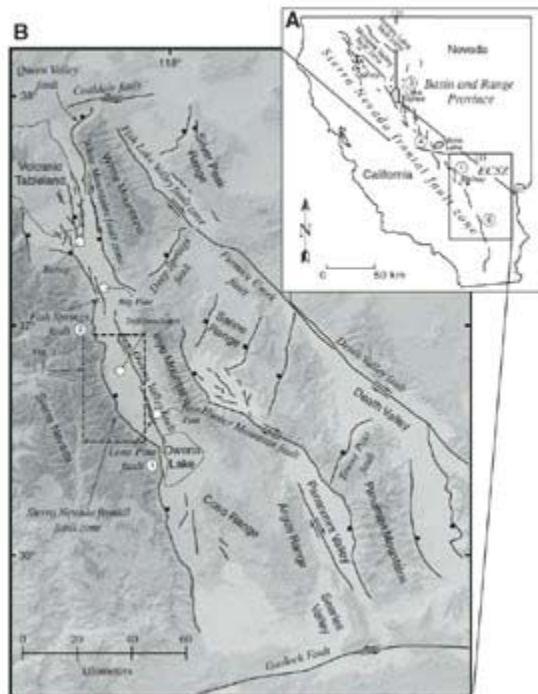
Most estimates of horizontal extension rates on the Sierra Nevada Frontal Fault Zone (SNFFZ) use an assumed normal fault dip of 60° (Le et al., 2007). Le et al. (2007) determined the slip rates of faults in the Lone Pine and Independence areas that facilitate the horizontal motion of this horst and graben system, but the orientation of the actual faults have never been determined in detail. The SNFFZ is located on the western edge of the Owens Valley where the steep face of the Sierra Nevada Mountains rise out of the valley floor (Figure 1). North of Bishop in the northern Owens Valley, Phillips and Majkowski (2011) found that east-facing normal faults dip consistently less than the typically assumed 60°, with dips from 26° to 52°. Farther south, near Lone Pine and Independence, fault dip of SNFFZ strands have not been documented. The goal of this study is to evaluate fault geometry of the SNFFZ in the vicinity of Lone Pine and Independence to test the hypothesis that these faults dip relatively shallowly.

Field reconnaissance of this area has yielded two areas of the SNFFZ with the topographic relief needed to determine the SNFFZ fault orientations. These include: (1) Independence Creek and (2) Shepherd Creek, where the Sierra Nevada range transitions into alluvial fan deposits of the Owens Valley (Figure 2). In these two areas the SNFFZ is exposed on the ground surface as mappable scarps. One scarp is identifiable in the Independence Creek area and two scarps are identifiable in the Shepherd Creek area; both these scarps were previously mapped by Le et al. (2007).

2. Geologic Background

The Owens Valley is structurally complex and currently active as evidenced by the 1872 Lone Pine Earthquake. The stress regime is partitioned at the surface into strike-slip motion on the Owens Valley and Lone Pine faults and dip-slip for the SNFFZ. Assumptions have been made on how these two faults interact at depth (Phillips and Majkowski, 2011), but no definitive conclusions have been made. Tectonically this area is driven by the stress imparted by the translational movement between the North American plate and the Pacific plate boundary regionally defined by the San Andreas Fault

Due to the stress imparted by the oblique motion of the Pacific plate relative to the Sierra Nevada micro-plate and the North American plate, the Owens Valley and the surrounding area are complexly fractured and faulted. To the east of the Sierra Nevada Province, Owens Valley marks the western extent of the Basin and Range Province. Major faulting has occurred in the Owens Valley along the Lone Pine Fault, the Owens Valley Fault, the SNFFZ, the White Mountains Fault and many other minor related faults.



The faults of the SNFFZ offset granitic basement rocks of the Sierra Nevada and Quaternary fan deposits of Owens Valley (Le et al., 2007). Figure 2 shows the varying Quaternary deposits in my field area as mapped by Le et al., (2007).

3. Quaternary deposits of Owens Valley

Surficial deposits found in this area are largely comprised of alluvial fan deposits of varying age from 124 ka to 3-4 ka (Le et al., 2007). Cause for deposition of these alluvial fans varies from glacial and non-glacial giving the deposits a number of different geomorphic characteristics. Because of varying deposit types, Le et al. (2007) chose to differentiate the fans observed in Owens Valley just east of the SNFFZ with seven sub-classifications, not including landslide deposits. Quartz-rich boulder samples were collected from the deposits for model CRN Beryllium-10 exposure age dating and recalculated using an erosion rate of 0.3 cm/k.y. of the boulder surface (Small et al., 1995) These deposits are all Quaternary in age with the oldest, Qf1 occurring approximately 123.7+/- 16.6 ka. Qf4 is the youngest and currently active channels are dated approximately 3-4 ka. Geophysical data suggest that the area between the Alabama hills and the Sierra Nevada Range it is underlain with approximately 100 m thick of alluvial deposits (Phillips & Majkowski, 2011).

4. Faults

Eastern Boundary-Sierra Nevada Frontal Fault Zone

The boundary between the Sierra Nevada and the Basin and Range provinces forms a complex fault system that includes the Sierra Nevada Frontal Fault Zone, the Owens Valley fault and the Lone Pine faults. Along the range front, the SNFFZ typically exhibits only normal, dip-slip faulting (Le et al., 2007). The Owens Valley and Lone Pine faults exhibit dextral strike slip and oblique slip, respectively.

Figure 1: Shaded relief map showing the location of the general study area (inside dashed box) and its relation to the faults of the part of the Eastern California Shear Zone. Balls on faults are on hanging-wall side of normal faults. Strike-slip faults have arrow showing relative offset direction. The study area is bound on west by the Sierra Nevada and on the east by Owens Valley. Map modified from Le et al. (2007).

The Owens Valley Fault is parallel to sub-parallel with the SNFFZ and is located a few kilometers to the east (Figure 1 & 2). The Lone pine Fault is located approximately 3-5 kilometers east of the range front and just south of the Owens Valley fault (Figure 1). These three faults facilitate both extension and dextral motion along the boundary of the Sierra Nevada and the Basin and Range provinces.

Le et al. (2007) conducted detailed studies of an area covering a 35 km long and 5 km wide section between Oak Creek and Lubkin creek of the SNFFZ. The strike of this fault system ranges from approximately 350 to 310°, with an average for the system approximately 334°. These faults typically dip to the east, but a few west dipping faults are present. In the hanging wall, Quaternary sediment is usually found next to granite or other Quaternary sediment. Of all the Quaternary deposits, Q4 is the only deposit not faulted in this region. All other Quaternary deposits exhibit offset along the SNFFZ faults. These faults are right-stepping, en echelon, NW striking, assumed to dip around 60° to the east, and display only dip-slip motion.

Moderately degraded and semi-vegetated fault scarps yield vertical offset measurements ranging from 41.0 +/-2.0 m to 2.0 +/-0.1 m (Le et al., 2007). Combined with CRN Be-10 age dating, vertical slip rate estimates of 0.2-0.3 +/- 0.1 mm/yr since ca. 124 ka., 0.2-0.4 +/- 0.1 mm/yr since ca. 61 ka, 0.3-0.4 +/- 0.2 mm/yr since ca. 26 ka, and 1.6 +/- 0.4 mm/yr since ca. 4 ka. Le et al., (2007) also calculated extension rates, assuming a 60° normal fault dip, range from 0.1-0.2 +/- 0.1 mm/yr to 0.9 +/- 0.4 mm/yr. Offset found near San Joaquin River is on the scale of approximately 980 meters, which implies a long term vertical slip rate of 0.3-0.4 mm/yr (Wakabayashi & Sawyer, 2001). The Le et al. (2007) results suggest that the rigid Sierra Nevada "micro-plate" has a late Pleistocene to recent rate of 3.0 mm/yr, at 331° (azimuth) relative to a fixed marker east of the Basin and Range province.

Southern and northeastern boundary

Bounding the south-eastern side of the Sierra Nevada, the Little Lake and Airport Lake faults display dextral motion and have helped to form the Indian Wells valley (Le et al., 2007). These faults transfer their slip over to the Owens Valley where more parallel faults can relieve accumulated stress more effectively in a dextral-normal slip (Phillips & Majkowski, 2011). Sub-parallel dextral, strike-slip faults in Mohawk Valley to the north also relieve the trans-rotational

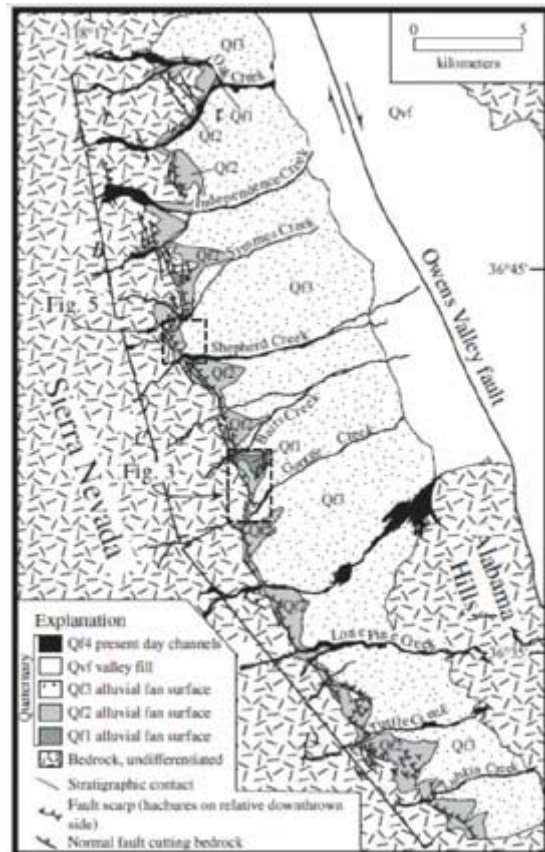


Figure 2: Geologic map of SNFFZ and the Owens Valley showing Quaternary deposits (Le et al., 2007). This map shows fault scarps of the SNFFZ trending northwest with an echelon dextral steps. These Quaternary deposits are offset due to the normal faulting of the SNFFZ. The creeks that cross the SNFFZ are shown. Map modified from Le et al. (2007).

forces formed by the rotation of the Sierra Nevada (Le et al., 2007). Also according to Le, Holocene slip rates of the Owens Valley are on the order of 1.8 – 3.6 mm/yr with an earthquake reoccurrence interval of 3000 to 4000 years. Paleosiesmic slip rates are approximately 3.3-3.8 mm/yr for the Owens valley fault. The dynamics of this region are similar to that of a horst and graben with the Sierra Nevada Mountain range and the Inyo mountains representing the horst features and the Owens Valley in between is the graben.



Figure 3: Topographic map taken from the USGS Kearsarge Peak Quadrangle 7.5- minute series showing the Union Valley road as it crosses the SNFFZ in the vicinity of the Independence Creek. The small red dots indicate data points where x,y,z coordinates were taken by the Garmin hand-held device as the fault scarp was walked out. North is to the top of the page.

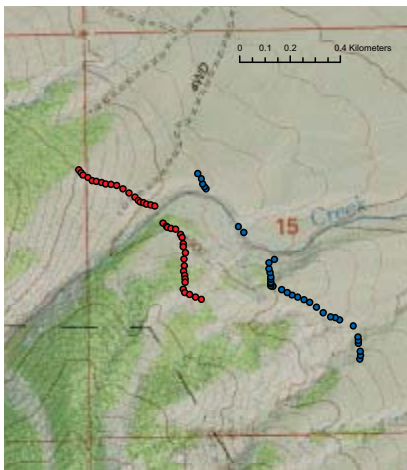


Figure 6: Topographic map of the Shepherd Creek area taken from the USGS Mt. Williamson Quadrangle 7.5- minute series showing the transition from mountains to fan deposits in the northwestern direction. The red and blue dots indicate data points where x,y,z coordinates were taken by the Garmin hand-held device as the fault scarp was walked out. North is to the top of the page.

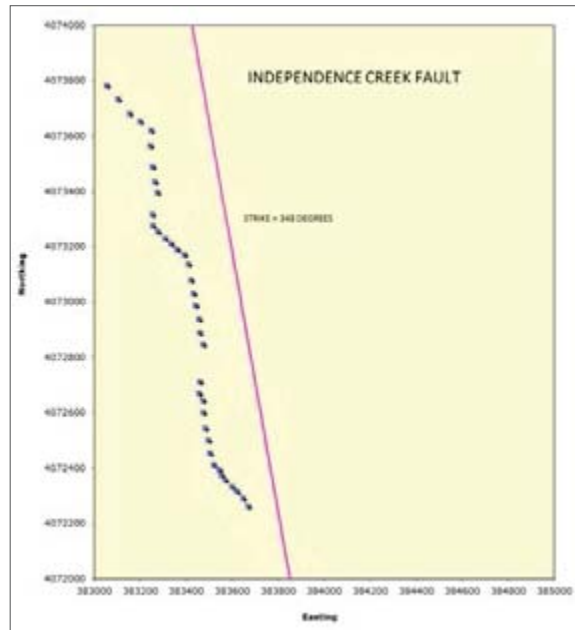


Figure 4: Plot of Topcon derived northing and easting data collected from Independence Creek study area. A strike-parallel line (in red) is added to this plot for the purpose of calculating the perpendicular distance from the line to a station point. This plot is generated from an Excel program donated by Professor Fred Phillips at New Mexico Tech, 2012.

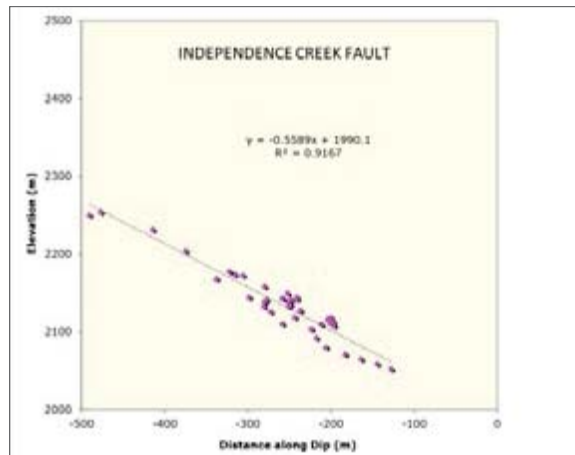


Figure 5: Plot of Topcon derived elevations in the Independence Creek area compared to the horizontal distance between the station and the strike-parallel line. This plot has no vertical exaggeration therefore depicting a visual representation of the fault dip of the SNFFZ in the Independence Creek area. This plot is generated from an Excel program donated by Professor Fred Phillips of New Mexico Tech, 2012.

5. Results

Fault Orientations

The main purpose of this study is to determine the dip angle of the SNFFZ in this area. Using the Excel spreadsheet program supplied by Professor Fred Phillips (F. Phillips, Personal Communication), a plot of the easting and northing data yields a best-fit strike line. Directly correlated to that plot is another plot that uses the strike to determine the dip of the fault. To determine the dip of the fault in degrees it is required the equation for the trend line in the second plot is displayed. With that equation ($y=mx+b$), taking the inverse-tangent function of the slope ("m") value will provide the fault dip in degrees. These two plots are the output of the Excel spreadsheet program and give us the strike and dip of each SNFFZ strand studied.

The Independence Creek strand strikes azimuth 348° or N 12° W (figure 4) and dips 29° east (figure 5). The Shepherd Creek east strand strikes azimuth 316° or N 44° W (figure 7) and dips 34° east (figure 8). The Shepherd Creek west strand strikes azimuth 320° or N 40° W (figure 9) and dips 34° east (figure 10).

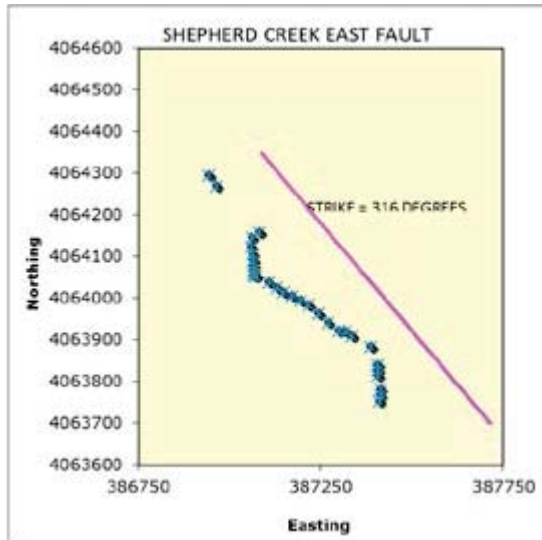


Figure 7: Plot of Topcon derived northing and easting data collected from Shepherd Creek east study area. A strike-parallel line (in red) is added to this plot for the purpose of calculating the perpendicular distance from the line to a station point. This plot is generated from an Excel program donated by Professor Fred Phillips of New Mexico Tech, 2012.

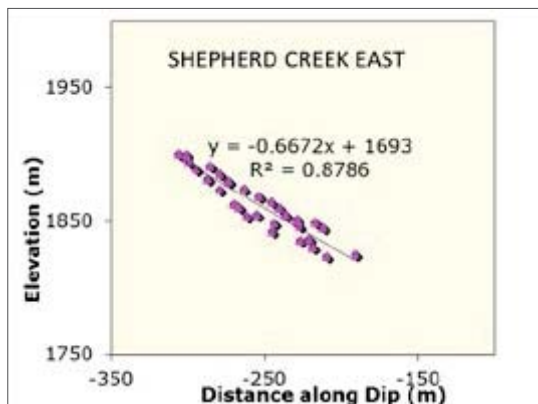


Figure 8: (bottom)- Plot of Topcon derived elevations in the Shepherd Creek east area compared to the horizontal distance between the station and the strike-parallel line. This plot has no vertical exaggeration therefore depicting a visual representation of the fault dip of the SNFFZ in the Shepherd Creek east area. This plot is generated from an Excel program donated by Professor Fred Phillips of New Mexico Tech, 2012.

6. Methods

The implications of this study directly relate to the calculated horizontal-extension rates of the Owens Valley, and possibly even the Basin and Range province. Previously published rates on this matter are underestimated if a 60°-dipping fault angle was assumed. Quantitatively determining how much the extension rates are underestimated is more difficult to do. Geometry of the White Mountains fault on the other side of the valley, a west-facing, normal-slip fault defining the other half of the graben, is also required. An underestimation of at least a third is plausible with making no assumptions to the geometry of the White Mountain Fault. If the other side of the graben were found to best be defined by low-angle normal faulting that number could double. Extrapolating fault dip angles that are too steep across the entire Basin and Range province could lead to serious implications about the long-term extension rates. If all the faults that are presently assumed to dip 60° really dip 30-35° as determined from the three faults studied in this project, overall, long-term extension rates could be underestimated by a factor of about three.

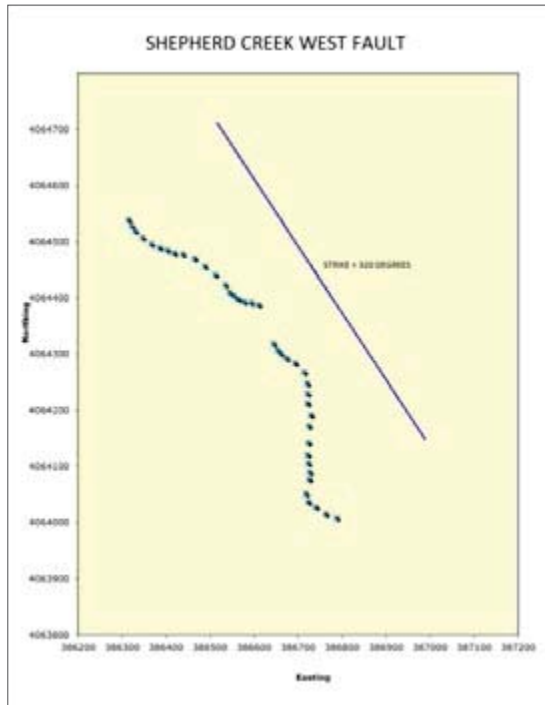


Figure 9: Plot of Topcon derived northing and easting data collected from Shepherd Creek west study area. A strike-parallel line (in red) is added to this plot for the purpose of calculating the perpendicular distance from the line to a station point. This plot is generated from an Excel program donated by Professor Fred Phillips of New Mexico Tech, 2012.

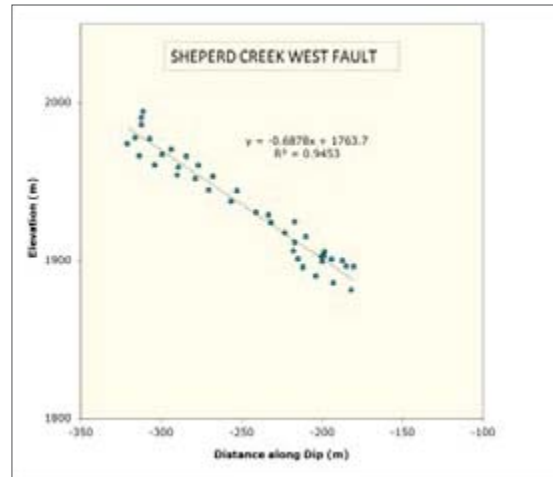


Figure 10: Plot of Topcon derived elevations in the Shepherd Creek west area compared to the horizontal distance between the station and the strike-parallel line. This plot has no vertical exaggeration therefore depicting a visual representation of the fault dip of the SNFFZ in the Shepherd Creek west area. This plot is generated from an Excel program donated by Professor Fred Phillips of New Mexico Tech, 2012.

7. Conclusions

The orientations of the three strands of the SNFFZ at Independence Creek and Shepherd Creek were determined. In the Independence Creek area, the section of the SNFFZ studied strikes N12°W and dips 29° east. In the Shepherd Creek field area two strands of the SNFFZ were studied. The east strand in the Shepherd Creek area strikes N44°W and dips 34° east. The west strand strikes N40°W and dips 34° east. All three strands of the SNFFZ studied are 1-2 km long fault exposures of a much more extensive fault system that spans hundreds of km. In order to fully understand the dip of the SNFFZ along its entirety, more studies that continue the work of this study, and the work of Phillips and Majkowski (2011), need to be completed.

References

- Argus, D.F., Gordon, R.G., 1991, Current Sierra Nevada-North America motion from very long baseline interferometry: Implications for the kinematics of the western United States, *Geology*, v. 19; no. 11; p. 1085-1088
- Bierman, P.R., Gillespie, A.R., and Caffee, M.W., 1995, Cosmogenic ages for recurrence intervals and debris flow fan deposition, Owens Valley, California: *Science*, v. 270, P. 447-450
- Gillespie, A.R., 1982, Quaternary glaciation and tectonism in the southern Sierra Nevada, Inyo County, California (PH.D. thesis); Pasadena, California Institute of Technology, p. 736
- Henry, C.D., 2009, Uplift of the Sierra Nevada, California, *Geology*, vol 37, p 575-576
- Hill, M., 2006, *Geology of the Sierra Nevada: Revised Edition (California Natural History Guides)*, May 15, 2006
- Le, K., Lee, J., Owen, L.A., Finkel, R., 2007, Late Quaternary slip rates along the Sierra Nevada frontal fault zone, California: Slip partitioning across the western margin of the eastern California shear zone-Basin and Range Province, *Geological Society of America Bulletin*, v. 119, p 240-256
- Phillips, F. M., Majkowski, L., 2011, The role of low-angle normal faulting in active tectonics of the northern Owens Valley, California, *Lithosphere*, v.3, p. 22 - 36
- Sauber, J., Thatcher, W., Solomon, S.C., Lisowski, M., 1994, Geodetic slip rate for the eastern California shear zone and the recurrence time of Mojave desert earthquakes, *Nature Publishing Group, Nature* 367, p 264 - 266
- Small, E.E., Anderson, R.S., 1995, Geomorphically driven late Cenozoic rock uplift in the Sierra Nevada, California: *science*, v. 270, p 277-281
- Henry, C.D., 2009, Uplift of the Sierra Nevada, California, *Geology*, vol 37, p 575-576
- Unruh, J., Barren, A., 2003, Transtensional model for the Sierra Nevada frontal fault system, eastern California, *Geology*; April 2003; v. 3, p. 327-330
- Wakabayashi, J., Sawyer, T.L., 2001, Stream Incision, Tectonics, Uplift, and Evolution of Topography of the Sierra Nevada, California, *The Journal of Geology*, v. 109, No. 5, p. 539-562

Reconstructing the Paleoenvironment of Orange County, California Using Eocene Plant Fossils

Department of Geological Sciences, California State University, Fullerton

Daniel Weiherer

Abstract

Plant fossils from the Eocene of Orange County, CA were analyzed to reconstruct their paleoenvironment. Orange County was hypothesized to be warmer and wetter and to have been covered in a tropical or subtropical rainforest. North America during the Eocene had an average temperature near 21 C° and rainfall of at least 150 cm. Qualitative leaf analysis was used to acquire a broad understanding of the paleoforest. It was tropical and mesic, but not wet enough to be a rainforest. This type of forest, called a tropical seasonal forest, has temperatures between 20-30 C° and rainfall between 100-250 cm per year. The mean annual temperature was calculated using the coexistence approach and leaf margin analysis. The coexistence approach yielded a temperature between 14.1-20.8 C° and leaf margin analysis yielded a temperature of 21.54 Co ± 4.16 C°. The mean annual precipitation was calculated using three unlike leaf area analysis equations. The first equation yielded a mean annual precipitation of 148.8cm ± 50.6 cm. The second equation yielded 30.9 cm. The third equation yielded a MAP of 57.5 cm. The latter two values were discredited since they were far outside of the accepted range of precipitation.

Petrographic and Geochemical Analysis of the Summit Gabbro and Associated Granitoids of the Kern Plateau, Southern Sierra Nevada, California

Department of Geological Sciences, California State University, Fullerton

Elizabeth White

Advisor: Dr. Diane Clemens-Knott

1. Introduction

The Sierra Nevada Batholith (SNB) is located in east California (Fig. 1) and is perhaps the best studied batholith on the planet. Emplaced during the Mesozoic Era, the SNB has since been exposed by Pleistocene glaciation and significant uplift during Basin and Range extension, both of which have provided excellent accessibility for geologists. However, because of its complexity, the origin of the batholith remains in debate. The SNB is a compound batholith, meaning that multiple episodes of arc magmatism occurred throughout the Mesozoic Era, developing a diverse and overlapping series of plutons within the batholith.

Arc batholiths, such as the Sierra Nevada, are important to understand because they record episodes of continental crustal growth. Calculating the amount of material that was transferred from the mantle to the crust is dependent on the composition of the mantle wedge. Whereas the rocks on the western side of the Sierra Nevada Batholith (SNB) show evidence of originating from magmas derived by partial melting of a depleted-mantle source (DePaolo, 1980), the rocks of the eastern SNB appear to reveal a different story. For example, isotopic evidence from the Lamarck Granodiorite suggests that enriched mantle may underlie the eastern SNB (Coleman, 1992). The weakness of this evidence is that existing studies focus on granitic rocks, which do not best represent mantle-derived magmas.

2. Background

The majority of rocks in the SNB are granitoids, which represent compositionally more evolved magmas, and the majority of published studies focus on these granitoids.

Only a fraction of the exposed rocks in the SNB are mafic, which as a whole only make up 5% of all rock types in the entire mountain range (Moore, 2000). Gabbros are crucial to these studies of mantle wedge composition since gabbros have experienced a minimal amount of fractionation and may represent a proxy for the mantle source below the batholith.

The Summit Gabbro

Little is currently known regarding the mineralogy and geochemistry of Summit Gabbro. Geochemical characterization of the Summit Gabbro may provide new information about the type of mantle underlying the eastern Sierra Nevada arc during the Mesozoic Era. Gabbros are mafic rocks, which by definition contain large quantities of magnesium- and iron-rich minerals, such as olivine (Gill, 2010).

The extent of differentiation of a magma can be approximately quantified using the magnesium-number (Mg#), which is calculated using the formula $Mg\# = [100 \text{ Mg} / (\text{Mg} + \text{Fe}^{2+})]$ where Mg and Fe^{2+} are atomic proportions. Higher Mg-numbers represent more primitive magmas—magmas that have not evolved much from their original, mantle-derived composition (Winters, 2010). The relationship between olivine composition and magma composition is depicted by the olivine phase diagram (Fig. 2). Mantle olivines have a composition between Fo_{88} - Fo_{92} , which is consistent planet wide. Olivine crystals of this composition are in thermal and compositional equilibrium with magmas having a composition of Fo_{72} - Fo_{65} . As temperatures drop, and olivine fractionates, the composition of stable olivine crystals become more iron-rich, as do the compositions of the coexisting magmas. Thus,



Figure 1: Google Earth image showing the location of the Sierra Nevada Batholith and the Kern Plateau field site. E. White, 2014.

gabbros with higher Mg-numbers are ideal for identifying mantle-derived magmas that have not experienced much differentiation and therefore can be used to determine whether the mantle source rock is either geochemically enriched or depleted.

To date, the highest Mg# measured from rocks of the eastern Sierra Nevada is Fo50 (Gevedon, 2013), a value significantly lower than what would be predicted for a rock that crystallized from a pristine mantle melt (e.g., Fo72-Fo65).

Further analysis of the Summit Gabbro suite targeting the most mafic rocks may lead to identifying higher Mg# rocks that could contribute to a better understanding of the source of the mafic magmas and how these magmas differentiated before emplacement. For example, the suite's mineralogy and the rock textures may reveal information regarding the crystallization history, and the whole-rock chemistry may provide data concerning the composition of the parental magma and its evolution. Because of the eastern Sierra location of the Summit Gabbro and its mafic composition, any findings will add to debate of whether the mantle-derived component of the eastern Sierra is depleted or enriched, which in turn will effect calculations regarding how

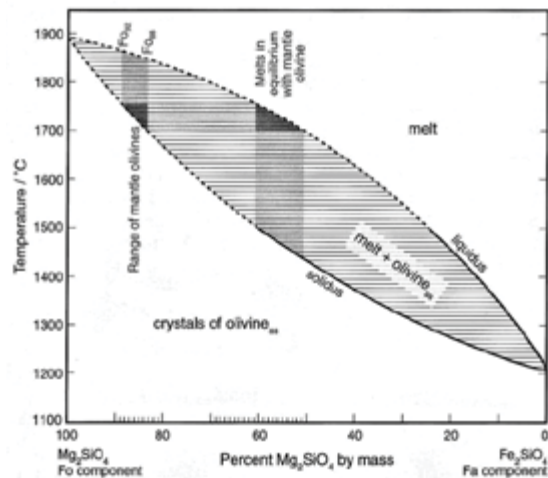


Figure 2: Olivine phase diagram (Gill, 2010).

much material was transferred from mantle to the crust during the Mesozoic Era. In brief, characterizing the Summit Gabbro is one of the first steps to determining how the western margin of the Laurentian continent was modified by Mesozoic arc magmatism.

3. Methods

Samples were collected from the Kern Plateau in June 2013. Prior to choosing samples it was important to pick rock bodies that were previously mapped as Mesozoic plutonic rock (i.e. gabbro), and were accessible either by vehicle or by hiking (Fig. 3). Table 1 in Appendix I contains the GPS locations for all samples.

Samples were crushed and powdered at California State University, Fullerton in preparation for X-ray fluorescence (XRF) analysis at Pomona College. Select rocks were shipped off to Texas Petrographics, Inc. to be made into both covered and uncovered, highly polished thin sections. The covered thin sections were analyzed using a petrographic microscope, while single crystal compositions were analyzed from the uncovered thin sections using the scanning electron microscope (SEM) housed at the Caltech Analytical Facility.

Chemical compositions of seventeen whole rock samples were determined using an XRF (model: Panalytical Axios). XRF instruments obtain their data by shooting samples with an intense x-ray known as an incident beam, which ejects electrons from the lower energy levels in the atoms. The ejected electrons are replaced by electrons from the higher energy shells that in turn release an x-ray. Each element has its own characteristic wavelength associated with this release of energy. XRF instruments measure those wavelengths to determine

the chemical composition of each sample. Samples must be homogenous to prevent faulty readings. To create homogenous samples, the pulverized rock powders were mixed in a 3:7 ratio of powdered sample to a flux (*dilithium tetraborate* $\text{Li}_2\text{B}_4\text{O}_7$), melted, powdered, and remelted. The repeated grinding and melting ensures that the glass beads are chemically homogenous. The final step is to polish the glass beads so incident beams refract off atoms in the sample instead of imperfections on the glass bead.

A scanning electron microscope (SEM) was used to analyze the chemical composition of individual crystals from the most mafic samples. The SEM generates a variety of data, including information about a crystal's chemical composition and morphology by focusing a beam of high-energy electrons onto the sample. If inner electrons are ejected, they are replaced by outer electrons—the difference in binding energy is released as a “characteristic X-ray” An energy dispersive detector (EDS) analyzes the X-ray energy spectrum electrons to determine the abundance of specific elements. A second detector records the back-scattered electrons (BSE), which produces images of the surface. When interpreting BSE images, the darker colored areas reflect minerals with lower densities, while the lighter area suggest denser minerals, such as metals and metal oxides.

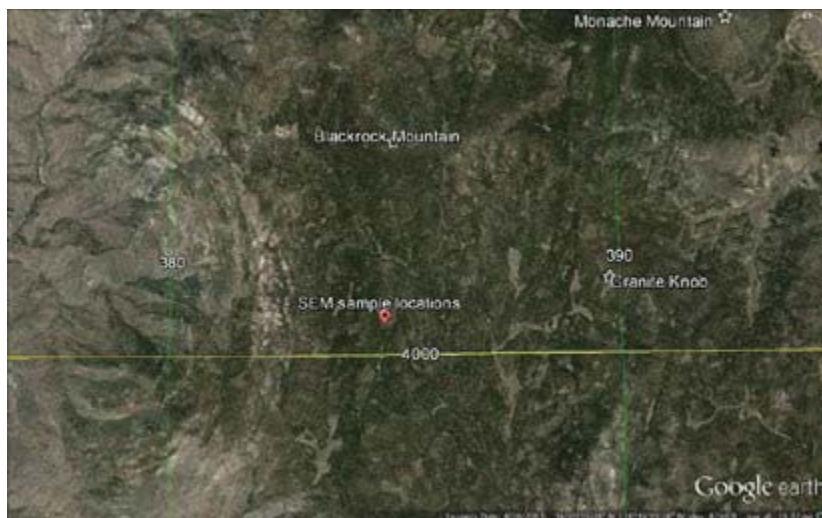
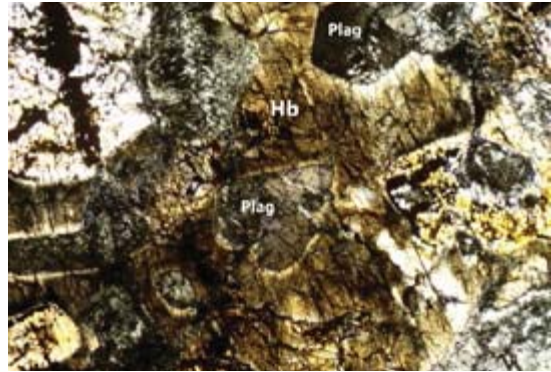
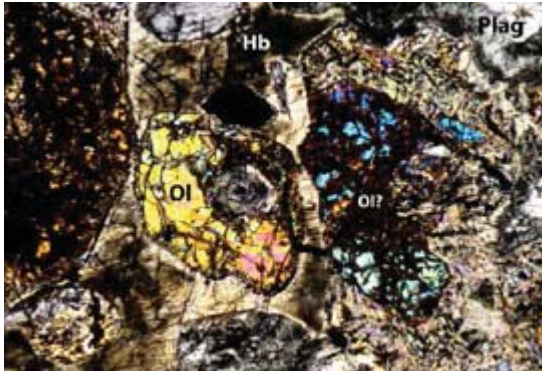


Figure 3: Location of hand samples used for SEM analysis.



Figures 4 and 5: Photomicrographs of Fr-120C; scale = 10x mm. The mineralogy of Fr-120C is characteristic of a gabbro, containing mafic minerals like olivine (ol) and calcium-rich plagioclase (plag). Hornblende (hb) is interstitial.

4. Results

Whole Rock Chemistry

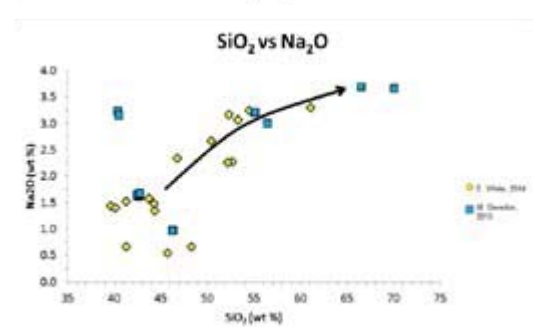
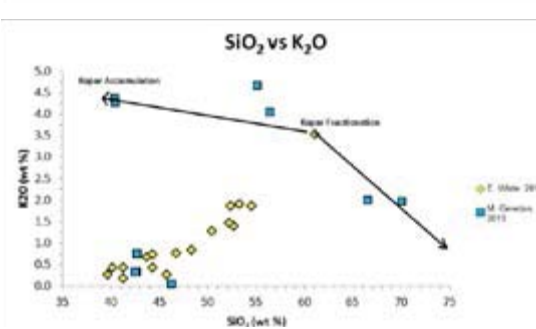
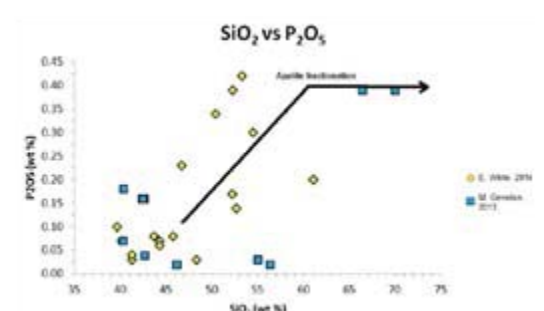
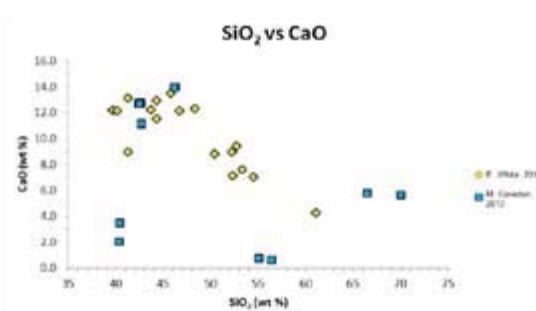
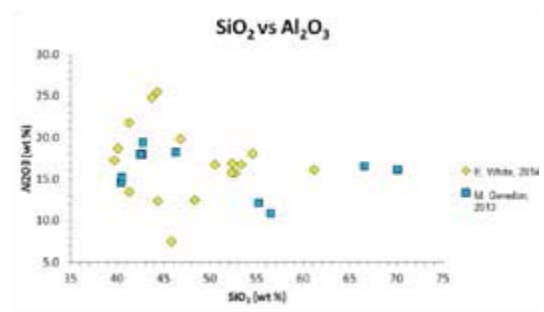
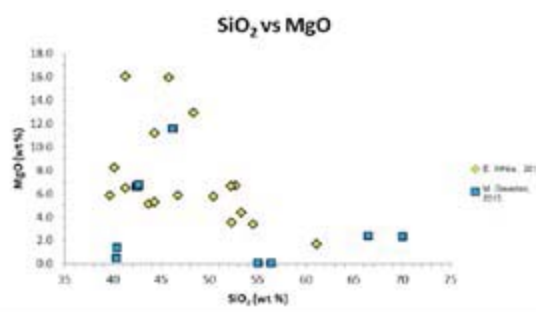
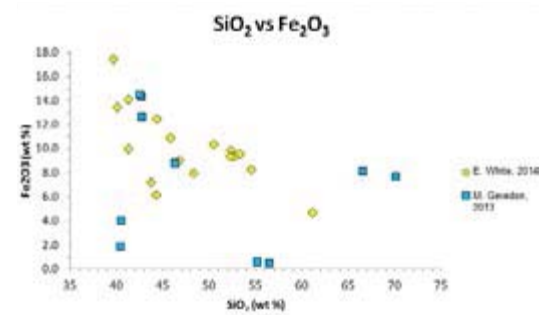
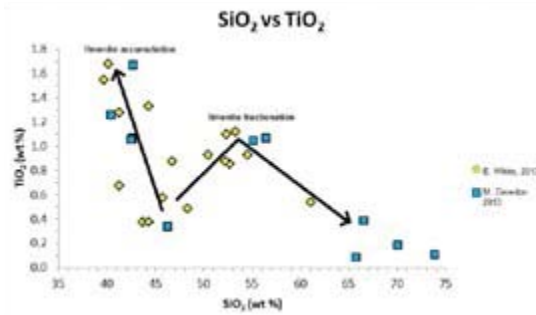
Seventeen samples were acquired from the Kern Plateau. Of those seventeen, three samples from the Summit Gabbro suite proved to be primitive enough for further analyses. Samples Fr-119A, Fr-119B, and Fr-120C (Figures 4 and 5) had Mg-numbers of 76.32, 74.33, and 69.33 respectively, which are all within the compositional range for mantle-derived olivines. Not far below the Fo_{65} threshold were samples Fr-121B and Fr-123A with Mg-numbers of 63.14 and 64.02 respectively. Upon petrographic analysis, however, Fr-119A and Fr-119B were determined to have undergone secondary alteration. Therefore these two samples were not appropriate for the study. A complete data table for all samples is located in Appendix II.

Harker Diagrams

The Harker diagrams display that the chemical variation within the Summit Gabbro is consistent with magmas evolving along similar differentiation paths. Their chemical variation paths are also consistent with fractional crystallization. Ilmenite (TiO_2) begins fractionating at 53% SiO_2 (Graph 1), and the iron-rich minerals, such as magnetite and amphiboles, started at about 54% SiO_2 (Graph 2). Similarly olivine (MgO) appears to begin crystallizing from earliest stages (48%) with the lower Si rocks possibly indicating that various amounts of olivine and plagioclase accumulation and fractionation occurred

(Graph 3). Beginning at about 48% SiO_2 , Al_2O_3 and CaO both decreased in SiO_2 (Graphs 4 and 5). These trends likely indicate fractionation of plagioclase began early during the magma crystallization process along with olivine. In graph 6, apatite does not appear to fractionate before the differentiating system reached approximately 55% SiO_2 . Lastly Graphs 7 and 8 display increases in $K_2O\%$ and $Na_2O\%$ as $SiO_2\%$ increases; greater variation at high $K_2O\%$ and $SiO_2\%$ values is likely due to fractionation and accumulation of potassium feldspar.

Additional detail is revealed by plotting $Na_2O\%$ against the differentiation index Mg-number (Fig. 10). The relationship between Mg-number and sodium content suggests that the Summit Gabbros evolved along two different trends, which diverge at a Mg# of about 60. The samples on the low-Na branch contain low amounts of SiO_2 : for example, sample Fr-114A contains as little as 39.51% SiO_2 (Table 6). These low-Na samples are likely cumulates of Ca-rich plagioclase and hornblende (note that hornblende is composed of less than 1.5% Na_2O). The samples on the high-Na trend, however, contain the greatest percentages of SiO_2 , with samples Fr-105 and Fr-106 both having SiO_2 contents of nearly 70% (Table 6). The high-Na branch likely represents the liquid line of descent, while the lower trend may be indicative of accumulated hornblende-anorthite gabbros.



Graphs 1-8: Harker diagrams for elements titanium, iron, magnesium, aluminum, calcium, phosphate, potassium, and sodium, respectively.

Table 2: Summary of SEM analysis of Fr-120C; Weight %

Olivine (n=8)									
	SiO2	TiO2	Al2O3	Fe2O3	MnO	MgO	CaO	Na2O	K2O
High Mg	17.99	0	0	19.64	0	21.85	0	0	0
Low Mg	31.88	0	0	1.27	0	18.18	0	0	0
Average	24.93	0	0	10.46	0	20.02	0	0	0
Amphibole (n=11)									
	SiO2	TiO2	Al2O3	Fe2O3	MnO	MgO	CaO	Na2O	K2O
High Mg	22.22	0.41	4.52	9.03	0.01	15.05	3.74	0.53	0.17
High Ca	22.96	0.81	3.45	6.20	0	8.56	14.20	0.57	0.18
High Fe	19.78	0.26	2.34	32.05	0	4.17	2.98	0.28	0.09
Average	21.65	0.49	3.44	15.76	0	9.26	6.97	0.46	0.15

Table 3: Summary of SEM analysis of Fr-120A; Weight %

Plagioclase (n=3)									
	SiO2	TiO2	Al2O3	Fe2O3	MnO	MgO	CaO	Na2O	K2O
High Ca	21.90	0	17.68	0	0	0	13.17	0.99	0
Low Ca	26.32	0	14.53	0	0	0	7.88	3.87	0
Average	24.11	0	16.11	0	0	0	10.53	2.43	0
Amphibole (n=3)									
	SiO2	TiO2	Al2O3	Fe2O3	MnO	MgO	CaO	Na2O	K2O
High Mg	0	0	0	0	0	0	0	0	0
High Ca	21.07	0.98	6.93	8.65	0	8.46	9.15	1.45	0.22
High Fe	19.90	1.11	7.33	12.44	0	8.31	7.29	0.88	0.48
Average	31.02	1.05	7.13	10.55	0	8.39	8.22	1.16	0.35

Table 4: Summary of SEM analysis of Fr-120D; Weight %

Plagioclase (n=8)									
	SiO2	TiO2	Al2O3	Fe2O3	MnO	MgO	CaO	Na2O	K2O
High Ca	21.69	0	17.75	0.26	0	0	13.23	0.91	0
Low Ca	26.28	0	14.62	0	0	0	7.97	3.70	0
Average	23.99	0	16.19	0.13	0	0	10.6	2.31	0

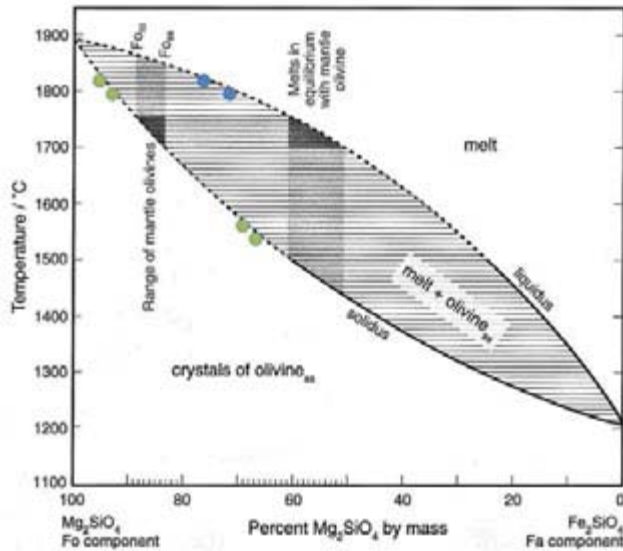


Table 5: Magnesium-number of individual olivine grains in sample Fr-120C

68.85355
68.3784
68.32296
68.05235
70.38926
97.45416
95.3691
96.91799

Figure 5: Olivine crystals from Fr-120C plotted by Mg-number.

SEM Data

Samples Fr-120A, Fr-120C, and Fr-120D were analyzed using SEM because of the presence of mafic minerals found in the hand samples (Tables 2-4). The whole-rock composition of Fr-120D was not determined with XRF. The Mg-numbers of the olivine crystals in Fr-120C were also calculated (Table 5).

Interpretation

The SEM data collected for this project showed evidence that sample Fr-120C may contain olivine crystals that were in equilibrium with mantle-derived magmas, which range in composition between Fo₈₈-Fo₉₂. The analyzed crystals plotted just above or below this range. Unfortunately the data provided no further evidence for the diverging Mg#-Na₂O trends since these samples all have high Mg-numbers. The relationship between Na₂O and Mg#, however, seem to be affected by the amount of Fe₂O₃, which may be associated with the fractionation of amphibole minerals.

Conclusion

Sample Fr-120C appears to be a promising target for future studies of mantle-derived magmas. For example, hafnium and oxygen isotopic analysis of zircons separated from rocks associated with Fr-120C may help determine whether or not the Mesozoic mantle beneath the eastern Sierra Nevada Mountains was enriched or depleted. Also, future SEM analysis of minerals from the low Mg-number rocks may better reveal the nature of the high-Na and low-Na trends.

Acknowledgments

This research project would not be possible with the generous ASI Research Grant I received from California State University or without the assistance of the my classmates and friends Natalie Hollis, Ryan Santos, Aaron Case, Chris Johnson, Matthew Hutchinson, and Ryck Daniels.

I would also like to give special thanks to Michelle Gevedon who helped me plan and organize my project in its beginning stages as well to my thesis advisor Dr. Diane Clemens- Knott for her guidance and knowledge through the end.

References

- Coleman, D.S., Glazner, A.F. and Frost, T.P., 1992, Evidence from the Laramack Granodiorite for Rapid Late Cretaceous Crust Formation in California: *Science*, v.258, n. 5090, p. 1924-1926.
- DePaolo, D.J., 1980, Sources of continental crust: Neodymium isotope evidence from the Sierra Nevada and Peninsular Ranges: *Science* v. 209, p. 684-687.
- Gevedon, Michelle, 2013, Paired oxygen and hafnium isotopic analysis on zircon from gabbros: identifying potential Mesozoic mantle heterogeneity of the Sierra Nevada Arc: MS thesis. California State University, Fullerton; California.
- Gill, Robin, 2012, *Igneous Rocks and Processes: A Practical Guide*, edition 1: Chichester, U.K.
- Moore, J. G., 2000, *Exploring the highest Sierra*. Stanford, California. Stanford University Press.
- Winter, J.D., 2010, *Principles of igneous and metamorphic petrology*, 2nd edition, Upper Saddle River, New Jersey.

Appendix

Appendix I. GPS Locations

Sample Number	UTM	Easting	Northing	Accuracy (m)
FR-110	11S	0391281	3990152	±5.18
FR-111	11S	0392229	4004007	±6.71
FR-112	11S	0392950	4004545	±5.49
FR-113	11S	0393667	4006184	±8.84
FR-114A	11S	0395107	4007496	±5.49
FR-115	11S	0395270	4006114	±4.57
FR-116A	11S	0395366	4003614	±5.18
FR-117	11S	0395366	4003614	±5.18
FR-119A	11S	0385260	4003333	±25.30
FR-119B	11S	0385260	4003333	±25.30
FR-120A	11S	0385636	4001017	±26.52
FR-120B	11S	0385636	4001017	±26.52
FR-120C	11S	0385636	4001017	±26.52
FR-120D	11S	0385636	4001017	±26.52
FR-121A	11S	0386802	3994621	±5.49
FR-121B	11S	0386802	3994621	±5.49
FR-123A	11S	0416304	3966966	±5.79
FR-123B	11S	0416304	3966966	±5.79

Table 1: GPS locations for sample analyzed with XRF.

Appendix I. GPS Locations

Sample name	SiO ₂ (%) Si	TiO ₂ (%) Ti	Al ₂ O ₃ (%) Al	Fe ₂ O ₃ (%) Fe	MgO (%) Mg	MnO (%) Mn	CaO (%) Ca	K ₂ O (%) K	Na ₂ O (%) Na	P ₂ O ₅ (%) P	SO ₃ (%) S
FR-102	42.56	1.06	18.13	14.42	6.71	0.16	12.77	0.34	1.62	0.16	0.01
FR-102	42.59	1.07	18.15	14.43	6.72	0.16	12.78	0.34	1.62	0.16	0.01
FR-102A	42.42	1.06	18.06	14.60	6.67	0.16	12.73	0.34	1.64	0.16	0.02
FR-102A	42.47	1.06	18.1	14.62	6.69	0.16	12.76	0.34	1.64	0.16	0.02
FR-100	46.24	0.34	18.36	8.91	11.62	0.15	14.01	0.07	0.97	0.02	0.02
FR-100	46.20	0.34	18.35	8.90	11.6	0.15	14.00	0.07	0.97	0.02	0.02
FR-103	40.34	1.26	19.48	12.75	6.84	0.11	11.16	0.77	1.67	0.04	0.01
FR-103	40.42	1.26	19.52	12.75	6.83	0.11	11.18	0.77	1.68	0.04	0.01
FR-105	69.99	0.19	14.75	1.95	0.54	0.06	2.08	4.38	3.23	0.07	0
FR-106	66.46	0.39	15.32	4.16	1.44	0.09	3.51	4.28	3.16	0.18	-0.03
FR-107A	55.06	1.05	16.27	7.79	2.40	0.16	5.65	1.99	3.66	0.39	-0.06
FR-107B	56.38	1.07	16.64	8.21	2.46	0.16	5.81	2.02	3.69	0.39	-0.08
FR-108A	73.80	0.11	12.28	0.70	0.12	0.01	0.78	4.68	3.21	0.03	-0.01
FR-108B	65.72	0.09	11.02	0.59	0.12	0.01	0.68	4.07	3.00	0.02	-0.01
FR-110	54.47	0.93	18.12	8.29	3.43	0.17	7.08	1.88	3.25	0.30	-0.09
FR-111	46.69	0.88	19.91	9.08	5.93	0.17	12.18	0.79	2.35	0.23	-0.06
FR-112	52.26	1.10	16.93	9.89	3.61	0.19	7.16	1.88	3.17	0.39	-0.10
FR-113	50.37	0.93	16.78	10.44	5.82	0.17	8.85	1.30	2.68	0.34	-0.07
FR-114A	39.61	1.55	17.29	17.5	5.93	0.17	12.25	0.28	1.44	0.10	0.08
FR-119A	48.25	0.49	12.57	8.00	13.01	0.18	12.37	0.86	0.67	0.03	-0.03
FR-119B	45.70	0.58	7.60	10.93	15.97	0.17	13.55	0.29	0.55	0.08	-0.02
FR-120A	41.20	1.28	21.85	10.01	6.57	0.11	13.16	0.44	1.53	0.03	0
FR-120B	40.05	1.68	18.72	13.48	8.32	0.17	12.18	0.44	1.41	0.07	-0.01
FR-120C	41.21	0.68	13.48	14.12	16.10	0.19	9.01	0.20	0.67	0.04	-0.03
FR-121A	43.67	0.38	24.86	7.20	5.20	0.08	12.29	0.69	1.59	0.08	-0.03
FR-121B	44.24	0.38	25.58	6.19	5.35	0.08	12.97	0.75	1.49	0.07	-0.04
FR-123A	44.26	1.33	12.44	12.52	11.24	0.22	11.57	0.44	1.36	0.06	-0.02
FR-123B	61.02	0.54	16.17	4.74	1.79	0.09	4.32	3.55	3.30	0.20	-0.07
FR-115	53.24	1.12	16.81	9.56	4.46	0.18	7.66	1.92	3.07	0.42	-0.10
FR-116A	52.61	0.86	15.8	9.31	6.77	0.17	9.47	1.41	2.28	0.14	-0.04
FR-117	52.14	0.88	15.86	9.36	6.70	0.17	9.00	1.49	2.27	0.17	-0.06

Table 6: XRF data for all samples.

Table 6: Summary of SEM analysis of Fr-120C; Atomic %

Olivine (n=8)									
	Si	Ti	Al	Fe	Mn	Mg	Ca	Na	K
High Mg	14.49	0	0	7.95	0	20.20	0	0	0
Low Mg	22.95	0	0	0.46	0	15.12	0	0	0
Average	18.72	0	0	4.21	0	17.66	0	0	0
Amphibole (n=11)									
	Si	Ti	Al	Fe	Mn	Mg	Ca	Na	K
High Mg	18.13	0.49	3.95	2.94	0	8.46	4.91	1.12	0.26
High Ca	19.29	0.21	1.28	1.84	0	7.92	9.43	0.39	0
High Fe	17.83	0	1.28	17.42	0	3.29	0.95	0	0.05
Average	18.42	0.23	2.17	7.40	0	6.56	5.10	0.50	0.10

Table 7: Summary of SEM analysis of Fr-120A; Atomic %

Plagioclase (n=3)									
	Si	Ti	Al	Fe	Mn	Mg	Ca	Na	K
High Ca	16.60	0	13.95	0	0	0	6.99	0.91	0
Low Ca	19.51	0	11.21	0	0	0	4.09	3.50	0
Average	18.06	0	12.58	0	0	0	5.54	2.21	0
Amphibole (n=3)									
	Si	Ti	Al	Fe	Mn	Mg	Ca	Na	K
High Mg	16.67	0.13	5.39	4.25	0	7.08	4.92	1.17	0.24
High Ca	16.59	0.45	5.68	3.43	0	7.70	5.05	1.40	0.13
High Fe	15.22	0.40	6.85	5.78	0	8.30	3.26	0.76	0.31
Average	16.16	0.33	5.97	4.49	0	7.69	4.41	1.11	0.23

Table 8: Summary of SEM analysis of Fr-120D; Atomic %

Plagioclase (n=8)									
	Si	Ti	Al	Fe	Mn	Mg	Ca	Na	K
High Ca	16.47	0	14.02	0.50	0	0	7.04	0.84	0
Low Ca	19.50	0	11.29	0	0	0	4.14	3.35	0
Average	17.99	0	12.66	0.50	0	0	5.59	2.10	0

Did Alpine Glaciers Exist on Sugarloaf Mountain During the Last Glacial (San Bernardino Mountains, California)?

Department of Geological Sciences, California State University, Fullerton

Alex Woodward

Abstract

Paleoclimatic research has shown that there have been four periods of alpine glaciation in the mountain ranges of Southern California during the last 22,000 years (Owen et al., 2003). The best examples of glaciation occur along the north facing lopes of Mt San Gorgonio within the San Bernardino Mountains. These sites of Alpine glaciation all share two key characteristics: 1) a minimum glaciation height of more than 9000' above sea level; and 2) a north or northeast facing slope. Sugarloaf Mountain of the San Bernardino Mountains is located approximately seven miles north of Mt San Gorgonio and shares these two key characteristics. It is hypothesized that an alpine glacier or a rock glacier occupied the north facing slope of Sugarloaf Mountain. To test this hypothesis, a field research project is proposed. This project will involve: a) extensive field mapping; b) a comparison of modern precipitation between the two sites; and c) direct subsurface temperature measurements. Features particular to alpine glaciation will be mapped with GPS, photographed, and described. Potential features include moraines, erratics, and striations. Subsurface temperature measurements will be taken within the talus of the north slope to help determine if glacial growth was possible during the colder climate of the last glacial. If the hypothesis is proven correct, future research separate from this project may include cosmogenic dating of specific glacial features. Evidence of glaciation, or lack thereof, will increase the knowledge of the past hydroclimatic conditions during the last glacial.

Galois Groups of Special Degree Four Polynomials

Department of Mathematics, California State University, Fullerton

Christopher Bang and Joseph Chavoya

Abstract

We study the Galois groups of a special class of degree four polynomials, namely those that are of the form

$$f(x) = x^4 + ax^3 + bx^2 + apx + p^2,$$

where p is some prime number, and a and b are integers that satisfy the inequalities

$$|a| \leq 4\sqrt{p} \quad \text{and} \quad 2|a|\sqrt{p} - 2p \leq b \leq \frac{a^2}{4} + 2p.$$

These polynomials (which we call p -Weil polynomials) arise in number theory from the study of solutions to certain congruences. In this article, we develop simple criteria for determining the irreducibility and the Galois groups of p -Weil polynomials over \mathbb{Q} . We apply the criteria to investigate how these properties vary amongst all p -Weil polynomials as the prime p grows to infinity.

1. Introduction

Let p be a prime number. Define a p -Weil polynomial of degree four to be a polynomial of the form $f_{a,b}(x) = x^4 + ax^3 + bx^2 + apx + p^2 \in \mathbb{Z}[x]$ such that

$$|a| \leq 4\sqrt{p} \quad \text{and} \quad 2|a|\sqrt{p} - 2p \leq b \leq \frac{a^2}{4} + 2p.$$

The study of p -Weil polynomials arises in number theory from examining certain congruences; for instance when counting solutions to congruences of the form

$$y^2 \equiv h(x) \pmod{p}$$

for polynomials $h(x) \in \mathbb{Z}[x]$ of degree of five or six where $h(x)$ does not have repeated roots in \mathbb{C} . Our interest in p -Weil polynomials is mainly involved with studying characteristics such as irreducibility and corresponding Galois groups. We have developed a means of determining irreducibility over \mathbb{Q} (Corollary 3.2), as well as a means of determining the Galois group of irreducible p -Weil polynomials (Theorem 4.1) based on the numbers a , b , and p . While these theorems are simple to apply to individual polynomials, it becomes more difficult to characterize general properties of the entire collection of p -Weil polynomials. Despite this, certain characteristics can be shown; for example, we show that as the prime p approaches infinity, the proportion of those p -Weil polynomials that are irreducible tends towards 1 (Theorem 5.1).

2. Preliminary Results

Define R_p to be the closed region $R_p \subset \mathbb{R}^2$ bounded by the curves $y = 2|x|\sqrt{p} - 2p$ and $y = \frac{x^2}{4} + 2p$ as below:

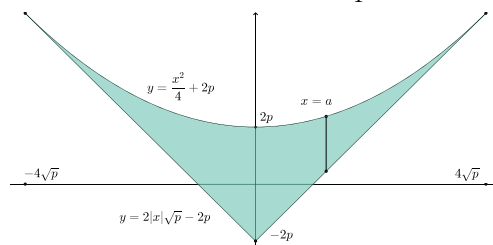


Figure 1: The region R_p corresponding to bounds induced by our definition of a p -Weil polynomial.

Recall that a lattice point in \mathbb{R}^2 is defined as a point with integer coordinates. We note by our definition of p -Weil polynomials that there is a bijective correspondence between the lattice points of R_p and the p -Weil polynomials $f_{a,b}(x)$.

The following Lemma will be used in proving

Proposition 2.2:

Lemma 2.1.

Given $x, y \in \mathbb{R}$, x and y will satisfy $|x - y| + |x + y| = 2 \max\{|x|, |y|\}$.

Proof. Let $x, y \in \mathbb{R}$ and without loss of generality suppose $x < y$ (note that the case in which $x = y$ is trivial, since $|x - y| + |x + y| = 0 + 2x = 2y = 2 \max\{|x|, |y|\}$). Since $x < y$, it follows that $x - y < 0$. Hence, $|x - y| = -(x - y)$. If $x \geq -y$, then it also follows that $x + y \geq 0$. Thus, since $-y \leq x < y$, it follows that $\max\{|x|, |y|\} = y$, and

$$\begin{aligned} |x - y| + |x + y| &= -(x - y) + (x + y) \\ &= 2y \\ &= 2 \max\{|x|, |y|\}. \end{aligned}$$

If on the other hand $x < -y$, then $x + y < 0$, and $y < x$. Thus, since $x < y < -x$, it follows that $\max\{|x|, |y|\} = -x$, and

$$\begin{aligned} |x - y| + |x + y| &= -(x - y) - (x + y) \\ &= 2(-x) \\ &= 2 \max\{|x|, |y|\}. \end{aligned}$$

Thus, $|x - y| + |x + y| = 2 \max\{|x|, |y|\}$, as needed. \square

The following Proposition (as well as its proof) are closely modeled upon [2, Lemma 3.1]:

Proposition 2.2.

A monic polynomial $f(x) \in \mathbb{Z}[x]$ of degree four is a p -Weil polynomial if and only if all roots of f have complex absolute value \sqrt{p} and if the constant term of f is equal to p^2 .

Proof. Suppose $f(x)$ is a monic polynomial of degree four in $\mathbb{Z}[x]$, whose roots have absolute value \sqrt{p} and whose constant term is equal to p^2 . Hence, we have that either

$f(x)$ will have four real roots, two real roots and two non-real roots, or four non-real roots r_1, r_2, r_3, r_4 each satisfying $|r_i| = \sqrt{p}$. Note that any real roots that satisfy $|r_i| = \sqrt{p}$ will be of the form $r_i = \pm\sqrt{p}$.

Case 1: Since the constant term of f must be p^2 , if all four roots are real, we have either $r_1 = r_2 = \sqrt{p}$ but $r_3 = r_4 = -\sqrt{p}$, or $r_1 = r_2 = r_3 = r_4 = \pm\sqrt{p}$. If $r_1 = r_2 = \sqrt{p}$ but $r_3 = r_4 = -\sqrt{p}$, then f may be simplified to $f(x) = (x - \sqrt{p})^2 (x + \sqrt{p})^2 = (x^2 - p)^2 = x^4 - 2px + p^2$, which is a p -Weil polynomial. Furthermore, $|a| = |0| \leq 4\sqrt{p}$, and $-2p \leq b = -2p \leq 2p$, as needed. If $r_1 = r_2 = r_3 = r_4 = \pm\sqrt{p}$, then $f(x) = x^4 \pm 4\sqrt{p}x^3 + 6px^2 \pm 4p\sqrt{p}x + p^2$. Certainly this satisfies $|a| = 4\sqrt{p} \leq 4\sqrt{p}$, and $6p \leq b = 6p \leq 6p$, however $4\sqrt{p}$ will not be an integer. Hence, $f(x)$ will not be a monic polynomial of degree four in $\mathbb{Z}[x]$, a contradiction. This exhausts the cases in which f has all four real roots.

Case 2: Suppose f has two real roots and two non-real roots. Without loss of generality, suppose $r_1, r_2 \in \mathbb{R}$, $r_3, r_4 \notin \mathbb{R}$, and $r_4 = \bar{r}_3$. It follows that

$$\begin{aligned} f(x) &= (x - r_1)(x - r_2)(x - r_3)(x - r_4) \\ &= x^4 - (r_1 + r_2 + r_3 + r_4)x^3 + (r_1r_2 + r_1r_3 \\ &\quad + r_1r_4 + r_2r_3 + r_2r_4 + r_3r_4)x^2 - (r_1r_2r_3 \\ &\quad + r_1r_2r_4 + r_1r_3r_4 + r_2r_3r_4)x + (r_1r_2r_3r_4). \end{aligned}$$

Since the only real numbers that will have absolute value \sqrt{p} will be $\pm\sqrt{p}$, then either $r_1 = r_2 = \pm\sqrt{p}$ or $r_1 = -r_2 = \pm\sqrt{p}$.

Case 2.1: In the event that $r_1 = r_2 = \pm\sqrt{p}$, it follows that

$$a = -(r_1 + r_2 + r_3 + r_4) = \mp 2\sqrt{p} - (r_3 + r_4),$$

while

$$b = 2p \pm 2\sqrt{p}(r_3 + r_4).$$

Ergo, we have that $\mp 2\sqrt{p}a - 2p = b$. Since $b \in \mathbb{Z}$, this implies that $2\sqrt{p}a \in \mathbb{Z}$. Since $\sqrt{p} \notin \mathbb{Q}$, this implies that $a = 0$, and hence $b = -2p$. Because

$$\begin{aligned} (r_1r_2r_3 + r_1r_2r_4 + r_1r_3r_4 + r_2r_3r_4) = \\ (r_1 + r_2 + r_3 + r_4)p = ap = 0, \end{aligned}$$

we have that $f(x) = x^4 - 2px^2 + p^2 = (x^2 - p)^2$, which has four real roots, a contradiction.

Case 2.2: In the event that $r_1 = -r_2 = \pm\sqrt{p}$, it follows that the constant term $(r_1r_2r_3r_4) = -p \cdot p = -p^2$, a contradiction.

Case 3: If f has four non-real roots, then the roots will be permuted by complex conjugation. Suppose without loss of generality that $r_1 \cdot r_2 = r_3 \cdot r_4 = p$.

Thus, f can be written in the form

$$\begin{aligned} f(x) &= (x - r_1)(x - r_2)(x - r_3)(x - r_4) \\ &= x^4 + ax^3 + bx^2 + apx + p^2, \end{aligned}$$

where $a, b \in \mathbb{Z}$. Note that $|a| = |-(r_1 + r_2 + r_3 + r_4)| \leq |r_1| + |r_2| + |r_3| + |r_4| = 4\sqrt{p}$. Now consider the function $g(x) = x^2 + ax + (b - 2p)$ with real roots $\pi_1 = r_1 + r_2$ and $\pi_2 = r_3 + r_4$. Since g has real roots, it must have discriminant $0 \leq a^2 - 4b + 8p$. Hence, $b \leq \frac{a^2}{4} + 2p$. To see that $2|a|\sqrt{p} - 2p \leq b$, note that $|\pi_1 - \pi_2| + |\pi_1 + \pi_2| = 2 \max\{|\pi_1|, |\pi_2|\} \leq 4\sqrt{p}$ (Lemma 2.1), $|\pi_1 - \pi_2|^2 = a^2 - 4b + 8p$ and $|\pi_1 + \pi_2| = |a|$, which results with

$$\begin{aligned} 4b &= a^2 + 8p - |\pi_1 - \pi_2|^2 \\ &\geq a^2 + 8p - (4\sqrt{p} - |\pi_1 + \pi_2|)^2 \\ &= a^2 + 8p - (4\sqrt{p} - |a|)^2 \\ &= a^2 + 8p - (-8\sqrt{p}|a| + 16p + |a|^2) \\ &= a^2 + 8p + 8\sqrt{p}|a| - 16p - |a|^2 \\ &= 8\sqrt{p}|a| - 8p. \end{aligned}$$

Rewriting this, we have that $2|a|\sqrt{p} - 2p \leq b$, as needed.

Conversely, suppose $f(x) = x^4 + ax^3 + bx^2 + apx + p^2$ is a p -Weil polynomial. Let

$$\pi_1 = -\frac{a}{2} + \sqrt{\frac{a^2}{4} - b + 2p}$$

and

$$\pi_2 = -\frac{a}{2} - \sqrt{\frac{a^2}{4} - b + 2p}.$$

Note that since f is a p -Weil polynomial, it follows that $\pi_1, \pi_2 \in \mathbb{R}$. Then, one may check that f factors \mathbb{R} as follows:

$$\begin{aligned} f(x) &= x^4 + ax^3 + bx^2 + apx + p^2 \\ &= (x^2 - \pi_1x + p)(x^2 - \pi_2x + p). \end{aligned}$$

Let $g(x) = x^2 - \pi_1x + p$ and $h(x) = x^2 - \pi_2x + p$. Note that $|\pi_1 - \pi_2|^2 = a^2 - 4b + 8p$ and $|\pi_1 + \pi_2| = |a|$. Hence,

$$\begin{aligned} a^2 + 8p - |\pi_1 - \pi_2|^2 &= 4b \\ &\geq 8\sqrt{p}|a| - 8p \\ &\geq a^2 + 8p - (4\sqrt{p} - |\pi_1 + \pi_2|)^2 \end{aligned}$$

implies that $|\pi_1 - \pi_2|^2 \leq (4\sqrt{p} - |\pi_1 + \pi_2|)^2$. Since $|\pi_1 + \pi_2| = |a|$, $4\sqrt{p} - |\pi_1 + \pi_2|$ will be non-negative, and hence $|\pi_1 - \pi_2| \leq (4\sqrt{p} - |\pi_1 + \pi_2|)$. Thus, by Lemma 2.1,

$$2 \max\{|\pi_1|, |\pi_2|\} = |\pi_1 - \pi_2| + |\pi_1 + \pi_2| \leq 4\sqrt{p}.$$

In particular, this implies that $|\pi_1| \leq \max\{|\pi_1|, |\pi_2|\} \leq 2\sqrt{p}$. Since $g(x)$ has discriminant $\pi_1^2 - 4p$ and $|\pi_1| \leq 2\sqrt{p}$, it follows that either g has one real root (in the case that $\pi_1 = \pm 2\sqrt{p}$) or that g has two distinct non-real roots.

Case 1: If $\pi_1 = \pm 2\sqrt{p}$, then by the quadratic formula, g has a single root, namely $\pm\sqrt{p}$.

Case 2: If $|\pi_1| < 2\sqrt{p}$, then g has two distinct non-real roots, say r_1 and r_2 . Then,

$$|r_1|^2 = |r_2|^2 = r_2\bar{r}_2 = r_1r_2 = p.$$

So, $|r_1| = |r_2| = \pm\sqrt{p}$

In either case, any root of g must have an absolute value of \sqrt{p} . Since a similar proof can be used to show that the roots of h have an absolute value of \sqrt{p} , it follows that the roots of f have an absolute value of \sqrt{p} , as needed. \square

3. An Irreducibility Criterion for p -Weil Polynomials

We now develop a simple method of determining whether a p -Weil polynomial $f_{a,b}$ is irreducible in terms of a , b , and p .

Theorem 3.1. *Let $f_{a,b}(x)$ be a p -Weil polynomial. Let $Q_1 = a^2 - 4(b - 2p)$. Then $f_{a,b}(x)$ is irreducible over \mathbb{Q} if and only if $\sqrt{Q_1} \notin \mathbb{Z}$, and either $a \neq 0$ or $\sqrt{-(b + 2p)} \notin \mathbb{Z}$.*

Proof. Suppose first that $f_{a,b}(x)$ is reducible over \mathbb{Q} ; then either $f_{a,b}(x)$ has a linear factor over \mathbb{Q} , or $f_{a,b}(x)$ splits into two irreducible quadratics over \mathbb{Q} . If $f_{a,b}(x)$ has a linear factor, then by the rational root test there are roots of the form $r \in \{\pm 1, \pm p, \pm p^2\}$. However, since $|r| = \sqrt{p}$ from Proposition 2.2, this is a contradiction. So there are no factors of degree one over \mathbb{Q} .

This implies $f_{a,b}(x)$ splits into two monic irreducible quadratics over \mathbb{Q} , represented as:

$$f_{a,b}(x) = (x^2 + mx + n)(x^2 + kx + l)$$

where each coefficient is an integer. Expanding the equation yields

$$f_{a,b}(x) = x^4 + x^3(k + m) + x^2(l + mk + n) + x(ml + kn) + nl.$$

Comparing the coefficients of the right side, $f_{a,b}(x)$ yields the following relations:

$$\begin{aligned} k + m &= a \\ l + mk + n &= b \\ ml + kn &= pa \\ nl &= p^2. \end{aligned}$$

Since $nl = p^2$ and $l, n \in \mathbb{Z}$ then $n = l = \pm p$ (note that we may exclude all other possibilities since all roots satisfy $|r_i| = \sqrt{p}$ by Proposition 2.2). Substituting $k = m - a$ and $l = n$ yields:

$$p^2 + n^2 - nm^2 - bn + mna = 0 \quad (1)$$

$$mp^2 + an^2 - mn^2 - apn = 0. \quad (2)$$

Since $n = \pm p$, we have two cases:

Case 1: If $n = p$, then equation (2) yields $0 = 0$, and hence gives no information.

Equation (1) becomes

$$m^2 - ma + (b - 2p) = 0.$$

Since m is an integer, this implies that the quadratic equation yields an integer solution. This occurs only when the discriminant $Q_1 := a^2 - 4(b - 2p)$ is a square integer. Thus, we conclude in this case that $a^2 - 4(b - 2p)$ is a square.

Case 2: If $n = -p$, then equation (2) simplifies to $a = 0$, while equation (1) yields

$$m^2 - m(0) + (b + 2p) = 0.$$

Similar to the previous case, the fact that m is an integer implies the discriminant $Q_1 := -4(b + 2p)$ is an even square. Thus, we conclude in this case that $a = 0$ and $-(b + 2p)$ is a square.

Hence if $f_{a,b}(x)$ is reducible, then either $a^2 - 4(b - 2p)$ is a square, or $a = 0$ and $-(b + 2p)$ is a square. For the other direction of the proof, we have two cases.

Case 1: Suppose $Q_1 = a^2 - 4(b - 2p)$ is a square. Define the number m as:

$$m := \frac{a + \sqrt{a^2 - 4(b - 2p)}}{2} = \frac{a + \sqrt{Q_1}}{2}.$$

Note that

$$Q_1 \equiv a^2 \pmod{4}$$

and hence m is an integer. Then one may check (essentially by reversing the steps in the work above) that the following explicit factorization holds true:

$$f_{a,b}(x) = (x^2 + mx + p)(x^2 + (a - m)x + p).$$

So in this case, $f_{a,b}(x)$ is reducible.

Case 2: Suppose $a = 0$ and $\sqrt{-(b+2p)} \in \mathbb{Z}$ for some integer b and prime p . Define the number m' as

$$m' := \frac{\sqrt{-4(b+2p)}}{2} = \sqrt{-b-2p}.$$

Since the quantity $-(b+2p)$ is a square, m' is an integer. Then, one may check that the following explicit factorization holds:

$$f_{a,b}(x) = (x^2 + m'x - p)(x^2 + (a - m')x - p).$$

So in this case, $f_{a,b}(x)$ is reducible.

Therefore, $f_{a,b}(x)$ is reducible if and only if either $a^2 - 4(b-2p)$ is a square, or $a = 0$ and $-(b+2p)$ is a square. \square

In particular, we note that $f_{a,b}(x) = x^4 - 2px^2 + p^2 = (x^2 - p)^2$ is a reducible p -Weil polynomial such that Q_1 is not a square. This polynomial corresponds to the lattice point $(0, -2p)$ (this is the bottom-most point in R_p). For the p -Weil polynomial corresponding to any other lattice point in R_p , we obtain the following (simpler) statement:

Corollary 3.2. Let $f_{a,b}(x) \neq x^4 - 2px^2 + p^2$ be a p -Weil polynomial. Let $Q_1 = a^2 - 4(b-2p)$. Then $f_{a,b}(x)$ is irreducible over \mathbb{Q} if and only if $\sqrt{Q_1} \notin \mathbb{Z}$.

Proof. Since $f_{a,b}(x) \neq x^4 - 2px^2 + p^2$, it follows that either $a \neq 0$ or $a = 0$ and $b \neq -2p$. If $a \neq 0$, then it follows that $a \neq 0$ or $-(b+2p)$ is not a square, as needed. Suppose instead that $a = 0$ and $b \neq -2p$. Referring back to R_p , we have that if $a = 0$, then $-2p \leq b \leq 2p$. Hence, $-(b+2p) \leq 0$. If $-(b+2p) = 0$, it follows that $b = -2p$, a contradiction. Thus, $-(b+2p) < 0$, and so $-(b+2p)$ is not a square.

In either case, $f_{a,b}(x) \neq x^4 - 2px^2 + p^2$ implies that either $a \neq 0$ or that $-(b+2p)$ is not a square, as needed. \square

Example 3.3. Let $g(x) = x^4 - 6x^2 + 25$. Since $\sqrt{0 - 4(6 - 2 \cdot 5)} = \sqrt{16} = 4 \in \mathbb{Z}$, it follows that $g(x)$ is reducible over \mathbb{Q} . In fact, it is easy to check that

$$g(x) = (x^2 - 4x + 5)(x^2 + 4x + 5).$$

Example 3.4. Let $f_{a,b}(x) = x^4 + 12x^3 + 74x^2 + (12 \cdot 199)x + 199^2$. Note that here $a = 12$, $b = 74$, and $p = 199$. Since $\sqrt{12^2 - 4(74 - 2 \cdot 199)} = 12\sqrt{10} \notin \mathbb{Z}$, we conclude that this polynomial is irreducible over \mathbb{Q} .

4. Galois groups of p -Weil polynomials

Now that we have determined a relatively easy method of determining the irreducibility of p -Weil polynomial, we turn to the question of determining the corresponding Galois group of that polynomial.

Theorem 4.1. Let $f_{a,b}(x)$ be a p -Weil polynomial. Let $Q_1 = a^2 - 4(b-2p)$, and let $Q_2 = (b+2p)^2 - 4pa^2$. If $f_{a,b}(x)$ is irreducible over \mathbb{Q} , then the following hold:

- i) If $\sqrt{Q_2} \in \mathbb{Z}$, then the Galois group of $f_{a,b}(x)$ is the Klein group V .
- ii) If $\sqrt{Q_2} \notin \mathbb{Z}$ and $\sqrt{Q_1 Q_2} \in \mathbb{Z}$, then the Galois group of $f_{a,b}(x)$ is the cyclic group C_4 .
- iii) If $\sqrt{Q_2} \notin \mathbb{Z}$ and $\sqrt{Q_1 Q_2} \notin \mathbb{Z}$, then the Galois group of $f_{a,b}(x)$ is the dihedral group D_4 .

Proof. Using the strategy proved in [1] for determining the Galois group of an arbitrary degree four polynomial, we let $r(x) = x^3 - bx^2 + (a^2p - 4p^2)x - (2a^2p^2 - 4bp^2)$ be the cubic resolvent of $f_{a,b}(x)$, and let $g(x) = (x^2 - 2px + p^2)(x^2 + ax + (b-2p))$. We may factor $r(x)$ as

$$r(x) = (x - 2p)(x^2 + (2p - b)x + (pa^2 - 2bp)).$$

Hence, $r(x)$ is always reducible over \mathbb{Q} . Note that $x^2 + (2p - b)x + (pa^2 - 2bp)$ has discriminant

$$Q_2 = b^2 + 4pb + 4p^2 - 4pa^2.$$

Case 1: If Q_2 is a square, then $x^2 + (2p - b)x + (pa^2 - 2bp)$ has roots in \mathbb{Q} . Hence, $x^2 + (2p - b)x + (pa^2 - 2bp)$ is reducible, and $r(x)$ splits into linear factors over \mathbb{Q} . Thus, the Galois Group of $f_{a,b}(x)$ is the Klein group.[1]

Note that If Q_2 is not a square, then $r(x)$ has splitting field $E = \mathbb{Q}(\sqrt{Q_2})$. By Corollary 3.2, we have $f_{a,b}(x)$ is irreducible if and only if Q_1 is not a square in \mathbb{Q} . We have Q_1 is a square in E if and only if $Q_1 = (\alpha + \beta\sqrt{Q_2})^2 = (\alpha^2 + Q_2\beta^2) + 2\alpha\beta\sqrt{Q_2}$ for $\alpha, \beta \in \mathbb{Q}$. Since $\alpha^2 + Q_2\beta^2 \in \mathbb{Q}$, it follows that $2\alpha\beta = 0$. That is, either $\alpha = 0$ or $\beta = 0$. By assumption, Q_1 is not a square in \mathbb{Q} . Hence $\beta \neq 0$, since otherwise $Q_1 = \alpha^2$. If $\alpha = 0$, then $Q_1 = Q_2\beta^2$. Multiplying Q_2 , then $Q_1Q_2 = (Q_2\beta^2)^2$. Hence, Q_1 is a square in $\mathbb{Q}(\sqrt{Q_2})$ if and only if Q_1Q_2 is a square in \mathbb{Q} .

Case 2: If Q_2 is not a square, then $r(x)$ has exactly one root in \mathbb{Q} . Since

$$\begin{aligned} g(x) &= (x^2 - 2px + p^2)(x^2 + ax + (b - 2p)) \\ &= (x - p)^2(x^2 + ax + (b - 2p)), \end{aligned}$$

it follows that $g(x)$ has roots p and $\frac{-a \pm \sqrt{Q_1}}{2}$.

Assuming Q_1Q_2 is a square, then Q_1 is a square in $\mathbb{Q}(\sqrt{Q_2})$, and hence $g(x)$ splits over E . Therefore, the Galois group of $f_{a,b}(x)$ is the cyclic group C_4 by [1].

Case 3: If Q_2 is not a square and Q_1Q_2 is not a square, then Q_1 will not be a square in E , so $r(x)$ has exactly one root in \mathbb{Q} and $g(x)$ does not split over E . Hence, the corresponding Galois Group is the dihedral group D_4 [1].

Example 4.2. Considering the example $f_{a,b}(x) = x^4 + 12x^3 + 74x^2 + (12 \cdot 199)x + 199^2$, we have that since

$$\begin{aligned} \sqrt{Q_2} &= \sqrt{(74 + 2 \cdot 199)^2 - 4 \cdot 199 \cdot 12^2} \\ &= 104\sqrt{10} \notin \mathbb{Z}, \end{aligned}$$

and

$$\begin{aligned} \sqrt{Q_1Q_2} &= \sqrt{Q_1}\sqrt{Q_2} \\ &= \sqrt{(74 + 2 \cdot 199)^2 - 4 \cdot 199 \cdot 12^2} \sqrt{12^2 - 4(74 - 2 \cdot 199)} \\ &= 104\sqrt{10} \cdot 12\sqrt{10} \\ &= 12480 \in \mathbb{Z}, \end{aligned}$$

it follows from Theorem 4.1 that $f_{a,b}(x) = x^4 + 12x^3 + 74x^2 + (12 \cdot 199)x + 199^2$ has Galois group C_4 .

5. Proportion of Irreducible p -Weil Polynomials

Using Theorem 4.1, we have a (comparatively easy) method of characterizing the Galois groups of p -Weil polynomials. Hence, it becomes possible to consider the occurrences of different Galois groups for any fixed prime p . For instance, considering the prime $p = 199$, we generate the following graph:

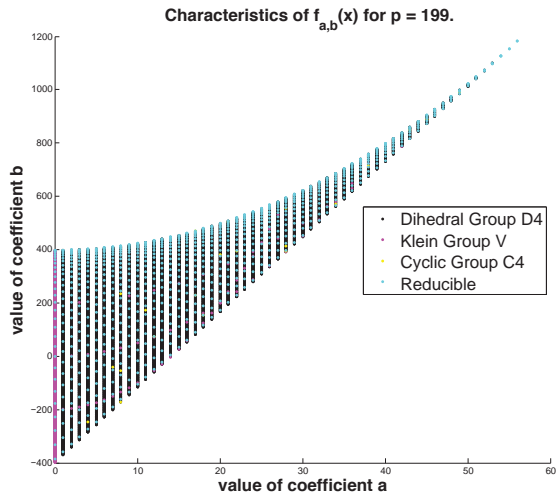


Figure 2: Plot of the occurrences of different Galois groups for the fixed prime $p = 199$.

After observing computer generated data (such as that shown in Figure 2), one observes that as p increases, the proportion of p -Weil polynomials that are irreducible also increases. In fact, using Corollary 3.2 we can prove the following:

Theorem 5.1. *As the prime p approaches infinity, the proportion of irreducible p -Weil polynomials tends to 1.*

Proof. We refer to the lattice point $(a, b) \in R_p$ as being reducible if the polynomial $f_{a,b}$ associated to that point is reducible. Similarly, we refer to the point (a, b) as being irreducible if the polynomial $f_{a,b}$ associated to that point is not reducible. Rather than showing that the number of irreducibles among all p -Weil polynomials tends toward 1, we will show the equivalent statement that the number of reducibles among all p -Weil polynomials tends toward 0.

To show this, note that a p -Weil polynomial $f_{a,b} \neq x^4 - 2px^2 + p^2$ is irreducible if and only if $\sqrt{a^2 - 4(b - 2p)} \notin \mathbb{Z}$ by Corollary 3.2. For a lattice point $(a, b) \in R_p$, we have

$$2|a|\sqrt{p} - 2p \leq b \leq \frac{a^2}{4} + 2p$$

for fixed a (see Figure 2). Note that for positive c there will be exactly $\lceil \sqrt{c} \rceil \leq \sqrt{c} + 1$ square integers in the interval $[0, c]$. Since $0 \leq a^2 - 4(b - 2p) \leq a^2 - 8|a|\sqrt{p} + 16p$, it follows that for $a \geq 0$ there will be at most $\sqrt{a^2 - 8a\sqrt{p} + 16p} + 1 = 4\sqrt{p} - a + 1$ square values of $a^2 - 4(b - 2p)$ attained on the line $x = a$ (for fixed a). Hence, $4\sqrt{p} - a + 1$ forms an upper-bound for the number of reducible points on the line $x = a$. By similar reasoning, there are exactly

$$\begin{aligned} \left\lfloor \frac{a^2}{4} + 2p \right\rfloor - \lceil 2a\sqrt{p} - 2p \rceil + 1 &\geq \left(\frac{a^2}{4} + 2p - 1 \right) - (2a\sqrt{p} - 2p + 1) + 1 \\ &= \frac{a^2}{4} + 4p - 2a\sqrt{p} - 1 \end{aligned}$$

lattice points on the line. Therefore, a lower-bound for the total number of lattice points in R_p along the given line

$x = a$. (for fixed a) will be $\frac{a^2}{4} + 4p - 2a\sqrt{p} - 1$.

Hence,

$$\sum_{a=1}^{4\lfloor \sqrt{p} \rfloor} (4\sqrt{p} - a + 1)$$

will be an upper-bound for the total number of reducible points in R_p for all positive a . Similarly,

$$\sum_{a=1}^{4\lfloor \sqrt{p} \rfloor} \left(\frac{a^2}{4} + 4p - 2a\sqrt{p} - 1 \right)$$

represents a lower-bound for the total number of lattice points for all positive a . Note that by symmetry, an upper-bound for the number of all reducible points in R_p will be

$$(4\sqrt{p} + 1) + 2 \sum_{a=1}^{4\lfloor \sqrt{p} \rfloor} (4\sqrt{p} - a + 1),$$

and a lower-bound for the number of lattice points in R_p will be

$$(4p - 1) + 2 \sum_{a=1}^{4\lfloor \sqrt{p} \rfloor} \left(\frac{a^2}{4} + 4p - 2a\sqrt{p} - 1 \right).$$

Hence, an upper-bound for the proportion of reducible points among all lattice points of R_p will be

$$\frac{(4\sqrt{p} + 1) + 2 \sum_{a=1}^{4\lfloor \sqrt{p} \rfloor} (4\sqrt{p} - a + 1)}{(4p - 1) + 2 \sum_{a=1}^{4\lfloor \sqrt{p} \rfloor} \left(\frac{a^2}{4} + 4p - 2a\sqrt{p} - 1 \right)}.$$

For $n \geq 1$, let

$$B(n) := \frac{(4\sqrt{p} + 1) + 2 \sum_{a=1}^n (4\sqrt{p} - a + 1)}{(4p - 1) + 2 \sum_{a=1}^n \left(\frac{a^2}{4} + 4p - 2a\sqrt{p} - 1 \right)}.$$

Then, for $n \geq 1$, we have

$$\begin{aligned}
B(n) &= \frac{(4\sqrt{p} + 1) + 2 \sum_{a=1}^n (4\sqrt{p} - a + 1)}{(4p - 1) + 2 \sum_{a=1}^n \left(\frac{a^2}{4} + 4p - 2a\sqrt{p} - 1 \right)} \\
&= \frac{(8\sqrt{p} + 2)n - n(n + 1) + 4\sqrt{p} + 1}{\frac{n(n + 1)(2n + 1)}{12} + 2(4p - 1)n - 2\sqrt{p}n(n + 1) + 4p - 1} \\
&= \frac{\frac{1}{12}((96\sqrt{p} + 24)n - 12n(n + 1) + 48\sqrt{p} + 12)}{\frac{1}{12}(2n^3 + (3 - 24\sqrt{p})n^2 + (-23 - 24\sqrt{p} + 96p)n + 48p - 12)} \\
&= \frac{-12n^2 + (96\sqrt{p} + 12)n + 48\sqrt{p} + 12}{2n^3 + (3 - 24\sqrt{p})n^2 + (-23 - 24\sqrt{p} + 96p)n + 48p - 12}.
\end{aligned}$$

Hence, evaluating $B(n)$ at $n = 4 \lfloor \sqrt{p} \rfloor$, we have that

$$B(4 \lfloor \sqrt{p} \rfloor) = \frac{384\sqrt{p} \lfloor \sqrt{p} \rfloor - 192 \lfloor \sqrt{p} \rfloor^2 + 48 \lfloor \sqrt{p} \rfloor + 48\sqrt{p} + 12}{128 \lfloor \sqrt{p} \rfloor^3 + (48 - 384\sqrt{p}) \lfloor \sqrt{p} \rfloor^2 + (-92 - 96\sqrt{p} + 384p) \lfloor \sqrt{p} \rfloor + 48p - 12}.$$

Using the bounds $\sqrt{p} - 1 \leq \lfloor \sqrt{p} \rfloor \leq \sqrt{p}$, it follows that

$$\begin{aligned}
B(4 \lfloor \sqrt{p} \rfloor) &= \frac{384\sqrt{p} \lfloor \sqrt{p} \rfloor - 192 \lfloor \sqrt{p} \rfloor^2 + 48 \lfloor \sqrt{p} \rfloor + 48\sqrt{p} + 12}{128 \lfloor \sqrt{p} \rfloor^3 + (48 - 384\sqrt{p}) \lfloor \sqrt{p} \rfloor^2 + (-92 - 96\sqrt{p} + 384p) \lfloor \sqrt{p} \rfloor + 48p - 12} \\
&\leq \frac{192p + 432\sqrt{p} - 180}{128p \cdot \sqrt{p} - 768p + 388\sqrt{p} - 48},
\end{aligned}$$

which approaches zero as p approaches infinity. That is, the proportion of reducibles among all p -Weil polynomials tends towards 0, as needed. \square

6. Future work

Data similar to that of Figure 2 suggests that (in addition to the proportion of irreducible p -Weil polynomials going to 1) the proportion of p -Weil polynomials with corresponding Galois group D_4 increases significantly as p increases. In fact, we form the following conjecture:

Conjecture 6.1. *As the prime p approaches infinity, the proportion of polynomials with corresponding Galois group D_4 among all p -Weil polynomials tends towards 1.*

Further research will attempt to prove Conjecture 6.1 by using Theorem 4.1 and modifying the methods used to prove Theorem 5.1.

7. Acknowledgments

This research was conducted at California State University, Fullerton, under the direction of Dr. Christopher Lyons. We are grateful for support from the CSUF Math Department Summer Research Program, the Louis Stokes Alliance for Minority Participation (LSAMP), as well as the CSU Office of the Chancellor. This research was funded in part by the National Science Foundation (grant No. HRD-1302873).

References

- [1] Luise-Charlotte Kappe, and Bette Warren, "An Elementary Test for the Galois Group of a Quartic Polynomial," *The American Mathematical Monthly* **90** (1989) 133–137.
- [2] Hans-Georg Rück, "Abelian Surfaces and Jacobian Varieties over Finite Fields" *Compositio Mathematica* [76] (1990) 351–366.
- [3] Thomas W. Hungerford, and David Leep. "Abstract Algebra: An Introduction". Brooks Cole Publish Company 2012.

The Impact of Modality Pertaining to Gender and Mathematical Self-Related Beliefs in a High-School Setting

Department of Mathematics, California State University, Fullerton, CA

Mirna Dominguez and Erick Venegas

Advisors: Dr. Sam Behseta and Dr. Cherie Ichinose

Abstract

Online mathematics courses have become a common learning source for K-12 learners. Moreover, there is an interest on whether the modality, face-to-face or online environment will affect the relationship between gender and mathematical self-related beliefs. Mathematics literature categorizes these beliefs into three constructs: self-efficacy, self-concept and math-anxiety. The variables utilized in this study include the gender of students and their corresponding scoring-levels to each construct. In this project we utilize hypothesis testing procedures, in particular permutation-based techniques in order to develop non-parametric approaches for studying the relationship between gender and the three constructs. Our research reveals a dependence between gender and mathematical self-related beliefs in the face-to-face group but not in the online group.

1. Introduction

Mathematical self-related beliefs reflect on how students' self-influence affect perseverance through math courses. The three constructs: self-efficacy, self-concept, and anxiety, have been identified as being the key predictors of mathematics achievement and behaviors (Bandura, 2002). Self-efficacy describes a student's conviction that they can successfully perform any given task at desired levels (Schunk, 1991). Students with low self-efficacy display a lack of confidence in their ability to organize and execute tasks. This prevents students from successfully reaching the appropriate benchmarks in math. Self-concept is used to describe a student's belief in their own

abilities (OECD, 2013). A student can exhibit high self-concept in mathematics, but low self-efficacy in a particular topic or task. The apprehensive emotions felt towards mathematics are referred to as math-anxiety. This could range from having feelings of stress and helplessness to having more physical reactions like pain when confronted with math (OECD, 2013). Mathematical self-related beliefs help determine an individual's growth and development of their mathematical skills and competence (Bandura, 1997).

Mathematical beliefs and performance have been shown to be different between genders. For instance, "girls tend to have more negative math attitudes, including gender stereotypes, anxieties, and self-concepts than boys" (Gunderson, 2011). Researchers suggest that the awareness of stereotypes favoring males in math begins at an early age and is quickly internalized. These social influences create insecurities in girls and are further reinforced by peers (Kiefer, A.K.; Sekaquaptewa, D., 2006). However, online learning may be able to reduce social influences, and as a result improve students' performance: "online learning not only provides the flexibility to learn at one's own pace and speed, but provides students with the anonymity to explore their mathematical learning regardless of the pressures that differences in gender, ethnicity or socioeconomic factors may produce" (Ichinose, 2012). Furthermore, "the neutral medium of online learning may help to balance mathematics achievement between males and female students" (Ichinose, 2012).

From 2003 through 2012, the Programme for International Student Assessment (PISA) has collected information on students' self-related beliefs in a face-to-face

learning environment (OECD, 2013). Now that technology has evolved, it has created a new learning modality for students. In the online learning community, students can freely log in and interact solely with computer-assisted instruction. California Virtual Academies (CAVA) is an example of a virtual high school that began in 2002. With this new sample of students, we are able to make comparisons between modalities and high school students.

1.1 Objective

In this study, we wish to determine the impact of modality, face-to-face (PISA) and online, on the inherent relationship between a student's gender and corresponding scoring-levels to each construct. Statistical methodologies such as permutation based chi-square, difference in proportions, odds ratios, Cochran-Mantel-Haenszel and Gamma will be used to gauge the statistical significance between the variables of interest.

1.2 Data

In this project we utilized two sources of data: 1-data generated by PISA and 2-the online data administered through CAVA. The study consists of 424 high school participants from CAVA and 258,570 high school participants from PISA. Each construct (self-efficacy, self-concept, and math-anxiety) consists of three questions such that each is scored using a 4 point Likert scale. For instance, a participant answering questions pertaining to self-concept and math-anxiety will respond with the range of: Strongly Disagree (1), Disagree (2), Agree (3), and Strongly Agree (4). However, questions related to self-efficacy are answered with the range of: Not At All Confident (1), Not Very Confident (2), Confident (3), and Very Confident (4). A participant is evaluated upon his/her response to each of the questions within a given construct. A participant's score associated with self-efficacy will be the sum of their responses. For instance, a student with the scores of 4 - 3 - 4 will be assigned the score 11. Since 8 roughly represents the median score of a given construct, then this participant's score (11) is classified as "High Self-Efficacy". It should be noted that medians differ per construct: the medians for self-efficacy, self-concept, and math-anxiety are 9, 8, and 7, respectively. Data is summarized through 2×2 contingency tables consisting of the two variables, gender and scoring-levels for each construct, where gender has two categories:

male and female; and where each construct has two scoring-levels, namely, low and high. Contingency tables 1 through 6 contain the counts and percentages of the categories associated with the variables per modality. Percentages are computed within each construct by gender. For example in Table 1, there is 30,775 (25.4%) males with "Low Self-Efficacy" and 90,567 (74.6%) males with "High Self-Efficacy."

1.2.1 Modality: PISA

Table 1: Gender and Self-Efficacy Scoring-Levels

	Low Self-Efficacy	High Self-Efficacy
Male	30,775 (25.4%)	90,567 (74.6%)
Female	42,902 (33.8%)	84,169 (66.2%)

Table 2: Gender and Self-Concept Scoring-Levels

	Low Self-Concept	High Self-Concept
Male	38,324 (31.8%)	82,172 (68.2%)
Female	53,260 (42.2%)	72,958 (57.8%)

Table 3: Gender and Math-Anxiety Scoring-Levels

	Low Math-Anxiety	High Math-Anxiety
Male	70,872 (58.8%)	49,611 (41.2%)
Female	62,584 (49.4%)	63,988 (50.6%)

1.2.1 Modality: Online

Table 4: Gender and Self-Efficacy Scoring-Levels

	Low Self-Efficacy	High Self-Efficacy
Male	29 (19.6%)	119 (80.4%)
Female	69 (27.1%)	186 (72.9%)

Table 5: Gender and Self-Concept Scoring-Levels

	Low Self-Concept	High Self-Concept
Male	62 (41.1%)	89 (58.9%)
Female	143 (55.9%)	113 (44.1%)

Table 6: Gender and Math-Anxiety Scoring-Levels

	Low Math-Anxiety	High Math-Anxiety
Male	84 (56.0%)	66 (44.0%)
Female	96 (38.2%)	155 (61.8%)

2. Methods

A series of hypothesis testing and permutation-based non-parametric techniques were developed to gauge the statistical significance of the inherent relationships between variables associated with a student's gender and scoring-levels.

2.1 Statistical Measures

2.1.1 Classical

Chi-square

Chi-square test statistic can be used to test the independence of variables associated with categorical data. Depending on the hypothesis and on how the data was collected, the chi-square test is modified. Consider the null hypothesis to be

$$H_0 : A \text{ and } B \text{ are independent.}$$

For 2×2 contingency tables, the chi-square statistic is calculated by the formula

$$\chi^2 = \frac{N(ad - bc)^2}{(a + b)(c + d)(b + d)(a + c)},$$

where the variables can be determined using Table 7.

	B (Type 1)	B (Type 2)	Total
A (Type 1)	a	b	a + b
A (Type 2)	c	d	c + d
Total	a + c	b + d	a + b + c + d = N

Furthermore, the degrees of freedom (df) is equal to the (number of columns minus one) \times (number of rows minus one), not counting the totals for rows or columns.

For 2×2 contingency tables, this gives $df = (2 - 1) \times (2 - 1) = 1$. Finally, we fail to reject the null hypothesis when the corresponding p -value with $df = 1$ is large.

Difference in Proportions

A two-proportion z -test, also known as difference in proportions, determines whether there is a significant difference between sampled proportions. Consider the null hypothesis to be

$$H_0 : p_1 - p_2 = 0,$$

where p_1 and p_2 are population proportions. Hypothesis testing requires pooled sample proportions (\hat{p}_1 and \hat{p}_2) to be calculated from the population. The test statistic is computed by

$$z = \frac{\hat{p}_1 - \hat{p}_2}{\sqrt{\frac{\hat{p}_1(1 - \hat{p}_1)}{n_1} + \frac{\hat{p}_2(1 - \hat{p}_2)}{n_2}}},$$

where n_1 and n_2 are sample sizes from population 1 and 2. Another approach to hypothesis testing is the use of a confidence interval. After choosing a confidence level, the confidence interval becomes

$$(\hat{p}_1 - \hat{p}_2) \pm z_{1-\alpha/2} \sqrt{\frac{\hat{p}_1(1 - \hat{p}_1)}{n_1} + \frac{\hat{p}_2(1 - \hat{p}_2)}{n_2}},$$

where $\pm z_{1-\alpha/2}$ are the corresponding z -scores for the level of confidence. If zero is contained in the confidence interval, then we fail to reject the null hypothesis. In the context of contingency tables, the above will be a function of marginal sums of the table associated with one of the variables (Moore, et al., 2009).

Odds Ratio

The odds ratio (OR) is a statistical measure used to draw conclusions about effects or events. OR data consist of counts for each set of conditions and outcomes are set up in 2×2 contingency tables, as in Table 7. The OR evaluates whether the odds of certain events or outcomes is the same for the two groups or whether the exposure is a factor for the outcome (McHugh, 2009). The OR is obtained by using the following formula:

$$\begin{aligned} \text{OR} &= \frac{a/b}{c/d} \\ &= \frac{a \times d}{b \times c}. \end{aligned}$$

The following conclusions can be drawn from the OR:

- OR = 1 Independence
- OR \neq 1 Dependence.

The precision of OR can be determined using a confidence interval. Shorter confidence intervals imply higher precision, while a wider confidence interval imply lack of precision. Note that a confidence interval does not measure statistical significance (Hailpern and Visintainer, 2003). Subsequently, the confidence interval is calculated by

$$\exp \left[\ln(\text{OR}) \pm z_{1-\alpha/2} \sqrt{1/a + 1/b + 1/c + 1/d} \right].$$

Gamma

Suppose we have two ordinal categorical variables X and Y . Let π_{ij} be the probability of the (i, j) cell in the associated contingency table. Consider the following two definitions for concordance, and discordance. A pair of subjects is called concordant if the subject ranked higher on X also ranks higher on Y . For example, suppose we have n_{11} observations (subjects) in the $(1, 1)$ cell of a contingency table, and n_{22} many subjects in the $(2, 2)$ cell of the same contingency table. Subsequently, all the subjects in the cell $(1, 1)$ of such a contingency table will be concordant to all the subjects in the cell $(2, 2)$. Consequently, there will be $n_{11} \times n_{22}$ pairs of concordant subjects associated with these two cells, and so on. A pair of subjects is called discordant if the subject ranked higher on X ranks lower on Y .

Consider the following representations for concordance and discordance, respectively:

$$\pi_c = 2 \sum_{i=1}^I \sum_{j=1}^J \pi_{ij} \left(\sum_{h>i} \sum_{k>j} \pi_{hk} \right)$$

$$\pi_d = 2 \sum_{i=1}^I \sum_{j=1}^J \pi_{ij} \left(\sum_{h>i} \sum_{k<j} \pi_{hk} \right).$$

Given that a pair is untied on both variables $\pi_c / (\pi_c + \pi_d)$ is the probability of concordance, and $\pi_d / (\pi_c + \pi_d)$ is the probability of discordance (Agresti, 2013).

Cochran-Mantel-Haenszel

The Cochran-Mantel-Haenszel (CMH) test evaluates the conditional independence in $2 \times 2 \times K$ contingency tables. CMH test conditions on row and column totals in each partial table. The count in the first row and first column in a partial table determines all the other counts in that table. Under the usual sampling schemes (e.g.,

binomial for each row in each partial table), the conditioning results in a hyper-geometric distribution for count n_{11k} in the cell in row 1 and column 1 of partial table k . The test statistic utilizes this cell in each partial table (Agresti, 2007).

In partial table k , the row totals are $\{n_{1+k}, n_{2+k}\}$, and the column totals are $\{n_{1+k}, n_{2+k}\}$. Given these totals, under H_0 ,

$$\mu_{11k} = E(n_{11k}) = \frac{n_{1+k} \cdot n_{1+k}}{n_{++k}}$$

$$\text{Var}(n_{11k}) = \frac{n_{1+k} \cdot n_{2+k} \cdot n_{1+k} \cdot n_{2+k}}{n_{++k}^2 (n_{++k} - 1)}.$$

The CMH test statistic summarizes the information from the K partial tables using

$$\text{CMH} = \frac{\left[\sum_k (n_{11k} - \mu_{11k}) \right]^2}{\sum_k \text{Var}(n_{11k})}.$$

This statistic has a large-sample chi-squared null distribution with $df=1$. The approximation improves as the total sample size increases, regardless of whether the number of strata K is small or large (Agresti, 2013).

2.1.2 Permutation Based

Suppose that we have two variables X and Y whose categories are shown by X_1, X_2, \dots, X_J and Y_1, Y_2, \dots, Y_J . The resulting table is of $I \times J$ dimension. Let's use the notation n_{ij} for the number of observations in the i th row and j th column: $i = 1, 2, \dots, I$; $j = 1, 2, \dots, J$. Let $n = \sum_i \sum_j n_{ij}$ be the total sample size.

	Y_1	\dots	Y_j	\dots	Y_J	Total
X_1	n_{11}	\dots	n_{1j}	\dots	n_{1J}	n_{1+}
\vdots	\vdots	\ddots	\dots	\dots	\vdots	\vdots
X_i	n_{i1}	\vdots	n_{ij}	\vdots	n_{iJ}	n_{i+}
\vdots	\vdots	\dots	\dots	\ddots	\vdots	\vdots
X_J	n_{J1}	\dots	n_{Jj}	\dots	n_{JJ}	n_{J+}
Total	n_{+1}	\dots	n_{+j}	\dots	n_{+J}	n

3. Results

3.1 Modality: PISA

Hypothesis tests of independence were implemented to understand the impact of a face-to-face setting on gender and self-related beliefs. We analyzed if there was an independence between gender and levels of construct. Chi-square, CMH, and Gamma test statistics reported statistically significant p -values. As a result, we rejected our null hypothesis and concluded there is dependence. The intensity of these occurrences was confirmed by the odds ratio analysis and suggested that there was a relationship between gender and self-related beliefs in the control group.

The implementation of the difference in proportions test revealed a significant difference in scoring levels between the two genders. More precisely, we tested whether there was a significant difference between the proportion of males and the proportion of females in the "Low Self-Efficacy" category. Moreover, confidence intervals suggested that there was a difference in proportions between males and females in all constructs.

Let W_{obs} be the statistic of interest, obtained through the counts in the observed table. That is, $W_{obs} = f(n_{ij}|\theta_{ij})$ where θ_{ij} is the underlying probability of cell (i, j) with the condition of $\sum_i \sum_j \theta_{ij} = 1.00$.

Suppose that $n_{1+}, n_{2+}, \dots, n_{I+}$ represents the marginal sums of the categories associated with X random variable and $n_{+1}, n_{+2}, \dots, n_{+J}$ represents the marginal sums from variable Y . Clearly, $n_{i+} = \sum_{j=1}^J n_{ij}$ and $n_{+j} = \sum_{i=1}^I n_{ij}$ and $\sum_{j=1}^J \sum_{i=1}^I n_{ij} = \sum_{i=1}^I \sum_{j=1}^J n_{ij} = n$. Without loss of generality, let X play the role of the explanatory variable, and Y represents response variable. The following scheme is independent of such allocation. However, that approach can facilitate the understanding of permutation-based test in a wider context of statistical non-linear modeling. We begin by shuffling the Y -data among the X -groups, that is by keeping $n_{1+}, n_{2+}, \dots, n_{I+}$ at the same value; we redistribute n_{ij} 's for $j = 1, \dots, J$ within the i -th row. This will be equivalent with putting all n_{i+} ($i = 1, \dots, I$) into a bucket, and randomly assigning n_{i+} many observations into the J categories, where each observation (out of n_{i+} many) has an equal chance of being allocated to categories $1, \dots, J$. Next, at each iteration of the above permutation (re-shuffling or reallocation) procedure, we calculate the test statistic of interest to obtain a version of $W^{(b)}$, where b refers to iteration (b) and thus $b = 1, \dots, B$.

Consequently, we can create permutation based values for the chi-square test, difference in proportions, odds ratio, Gamma and Cochran-Mantel-Haenszel statistics as $\chi^{2(b)}$; $z^{(b)}$; $OR^{(b)}$; $\gamma^{(b)}$; and $CMH^{(b)}$, respectively. To calculate p -values associated with each W ; we can simply obtain the region above the W_{obs} per test statistic, that is permutation

$$p\text{-value} = \frac{\#W^{(b)} \geq W_{obs}}{B}.$$

To obtain the permutation-based $100(1 - \alpha)\%$ confidence interval for each test statistic, we can find the interval surrounded by $100(\alpha/2)\%$ and $100(1 - \alpha/2)\%$ of the empirical or permutation based distribution of that test. That is a $100(1 - \alpha)\%$ confidence interval for w may be found via

$$(w^{(\lfloor B \times \alpha/2 \rfloor)}, w^{(\lceil B \times (1 - \alpha/2) \rceil)}),$$

where $\lfloor \cdot \rfloor$ and $\lceil \cdot \rceil$ denotes the closest integer to the result of the operation defined in it.

Chi-Square	χ^2 : 2098.919	p -value: 2.2e-16
Difference in Proportions	Low Self-Efficacy	(0.0804, 0.0876)
	High Self-Efficacy	(-0.0876, -0.0804)
Odds Ratio Analysis	Ratio: 0.4866	(0.4782, 0.4952)
Cochran-Mantel-Haenszel	p -value: 0	CMH = 2099.3136
Gamma	p -value: 0	(0.0007, 4.9007)

Chi-Square	χ^2 : 2098.992	p -value: 2.2e-16
Difference in Proportions	Low Self-Concept	(0.1058, 0.1137)
	High Self-Concept	(-0.1137, -0.1058)
Odds Ratio Analysis	Ratio: 1.5563	(1.5317, 1.5812)
Cochran-Mantel-Haenszel	p -value: 0	CMH = 2099.3136
Gamma	p -value: 0	(0.0013, 5.1231)

Chi-Square	χ^2 : 2185.129	<i>p</i> -value: 2.2e-16
Difference in Proportions	Low Math-Anxiety	(-0.0977, -0.0899)
	High Math-Anxiety	(0.0899, 0.0977)
Odds Ratio Analysis	Ratio: 0.6846	(0.6738, 0.6956)
Cochran-Mantel-Haenszel	<i>p</i> -value: 0	CMH = 2185.4980
Gamma	<i>p</i> -value: 0	(0.0012, 5.2237)

3.2 Modality: Online

Hypothesis tests of independence were utilized to understand the impact of an online setting on gender and self-related beliefs. We analyzed if there was an independence between gender and levels of construct. Results of independence tests in the online group were not as consistent as in the PISA group. Although self-concept and math-anxiety reported statistically significant *p*-values for chi-square, CMH, and Gamma test, self-efficacy did not. The intensity of these occurrences was confirmed by the odds ratios analysis and suggested that self-concept and math-anxiety were associated with gender. However, odds ratio for self-efficacy revealed independence.

The implementation of the difference in proportions test revealed a significant difference in scoring levels between the two genders. More precisely, we tested whether there was a significant difference between the proportion of males and the proportion of females in the "High Math-Anxiety" category. Our confidence intervals suggested both self-concept and math-anxiety had a significant difference in proportion between males and females. However, the confidence interval for self-efficacy revealed independence.

Chi-Square	χ^2 : 11.9317	<i>p</i> -value: 0.118
Difference in Proportions	Low Self-Efficacy	(-0.0094, 0.1587)
	High Self-Efficacy	(-0.1587, 0.0094)
Odds Ratio Analysis	Ratio: 1.5222	(0.9316, 2.4873)
Cochran-Mantel-Haenszel	<i>p</i> -value: 0.0577	CMH = 2.8280
Gamma	<i>p</i> -value: 0.1125	(-0.2371, 0.2232)

Chi-Square	χ^2 : 7.7403	<i>p</i> -value: 0.0054
Difference in Proportions	Low Self-Concept	(0.0487, 0.2473)
	High Self-Concept	(-0.2473, -0.0487)
Odds Ratio Analysis	Ratio: 1.8166	(1.2087, 2.7302)
Cochran-Mantel-Haenszel	<i>p</i> -value: 0.0040	CMH = 8.3013
Gamma	<i>p</i> -value: 0.0045	(0.0001, 5.0440)

Chi-Square	χ^2 : 11.2547	<i>p</i> -value: 0.0054
Difference in Proportions	Low Math-Anxiety	(-0.2772, -0.0779)
	High Math-Anxiety	(0.0779, 0.2772)
Odds Ratio Analysis	Ratio: 0.4866	(0.3227, 0.7338)
Cochran-Mantel-Haenszel	<i>p</i> -value: 0.0006	CMH = 11.9317
Gamma	<i>p</i> -value: 6e-04	(0.0047, 4.9000)

4. Conclusion

This study confirms previous work in mathematics education literature (Gunderson, 2011) that females in the face-to-face learning environment tend to have lower mathematics self-concept and higher mathematical anxiety than their male counterparts. This is also true in the online setting. That is, the learning modality did not present itself as a change in gender behavior with respect to mathematical anxiety and self-concept.

Our study shows, however, that modality has a statistical effect on genders' mathematical self-efficacy. That is, in the face-to-face setting, male students had higher levels of mathematical self-efficacy. In the online group, mathematical self-efficacy is not dependent on the gender of the student. This implies that the new learning modality creates an unbiased setting between genders. In other words, the dynamics of online learning seems to balance students' mathematical motivation and beliefs. Further discussion should explore how online learning continues to impact self-beliefs in students taking math courses.

There is limited research pertaining to online learning, specifically research relating to learning mathematics. Researching students and their interactions in an online setting would be useful in helping educators strengthen online and classroom learning. For instance, if educators are able to mirror characteristics of an online setting, then it may reduce the existing gender bias in mathematics.

5. Acknowledgments

In publishing our first academic paper, we had to seek guidance from professors, who deserve our greatest gratitude. We would like to extend our gratitude to Dr. Sam Behseta and Dr. Cherie Ichinose. We would like to thank Dr. Cherie Ichinose for sharing her research with us and for her admirable words of encouragement. We would also like to thank Dr. Sam Behseta for allowing us to grow as researchers and scholars. His expertise and wisdom motivates us to pursue higher education and further grow as individuals. Additionally, we would like to give thanks to Dr. Christina Goode and Leslie Montoya for including us in the Louis Stokes Alliance for Minority Participation (LSAMP) Research Scholarship Program and thus funding our research.

References

- [1] Agresti, A. (2007). *An Introduction to Categorical Data Analysis*, 2nd ed., Wiley, 114-115.
- [2] Agresti, A. (2013). *Categorical Data Analysis*. 3rd ed., Wiley, New York.
- [3] Bandura, A. (1997). *Self-efficacy: The Exercise of Control*. New York: W.H. Freeman and Company.
- [4] Gunderson, E. A.; Ramirez, G.; Levine, S. C.; Beilock, S. L.. (2011). *The Role of Parents and Teachers in the Development of Gender-Related Math Attitudes*. Springer Science+Business Media, LLC. Retrieved from https://www.academia.edu/637907/The_Role_of_Parents_and_Teachers_in_the_Development_of_Gender-Related_Math_Attitudes.
- [5] Ichinose, C. (2012). Online Learning and Gender Equality. *Russian-American Education Forum: Online Journal*; Volume 4, Issue 1.
- [6] Hailpern, S.; Visintainer, P. (2003) *Odds ratios and logistic regression: further examples of their use and interpretation*. The Stata Journal, Number 3, pp. 213–225.
- [7] McHugh, M. L.. (2009). *The odds ratio: calculation, usage, and interpretation*. *Biochemia Medica* 2009, 19(2), 120-6.
- [8] Moore, D.S.; McCabe, G.P.; Craig, B.A. (2009), *Introduction to the Practice of Statistics*. Sixth Edition. W.H. Freeman and Company. New York.
- [11] Organization for Economic Co-operation and Development (OECD). (2013). PISA 2012 Results: Ready to Learn, Students' Engagement, Drive and Self-Beliefs, Volume III, 79-95. www.oecd.org/pisa
- [12] Schunk, D. H.. (1991). *Self-Efficacy and Academic Motivation*. *Education Psychology*, 26, 207-231.
- [13] The Pennsylvania State University. (2015). *5.4.5 Cochran-Mantel-Haenszel Test*. Retrieved from <https://online-courses.science.psu.edu/stat504/node/113>.
- [14] Kiefer, A.K.; Sekaquaptewa, D. (2006) *Implicit stereotypes and women's math performance: How implicit gender-math stereotypes influence women's susceptibility to stereotype threat*. *Journal of Experimental Social Psychology*.

Importance of Sampling Pattern and Regularization in Under-Sampled Magnetic Resonance Imaging (MRI)

Department of Mathematics, California State University, Fullerton

Erick Ortega and Rudolph V. Saenz

Advisor: **Dr. Angel R. Pineda**

Abstract

Our project seeks to optimize under-sampled Magnetic Resonance Imaging (MRI). We look at the effectiveness of accelerated acquisition and constrained reconstruction using the Shepp-Logan phantom. Our current research focuses on determining how different sampling methods can either improve or hinder the effect of reconstructing an object from incomplete frequency samples using a total variation regularization method. In our approach, we implemented a total variation reconstruction to an under-sampled Fourier data, where the sampling methods include Evenly Spaced (ES), Beginning-Middle-End (BME), and Low Frequency (LF) sampling. We analyze the relationship between an alpha constraint, the strength of the total variation regularizer, in our reconstruction and the amount of data that is collected during the sampling methods in order to determine the optimal alpha value. We found that the BME sampling method gave us the best performance in terms of the mean squared error. Future work will compare this result with a task-based approach.

1. Introduction

1.1 Motivation

In the medical imaging field, as well as many other disciplines, reconstructing an object (particularly a signal or an image) from incomplete or under-sampled Fourier data is of great interest and, if successfully implemented, can substantially accelerate the speed of data acquisition. We focus on Magnetic Resonance Imaging (MRI). Currently the MRI process is slow, requiring patients to remain still for long periods of time. The speed of a MRI is limited by

both physical and physiological constraints. Our project seeks to reduce the amount of data necessary to create a useful image. This reduction in the amount of data needed significantly accelerates the process.

1.2 Background

The Fourier transform is a useful and powerful tool in mathematics with a variety of applications. In the simplest sense, the Fourier transform represents wave-forms using complex exponentials at different frequencies that can be represented in terms of cosine and sine waves using Euler's equation.

A full two-dimensional Fourier transform performs a 1-D transform on every line or row of the image, and another 1-D transform on every column of the image, producing a 2-D Fourier transform of the same size as the original image.

The Fourier transformation $F(k)$ is given by

$$F(k) = \int_{-\infty}^{\infty} f(x)e^{-2\pi ikx} dx$$

for the 1-dimensional transformation where $f(x)$ is the input signal, k is the spatial frequency, and x is the spatial domain. Note that $F(0)$ is given by

$$F(0) = \int_{-\infty}^{\infty} f(x) dx$$

and is just the integral of the function, and $F(1)$ is the inner product of $f(x)$ with $g(x) = e^{2\pi ix}$.

$$F(1) = \langle f, g \rangle = \int_{-\infty}^{\infty} f(x)e^{-2\pi ix} dx$$

The transform in 2-Dimensions $F(k_x, k_y)$ is given by

$$F(k_x, k_y) = \int_{-\infty}^{\infty} \int_{-\infty}^{\infty} f(x, y) e^{-2\pi i(k_x x + k_y y)} dx dy$$

where $f(k_x, k_y)$ is the function in the spatial domain and k_x and k_y are the spatial frequencies in the x and y directions respectively.

When taking a Fourier transform, it is important to remember that the result will be complex. Our tests will also rely on the Shepp–Logan Phantom (SLP) [1] which can be obtained using MATLAB. Using MATLAB we can compute the 1-D and 2-D Fourier transformation of the SLP. We can also obtain the inverse Fourier transformation. Figure 1 and figure 2 show the 1-D and 2-D Shepp–Logan phantom respectively with their discrete Fourier transformations.

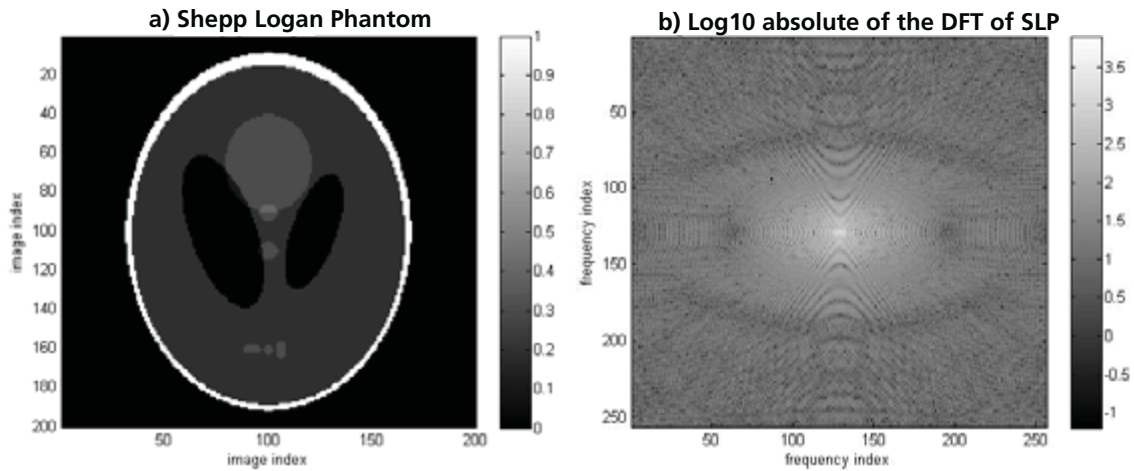


Figure 1: (a) A 200×200 image of the Shepp–Logan Phantom. (b) The Discrete Fourier transformation of the SLP. The DFT has been shifted so that the zero frequency is at the center and the absolute value is displayed in log scale.

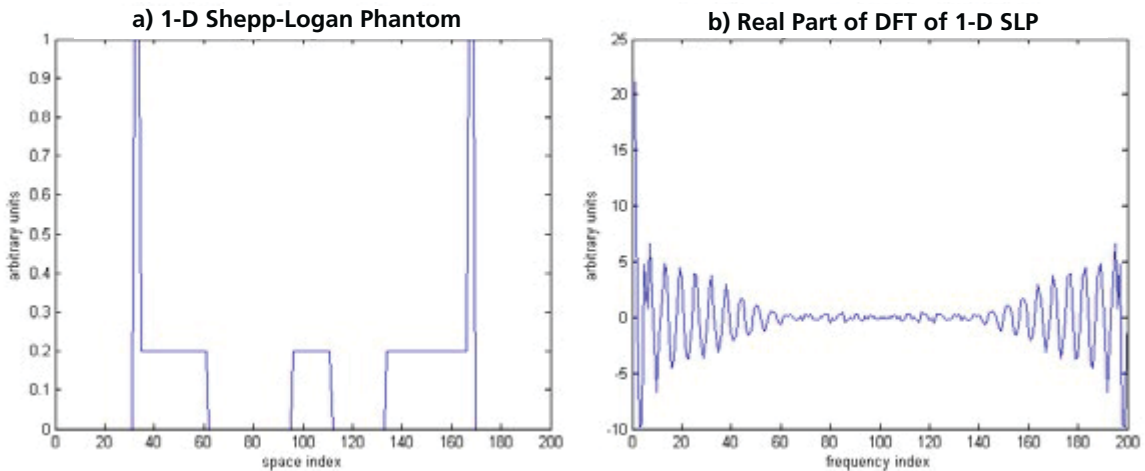


Figure 2: (a) The 1-Dimensional Shepp–Logan Phantom. A plot of the 100th line from figure 1(a). (b) The Discrete Fourier transformation of the 1-D SLP. The real portion of the DFT is shown. (note: This DFT is not shifted)

2. Methods

2.1 Accelerating MRI

To simulate under-sampled images we apply a mask to the Fourier transformation of the SLP, zeroing out a specified amount of data. After we apply the mask, we take the “sub-sampled” data and estimate the object. We seek to minimize the following least squares functional

$$\operatorname{argmin}_{\vec{x}} \|F(\vec{x}) - d\|^2$$

where \vec{x} is our guess of the object—the 1-D plot or 2-D image, F is the Discrete Fourier Transformation (DFT), and d is our data—the measurements taken in the DFT domain. In our work, we demonstrate the process of sub-sampling and reconstruction in the 2-D case, but will focus on the 1-D as a proof of concept to save computing time associated with the 2-D case. We then extend this process by adding the constraint $\|\nabla\vec{x}\|$, our total variation regularizer [2,3]. The functional then becomes

$$\operatorname{argmin}_{\vec{x}} \{ \|F(\vec{x}) - d\|^2 + \alpha \|\nabla\vec{x}\| \}$$

where we define $\nabla\vec{x}$ to be the one-sided gradient in the 1-D case given by

$$\nabla\vec{x} = x_{i+1} - x_i.$$

2.2 2-D Simulation

In simulating sub-sampling for a 2-D Shepp–Logan Phantom, we first compute the DFT. We construct our mask to obtain data from spokes crossing through the origin of the shifted DFT (shown in figure 1(b)). We start with a matrix of all zeros and create a loop for values close to the spokes figure 3(a) and makes these values one. Once we obtain this mask, we multiply it—element by element—with the DFT. This results in our sub-sampled image figure 3(b). For the purpose of this demonstration, we use a 200×200 SLP and twenty spokes.

To look at the reconstructed image from this data we then computed the inverse Fourier transformation of the sub-sampled data. The resulting image figure 4(a) resembles the original image, even having only used 13.4% of the data from the original image. We then increased the number of spokes to determine at what point would we return an image comparable to the original image. With 80 spokes, we obtain a decent result figure 4(b) using only 48.7% of the data from the original image.

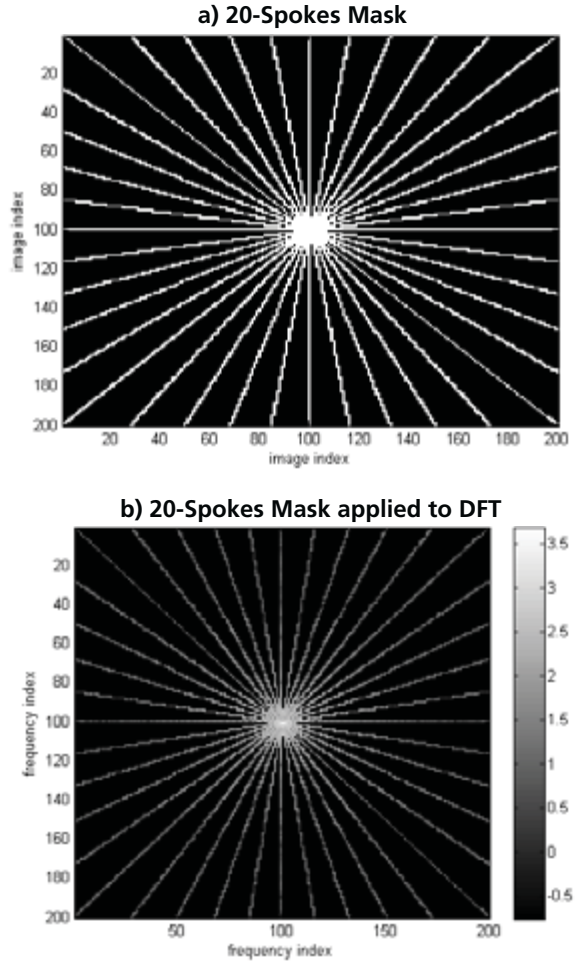
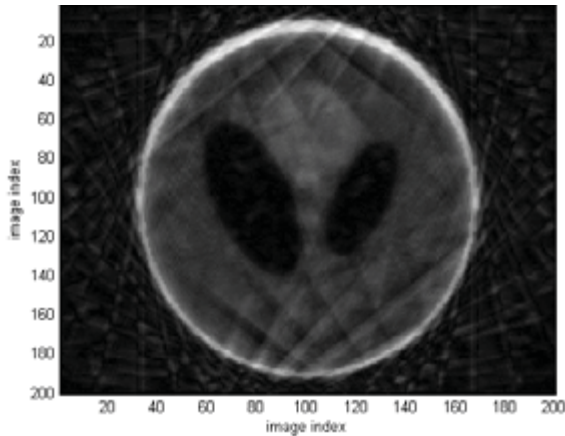


Figure 3: (a) The mask which will be applied to our data to represent sub-sampling. The mask has 20 spokes, it will keep approximately 13.4% of the data. (b) The DFT of the SLP after our mask is applied to it by multiplying the two, element by element. This is our “sub-sampled” data.

a) 20-Spokes Inverse Transform using 13.375% of the Data



b) 80-Spokes Inverse Transform using 48.66% of the Data

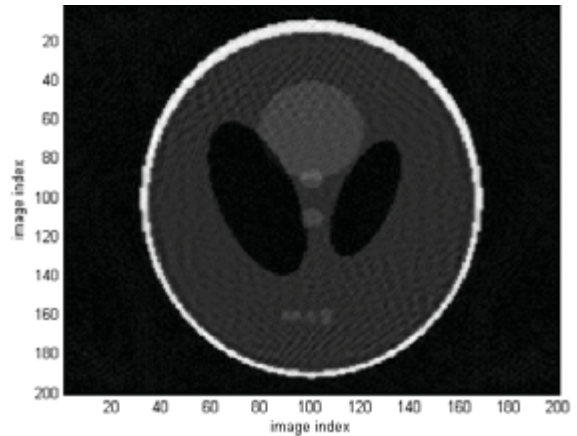
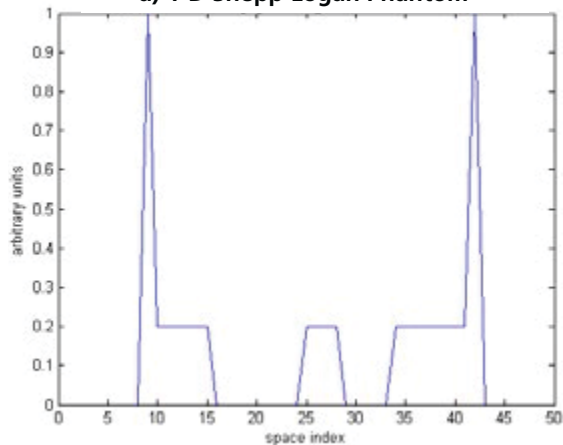


Figure 4: (a) The inverse Fourier transformation of our sub-sampled data using the twenty-spoke mask. This reconstruction uses only 13.4% of the data from the original image. (b) The inverse Fourier transformation of our sub-sampled data using an eighty-spoke mask. This reconstruction only uses 48.7% of the data from the original image.

a) 1-D Shepp-Logan Phantom



b) Real Part of DFT of 1-D SLP

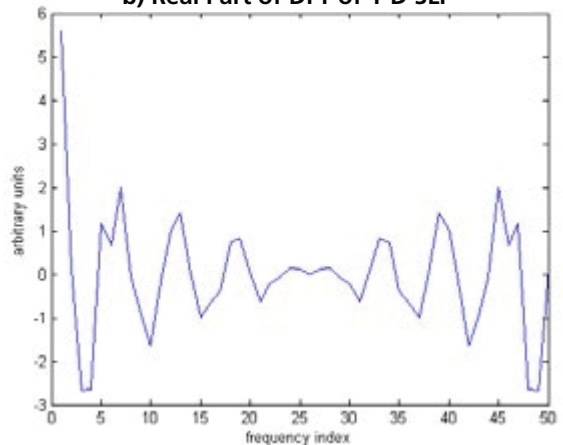


Figure 5: (a) The plot of the 25th line from a 50×50 SLP. (b) A plot of the real part of the DFT of this line.

2.3 Numerical Implementations

In order to minimize our functionals, we used the *fminunc* function provided in MATLAB. This particular function attempts to find a minimum of a scalar function of several variables, starting at an initial estimate. It utilizes the 'quasi-newton' algorithm.

To calculate the gradient that will be used for the alpha-constrained least squares functional, we will use the *diff* function provided in MATLAB as well. The *diff* function calculates differences between adjacent elements along a vector or array whose size does not equal 1, thus giving us a one-sided gradient.

2.4 1-D Sampling Methods

Now that we have verified we can obtain a reasonable image with our sub-sampling method, we seek to estimate the original image. As a proof of concept, we restrict this testing to a 1-Dimensional space and use a smaller SLP to save on computation time. We first attempt to minimize the least squares functional in Equation (1). In dealing with a 1-D model, we take a single line figure 5(a) from a 50 × 50 SLP, near the middle of the image, and then take the DFT of that particular line figure 5(b). We note that figure 5(b) shows the un-shifted DFT. This means that the center of the image contains the high frequencies. Moving away from the center in either direction corresponds to a lower frequency, with the zero frequency at the first value[4].

In estimating the effect of under-sampled data, we experiment using three different methods of sub-sampling. For each of these sampling methods, we try to minimize the 1-dimensional version of Equation (1) where our initial guess, \vec{x} , is a vector of all zeros. Once we have minimized Equation (1), we extend the process by using our regularized least squares functional, Equation (2). For each sampling method, we first sub-sample using 50% of the data and use an alpha value of 0.5 to compare each sampling method with set parameters.

Once we compare these results for each sampling method, we then seek out the optimal method. We calculate the Mean Squared Error (MSE) for different data percentages and different alpha values,

$$\text{MSE} = \frac{1}{n} \sum_{i=1}^n (D_i - \hat{D}_i)^2$$

where D_i is the i^{th} value of the original line from the SLP and \hat{D}_i is the i^{th} value of the line obtained from estimation.

2.4.1 Evenly Spaced Sampling

In this method, we sub-sample by setting evenly spaced data-point on the phantom line transform to zero to simulate obtaining the required percent of data. For the given 50% of data, this results in a special case where we take every other data-point. The inverse transform of the sub-sampled DFT of the phantom line can be seen in figure 7(a). The real portion of the DFT of the original line with the ES mask applied, our sub-sampled data, can be seen in figure 8(b).

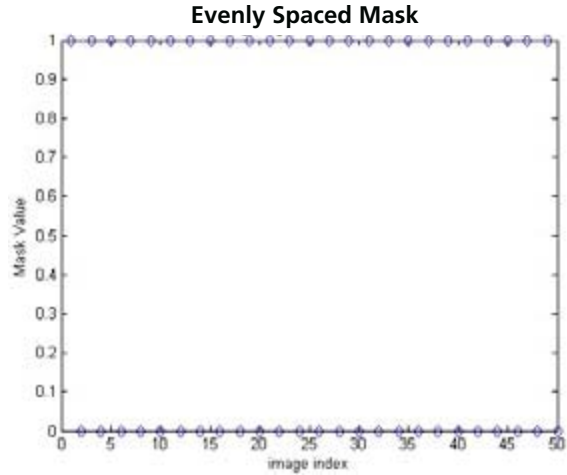


Figure 6: The mask used for the Evenly Spaced sampling using 50% of the data. Data points with mask value 1 are kept, data points with mask value 0 are thrown out. This uses an even amount of data across high and low frequencies.

After minimizing the function, we obtain the results seen in figure 8(a). We can see a resemblance to our inverse transform of the sub-sampled DFT. After the minimization of Equation (2), we obtained the results seen in figure 8(b). The results show that there is no significant difference between using the alpha constraint, and not using it with this particular sampling scheme for the given percentage. The underlying reason for why this occurs is related to a phenomena known as ‘aliasing’ brought about by the way that the data was sampled [4]. The sub-sampled image is already piece-wise constant, so the total variation constraint has minimal effects.

We now seek to minimize the MSE using this sampling method. The chart below shows the MSE obtained for the given alpha and percentage value. Contrary to what we previously determined in our test with an alpha of 0.5 and using 50% of the data, the alpha value does show a difference when using different percents of data. Our tests show that at the 20%, 40%, and 60%, a higher alpha value results in lower MSE. The higher percentages, 80% and 100% do not benefit from a high alpha value, the higher alpha value actually raises the MSE.

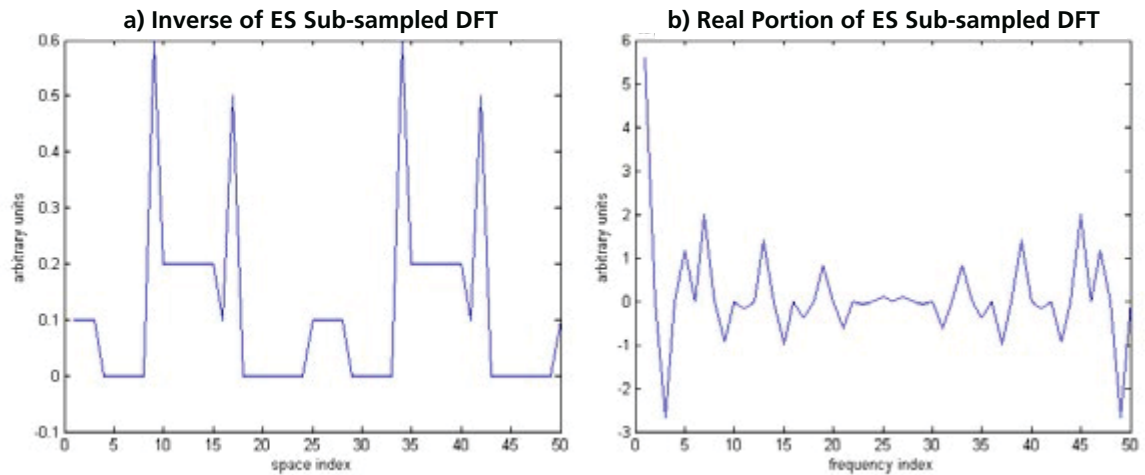


Figure 7: (a) The inverse Fourier transformation of the sub-sampled DFT, using the evenly spaced sampling method. (b) The sub-sampled DFT of the phantom line (refer to figure 5(b)) with every other point set to zero.

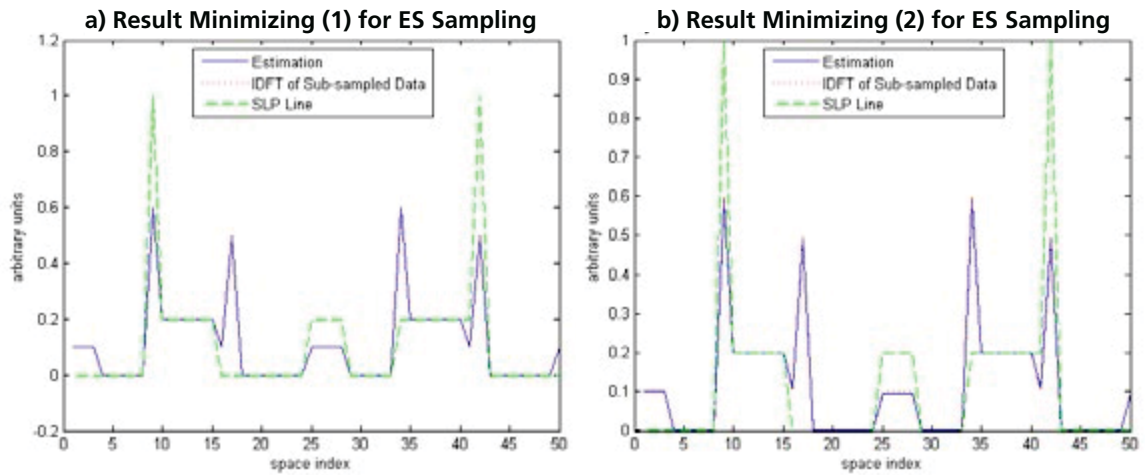


Figure 8: (a) The result obtained through minimizing Equation (1), where the alpha constraint is not considered. (b) The result obtained through minimizing Equation (2) with $\alpha = 0.5$. Note: For this α both reconstructions are very similar.

	$\alpha = 0$	$\alpha = 0.0001$	$\alpha = 0.001$	$\alpha = 0.01$	$\alpha = 0.1$	$\alpha = 0.5$
20%	0.03744	0.03744	0.03744	0.03744	0.03745	0.03752
40%	0.02194	0.01783	0.01102	3.554e-08	3.336e-06	8.691e-05
50%	0.01840	0.01840	0.01840	0.01840	0.01840	0.01844
60%	1.449e-14	1.040e-12	7.469e-11	7.109e-09	6.980e-07	1.743e-05
80%	1.003e-16	4.680e-13	5.138e-11	3.559e-09	3.552e-07	8.897e-05
100%	5.552e-17	5.301e-13	2.446e-11	2.550e-09	2.564e-07	6.312e-06

Table 1: The mean squared error obtained for comparing the estimated data using the evenly spaced sampling method against the line obtained from the Shepp–Logan phantom. The MSEs for different combination of alpha and percentages of data used in sampling is given.

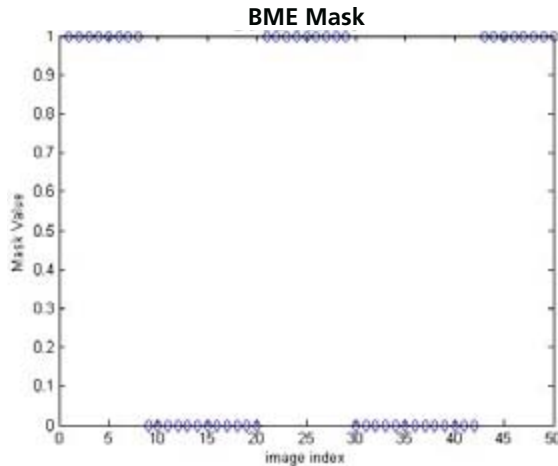


Figure 9: The mask used for B-M-E sampling using 50% of the data. Data points with mask value 1 are kept, data points with mask value 0 are thrown out. This method uses both the lowest and highest frequencies.

2.4.2 BME Sampling

In this sampling method, we take two-thirds of the required amount of data from the lowest frequencies, and a third from the highest frequencies. For our example, using a phantom line of length 50, for a 50% data measurement, we take a sample of 8(16%) from the beginning of our DFT (low frequencies), 9(18%) from the middle (the highest frequencies), and 8(16%) from the end(low frequencies), thus gathering the required 50% of data. Figure 9 shows the mask used and figure 10 shows the images for our data using this sampling method.

After minimizing Equation (1) for this sampling method, we obtain figure 11(a) below. We can see the minimization works, as the line from figure 11(a) and figure 10(a) lie on top of each other. We then seek to minimize Equation (2) resulting in figure 11(b) below. In this sampling method, we can see just by observation that the line obtained using the total variation regularizer has a drastic improvement. This line closely resembles the original line shown in figure 5(a).

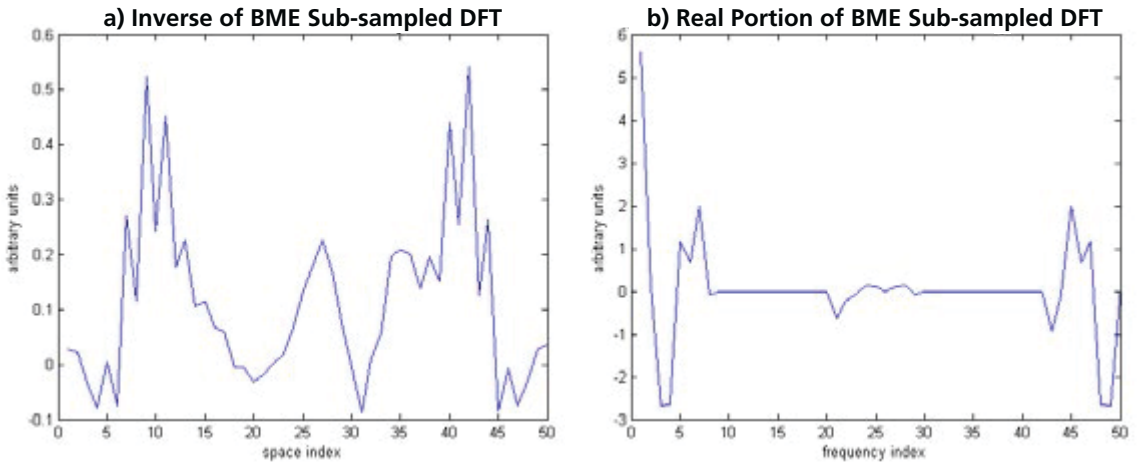


Figure 10: (a) The inverse Fourier transformation of the our sub-sampled DFT, using the BME sampling method. (b) The sub-sampled DFT of the phantom line (refer to figure 5(b)) with only the beginning, middle, and end data values(i.e., the low and high frequencies).

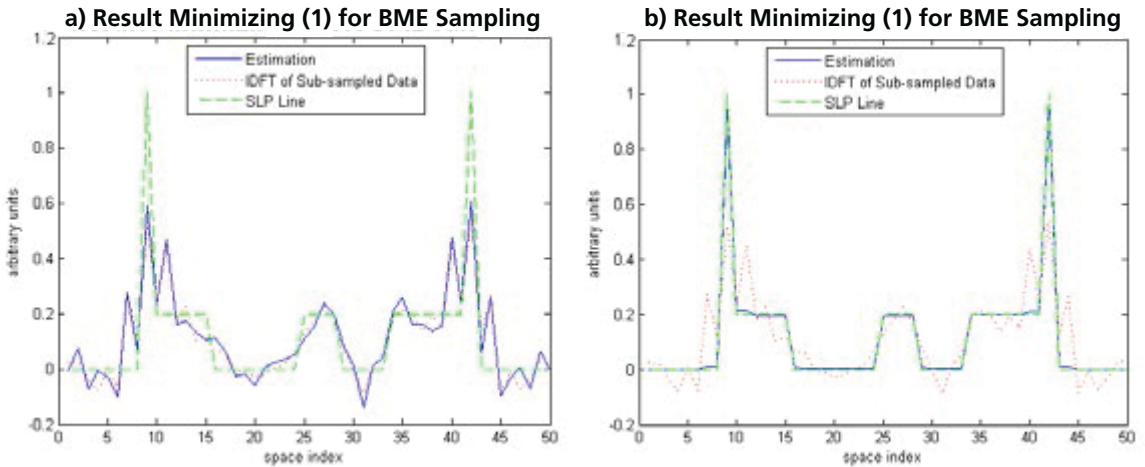


Figure 11: (a) The result obtained through minimizing Equation (1), where the alpha constraint is not considered. (b) The result obtained through minimizing Equation (2) with $\alpha = 0.5$.

For this sampling method, we seek to minimize the MSE. Table 2 obtained verifies our intuition that for BME sub-sampling using less data, a higher alpha value gives a better result. We expected the low frequencies would help reconstruct the shape of the line, the high frequencies would help reconstruct the peaks and edges, and the total variation constant would help flatten the line,

thus making it piece-wise constant. For BME sub-sampling using more data, alpha values helps to a point, but then begins to hurt our result. That is the optimal alpha value and the percent of data used are inversely related. This appears to be true for very small alpha values as for 60% and 80%, the respective optimal alpha values are 0.001 and 0.0001.

	$\alpha = 0$	$\alpha = 0.0001$	$\alpha = 0.001$	$\alpha = 0.01$	$\alpha = 0.1$	$\alpha = 0.5$
20%	0.02584	0.02527	0.02532	0.01964	0.02212	0.01730
40%	0.02048	0.02005	0.01591	0.01584	0.00034	0.00520
50%	0.01525	0.01376	3.897e-06	3.541e-08	3.952e-06	9.959e-05
60%	0.01222	0.01041	1.203e-10	1.301e-08	1.345e-06	3.330e-05
80%	0.00534	7.504e-13	5.195e-11	3.537e-09	3.490e-07	8.772e-06
100%	5.552e-17	5.301e-13	2.446e-11	2.550e-09	2.564e-07	6.312e-06

Table 2: The mean squared error obtained for comparing the estimated data using the BME sampling method against the line obtained from the Shepp–Logan phantom. The MSEs for different combination of alpha and percentages of data used in sampling is given.

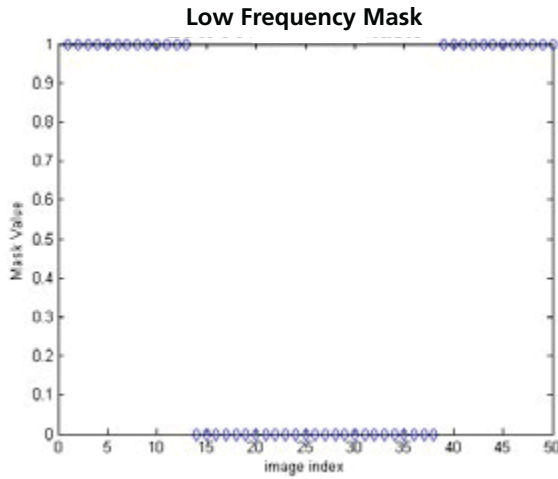


Figure 12: The mask used for Low Frequency sampling at 50%. Data points with mask value 1 are kept, data points with mask value 0 are thrown out. This method only uses low frequencies from the DFT of our original line.

2.4.3 Low Frequency Sampling

In this sampling method, we take the required amount of data from the low frequencies of the Fourier transformation. Again, for comparison among the different sampling methods, we will keep 50% of the data, and use an alpha of 0.5.

After minimizing Equation (1) for this sampling method we obtain figure 14(a) below. We can see that using this sampling method, the minimization begins to capture the overall shape of the original line. We next seek to minimize Equation (2) resulting in the figure below. Visually comparing, we can see using the alpha of 0.5 results in “flatter” reconstruction than without using alpha.

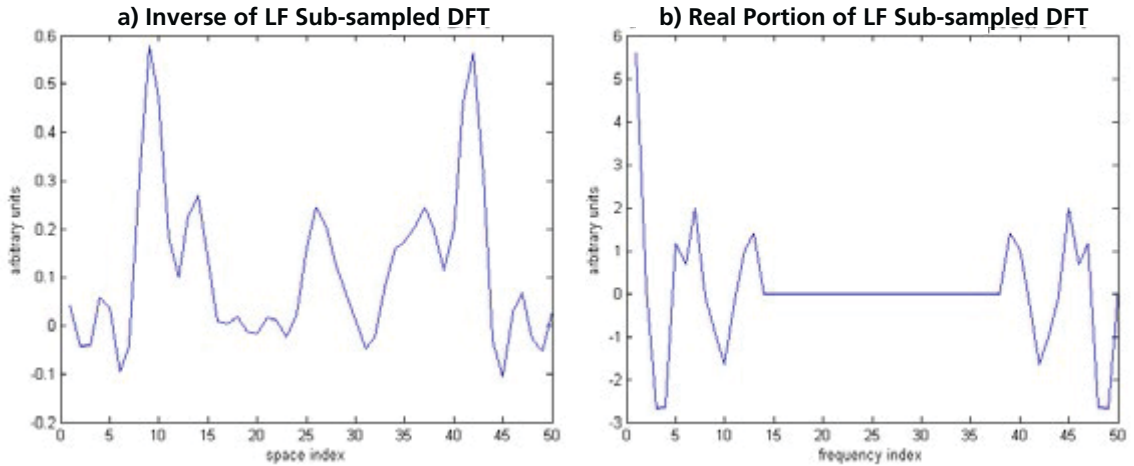


Figure 13: (a) The inverse Fourier transformation of the our sub-sampled DFT, using the low frequency sampling method. (b) The sub-sampled DFT of the phantom line (refer to figure 5(b)) with only the beginning values.

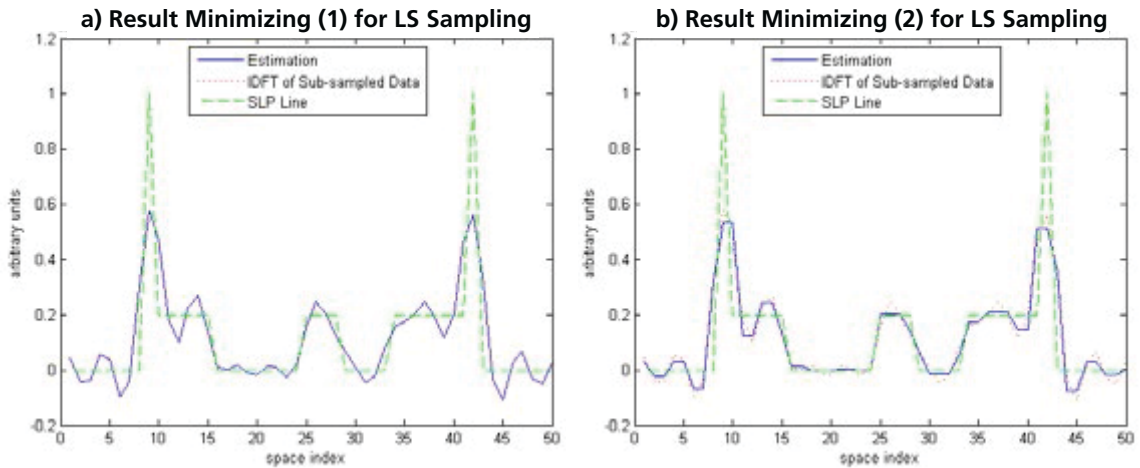


Figure 14: (a) The result obtained through minimizing Equation (1), where the alpha constraint is not considered. (b) The result obtained through minimizing Equation (2) with $\alpha = 0.5$.

Table 3: MSE for Low Frequency Sampling

	$\alpha = 0$	$\alpha = 0.0001$	$\alpha = 0.001$	$\alpha = 0.01$	$\alpha = 0.1$	$\alpha = 0.5$
20%	0.02809	0.02806	0.02720	0.02810	0.02907	0.02907
40%	0.01984	0.02026	0.02146	0.02145	0.02135	0.02147
50%	0.01600	0.01614	0.01732	0.01916	0.01940	0.01922
60%	0.01205	0.00937	0.00966	6.277e-08	5.261e-06	0.00013
80%	0.00596	0.00092	4.527e-11	4.591e-09	4.708e-07	1.177e-05
100%	5.552e-17	5.301e-13	2.446e-11	2.550e-09	2.564e-07	6.312e-06

Table 3: The mean squared error obtained for comparing the estimated data using the low frequency sampling method against the line obtained from the Shepp-Logan phantom. The MSEs for different combination of alpha and percentages of data used in sampling is given.

Again, we seek to minimize the MSE, the chart below reflects the obtained MSEs for given alpha values and percentages of data used. Using the LF sampling method, there is no general relationship between percent of data used and optimal alpha value. For lower percentages, the total variation regularizer makes little difference in MSE, but for higher percentages, it begins to help.

3. Discussion

After implementing different sampling techniques, it became apparent that the method in which the data is sampled, as well as the percentage of data and our alpha value, can yield drastically different results.

As shown by our evenly spaced sampling, when data is poorly sampled, occurrences such as aliasing can lead to peculiar results such as having the alpha constraint, have little effect. This outcome was puzzling since we expected an alpha constraint to be an improvement over our alpha-less functional. The reason for this lies in the total variation regularizer. It works to “flatten” by reducing changes from one location in the image to the next. As the minimization result without the regularizer was already piece-wise constant (i.e. flat) with minimal changes, it had no real effect for the 50% used. According to our MSE chart, overall regularized least squares functional had no significant improvement over or first least squares functional. For the 40% case though, we see a small increase in alpha does help, this

has to do with the particular way our code handles the 40% ES mask which does not lead to aliasing exactly as the 50% case does. This does indicate the possibility of an improved sampling method when using 40% of the data. The overall behavior of the MSE chart can be attributed to how the ES samples at different percentage values. The different percentages lead to different types of structures in the sampling.

The beginning-middle-end sampling pattern yielded very important results. Minimizing the normal least squares functional resulted in a very jagged image taking on the overall shape of the original image. The resemblance between our regularized least squares functional and the original line taken from the Shepp-Logan Phantom is apparent. Using 50% of data and with an alpha value of 0.5, after minimizing the regularized least squares function, between the original line and our new minimized line, we get an mean squared error of 3.59×10^{-8} . Reviewing the MSE chart, we can see this is not even the optimal alpha value, but still results in a very close reconstruction. We expected our alpha to improve our results, but we did not expect the results to improve so drastically. We believe the improvement was due to our sampling pattern using both low and high frequencies.

The low frequency sampling pattern's results showed a relatively smooth curve when we minimized our unregularized least squares functional. The results after minimizing our regularized least squares functional showed that the peaks of the results from the normal functional were flattened. This occurred because our sampling pattern

only used low frequencies, which captures the overall trend of the data but ignores the high frequencies, which are responsible for well defined edges. For the lower percentages, there was little to no improvement using the regularized functional. For higher percentages, we start to see a trend similar to that of the BME method. This is because as you go past the 50% mark, you begin to capture the high frequencies. As seen with the BME, having both adjacent high and low frequencies results in a benefit when using the regularized functional.

Throughout our research, we used the 50% as our overall benchmark as being able to halve the acquisition time would be a great improvement. Using our MSE charts for comparison, we can determine our optimal sampling pattern and alpha value combination for 50% is the BME sampling pattern with an alpha value of 0.01. This results in an MSE of 3.54×10^{-8} . This is shown in figure 15. Both the line obtained through minimization and the original line almost lie on top of each other.

3.1 Future Work

As our research continues, we plan to extend our simulation results to two dimensions. We also plan to add a small perturbation to the phantom to model a tumor. We will then use statistical detection methods to evaluate the effect of the total variation constraint[5,6].

References

- [1] Larry A. Shepp, Benjamin F. Logan. The Fourier Reconstruction of a Head Section. IEEE Transactions on Nuclear Science. 21(3):21-43 (1974).
- [2] Michael Lustig, David Donoho, John M. Pauly. Sparse MRI: The Application of Compressed Sensing for Rapid MR Imaging. Magnetic Resonance in Medicine. 58(6):1182-1195 (2007).
- [3] Emmanuel J. Candès, Justin Romberg, Terence Tao. Robust Uncertainty Principles: Exact Signal Reconstruction From Highly Incomplete Frequency Information. IEEE Transactions on Information Theory. 52(2):489-509 (2006).
- [4] Omer Demirkaya, Musa H. Asyali, Prasanna K. Sahoo. Image Processing with Matlab: Applications in Medicine and Biology. CRC Press (2008).
- [5] Jongduk Baek, Angel R. Pineda, Norbert J. Pelc. To Bin or Not to Bin? The Effects of CT System Limiting Resolution on Noise and Detectability. Physics in Medicine and Biology. 58(5):1433-1446 (2013).
- [6] Craig K. Abbey, Harrison H. Barrett. Human- and Model-Observer Performance in Ramp-Spectrum Noise: Effects of Regularization and Object Variability. Journal of the Optical Society of America. A, Optics, Image Science, and Vision. 18(3):473-488 (2001).

Optimal Reconstruction for 50% of the Data

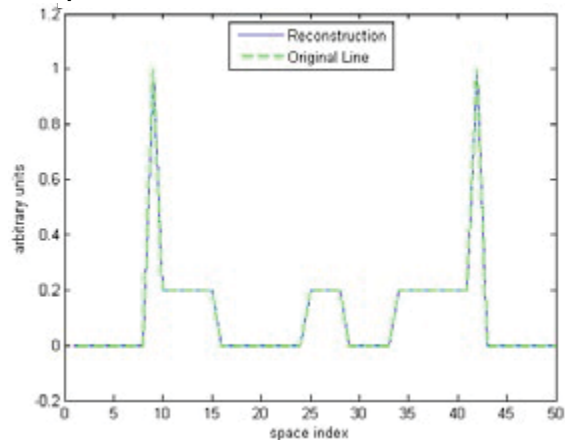


Figure 15: The optimal sampling method when obtaining 50% of the data. This optimal method is the BME sampling pattern with $\alpha = 0.01$.

4. Acknowledgments

We acknowledge support from the Louis Stokes Alliance for Minority Participation (LSAMP) through the National Science Foundation Grant number (NSF:HRD-1302873).

Number Theory in the *Revista Matematică din Timișoara*

Troy High School and Fullerton Mathematical Circle, California State University Fullerton

Shreya Havaladar

Advisor: **Dr. Bogdan Suceavă**

Abstract

Mathematical Review of Timișoara is known to the North American audiences since problems originally published there have been included in various problems, books, eg, *Mathematical Olympiad Challenges*, by Titu Andreescu and Răzvan Gelca, Birkhäuser, 2000; or *Mathematical Olympiad Treasures*, by Titu Andreescu, Birkhäuser, 2004.

Mathematical Review of Timișoara was founded in 1921 by Traian Lalescu, a former doctoral student of Emile Pircard. Among Pircard's doctoral students were Jacques Hadamard, Henri Villat, Gaston Julia, and Andre Weil.

Traian Lalescu defended his doctoral thesis at the Normal Superior School in Paris in 1908, then taught mathematics at the University of Bucharest. He saw how important it is to have a mathematical monthly published for an interested audience in the success of the Bucharest-based *Mathematical Gazette*. In 1920, he was appointed as the first president of the new founded Polytechnic University in Timișoara.

1. Introduction

In one of our workshops of the Fullerton Mathematical Circle in the Spring of 2014, the students were presented with a series of number theory problems originally published in *Mathematical Review of Timișoara*. We present here some of these problems.

2. Problems

Problem No. 1521: M.P. Tică-Gall, June 15, 1937.

Find the perfect square $\overline{abc\bar{a}}$ in which \overline{ab} and $\overline{c\bar{a}}$ are both perfect squares.

Solution: We start from the information that both \overline{ab} and $\overline{c\bar{a}}$ are both perfect squares. The only possible two-digit squares are: 16, 25, 36, 49, 64, 81. Since a is both the starting number and ending number, there are only 4 combinations which satisfy this condition: 1681, 4964, 6416, 6436. Only 1681 is a perfect square since $41^2 = 1681$. Therefore, the answer is 6481.

Problem No. 1513: N. Grumăzescu, June 15, 1937.

Find a perfect square \overline{abaca} in which the difference between a and c yields the square root of a and b is prime.

Solution: It is given that \overline{abaca} is a perfect square, $|a-c|$ is the square root of a , and b is prime. Using this information, we can deduce that

- since the square ends in a , a can only be one of the following: 1, 4, 9, 6, 5 or 0;
- a must be a perfect square itself, since the difference between two integers is the square root of a ;
- \overline{abaca} is a five digit number, where a is both the starting and ending digit.

We can conclude that a has only three options: $a = 1, 4,$ or 9 . Since \overline{abaca} is also a five digit integer, it must be a perfect square in one of the following ranges:

10001-19991, where \overline{abaca} must end in 1;
 40004-49994, where \overline{abaca} must end in 4;
 90009-99999, where \overline{abaca} must end in 9.

So, \overline{abaca} must be one of the following numbers:

10, 201 = 101 ²	19, 881 = 141 ²
17, 161 = 131 ²	49, 284 = 222 ²
44, 944 = 212 ²	14, 641 = 121 ²
97, 969 = 313 ²	40, 804 = 202 ²
12, 321 = 111 ²	91, 809 = 303 ²

However, only two of these numbers follow the pattern \overline{abaca} , where a is the middle digit as well:

97, 969 = 313² 17, 161 = 131².

We also know that b , the second digit is prime. For example,

97, 969 17, 161.

Both of these numbers also satisfy that condition. There is still one more condition to test: $|a-c|$ is the square root of a . For 97, 969, $|9-6|=3$, and the square root of 9 is also 3. For 17, 161, $|1-6|=5$, and 5 is not the square root of 1. Therefore, the answer is 97, 969.

Problem No. 921: V. Alaci, January 15, 1931.

Prove that the square of the sum of the squares of two consecutive integers can be written as the sum of two squares, and that these two squares are relatively prime integers.

Solution: We will present a proof of induction. The statement holds for $n = 1$, since $1^2 + 2^2 = 5$, and $5^2 = 25 = 9+16$, where 9 and 16 are relatively prime. The statement also holds for $n = 2$, since $2^2 + 3^2 = 16$, and $16^2 = 169 = 25 + 144$, where 25 and 144 are relatively prime. This also holds for $n = k$, since

$$\begin{aligned} [k^2 + (k+1)^2]^2 &= [k^2 + k^2 + 2k + 1]^2 \\ &= (2k^2 + 2k + 1)^2 \\ &= 4k^4 + 4k^2 + 1 + 8k^3 + 4k^2 + 4k. \end{aligned}$$

We can rewrite the last expression as: $4k^2 + 4k + 1 + 4k^4 + 8k^3 + 4k^2$, which becomes the sum of two squares

$$4k^2 + 4k + 1 + 4k^4 + 8k^3 + 4k^2 = (2k+1)^2 + [2k(k+1)]^2.$$

To prove $(2k+1)^2$ is relatively prime to $[2k(k+1)]^2$, it is sufficient to prove $(2k+1)$ is relatively prime to $2k(k+1)$. We have to prove $2k+1$ is relatively prime to both $2k$ and $k+1$ separately in order for it to be relatively prime to their product.

Remark that $2k+1$ is relatively prime to $2k$, because it is impossible for two consecutive integers to share any factors other than 1. On the other hand, $2k+1$ can be rewritten as $[k+(k+1)]$. Since we know $k+1$ is relatively prime to k , it is impossible for $2k+1$ to have any factors in common with $k+1$. Therefore, $(2k+1)$ and $2k(k+1)$ are relatively prime integers.

This holds for $n = k+1$, since

$$\begin{aligned} [(k+1)^2 + ((k+1)+1)^2]^2 &= [(k+1)^2 + (k+2)^2]^2 \\ &= (k^2 + 2k + 1 + k^2 + 4k + 4)^2 \\ &= (2k^2 + 6k + 5)^2 \\ &= 4k^4 + 36k^2 + 25 + 24k^3 + 20k^2 + 60k \\ &= 4k^4 + 24k^3 + 56k^2 + 60k + 25. \end{aligned}$$

This can be regrouped as the sum of two squares:

$$\begin{aligned} 4k^4 + 24k^3 + 4k^2 + 36k^2 + 16k^2 + 12k + 48k \\ + 9 + 16 &= (2k+3)^2 + 4(k+3k+2)^2 \\ &= (2k+3)^2 + [(2k+2)(k+2)]^2. \end{aligned}$$

To prove $(2k+3)^2$ is relatively prime to $[(2k+2)(k+2)]^2$ again be sufficient to prove $(2k+3)$ is relatively prime to $(2k+2)(k+2)$. $2k+3$ is relatively prime to $2k+2$ because it is impossible for two consecutive integers to share any factors other than 1. Moreover, $2k+3$ can be rewritten as $[(k+1) + (k+2)]$. Since we know $k+2$ is relatively prime to $k+1$, it is impossible for $2k+3$ to have any factors in common with $k+2$. Therefore, for all integers n , $[n^2 + (n+1)^2]^2$ can be written as the sum of two squares, where the two squares are relatively prime.

3. Acknowledgments

Many thanks to the Fullerton Math Circle, for introducing me to the *Mathematical Review of Timișoara* journal, Professor Bogdan Suceavă, all of my past math teachers, and the Mathematical Association of America, for allowing me to present this work at the 2014 So-Cal Nevada Fall conference.

Editor's Note: Fullerton Mathematical Circle is the outreach program of the Department of Mathematics at Cal State Fullerton. The first meeting of the Fullerton Mathematical Circle was held on September 24, 2011 and meetings have been held on numerous Saturdays since at California State University, Fullerton's campus. The format of our sessions is inspired from the experience of similar events developed around the monthly publication *Gazeta matematică*, a journal established in 1895. Our Math Circle hosts American Mathematical Competitions AMC 8, AMC 10, AMC 12, as well as AIME and USAMO. The younger students participating to the Fullerton Mathematical Circle are solving problems from Abacus International Challenge. Some of our sessions are inspired from themes presented in the books published in the AMS and MSRI book series Math Circle Library.

The Impact of Supplemental Instruction on the SI Leader

Department of Mathematics, California State University, Fullerton

Kelly Hartmann and Christina Tran

Advisor: Dr. Martin Bonsangue

Abstract

The impact of Supplemental Instruction (SI) has been shown to be positive for students taking gateway STEM courses; we focus instead on the impact of leading SI workshops on the SI leaders. While the impact of SI on the leaders themselves has long been thought to be positive, evidence for this has been largely anecdotal. This study conducted at California State University, Fullerton attempted to examine this impact with more quantifiable evidence and on a larger scale than past studies may have reported. Variables included gender, first generation college status, and underrepresented minority status (URM). While the subgroups were not significantly different on variables linked to academic background and achievement such as grade point average, several significant differences emerged. For example, results showed that a higher proportion of men than women reported increased confidence and effectiveness in communicating with professors, peers, and students. Additionally, URM leaders reported increases in effectively handling with student conflict and communicating with peers than did their non-URM counterparts. This information may help inform how to improve the structure of supplemental instruction programs and how to train SI leaders to better benefit both the SI students as well as the SI leaders.

1. Background

CSUF's Supplemental Instruction Program first started in 2007 with two calculus workshops and two biology workshops. Our goal was to reduce the achievement gap between URMs and others in STEM field, and to improve retention and course completion of STEM majors. In Spring 2014, CSUF's

SI program had seventy-nine workshops that were linked to 123 courses across nine departments including Mathematics, Biology, Chemistry, Computer Science, Philosophy, Business, etc. The growth of the SI program led us to believe that the impact of the program goes beyond the workshop and its students. Previous studies showed effects of SI workshops on SI students, but we seek to investigate the effects of leading a workshop on the SI leader.

According to Lockie and Lanen, SI leaders "improved leadership, communication skills and self-confidence as a result of their SI experience" [1]. Additionally, Stout and McDaniel state, "Leaders report academic improvement, increased communication and relationship-building skills, and personal and professional development" [2]. In his study, Zaritsky found that "ninety-eight percent of SI leaders reported that being an SI leader helped them gain self-confidence. SI gave them the opportunity to strengthen their leadership and communication skills" [3]. Previous studies indicate that leading a workshop is beneficial to the leader. In our study, we investigated the effects on communication and leadership skills from leading an SI workshop.

2. Methods

For this study, we created a questionnaire in Google Forms containing twenty-six questions. The purpose of the questionnaire was to examine the benefits of leading a supplemental instruction workshop. The questionnaire started with background questions about the SI leader's gender, ethnicity, parent's level of education, etc. and followed with Likert-scale questions asking about the effect that leading

Figure 1: Sample Questions from the Questionnaire

	Strongly Disagree	1	2	3	4	5	Strongly Agree
12. Being an S.I leader has had a strong influence on my career choice.	1	2	3	4	5		
13. Being an S.I leader has positively influenced my communication skills.	1	2	3	4	5		
14. Being an S.I leader has improved my leadership skills.	1	2	3	4	5		
15. Being an S.I leader, I have become more aware of campus resources.	1	2	3	4	5		
16. Being an S.I leader has taught me skills that have improved other areas of my life.	1	2	3	4	5		
17. Being an S.I leader has helped me deal with student conflict.	1	2	3	4	5		
18. Being an S.I leader has helped me become more effective when communicating with professors.	1	2	3	4	5		
19. Being an S.I leader has helped me become more effective when communicating with peers.	1	2	3	4	5		
20. Being an S.I leader has helped me become more effective when communicating with students.	1	2	3	4	5		
21. Being an S.I leader has helped me deepen my understanding of core concepts.	1	2	3	4	5		

a supplemental instruction workshop had on him/her. The focus of the Likert- scale questions was on communication skills and professional growth. Questions on communication skills focused on how to handle student conflict and capability in talking with professors, peers, and students. Questions on professional growth focused on determining career choice and leadership skills.

The survey was e-mailed to 153 supplemental instruction leaders who led workshops between 2009 and 2013 at California State University, Fullerton. The survey was conducted in the fall of 2013 and had a 58% response rate. A majority of the leaders were from the College of Natural Sciences and Mathematics.

3. General Results

We first examined and compared the percentage of respondents who gave a score of 4 or 5. We found that leading a workshop did not effect the SI leader's career choice, but they felt a strong increase in communication skills (Figure 2). We further analyzed the increase in communication skills and looked at the percentage of respondents who gave a score of 4 or 5 in communication with professors, peers, and their students. As shown in Figure 3, SI leaders felt the strongest increase in improved communication skills with their students. With further analysis, we compared the percentage of respondents that gave a score of 4 or 5 when looking at how much they learned to handle student conflict and how much they learned to communicate with their students. In Figure 4, we see there is not a strong increase in learning how to handle student conflict.

Figure 2

Categories	Response of 4 or 5
Communication Skills	94%
Leadership	87%
Skills	81%
Career Choice	62%

Figure 2: Shows the percentage of respondents that gave a score of 4 or 5 in skills that transfer to another area, improved their leadership skills, helped with determining their career choice, and improved their communication skills.

Figure 3

Categories	Response of 4 or 5
Communication Skills	94%
Communicating with Students	97%
Communicating with Professors	78%
Communicating with Peers	77%

Figure 3: Shows the percentage of respondents that gave a score of 4 or 5 in overall communication skills, communicating with professors, peers, and their students.

Figure 4

Categories	Score of 4 or 5
Communicating with Students	97%
Student Conflict	62%

Figure 4: Shows a comparison of the percentage of respondents that gave a score of 4 or 5 when looking at how much they learned to handle student conflict compared to how much they learned to communicate with their students.

4. Results

Figure 5

Question	Population	Mean	Standard Deviation
18. Being an S.I. leader has helped me become more effective when communicating with professors.	Female (n = 44)	3.95	1.12
	Male (n = 43)	4.37	0.98
19. Being an S.I. leader has helped me become more effective when communicating with peers.	Female (n = 44)	4.00	1.12
	Male (n = 43)	4.28	1.05
20. Being an S.I. leader has helped me become more effective when communicating with students.	Female (n = 44)	4.41	0.58
	Male (n = 43)	4.70	0.51

Figure 5: The population, mean, and standard deviation of responses with respect to gender.

Figure 6

Scale	Females	Males
1	2%	2%
2	11%	5%
3	16%	7%
4	30%	26%
5	41%	60%

Figure 6: Shows the percentage breakdown of respondents to "Being an SI leader helped me become more effective when communicating with professors."

Figure 7

Scale	Females	Males
1	2%	5%
2	11%	2%
3	14%	9%
4	30%	28%
5	43%	56%

Figure 7: Shows the percentage breakdown of respondents to "Being an SI leader helped me become more effective when communicating with peers."

We examined certain populations of SI leaders to see if they were gaining more from leading workshops. We first examined respondents who identified themselves as female or male, first generation student or non-first generation student, and URM or non-URM. We first examined those who identified themselves as female and male. Shown in Figure 5, we looked at the number of respondents, the mean, and standard deviation to certain questions. Figure 6 shows the percentages of leaders' response to increased effectiveness in communication skills with professors. When examining those who gave a score of 4 or 5, we see that males felt a stronger improvement in communication skills with professors. The same result holds when looking at the percentage breakdown of responses to increased effectiveness in communicating with peers, shown in Figure 7.

Next, we looked at SI leaders who identified themselves as first generation students and non-first generation students. Figure 8 shows the number of respondents, the mean, and standard deviation to questions about handling student conflict and effectiveness in communicating with professors. Figure 9 shows the percentage of those who gave a score of 4 or 5 in increased effectiveness in communicating with professors. We found that non-first generation SI leaders felt they became more effective when communicating with professors than first generation SI leaders. In Figure 10, the percentage of those who gave a score of 4 or 5 in dealing with student conflict was higher for first generation SI leaders.

Figure 8:

Question	Population	Mean	Standard Deviation
17. Being an S.I leader has helped me deal with student conflict.	First generation (n = 35)	4.14	1.03
	Non-first generation (n = 52)	3.60	1.26
18. Being an S.I leader has helped me become more effective when communicating with professors.	First generation (n = 35)	3.94	1.30
	Non-first generation (n = 52)	4.32	0.85

Figure 8: The population, mean, and standard deviation of responses with respect to first-generation and non-first generation leaders.

Figure 9

Scale	First Generation	Non-First Generation
1	6%	0%
2	12%	6%
3	17%	7%
4	14%	36%
5	51%	51%

Figure 9: Shows the percentage breakdown of respondents to "Being an SI leader helped me become more effective when communicating with professors."

Figure 10

Scale	First Generation	Non-First Generation
1	3%	6%
2	3%	15%
3	20%	25%
4	26%	21%
5	48%	33%

Figure 10: Shows the percentage breakdown of respondents to "Being an SI leader helped me deal with student conflict."

We then looked at the responses from URM SI leaders and non-URM SI leaders. Figure 11 shows the number of respondents, the mean, and standard deviation to questions about awareness of campus resources, effectiveness in handling student conflict, and effectiveness in communication with peers. When looking at the percentage

of respondents who gave a score of 4 or 5 in effectiveness when communicating with peers, we found that there was a very strong increase for URM SI leaders (Figure 12). When looking at how URM SI leaders and Non-URM SI leaders handle student conflict, Figure 13 shows that URM SI leaders felt increased effectiveness in handling student conflict.

Figure 11

Question	Population	Mean	Standard Deviation
15. Being an S.I. leader has made me become more aware of campus resources.	Minority (n = 26)	4.12	1.11
	Non-minority (n = 50)	3.54	1.22
16. Being an S.I leader has helped me deal with student conflict.	Minority (n = 26)	4.31	0.88
	Non-minority (n = 50)	3.66	1.22
17. Being an S.I leader has helped me become more effective when communicating with peers.	Minority (n = 26)	4.50	0.91
	Non-minority (n = 50)	3.98	1.22

Figure 11: The population, mean, and standard deviation of responses with respect to URM and non-URM leaders.

Scale	URM	Non-URM
1	4%	6%
2	0%	8%
3	4%	14%
4	27%	26%
5	65%	46%

Figure 12: Shows the percentage breakdown of respondents to "Being an SI leader helped me become more effective when communicating with peers."

Scale	URM	Non-URM
1	0%	6%
2	0%	12%
3	27%	24%
4	15%	26%
5	58%	32%

Figure 13: Shows the percentage breakdown of respondents to "Being an SI leader helped me deal with student conflict."

5. Future Research

We seek to further understand the impact of leading SI workshops on the SI leader in areas of professional and personal growth with respect to other variables. Future research include: qualitative research on the SI leader; conducting a longitudinal study with incoming SI leaders about how their attitudes change over time; conducting a longitudinal study on incoming SI leaders growth in time management, organizational, and professional skills; conducting a longitudinal study on incoming SI leaders personality psychology; and researching SI leaders backgrounds by looking at their academic records, involvement in on- and off-campus events and organizations, and previous and current professional experiences.

6. Acknowledgments

We thank Dr. Martin Bonsangue and Dr. Todd CadwalladerOlsker for all of their support with this project and for pushing us to reach our greatest potential as researchers and as scholars. We thank Dr. Martin Bonsangue for his patience and his guidance and for developing and fine-tuning every detail of this project. We thank Dr. Todd CadwalladerOlsker for his astounding presence and leadership in the renowned Supplemental Instruction program for the Mathematics Department, which undeniably helped us produce such profound results. Additionally, We acknowledge the support from the Robert Noyce Teacher Scholarship for helping to fund this project.

References

- [1] Lockie, N. M., & Van Lanen, R. J. (2008). Impact of the Supplemental Instruction Experience on Science SI Leaders. *Journal Of Developmental Education*, 31(3), 2-4.
- [2] Stout, M., & McDaniel, A. J. (2006). Benefits to Supplemental Instruction Leaders. *New Directions For Teaching & Learning*, (106), 55-62. doi:10.1002/tl.233
- [3] Zaritsky, J. (2006). Supplemental Instruction at a Community College: The Four Pillars. *New Directions For Teaching & Learning*, (106), 23-31.

Understanding Sophie Germain

Department of Mathematics, California State University, Fullerton

Christina Tran

Advisor: **Dr. Bogdan Suceavă**

Abstract

We hear women graduate from top-tier universities despite being discouraged by their male counterparts, administrators, and professors and each time we are vexed with the lack of support available to them. We seek to explore the mindset of women who were discriminated against but pressed on with their mathematics studies and research. We begin by understanding history to see what empowered and motivated women to move forward with their research and exploration regardless of the oppressed environment they lived in. In particular, we explore French mathematician Sophie Germain (1776-1831), a forward-thinking woman who excelled in and contributed greatly to mathematics. Germain is remembered today for discovering mean curvature, a geometric invariant crucial for the understanding of surface tension. Because the results of her research created important consequences in mathematics, while she was not granted the same opportunities or rights as her male contemporaries, studying Germain and her thought processes in exploring mathematics in a suppressed environment is the topic of interest. In this paper, we present a background of the historical period and of the European political context from the period of the Napoleonic wars, an analysis from several of Germain's texts that have not been analyzed before, translations from *Oeuvres Philosophiques de Sophie Germain, Suivies de Pensées et de Lettres Inédites*, Elibron Classics, Paul Ritti, Paris, 1879, and an analysis of how interesting and relevant are her essays.

Predicting Binary Black Hole Collisions Using Numerical Methods in Collaboration with LIGO

Department of Physics, California State University, Fullerton

Nousha Afshari

Abstract

Detecting astronomical gravitational waves will soon open a new window on the universe. The effects of gravitational waves have already been seen indirectly, but a direct observation of these waves will test Einstein's theory of general relativity under the most extreme conditions. The Laser Interferometer Gravitational-Wave Observatory, or LIGO, will soon begin searching for gravitational waves, and the first direct detections are likely in the next few years. To help LIGO detect as many gravitational waves as possible, a major research effort is underway to accurately predict the expected waves. In this presentation, I will discuss new supercomputer simulations of merging black holes---some of the brightest sources of gravitational waves---that I have completed using the Spectral Einstein Code (black-holes.org/SpEC.html).

A time focusing mass spectrometer for electron attachment to nucleotide molecules

Department of Physics, California State University, Fullerton

Jessica Duron

Abstract

Dissociative attachment (DEA) by sub-ionizing electrons to the molecular constituents of DNA is now understood to be one of the major drivers of cellular damage in cancer patients during radiation therapy. We are currently developing a new spectrometer that will make detailed studies of the DEA process in the primary nucleobases. This spectrometer is essentially a modified time-of-flight mass spectrometer, that employs time focusing and position sensitive detection to make measurements of dissociation pathways, dissociation cross sections and molecular frame dynamics. In this project, we present numerical simulations of the spectrometer performance, to study the mass resolution of our instrument design. Ultimately, understanding how low-energy electrons are affecting the molecules of DNA will enhance cancer therapy by making it less invasive to the patient's health.

Constructing Hybrid Gravitational Waveforms for Merging Black Holes and Neutron Stars

Department of Physics, California State University, Fullerton

Eric Flynn

Abstract

Gravitational waves emitted by neutron-star/neutron-star or black-hole/neutron-star may be used to determine properties of dense matter in the cores of neutron stars. To best measure these properties, we need hybrid waveforms which combine waveform predictions in two different regions: an analytic solution to Einstein's field equations that are accurate when the objects are far apart, and a numerical solution which are computationally expensive but are required when the objects fall closer together. Since the Post-Newtonian approximations are only accurate for objects that are far apart, our measurements of the matter properties would be inaccurate for regions where the objects are close together. So as the two objects spiral toward each other, we want to match a numerical solution for the late inspiral onto a complete post-Newtonian solution, ultimately replacing the the inaccurate portion of the post-Newtonian. To combine these, we can define an inner product for gravitational waves and use it to see how the two waveforms are correlated[1]. With this method we can find the best place to combine the two waveforms, and once the best overlap is found we combine the two with a window function.

References

- [1] Jocelyn S Read, Luca Baiotti, Jolien DE Creighton, John L Friedman, Bruno Giacomazzo, Koutarou Kyutoku, Charalampos Markakis, Luciano Rezzolla, Masaru Shibata, and Keisuke Taniguchi. Matter effects on binary neutron star waveforms. *Physical Review D*, 88(4):044042, 2013.

Visualizing Binary-Black-Hole Simulations and Exploring Initial Data for Merging Black Holes

Department of Physics, California State University, Fullerton

Haroon Khan

Abstract

Gravitational waves are ripples of space and time that are created when the universe unleashes its violent nature in the presence of strong gravity. An example of such violence is the collision and interaction of black-hole binary systems. In order to detect and physically study the gravitational waves emitted by merging black holes with ground based detectors, we must accurately predict how the waveforms look and behave. This can only be done by numerically simulating black-hole mergers on supercomputers, because all analytical approximations fail near the time of merger. The initial data for such mergers determine the behavior of the waveforms: Specifically, initial data for a simulation describe a binary black hole at a moment in time when the two holes have spiraled together and are almost in a circular orbit as they are about to collide. Using the Spectral Einstein Code, I constructed conformally flat initial data for merging black holes with equal masses, varying spins, and far separation in order to generalize the data and results by Lovelace *et al.* [1]. Furthermore, to visualize binary-black-hole mergers, I also rendered 3-dimensional animations of previous simulations by the SXS collaboration (available at black-holes.org/waveforms). I automated the process of creating animations and putting a number of the simulations in one video in order to visually compare them.

1. Introduction

Gravitational waves are ripples of space and time that are created when the universe unleashes its violent nature in the presence of strong gravity. Black holes are astrophys-

ical objects which result from imploding stars. They have such a strong gravitational force that nothing can escape from inside a hole's horizon (surface), including light [2] [3]. Furthermore, black holes warp time and space in such an intense manner that a distant observer would see time sufficiently close to the surface of a black hole flow millions of times slower than a distant observer's local time [2]. Gravitational waves are ripples of space- time curvature, which also are predictions of Einstein's theory of General Relativity. Studying coalescing binary- black-hole systems, which are one of the most promising sources of gravitational waves in the universe, gives us insight to the dynamics of gravity and the behavior of black holes when they interact [4].

The coming era of gravitational wave astronomy will enable us to learn and explore the nature of space-time under the most extreme conditions. Currently, several gravitational-wave detectors have been installed in different parts of the world, and a few more are on their way. These detectors, such as LIGO (the Laser Interferometer Gravitational Wave Detector) [5], use lasers and sensitive mirrors to detect subatomic (smaller than 1000 times the radius of a proton) shifts in lengths along two perpendicular arms. We need accurate predictions of the expected waves to help find gravitational wave signals in the detector's data. LIGO detectors have not yet found any gravitational waves, but Advanced LIGO is set to begin searching for gravitational waves with much better sensitivity in the next two years, with high confidence that the gravitational waveforms will be directly seen for the first time (e.g Abadie *et al.* [6]).

One of the most important sources of gravitational wave is the collision and interaction of binary-black-hole (BBH) systems. A binary system is a system in which two objects interact; black-hole binary systems are astronomical objects in which one object is a black hole and the other is a neutron star or another black hole. This research focuses on a system in which two black holes collide. When black holes interact with each other, they orbit one another and energy is radiated in the form of gravitational waves; the loss of energy leads to the black holes getting closer and closer, eventually colliding and forming a single, more massive black hole.

Merging binary black holes are thus an important astrophysical target for gravitational wave-detectors on Earth. By simulating BBHs, we work toward modeling the emitted gravitational waves, to help make, as accurately as possible, the many gravitational-wave templates used to search for signals in gravitational-wave detectors. To understand the detected waveforms' sources and to maximize the number of detections, we need precise understanding of the expected gravitational waves.

By constructing initial data on the ORCA (Orange county Relativity Cluster for Astronomy) supercomputer at CSUF, I have explored how the conformally flat initial data solver determines the same angular frequency (Ω_7) for different spins of equal mass black holes with a far separation. I also have created visual a 3D movie of multiple simulated black hole collisions that give the viewer an intuitive understanding of different holes' behaviours as they spiral together and merge.

2. Methods And Procedures

A. Creating Visualizations of the SXS Catalog

The Simulating eXtreme Spacetimes collaboration has created a catalog of 178 colliding black holes and the gravitational waves that they send out across the universe [7]. To get a visual understanding of the different black-hole collision simulations in the catalog, I rendered a 3D visualization that includes all of the simulations in one video. The first step of this project required me to select the highest resolution (i.e. most accurate) version of each simulation. I did this by writing a bash shell script. Next, I wrote another bash script that converts the data from HDF5 (an open-source binary format) to a plain

text format that other tools can read. Once the data was converted, I downloaded it to a local workstation. By developing a python script, I generated jpeg image frames for each simulation using ParaView, an open-source 3D visualization program. I then appended the frames together using a final bash script that I created to make a set of jpeg frames, with each frame showing data from all of the simulations. Finally, I merged the frames into a movie using a third-party utility.

B. Recreating Initial Data using conformally-flat method

The initial data for a simulation represents a moment in time when two holes have spiraled together from a large distance are almost in a circular orbit and are about to collide. The initial data must satisfy Einstein's constraint equations.

Two methods are available to construct initial data include conformally flat (CF) [1] and superposed Kerr-Schild (SKS). When we measure distance between two points on a flat plane, we use the Pythagorean theorem,

$$S^2 = x^2 + y^2.$$

However, if we want to measure the distance between two objects in a curved 3-dimensional space the following equation is used:

$$ds^2 = \sum_{i,j} g_{ij} dx^i dx^j = g_{ij} dx^i dx^j$$

The last equality introduces the Einstein summation, where repeated indices imply summation. Here g_{ij} depend on where you are in the space (i.e. they are functions of your position). Note that because multiplication commutes, $g_{ij} = g_{ji}$. These coefficients together make up the "metric". When we construct initial data, we assume that the initial metric has the form

$$g_{ij} = \psi^4 \tilde{g}_{ij}$$

where \tilde{g}_{ij} is called the "conformal metric" and ψ is called the "conformal factor." Both depend on where you are in the space.

The conformally flat initial (CF) data sets take the form

$$\tilde{g}_{ij} = f_{ij}$$

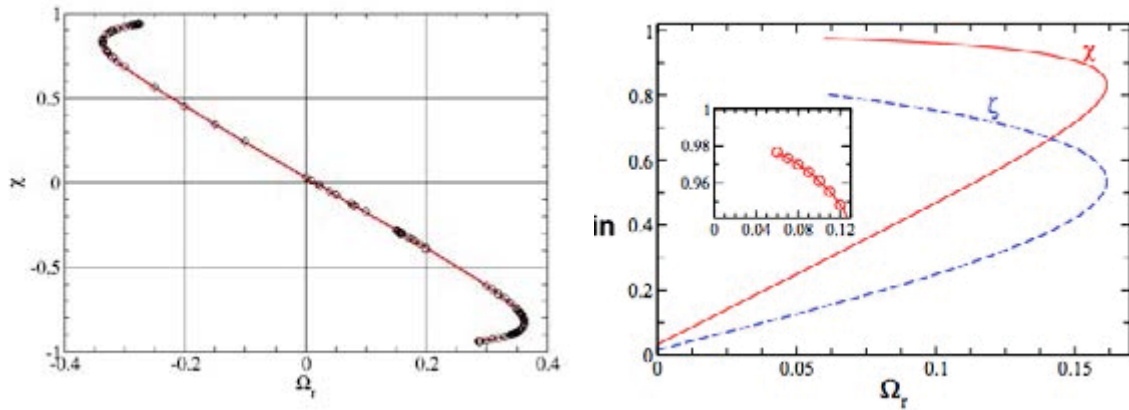


Figure 1: These plots show the black hole's spin vs Ωr (angular frequency). Top: This plot shows the results that I have generated using the CF initial data method. Bottom: The spin of the black hole vs a parameter Ωr that indirectly controls the spin of each hole. Each value of Ωr results in two different spin values, one for each initial guess giving solutions on both a "lower branch" and an "upper branch". [1]

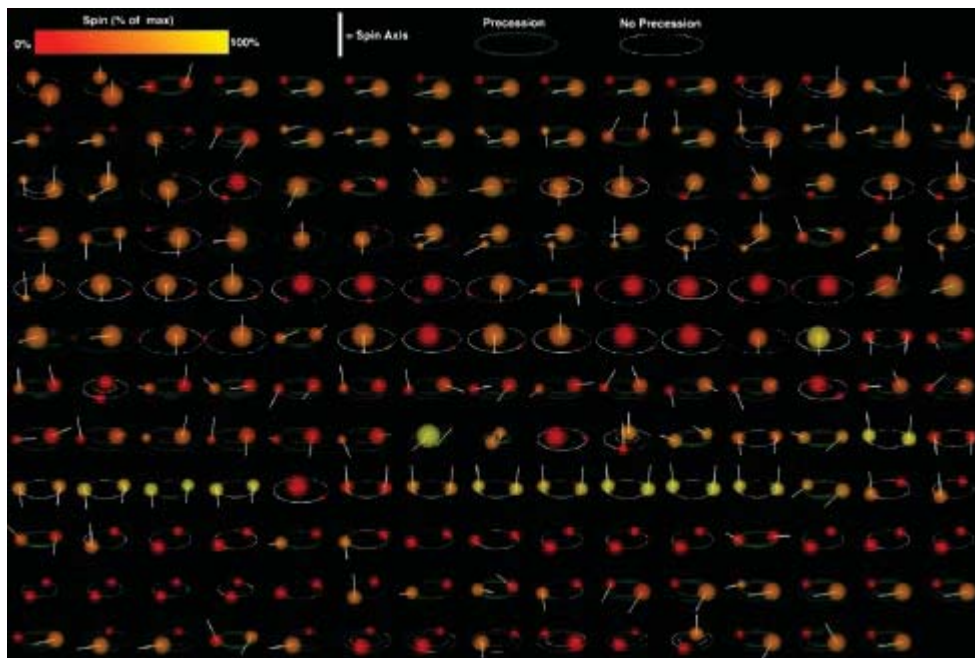


Figure 2: The figure depicts that a still image of multiple BBH simulations included in one video. The relative sizes and positions of the holes are indicated by spheres (enlarged for clarity).

where f_{ij} is the metric of flat space. We assume the space-time around the black holes is conformally flat, i.e. proportional to flat space time. Conformally flat initial data is usually used because it's easier to construct numerically. But we are interested in exploring a particular feature it exhibits: non-uniqueness.

In the case of SKS initial data, \tilde{g}_{ij} takes into account the spacetime curvature near the black holes based on their spin. It adds the spacetime curvature for the two spinning black holes in a weighted superposition.

Following reference [2], I used SpEC [8] to construct initial data for black holes with equal mass and equal spins aligned or antialigned with the orbital angular momentum. To solve Einstein's constraint equations, we start with an initial guess and then adjust it to approach the solution Pfeiffer *et al.* [9]. However, different initial guesses can lead to different initial data (e.g. data with different spins) [10]. For the same angular frequency parameter, Ωr there are two different solutions of the constraint equations, each with different spin values. I made initial data using the conformally flat method of equal mass black holes at different spin intervals. For each set of initial data, I increased the Ωr to get higher and higher spins. I then compared the input parameters and the hole's spins (calculated by the code) to those determined by Lovelace *et al.* [1] with the ultimate goal of obtaining the highest spin possible using the CF method.

3. Results

The visualization that I created was based on the Kepler Orrery II [11] a video. A still image of the animation of my visualization is shown in Fig. 2. This animations shows the trajectories and spin of the holes from the high- est levels of the simulations in the catalog [12]. I plan to further improve this movie by making another version that will include all the simulations along with the gravitational waves they emit.

I have made several sets of initial data. Fig. 1 bot- tom shows the results found by Lovelace *et al.* [1] while the top plot shows the data that I have constructed. I extended Lovelace *et al.* [1] to include antialigned spins. My future work will be to better understand the Spectral Einstein code [13] so that I can evolve "upper branch" data. After which, I compare the results with that of the SKS method.

4. Conclusion

Gravitational waves were predicted in 1916 by Einstein's theory of general relativity, and we are on the cusp of detecting them for the first time. Experts predict that with the implementation of Advanced LIGO, gravitational waves will be seen for the first time. Predicting the waveforms LIGO will see through simulations is becoming more important than ever, these predictions can be made by running more simulations with different sets of initial data and adding them to an expanding catalog. When successfully detected and studied, scientists hope to use gravitational waves to test Einstein's theory of relativity under the most extreme conditions. My research has helped contribute towards the long term goal of creating simulated gravitational waveforms for Advanced LIGO and also has helped visualize the behaviours of merging black holes, an important source of gravitational waves for LIGO.

5. Acknowledgements

This research is part of the Gravitational Wave and Physics and Astronomy Center at Cal State Fullerton, which studies gravitational waves computationally, theoretically, and experimentally. This work was supported in part by NSF grant PHY-1307489, by Dept. of Ed. grant P031C110116-12, and by California State University, Fullerton. Some of the computations in this pa- per were performed on the ORCA cluster supported by NSF grant PHY-1429873, by the Research Corporation for Science Advancement, and by California State University, Fullerton.

References

- [1] G. Lovelace, R. Owen, H. P. Pfeiffer, and T. Chu, Physical Review D 78, 084017 (2008).
- [2] K. S. Thorne, *Black holes and time warps: Einstein's outrageous legacy* (WW Norton & Company, 1994).
- [3] G. Lovelace, "Presentation Slides,".
- [4] B. Garcia, G. Lovelace, L. E. Kidder, M. Boyle, S. A. Teukolsky, M. A. Scheel, and B. Szilagyi, Physical Review D 86, 084054 (2012).
- [5] G. M. Harry, L. S. Collaboration, *et al.*, Classical and Quantum Gravity 27, 084006 (2010).
- [6] J. Abadie, B. Abbott, R. Abbott, M. Abernathy, T. Accadia, F. Acernese, C. Adams, R. Adhikari, P. Ajith, B. Allen, *et al.*, Classical and Quantum Gravity 27, 173001 (2010).
- [7] "Spectral Einstein Code," <http://www.black-holes.org/>, year = 2013.
- [8] "Spectral Einstein Code," <http://www.black-holes.org/SpEC.html>, year = 2013.
- [9] H. P. Pfeiffer, L. E. Kidder, M. A. Scheel, and S. A. Teukolsky, Computer physics communications 152, 253

Parameter Estimation using Markov chain Monte Carlo

Department of Physics, California State University, Fullerton

Sean Hatcher

Abstract

Parameter estimation is a process applied to a gravitational waveform in order to find properties of the neutron stars or black holes that generated it. It uses an approximation method called Markov chain Monte Carlo (MCMC) to estimate the most likely parameters.

MCMC tends to have smaller statistical error than other parameter estimation methods. Error in some statistical methods depends exponentially on number of dimensions in the parameter space, making them unfeasible for measurements with many parameters.

It does a random walk through the parameter space, comparing to measured values to determine probability of a set of parameters. The location within our parameter space that MCMC chooses to sample from is crucial. Taking a large number of observations at the wrong location would not be useful. Since each step taken is determined by the probability of the parameters, we can sample the relevant space more quickly than if we were to sample uniformly throughout all of the parameter space.

This method of moving through parameter space to determine probability of parameters generates a Bayesian statistic called posterior probability. Posterior probability is the probability of a set of parameters given observed data. It is different from the likelihood function, which is the probability of data, given certain parameters.

MCMC does not need an estimate of all of the parameters to begin. It can start anywhere in the parameter space. It then works its way to a region of high probability. It then discards the previously sampled data. This is known as “burn-in”, or the period before a Markov chain

gets to a region of consistently high probability. The data taken during burn-in is discarded. The deciding factor for when to cut off data is sometimes unclear. The length of time burn-in takes is variable, and not a good indicator. A better way is the difference in probabilities as more samples are added. When the difference is below a preset threshold, the previous data is discarded, and calculation can begin.

Conclusion

MCMC works well where other methods would be unreliable, or ultimately fail, such as when the parameters are nonlinear. It also avoids the curse of dimensionality, which exponentially increases the time needed to get an accurate estimate as more dimensions are added. Increasing dimensionality also exponentially increases computing time, and is a major source of errors. Both of these problems are mitigated by the “randomness” of Markov chain sampling. Markov chain lets us take relatively few data points, and still returns a reliable sampling of the model. It accomplishes this by spending time in more probabilistically accurate portions of the parameter space. Before MCMC can sample from these high probability zones, it must “burn-in”, or go through unwanted areas, first. Some assumption of parameter uniformity must be made, which would induce an error bias. MCMC samples frequently from the higher probability locations, and this overcomes any bias from the initial assumption.

Studying How Spin Affects Orbits of Colliding Black Holes

Department of Physics, California State University, Fullerton

Kevin Kuper

Abstract

The Advanced Laser Interferometer Gravitational-wave Observatory (Advanced LIGO) [1] will soon begin searching for gravitational waves, or ripples in space time. This is especially challenging because the distances between Earth and even the brightest sources of gravitational waves, such as colliding black holes and neutron stars, are so great that the waves are very faint by the time they reach Earth. Predictions of the expected waves, which can only be made using supercomputer simulations are essential for helping Advanced LIGO detect as many gravitational waves as possible. Codes such as the Spectral Einstein Code (SpEC) [2] predict the behaviors of orbiting pairs of black holes (i.e. black-hole binaries). As two black holes orbit each other, they emit gravitational waves, and they spiral together, eventually colliding to make a new, larger black hole. This article discusses how black-hole spins affect the holes' orbits, causing some systems to undergo more orbits than others depending on the orientation of the holes' spin axes. The analysis relies on numerical simulations by the Simulating eXtreme Spacetimes (SXS) collaboration performed using SpEC [3, 4].

1. Introduction

The most violent events in the universe emit gravitational waves, or ripples in space-time. Einstein's theory of general relativity predicts these waves' existence, but they have not yet been directly measured. Detecting gravitational waves will open a new window on the universe and will test general relativity under the most extreme conditions.

Soon, gravitational-wave detectors such as [1, 5, 6, 7] will begin searching for gravitational waves. These waves are very faint when they reach Earth because their sources are so far away. One of the most promising sources of gravitational waves is a black-hole binary (two black holes orbiting each other). When two black holes are orbiting each other, they spiral together and will eventually merge, forming a single remnant black hole. In the process, the binary emits gravitational waves.

A black hole is a star so massive that the star's gravity overwhelmed the forces opposing it when the star's fuel is exhausted. Once this happens, the star collapses, and a horizon forms. Anything that crosses this horizon, even light, can never escape back across. Black holes are characterized by their masses and spins. The mass determines how big the hole is; how fast the hole spins determines its shape.

Gravitational waves are ripples in space-time curvature. Space-time curvature is also gravity. The presence of mass curves space-time. The greater the curvature at a particular point, the stronger the gravitational pull an object at that point experiences.

To help detectors find as many of these waves as possible and to learn as much as possible about their sources, scientists perform simulations of black-hole binaries and the waves they produce using supercomputers. In particular, the simulations are necessary for predicting the final seconds of the holes' orbits as they spiral together, their merger, and the ringing down of the remnant black hole. The simulated gravitational waveform is then added to a catalog, which consists of many different gravitational waves produced by simulations of different sources. Having accurate waveforms is crucial in producing meaningful predictions of the waves Advanced LIGO will observe.

2. Methods

The gravitational waves produced by black-hole binaries are affected by the mass and spin of each hole. Different spin alignments and mass ratios produce unique gravitational-wave signatures. Here, we employ the use of the spin parameter χ , defined as $\chi = \frac{S}{M^2}$, where S is the spin angular momentum of the black hole and M is the Christodoulou Mass of the black hole. With this definition, $\chi \leq 1$ (in units where Newton's constant G and the speed of light c are $G = c = 1$). A black hole that is not spinning will have $\chi = 0$, and a black hole that is spinning at the theoretical maximum will have a $\chi = 1$. Recent developments in computational methods have made simulating black holes with a variety of spins possible [8, 9, 10, 11], including $\chi \approx 1$ [12, 13, 14, 15, 16].

This paper focuses on the case where both black holes are the same mass and have equal spins aligned or anti-aligned (in the same or opposite direction as) with the orbital angular momentum. With these choices, the spins' magnitude has an effect on the orbital trajectories of the holes commonly called "orbital hangup." This effect was discovered by Damour using an effective-one-body model to approximate the motion of two orbiting black holes [17], and demonstrated for numerical simulations of black-hole binaries by Campanelli, Lousto, and Zlochower [18]. When the spins are aligned with the orbital angular momentum, the holes spiral together more slowly, undergoing more orbits before merger, with the effect increasing with greater spin magnitudes (i.e. with faster spins). The opposite is true when the spins are anti-aligned with the orbital angular momentum. For greater spin magnitudes, the holes spiral together faster. Recent progress in computational techniques allow us, for the first time to examine this effect at spins near the theoretical maximum.

Learning more about the orbital hangup effect could help illuminate the effects of spin on the gravitational waves produced by black hole binaries since the orbital motion influences the waves. We provide a quantitative description of the effect by examining 25 simulations produced by the SXS collaboration [4, 15].

Each simulation contains the locations of the black holes, the holes' masses and spins, and the space-time curvatures for each time step of the simulation, as well as the emitted gravitational waves. In our analysis, we will examine the gravitational waves, the spins, and the trajectories of the black holes.

3. The Orbital Hangup

In the case where the spins of the black holes are both in the same direction as the orbital angular momentum, we first explored the relationship between the spin and the number of orbits by examining the holes' trajectories from the 8 highest-spinning simulations in the SXS catalog. Because each simulation began at different initial separations with slightly different initial conditions, simply counting the number of orbits in each simulation would not be sufficient, since these differences also affect the number of orbits. We decided to select an orbital frequency that was common to all of the simulations and then count the number of orbits from the time when the holes orbited at that frequency until the holes merged.

We calculated the locations of the holes and the orbital phase (i.e. the angle swept out by the holes) for each time in each simulation. We then took a time derivative of the phases to compute the orbital frequency, choosing a common orbital frequency $M\omega_0 = 0.016$ (where here and throughout this paper, $G = c = 1$). We compared when the holes orbited at this frequency to the phase at the time of merger. The latter is less trivial, as it involves calculating a precise time when a common horizon forms around both the black holes. We relied on previous work for the merger times [19]. With these two phases, we computed the number of orbits.

$$\Delta\phi = \phi_{\text{merger}} - \phi_{\text{initial}}$$

$$\text{Orbits} = \frac{\Delta\phi}{2\pi}$$

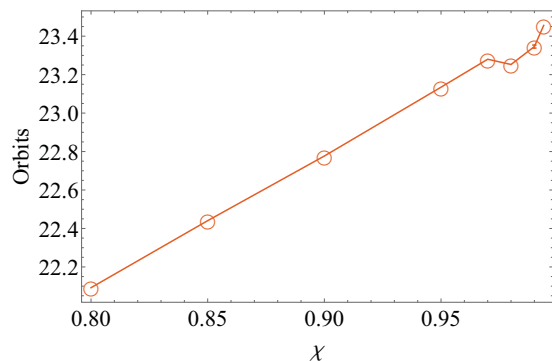


Figure 1: Plot of the number of orbits as a function of the spin parameter χ . Beginning times were taken to be the moment when the orbital frequency reached a value of 0.016. Error bars were calculated from different resolutions of each simulation.

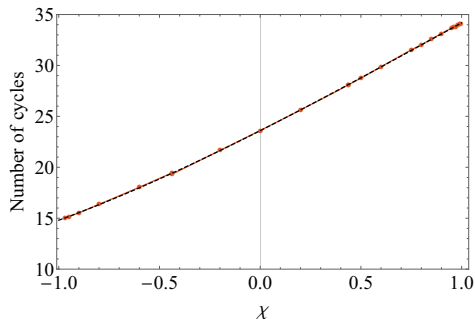


Figure 2: Plot of the number of gravitational wave cycles as a function of the spin parameter χ . A cubic fit is given by the dashed line. The waves are counted between the moment when the gravitational-wave frequency reached a value of 0.039 and the moment when the wave amplitude is maximal (i.e. at the time of merger).

The results are shown in Figure 1. The relationship between the orbits and the spins is roughly linear. However, there are some deviations from the overall linear pattern especially at high spins. We suspected that these deviations were the result of differences between the coordinate systems within the simulation and from difficulties in finding an unambiguous value for the time of merger.

In order to obtain a less ambiguous quantitative description of the effect, we chose to examine the dominant ($l = m = 2$ spherical harmonic) mode of the gravitational waves. These waves are measured at large distances from the holes and then extrapolated out to infinity so there is less dependence on specific coordinate systems. We chose to start at a gravitational wave frequency of $M\omega_{l=2,m=2} = 0.039$. The waves will have twice the frequency of the orbital frequency because of the symmetry of the quadrupolar $l = m = 2$ waves (this part of the waves is symmetric about 180° rotations).

Instead of taking data from only the highest spinning cases, we examined 25 simulations with equal mass and spin magnitude with spins either aligned or anti-aligned with the orbital angular momentum. Using a similar calculation to that used with the trajectories, we found the relationship between the spin χ , and the number of gravitational wave cycles (equal to twice the number of orbits). Both Fig. 2 and Fig. 3 summarize their relationship. Even for the highest spinning cases where the spins are aligned with the orbital angular momentum ($\chi > 0$), the relationship is nearly linear. The inclusion of the anti-aligned cases ($\chi < 0$) shows some nonlinear effects in the spins. The dashed line

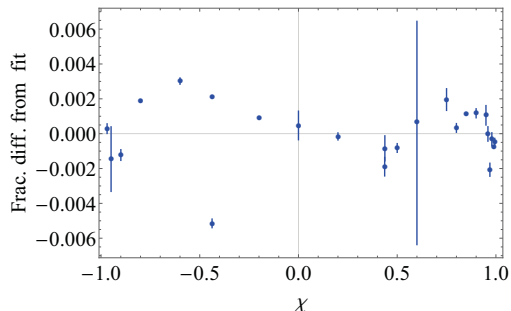


Figure 3: Plot of the fractional differences between the data and a cubic fit for the 25 cases examined. Error bars were calculated from different resolutions of each simulation.

in Figure 2 is a cubic fit to the data, with Figure 3 showing the fractional differences. Given here is the cubic fit:

$$\text{Cycles} = 23.5965 + 10.006\chi + 0.895981\chi^2 - 0.318349\chi^3$$

4. Conclusion

We have seen that there does exist an approximately linear relationship between the spins and the number of orbits the black holes undergo when the spin axes are both in the same direction as the orbital axis. This is seen in both the gravitational waves and the trajectories of the black holes. While our analysis of the gravitational waves was a more robust measure of the relationship between the spins and the orbits since that measure is less ambiguous, there were still differences from the cubic fit greater than our estimated uncertainties. Simulations with even higher degrees of accuracy may be necessary to resolve these differences to verify whether they are physical or a result of numerical error.

5. Acknowledgments

This work was supported in part by NSF grant PHY-1307489, by Dept. of Ed. grant P031C110116-12, and by California State University, Fullerton. Some of the computations in this paper were performed on the ORCA cluster supported by NSF grant PHY-1429873, by the Research Corporation for Science Advancement, and by California State University, Fullerton.

References

- [1] G. M. Harry (Ligo Scientific Collaboration), *Class. Quant. Grav.* **27**, 084006 (2010).
- [2] K. S. Thorne, *Black holes and time warps: Einstein's outrageous legacy* (WW Norton & Company, 1994).
- [3] <http://www.black-holes.org/waveforms>.
- [4] A. H. Mroue, M. A. Scheel, B. Szilagyi, et. al., *Phys. Rev. Lett.* **111**, 241104 (2013) arXiv:1304.6077 [gr-qc]
- [5] The Virgo Collaboration, "Advanced Virgo Baseline Design," (2009), [VIR-0027A-09].
- [6] The Virgo Collaboration, "Advanced Virgo Technical Design Report," (2012), [VIR-0128A-12].
- [7] K. Somiya and the KAGRA Collaboration, *Class. Quantum Grav.* **124007** (2012).
- [8] J. Centrella, J. G. Baker, B. J. Kelly, and J. R. van Meter, *Rev. Mod. Phys.* **82**, 3069 (2010).
- [9] H. P. Pfeiffer, *Class. Quant. Grav.* **29**, 124004 (2012), arXiv:1203.5166 [gr-qc].
- [10] M. Hannam, (2013), arXiv:1312.3641 [gr-qc].
- [11] A. Le Tiec, *Int. J. Mod. Phys. D* **23**, 1430022 (2014), arXiv:1408.5505 [gr-qc].
- [12] G. Lovelace, M. A. Scheel, B. Szilagyi, *Phys. Rev. D* **83** 024010 (2011), arXiv:1010.2777 [gr-qc].
- [13] G. Lovelace, M. Boyle, M. A. Scheel, B. Szilagyi, *Class. Quantum Grav.* **29** 045003 (2012) arXiv:1110.2229 [gr-qc].
- [14] G. Lovelace, M. A. Scheel, R. Owen, et. al., (2014), arXiv:1411.7297 [gr-qc].
- [15] M. A. Scheel, M. Giesler, D. A. Hemberger, et. al., (2014), arXiv:1412.1803 [gr-qc].
- [16] S. Dain, C. O. Lousto, Y. Zlochower, *Phys. Rev. D* **78**, 024039 (2008), arXiv:0803.0351 [gr-qc].
- [17] T. Damour, *Phys. Rev. D* **64**, 124013 (2001), arXiv:gr-qc/0103018 [gr-qc].
- [18] M. Campanelli, C. O. Lousto, and Y. Zlochower, *Phys. Rev. D* **74**, 041501(R) (2006), gr-qc/0604012.
- [19] G. Lovelace, M. A. Scheel, R. Owen, et. al., arXiv:1411.7297 [gr-qc], accepted for pub. in CQG in press (2015).

Orbital Dynamics of Merging Neutron Stars

Department of Physics, California State University, Fullerton

Phillipe D. Rodriguez

Abstract

A neutron star is an extremely dense remnant of a supernova. When two neutron stars orbit each other, they will emit gravitational waves - ripples in space-time predicted by Einstein - and slowly fall closer together. When they merge, it is hypothesized that they will form into a massive neutron star or collapse into a black hole. Together with my advisor Dr. Jocelyn Read, I will explore a time evolution model of binary neutron star systems, over the last orbits before the merger based upon hypothesized resonant frequencies, varying equations of state, and an expected range for neutron star masses. The resonant frequency of a neutron star is the natural frequency at which it oscillates. As the neutron stars fall together, the frequency of the binary system will increase. When it matches the resonant frequency, extra energy is lost from the orbit, accelerating the merger. The equations of state are different predictions for the description of matter inside the star. It will be shown how the time evolution model depends upon each of the parameters that impact the binary neutron star system. I will compare the time evolution model to numerical-relativity simulations with similar system parameters. Then, it can be determined how well the model agrees with numerical simulations over the last orbits. If the model matches well enough, it could be used for analysis of future gravitational-wave signals.

About the Authors



Nicholas Armada

Nicholas Armada is a senior pursuing a Bachelor of Science degree in Biochemistry. He is a part of the Maximizing Access to Research Careers (MARC) program, which is funded by the National Institutes of Health. He currently works in the laboratory of Dr. Peter de Lijser, exploring the reactive intermediates involved in photo-induced, oxidative cyclization reactions of oximes and oxime ethers. After acquiring his bachelors degree, he plans to apply to PhD programs in synthetic organic chemistry or materials science. When Nicholas is not in the lab, he enjoys playing drums and riding his bicycle.



Nousha Afshari

Nousha Afshari is a physics major who, in 2013, joined the Gravitational Wave Physics and Astronomy Center at CSUF (GWPAC). Her research consists of predicting binary black hole collisions using numerical methods and maintenance of the research group's super computer. The active role she plays in research collaboration brought on the realization that successful programs need community involvement. This led her to take on leadership positions as a Physics Club officer and NSM Inter-Club Council member to create excitement among the student body. From these positions, she has recruited more students to participate in on and off campus internships than previous representatives.



Christopher Bang

Christopher Bang received his Bachelors of Science in Mechanical Engineering, graduating cum laude in 2013. Christopher took courses in computer science and mathematics to supplement his academic career. He is pursuing a Masters of Arts in Mathematics while studying child development and pedagogy, and is expected to graduate in the spring of 2016. He seeks to understand the historical development of theorems taught in algebra and geometry, and thus teach and tutor in those subjects. During his free time, Christopher reads science fiction and fantasy novels in conjunction with applying academic material to problem solving scenarios.



Arthur Barraza

Arthur Barraza is a senior pursuing a Bachelor of Science degree in Biological Sciences with emphasis in Marine Biology. He will be attending CSU Long Beach in the fall to obtain his masters in Biology investigating toxin accumulation in Green Sea Turtles (*Chelonia Mydas*) with Dr. Lowe. Arthur is also finishing a research project that investigates the reproductive morphology of Black Perch (*Embiotoca Jacksoni*). He is often found studying inside the SCERP room in McCarthy Hall.



Joseph Chavoya

Joseph Chavoya is a senior Mathematics major set to graduate in the spring 2015 from California State University, Fullerton. In addition to his undergraduate research in collaboration with Dr. Christopher Lyons, Joseph has also participated in the 2013 PUMP program at UC Northridge, as well as the summer undergraduate research experience MSRI-UP 2014. Post-graduation, Joseph hopes to continue pursuing his goal of attaining a Ph.D. in pure mathematics.



Jeremy Cordova

Jeremy Cordova is an alumni of CSUF who conducted Paleotsunami research at the Los Penasquitos Lagoon, in San Diego, for the purpose of geohazard assessment. He is attending Western Washington University for a masters in structural geology and tectonics, working on the development of the Cascade Mountains. Jeremy spends his free time exploring the American West in search of great places to understand the geology of the region, and enjoy a night outdoors. Once finished with his masters Jeremy plans to go on to a career with the USGS and earn a PHD, so that he may teach and do research as well.



Precious Daileg

Precious Daileg is a senior pursuing a Bachelor of Science Degree in Biology with a concentration in Cell and Developmental Biology. She works in Dr. Merri Lynn Casem's education lab, looking at different aspects that influence students' learning and how to help students perform better in biology courses. She is also a Supplemental Instruction Leader for the Biology Department with her specialty being Biol 172: Cellular Basis of Life. She will be applying to the teaching credential program at CSU Fullerton upon graduation to continue her path to attaining a teaching career in secondary education.



Criselda Dillague

As a third year student, Criselda Dillague is majoring in Biology concentrating on Molecular Biology and Biotechnology with a Chemistry minor. She has been involved in research since Fall 2014 and is planning to continue until she graduates. Since beginning her research Criselda has presented at two conferences: Southern California Conference for Undergraduate Research(SCCUR) and California State University Biotechnology Symposium(CSUPERB). After CSUF, Criselda hopes to pursue a PhD and do research on her own.



Mirna Dominguez

Mirna Dominguez is currently in her fifth year and graduating spring 2015 with a Bachelors in Mathematics. She has spent this past year working as a Supplemental Instructor, Transforming Academic and Cultural Identidad through Biliiteracy (TACIB) assistant researcher and grader. Currently, she is a Louis Stokes Alliance for Minority Students (LSAMP) scholar working with her mentor Dr. Sam Behseta and a Math Alliance scholar. Along the side of her mentor, Mirna has worked on analyzing categorical data through non-parametric techniques. She is looking forward to attending graduate school at Cal State University, Fullerton and pursuing a Ph.D. in statistics.



Jessica Duron

Jessica Duron is a third-year undergraduate majoring in Physics and Biology. Working with Dr. Leigh Hargreaves, she is currently designing a new spectrometer for studying the dissociative electron-attachment process (DEA) in the primary nucleobases. The data from Jessica's research will contribute to enhanced radiation dosage calculations, leading to improvements in patient safety for cancer sufferers. As a result of her research experience, Jessica has developed a strong interest in medical physics that has inspired her to apply to medical school with a specialty in radiation oncology.



David Eng

David Eng is a senior graduating this spring with a BS in molecular biology and biotechnology. He has conducted research with Dr. Esther Chen for the past 2 years. He also has served as a tutor at the NSM Opportunity Center (OCSAMS), a member of the NSM Inter-club Council, and an officer for Student Health Professions Association. The past 3 summers, he went on several medical mission trips to Mexico and Honduras. In his free time, he enjoys board games, baseball, and spending time with his 9 younger siblings. This fall, David will begin medical school at Loma Linda School of Medicine and his career goal is to become a physician and serve on medical mission trips around the world.

Eric Flynn

Eric Flynn is a third year undergraduate double major in applied mathematics and physics. He began his gravitational wave research under Dr. Jocelyn Read with a Mentoring Undergraduates in Research grant his sophomore year. From there he began to research a method of using gravitational waves as a measurement of dense matter properties of compact stars. While working with Dr. Read, Eric has developed a passion in dense matter and nuclear physics and hopes to find more interesting problems in this field that he can hopefully work on later in his academic career.



Brian Gadbois

Brian Gadbois is a senior pursuing a Bachelor's of Science in Geology. He is an active member of the Geological Society of America, where he attends section and national meetings semi-annually. Brian and co-authors were recently awarded "Outstanding Undergraduate Research" by the Cordilleran Section of GSA for their work on the Sierra Nevada Frontal Fault Zone in Owens Valley, CA. After graduation, Brian will seek his Master's Degree with a focus in Geophysics. His academic interests include Quaternary Tectonics, Geophysics, Geography Information Systems, and Military Geology. Brian's favorite pastime is photographing and sketching landforms associated with active faulting.



Kelly Hartmann

Kelly Hartmann currently teaches mathematics at Brea Junior High School in Brea. She completed her Bachelors of Arts in Mathematics and her Single Subject Credentials at California State Univeristy, Fullerton, graduating Cum Laude. This year she is pursuing a Master's degree in Secondary Education and is a part of the Noyce Grant at CSUF. During the last few years as a CSUF student, Kelly worked on education research in the mathematics department. She is currently working with Dr. Bonsangue on the impact of supplemental instruction on the SI leader.

Sean Hatcher

Sean Hatcher is a fifth-year undergraduate majoring in physics. He began his research in fall of 2013 at Gravitational Wave Physics and Astronomy Center working with Dr. Jocelyn Read on parameter estimation of modeled signals of gravitational waves generated by inspiraling binary neutron stars and black holes. He has helped to install and update both hardware and software on ORCA, the supercomputer used by GWPAC to run simulations. Through Sean's experience in GWPAC, he has developed an interest in both astrophysics and computational physics.



Christopher R. Hugh

Christopher Hugh is a former working professional and current senior pursuing a Bachelor of Science degree in Geology. He is set to graduate this summer after attending field camp and investigating the regional geology of Montana at the University of Montana-Western. He also will be attending a hydrogeology field camp at Western Michigan University. This fall, Christopher will begin his Master of Science degree in Environmental Studies, with a focus in hydrogeology. Eventually, it is Christopher's goal, that he will have a successful career in the fields of environmental and hydrogeology.



Shreya Havaladar

Shreya Havaladar is currently a sophomore at Troy High School in Fullerton. She has a deep interest in number theory and trigonometry, and is a dedicated member of Fullerton Math Circle. Along with mathematics, she also enjoys programming and chemistry. She is on the water polo and swim team at her high school, and serves on the board of a club that provides books for underprivileged children. Shreya aspires to major in computer science and applied mathematics during her upcoming college years, and is set to graduate from Troy in 2017.



Aneta Jelowicki

Aneta Jelowicki is a fourth year pursuing a Bachelor of Science degree in Biochemistry. She is set to graduate in the spring of 2016. Aneta is a scholar in the program called Maximizing Access to Research Careers (MARC), where she is working on the synthesis of small organic molecules to use in biochemical and biological assays to determine how the structure of the molecule affects cancer cell lines. Her educational career goal is to be accepted into a Ph.D. granting program, specifically one that focuses on medicinal chemistry.

Haroon Khan

Haroon Khan is a third year community college transfer student majoring in Electrical Engineering. He moved to Southern California in Summer 2011 and began his education at Santiago Canyon College. At the college Haroon obtained a summer research internship at CSUF with Dr. Geoffrey Lovelace, doing simulations of merging black holes. The research position along with CSUF's great engineering program motivated Haroon to transfer to CSUF. Along with being a research assistant, Haroon also works with STEM2 where he helps to enhance STEM transfer awareness to underrepresented communities at local community colleges. Haroon's long-term goal is obtain a graduate degree in Electrical Engineering specializing in avionics and satellite communication systems.



Michael Ko

Michael Ko will graduate Cum Laude with a Bachelor of Science in Biochemistry. He is a Dean's Scholar in the College of Natural Sciences and Mathematics. During college, he was a member of the research program called Maximizing Access to Research Careers (MARC) and conducted chemistry research under Dr. Peter de Lijser starting in his sophomore year. He received the Glenn Nagel Scholar award for his undergraduate research. For his senior honors project, Michael studied the photoinduced oxidative cyclizations of *o*-aryalkynoximes. Michael will attend graduate school in the fall to pursue a chemistry doctorate degree.



Kevin Kuper

Kevin Kuper is a fourth-year undergraduate majoring in Physics. His experience in undergraduate research began in the Fall of 2013, where he accepted the invitation to work with Dr. Lovelace in the Gravitational Wave Physics and Astronomy Center (GWPAAC) at CSUF. There, he worked with supercomputers and developed skills to conduct research on the gravitational waves produced by binaries of black holes and neutron stars. Kevin will continue his passion for physics in graduate school, where he hopes to earn his Ph.D. in the physical sciences.



Man Lou

Man Lou is a senior pursuing a Bachelor of Science in Biochemistry, looking forward to graduation in spring 2016. He is enrolled in undergraduate research in Dr. Rasche's lab. The lab gave him many valuable social and lab experiences in biochemical research. This year, Man is the NSM-ICC representative for Chemistry and Biochemistry Club. With one more year until graduation, Man has not decided what he wants to do after graduation. As of now he is thinking of entering a career in teaching or industry, or pursuing a Master's degree.



Joshua McKinley

Joshua McKinley is a senior pursuing a Bachelor of Science degree in Biological Sciences with a concentration towards Cellular and Developmental Biology. Joshua is passionate about marine biology and mentoring students. He has multiple mentoring opportunities through various on-campus programs such as S.T.E.M², S.U.C.C.E.S.S and B.U.R.S.T. Joshua is also a supplemental instructor for Cellular biology where he helps reinforce course material. Joshua plans on becoming a physician and mentoring underprivileged and underrepresented groups to become more involved in STEM and medical careers. When not performing research or focusing on his academics Joshua can be found playing the piano, his favorite hobby.



Alicia Mendoza

Alicia Mendoza is a senior pursuing a Bachelor of Science in Biology. She anticipates graduating this Fall. She then plans on applying for the Teaching Credential Program at California State University, Fullerton for Spring 2016. Her goal is to accomplish a single subject teaching credential in Biology and possibly also in Math. She has worked in the lab of Dr. Joel Abraham for two semesters, where she has researched graphing in introductory biology textbooks. She plans on taking the information she has gained while researching the issues students struggle with, concerning graphing to help better prepare her future students.



Theory Monh

Theory Monh is a graduating senior majoring in Chemistry. With his degree he hopes to continue his studies into graduate school with a Masters in Environmental Engineering. Along with his studies, Theory is involved with the ASI Environmental Sustainability Committee as the director. Currently, the committee is involved in a collaborative effort with the CSUF Center for Sustainability, Facilities and Operations, and other student clubs and organizations in planning for this year's Earth Week. In his spare time, Theory also freestyle dances and is the vice president for the Titan Break Club, the breakdancing club on campus. The club serves as an outlet for students to creatively express themselves in hip hop.



Rosa Murrieta

Rosa Murrieta is a first generation and transfer student pursuing a Bachelor of Science degree in Geology, and is set to graduate for the Spring of 2017. This Spring Rosa is immersed in a Geological Field Techniques course, investigating the regional geology of Rainbow Basin, and the Marble Mountains. For the fall, she plans to begin her thesis with a focus in environmental hazards. When she is not immersed in her coursework, Rosa can be found fulfilling her student and or family obligations.



Erick Ortega

Erick Ortega recently graduated in the fall of 2014 with a Bachelors of Arts in Applied Mathematics. Currently, he is working on research involving magnetic resonance imaging (MRIs) with Dr. Angel Pineda. He is interested in pursuing a career in data science and plans to enroll in the Masters in Statistics program offered at California State University, Fullerton in the fall 2015. When Erick is not working on research, he spends his time consulting with companies to develop web-scraping programs that streamline workflow.



Daniel Philo

Daniel Philo graduated *cum laude* from Cal State Fullerton in 2014 with a Bachelor's of Science in Geology. He is currently pursuing a Master's of Science in Geology at Fresno State. As an undergrad, Daniel's research focused on seismology, and while he found this interesting, his current research is on carbonate sedimentology and stratigraphy. Specifically, Daniel is quantifying sea-level changes through time by examining cyclic variability in accommodation space in Devonian carbonates. Daniel is also a teaching assistant at Fresno State, where he teaches several geology labs. After earning his master's, Daniel plans on continuing his career in geology by entering the petroleum industry.



Cristy Rice

Cristy Rice is graduating summer 2015 with a B.S. in Biology and an emphasis in Marine Biology. She was selected as a Southern California Ecosystems Research Program (SCERP) scholar in the Summer of 2012 and as a Biology Undergraduate Research Student Training (BURST) program scholar in Spring 2014. As well as being in the process of submitting her research for publication, her work will contribute to a dichotomous identification key for the pipefishes. She has presented her work at numerous symposiums and conferences and won a research grant, best poster award, and honorable mention for oral presentation from the Southern California Academy of Science annual meetings. She plans to pursue graduate school to study ichthyology, fisheries biology, and ecology.



Rudolph Saenz

Rudolph Saenz is a senior pursuing a Bachelor of Arts degree in Mathematics, concentrating on Probability and Statistics. He is set to graduate this spring. This fall, he plans to begin his Masters in Statistics program at California State University, Fullerton. When he is not immersed in coursework, Rudolph is studying material for exams from the Society of Actuaries and Casualty Actuarial Society. After his master's degree, he plans to pursue a career in the actuarial field and is also considering pursuing a Ph.D.



Emily Sanchez

Emily Sanchez is a senior finishing her last semester at CSUF, and will be graduating with a Bachelor of Science degree in Biological science with a concentration in Ecology, Biodiversity and Conservation. She is a second year scholar in the Southern California Ecosystems Research Program (SCERP) at CSUF and works in Dr. Christopher Tracy's physiological ecology lab. Her work, investigating sex differences in the thermoregulatory activity of common chuckwallas, will culminate in a senior thesis. After graduation, Emily plans to find volunteer or short-term positions in ecological research before returning to graduate school the following year. When she is not busy with coursework and research, you can find Emily camping or hiking with her friends, family and/or dogs.



Greg Shagam

Greg Shagam graduated from California State University, Fullerton in 2012 with a BS in Geological Sciences and a Minor in Business Administration. During his academic career at CSUF, Greg received the John D. Cooper Field Camp Award for exemplary performance during field camp in Montana. He also received recognition by winning best undergrad thesis poster at the Annual Geology Research Day. Working under Dr. Phil Armstrong as his thesis advisor, Greg spent many weekends in the field surveying the fault geometries of the SNFFZ in the vicinity of Lone Pine & Independence, Ca. He is currently working as a Project Geologist for GeoKinetics, a geotechnical and environmental engineering firm in Irvine, where he is accruing work experience to be able to take the P.G. Exam in October 2015.



Christina Tran

Christina Tran will obtain her Bachelor of Arts degree in Mathematics this spring. Working as a Supplemental Instruction leader and Math Circle facilitator solidified her career path of studying and researching mathematics education. Working on several research projects as a McNair Scholar under Dr. Bogdan Suceavă led to her interest in pursuing her Master's Degree and later her Ph.D. After presenting her research at the MAA Mathfest 2014 in Portland, Oregon, she fell in love with Portland State University, which is where she will begin her graduate studies this fall. Before she immerses herself in the rigor of graduate coursework, she plans to travel to her favorite U.S. cities.



Erick Venegas

Erick Venegas is a senior Mathematics major at California State University, Fullerton. His research allows him to apply modern statistical approaches in order to assess the significance between variables on categorical data. Participating in research also allows him to achieve a deeper appreciation for the study of statistics and its applications. He is very grateful to be accepted into the Louis Stokes Alliance for Minority (LSAMP) Research Scholarship Program and is committed to grow as a researcher. He will graduate in spring 2016 and is planning to apply to the Masters in Statistics program at Cal State University, Fullerton.



Daniel Weiherer

Daniel Weiherer is pursuing a B.S. in Biological Science with a concentration in Ecology and Evolutionary Biology. He has a strong interest in Ecology and Botany among many other disciplines. Daniel has received roughly two years of experience preparing, curating, and researching fossils at the Cooper Center through participation in internships, volunteering, and working. He also is conducting research in a physiological plant ecology lab. Additionally, this summer Daniel is going to Thailand to perform biological research at Chiang Mai University through the SMRT program. Finally, after another year he will graduate and continue on to obtain a graduate education in Biology. Ultimately, through his passion for the outdoors, Daniel wants to conduct biological research in the field.



Liz White

Elizabeth White is an alumni who completed her BS in Geology (2014) at CSUF, and is now pursuing her MS in Geology at San Diego State University. Her current research focuses on the effects of orbital forcings on Neogene diatomaceous shales in Baja California, Mexico. She is an active member and secretary of SDSU's American Association of Petroleum Geologists (AAPG) Student Chapter, and also is participating in the 2015 Imperial Barrel Awards Program. When not completely immersed in her studies, Elizabeth is an avid rock climber and spends the majority of her free time traveling in search for new mountains and rock faces to scale



Alex Woodward

Alexandre Woodward is a senior pursuing a Bachelor of Science degree in Geology. He is set to graduate this fall after attending field camp and investigating the regional geology of Montana at the University of Montana-Western. He also traveled to Thailand as part of the Earth Science in Thailand (ESIT) class offered as a joint program between CSUF and Chiang Mai University last Summer. For the last two years Alex has been the laboratory technician for the CSUF Kirby Paleoclimatology and Paleotsunami Laboratory run by Dr. Kirby. When he is not in the laboratory he can be found hiking in the local Santa Ana Mountains

About the Editors



Neha Ansari

Neha Ansari, a President's Scholar, will graduate Magna Cum Laude with a Bachelor of Science in Biochemistry. Neha has served as an Orientation Leader, the Chemistry and Biochemistry Editor for Dimensions Science Journal, and as a member of the ASI Board of Directors. This past year, she was elected Chair of the ASI Board of Directors and served on the Academic Senate and Titan Student Centers Governing Board. Neha has also worked in Dr. Peter de Lijser's research lab on campus, participated in the Amgen Scholars Program at the University of Washington, and was awarded Outstanding President's Scholar of the Year in 2014 and the Titans Leaving Their Legacy Award in 2015.



Reina Galvez

Reina Galvez is a California State University, Fullerton graduate with a Bachelor of Arts in Mathematics and is currently a Mathematics Single Subject Teaching Credential candidate. Reina is the current editor-in-chief for Dimensions. During her time at CSUF, she has always been involved in many areas of NSM. She would like to thank Dr. Margaret Kidd, Amy Mattern, and Dr. Sam Behseta for helping cultivate the successful young woman she is today.



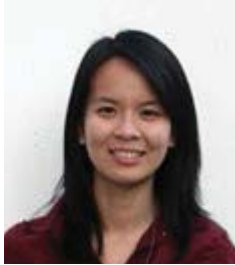
Niv Ginat

Niv Ginat is a graduating graphic design student from Los Angeles, California. Motivated by his love for design and hunger for knowledge, Niv draws his experience from a wide range of projects that he has worked on since embarking on his creative journey. In 2013, he was awarded the Jerry Samuelson Scholarship for his commitment and artistic potential as a graphic designer. He hopes to one day be able to carry his work with him as he travels around the world.



Alfred Harris III

Alfred Harris is a graphic designer from Pomona, California. Driven by his relentless passion for design and knowledge, Alfred continually strives to become better and improve his creative abilities and understanding. In 2014, Alfred was awarded the Jerry Samuelson Scholarship for his commitment and his promise as an artist. He hopes that his passion can one day help improve the lives of those around him.



Shiline Nguyen

Shiline Nguyen is an undergraduate student at CSUF where she is pursuing a Bachelor of Arts degree in Mathematics with a teaching concentration. With an undeniable passion for teaching, she also plans to attend their credential program. She is very involved with the Math Club, S.M.A.R.T. Girls Support Group, tutoring, grading, and supplemental instruction. Aside from math and teaching, Shiline loves to expand her understanding of the world by travelling to Vietnam, Australia, and Europe. She would like to thank her network of teachers, and math professors for their unconditional support and guidance.



Phillippe Diego Rodriguez

Phillippe is currently a third year physics emphasis business major. Phillippe is part of University Honors Program, Dan Black Physics Business Program, and Cal State D.C. Scholars Program. With an interest in both physics and business, Phillippe plans to obtain a career in aerospace and defense program management. Phillippe stays involved on and off campus as an officer in multiple physics and business organizations, a presidential appointee, and a youth soccer coach. Currently, Phillippe is working with Dr. Jocelyn Read on the Orbital Dynamics of Merging Neutron Stars for his Senior Honors Project. After his undergraduate education, Phillippe plans to attain a Master of Business Administration degree.



Matt Scanlon

Matt is a senior finishing up his last semester at CSUF, graduating with a degree in Biological Science with a concentration in Marine Biology. He is a Southern California Ecosystems Research Program (SCERP) scholar, working in Dr. Kristy Forsgren's fish reproductive physiology lab. His project compares the reproductive health of California halibut among locations in southern California. Matt plans to attend graduate school after graduation and eventually wants to be a fisheries biologist. He had a great time being the Biology section editor member of the Dimensions team. Matt loves the beach, good music, and baseball.



Jazmine Titular

Jazmine is currently an undergraduate and will be earning her Bachelor of Science in Geology during summer 2016. She is currently editor for the Department of Geology in Dimensions. Jazmine has been actively involved with (STEM)², LSAMP, and the Geology Club. In her free time, she enjoys spending time with friends and family, as well as enjoying nature by participating in nature activities.